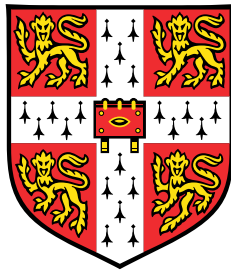


Transition-Edge Sensors for Electron Spectroscopy



Kunal Manish Patel

Department of Physics
University of Cambridge

This dissertation is submitted for the degree of
Doctor of Philosophy

Selwyn College

August 2023

Declaration

I hereby declare that except where specific reference is made to the work of others, the contents of this dissertation are original and have not been submitted in whole or in part for consideration for any other degree or qualification in this, or any other university. This dissertation is my own work and contains nothing which is the outcome of work done in collaboration with others, except as specified in the text and Acknowledgements. This dissertation contains fewer than 60,000 words, including summary/abstract, tables, footnotes and appendices, but excluding table of contents, photographs, diagrams, figure captions, list of figures/diagrams, list of abbreviations/acronyms, bibliography and acknowledgements.

Kunal Manish Patel

August 2023

Acknowledgements

Firstly, I am extremely grateful to Prof. Stafford Withington for his years of supervision and continued support and guidance from the very start of this project, in particular his ability to look further and show me the value of my own work! I would also like to thank Dr. Alex Shard for his considerable help in this project, not just with everything electron-related, and who was instrumental in making this PhD such a rewarding experience.

I am very thankful to Dr. David Goldie for all of his training and advice regarding TESs and for all of his help in setting up my first electron and electric field measurements. I am also grateful to Dr. Chris Thomas for his help across so many topics but especially his tireless work with Michael Crane fabricating TESs for this project.

Dennis Molloy and David Sawford have both been incredibly important in all aspects of the experimental work in this project, helping to design and then creating many different components, followed by troubleshooting whenever I decide to make a change!

I would also like to thank Songyuan, Emily, Tess, Jonah, Rebecca for being so welcoming when I first joined the group, before we were all separated by COVID lockdowns. I should thank Rebecca in particular for also providing excellent detectors that ended up being extremely useful for measuring electrons!

During my too brief time at the National Physical Laboratory, I was fortunate to meet so many great people but I am especially thankful to Steve Spencer, Dr. Ben Reed and Dr. David Cant in particular for all of their help in teaching me how to use the XPS system, and supporting my experiments.

I would like to thank Prof. Stephan Hofmann for all of his assistance in administrative aspects of my PhD and especially in navigating the last stretch of my PhD. I am also appreciative to the rest of the EPSRC CDT in Nanoscience and Nanotechnology (NanoDTC), both for funding my PhD studentship and for the great community within it. I am especially grateful to all of the members of my cohort; I have a hard time imagining a better group to have gone through this PhD with.

The list of acknowledgements would not be complete without including my family, and so I have to thank my brother for always being there to offer help when needed. Finally, and

most important of all, is my thanks for my parents for everything they have done to provide me with the ability to choose what I wanted to do knowing they are there to support me.

Transition-Edge Sensors for Electron Spectroscopy

Kunal Manish Patel

Transition-edge sensors (TESs) are highly-sensitive detectors capable of both radiative flux and single photon measurements. TESs have found a number of applications including astronomical photon measurements, neutrino mass measurements and in the search for dark matter. Despite this versatility, the use of TESs as massive particle spectrometers has received remarkably little attention, notably within the field of electron spectroscopy where TESs could provide significant advantages over existing electron spectrometers. In this thesis, I present the first investigation into the capabilities of TESs in electron spectroscopy using a combination of numerical simulations and experimental measurements. Through the use of numerical simulations, I show that TESs are capable of matching the energy resolution of traditional electron spectrometers whilst providing order of magnitude improvements in measurement efficiency. I then describe the design and testing of a TES electron detection system that I used to perform a set of proof-of-principle TES electron measurement experiments. The results of these experiments are presented, showing the successful detection and energy measurement of individual electrons with energies spanning between 0 and 2000 eV with an energy resolution of 3 eV. An important consideration for TES electron spectrometers is their sensitivity to electric and magnetic fields arising from nearby electron optical components. The sensitivity of TESs to magnetic fields has been investigated before, but the impact of strong electrostatic fields on TESs has not been. I show that the application of electric fields up to 90 kV m^{-1} had no observable effect on the TESs tested, demonstrating that TESs can be operated in strong DC field environments, as may be found in TES electron spectrometers. Having demonstrated the suitability of TESs as electron spectrometers, I then present designs for a set of TESs, made specifically for electron calorimetry with a dedicated electron absorber structure. I show the results of a set of electron absorption measurements used to determine appropriate materials to be used in this structure. I conclude the thesis by summarising the capabilities and benefits of TES electron spectroscopy as well as the challenges that will need to be overcome to realise this technology.

Table of contents

List of figures	xiii
List of tables	xxv
1 Introduction	1
1.1 Overview	1
1.2 Introduction to Electron Spectroscopy	2
1.3 Concentric hemispherical analysers	3
1.4 Introduction to TESs	6
1.5 TES Applications	9
1.6 Comparison with CHAs	11
1.7 Thesis Outline	13
2 TES Calorimetry Theory	17
2.1 Introduction	17
2.2 Basic Calorimetry	17
2.3 TES Calorimetry	18
2.3.1 Thermal Response	19
2.3.2 Electrothermal Response	23
2.3.3 Energy Integral	25
2.4 Saturation Energy	26
2.5 Energy Resolution	27
2.6 Large-Signal Response	29
2.7 Conclusion	31
3 TES Electron Spectroscopy Simulation	33
3.1 Introduction	33
3.2 Simulation Model	33
3.2.1 Data Simulation	34

3.2.2	Data Analysis	40
3.3	X-ray Photoelectron Spectroscopy Simulation	43
3.4	Fisher Information	45
3.5	TES Electron Spectrometer Requirements	49
3.6	Conclusions	53
4	Electron Measurement System	55
4.1	Introduction	55
4.2	Overview	55
4.3	Electron Source	56
4.4	Electron Beam Pathway	59
4.4.1	Heat Shield Modifications	59
4.4.2	Magnetic Shielding	61
4.4.3	TES Module Modifications	62
4.4.4	Graphite Target Fixture	65
4.5	TES Measurement System	66
4.6	Software	70
4.7	Conclusions	74
5	Experimental TES Electron Calorimetry	77
5.1	Introduction	77
5.2	Direct Beam Experiments	77
5.2.1	Initial Measurements	77
5.2.2	Realigned Measurements	87
5.3	Scattered Beam Experiments	95
5.3.1	Initial Measurements	95
5.3.2	Reduced Secondary Electron Measurements	103
5.3.3	Grounded Target Measurements	111
5.4	Conclusions	115
6	TES Electric Field Sensitivity	117
6.1	Introduction	117
6.2	Apparatus	118
6.3	Static Field Measurements	119
6.3.1	TES I-V	119
6.3.2	TES Response	122
6.4	Dynamic Field Measurements	125

6.5	Conclusions	127
7	Electron Calorimetry TES Design	129
7.1	Introduction	129
7.2	Electron Absorption Measurements	130
7.2.1	Candidate Materials	130
7.2.2	Absorption Efficiency Measurement Apparatus	132
7.2.3	Absorption Efficiency Results	134
7.3	TES Design	137
7.4	R-T Characterisation	145
7.5	Conclusion	148
8	Outlook for TES Electron Spectroscopy	155
8.1	Introduction	155
8.2	Spectrometer Design Considerations	156
8.2.1	Temperature and Pressure	156
8.2.2	Energy Resolution	157
8.2.3	Electron Absorption Efficiency	158
8.2.4	Count Rate	161
8.2.5	TES Geometry	163
8.3	TES Electron Spectrometer Configurations	165
8.3.1	Direct Spectrometer	165
8.3.2	Hybrid Spectrometer	166
8.3.3	Bolometric Spectrometer	168
8.4	Electron Coincidence Spectroscopy	169
8.5	Conclusion	174
9	Conclusions	177
9.1	Summary of Key Results	177
9.2	Future Outlook	180
	References	183

List of figures

1.1	Operating principle of a concentric hemispherical analyser.	3
1.2	Positional measurement of incident electrons using microchannel plate in combination with a delay-line detector.	5
1.3	Difference in TES response between bolometric and calorimetric measurements.	7
1.4	Timeline of past and future projects utilising TES measurement across a range of applications.	8
1.5	TES energy resolution limit plotted against transition temperature and TES saturation energy. The values have been calculated for a device with $n = 2$	12
2.1	Response of a thermal calorimeter to the absorption of a particle with energy E_k	18
2.2	TES calorimeter response to a particle absorption event in terms of TES resistance (left) and current (right). At time 1, the particle is absorbed with the TES response occurring over the region of 2.	22
2.3	TES bias circuit with TES resistance of $R(T)$, bias voltage V , load resistance of R_L and inductance L	23
2.4	TES temperature and current response to a thermal impulse at time zero numerically calculated from Eqn. 2.24 and Eqn. 2.25.	24
2.5	Estimation of superconducting transition width in temperature assuming a linear resistance-temperature dependence. The normal state resistance (R_n) and central transition temperature (T_c at $R = R_n/2$) are marked. TES saturation energy can be estimated as $C\Delta T$ where C is the TES heat capacity.	26
2.6	Variation of measured TES response shapes with TES bias voltage. The TES bias point is shown as a fraction of the normal state resistance, R_n	27

2.7	a) Average TES pulse shapes grouped by measured event energy, from Section 5.3.2. b) TES event energy plotted against averaged maximum pulse current. In both plots, the event energy has been calculated from the area beneath the peak.	29
3.1	Software block diagram showing the steps used to generate and analyse simulated TES measurement data. The green block represents the particle source properties including energy spectrum, purple blocks describe TES properties. Steps used in the construction of the simulated dataset are shown in orange, and data analysis is shown in blue.	34
3.2	Random sampling from probability density function $P(x)$ using inverse transform sampling. A set of uniform random numbers are represented as the horizontal lines intersecting $F(x)$, the cumulative distribution function of $P(x)$. The vertical lines represent the output after transformation by $F^{-1}(x)$	35
3.3	Generated particle events inserted into a time series with randomly generated or periodic arrival times. The pulsed source shows periodic pulses with a given pulse duration therefore allowing multiple electrons per pulse. In this example, the pulse width is smaller than the sampling frequency and so the particles events are concurrent. The different electrons have been distinguished by colour.	36
3.4	Simulated TES measurement using the random arrival time particles and energies in Fig. 3.3. Dashed lines show the particle arrival times.	37
3.5	Scaled secondary electron energy distributions relative to the vacuum level, calculated using Eqn. 3.5 using work functions of 3 eV (red line) and 5 eV (black line)	39
3.6	Measurements of total electron yield emitted from highly-oriented pyrolytic graphite (HOPG), titanium, niobium and gold samples at various primary electron energies.	40
3.7	a) Identification of a particle measurement event from a simulated TES measurement. The lower horizontal line represents the noise threshold and the upper line is the event threshold. The dashed vertical lines show the calculated data segment containing the event. b) Output of matched filter applied to (a) with vertical lines showing the identified particle arrival times. c) Calculated particle energies using a least-squares minimisation procedure overlaid onto the measurement data.	42

3.8	a) Noise-free XPS spectrum of silver from SESSA simulation software [100]. b) Simulated measurement of XPS spectrum from (a) using a 100 μs response TES sampled at 10 MHz for 1000 s. The input electron rate was set at 1000 s^{-1} . The ideal line in black represents the observed spectrum in the case of where every electron energy is measured perfectly. The red measured line is the result after applying the data analysis method to the data. Reproduced from [101].	44
3.9	Simulated measurement of the XPS spectrum of silver with the inclusion of secondary electron losses. The simulation was performed in the same manner as Fig. 3.8 but including secondary emission from an absorber with 4.8 eV work function.	45
3.10	Measured energy spectra of monoenergetic 1000 eV electrons at different simulated noise-equivalent powers (NEPs). Each simulation was performed with a detector response time of 100 μs at a 100 MHz sampling frequency measuring 5×10^5 electrons. The observed energy resolutions are compared (ΔE_{meas}) with the Cramer-Rao lower bound (ΔE_{CR}) calculated from Eqn. 3.26. Reproduced from [101].	48
3.11	TES energy resolution limit across a range of transition temperatures and saturation energies. For reference, the aluminium $\text{K}\alpha$ energy has also been shown.	49
3.12	Effect of different pileup rates (λ) on the measured XPS spectrum of silver. Every simulation was performed with a 100 μs response time TES sampled at 20 MHz measuring 5.75×10^5 electrons. $\lambda = 0$ was simulated using periodic electron arrivals spaced at $10\tau_{\text{eff}}$ λ of (b) 0.05, (c) 0.1 and (d) 0.5 were simulated using random particle arrival times with mean fluxes of arrival rates of 500 s^{-1} , 1000 s^{-1} , 5000 s^{-1} , respectively. Partially reproduced from [101].	50
4.1	TES electron measurement experiment in the scattered electron measurement beam configuration.	57
4.2	a) CC-ADR cryostat with mounted electron source used for electron measurement experiments. b) 4 K stage with TES module mounted to 100 mK stage in the direct beam configuration.	57
4.3	a) Electron source assembly mounted onto the cryostat vacuum jacket. b) Faraday cup and aperture into cryostat.	59

4.4	a) 4 K (top) and 45 K (bottom) brass tubes and aperture assemblies for confining stray electrons and reducing infrared radiation entering the cryostat. b) Optical microscope image of 1500 lines per inch copper mesh.	60
4.5	Estimated electron beam deflection due to ambient magnetic fields. The coloured regions represent different components the beam passes through from the tip of the electron source to the devices. The cryostat entrance includes both the gate valve and cryostat vacuum jacket window. Beam paths were calculated under magnetic fields of $40 \mu\text{T}$ and shielding was assumed to reduce the magnetic field by a factor of 5 in each region except for the cryostat entrance which was left unshielded. Labelled distances show the separation between the beam path and the central axis at the entrance aperture of the 45 K tube.	62
4.6	a) TES module entrance and device clamping. b) Front and rear faces of the TES aperture plate with an array of 30 $200 \mu\text{m}$ holes.	63
4.7	a) Two TES module arms used to mount the module on the 100 mK stage for direct and scattered beam experimental configurations shown in b) and c), respectively.	63
4.8	a) Graphite target holder with graphite foil clamped in place and connected to two bias wires. b) Graphite target mounted onto 4 K tube and positioned in front of TES module. c) Collimator aperture fixed onto the target holder to block off-axis electrons reaching the detectors. d) Fully-assembled graphite target, surrounded by an aluminium cup and foil to contain scattered electrons.	65
4.9	Microscope images of a) $70 \mu\text{m}$ and b) $20 \mu\text{m}$ width Mo/Au TESs without gold bars, suspended on four silicon nitride legs.	67
4.10	Circuit diagram of the TES bias and two-stage SQUID amplifications. . . .	68
4.11	a) - d) Beam current images of the Faraday cup measured at different electron beam energies. White regions represent net electron absorption, orange colours show net electron emission and black shows no net current measurement. e) - h) Beam current images from a) - d) with superimposed differences between current measurements with and without magnetic shielding around the electron source chamber. Blue colours show an absolute decrease in current measurement by adding shielding and red shows absolute current increase. The images all display the cup appearing to shift to the right after adding shielding to the chamber.	70

4.12	a) Custom box lid with four copper pads, each with its own electrical connection for current measurement. b) - f) Beam current images at different beam energies measured through the four pads and the 4 K aperture (labelled as plate).	71
4.13	a) Software block diagram of the synchronised beam scan and TES data collection procedure. b) Measurements of different initiation pulses as recorded by the TES measurement PC.	73
4.14	a) Beam current images of the Faraday cup as recorded by a) the electron source controlling PC and b) TES measurement PC. Both images were recorded simultaneously with the image divided into 20 second recording segments.	73
5.1	a) Voltage-current relation of a 100 μm square, voltage-biased Mo/Au bilayer TES. Measurement was performed at 120 mK. b) Voltage-resistance corresponding to the measurement in (a).	78
5.2	Power flow of TES 24 from the TES to the thermal bath. Each measurement was taken on different days following initial cooldown of the cryostat to 4 K. All data were taken at a nominal bath temperature of 120 mK.	79
5.3	Current noise spectral density (NSD) of TES 24 measured at 120 mK. The black line shows the fitted roll-off for a TES with 1.6 ms τ_{eff}	80
5.4	Change in TES current from equilibrium, measured at different electron beam angles. The beam was scanned left to right in rows from -7° to -5° in the y-direction. The TES current is shown on a colour scale from black to yellow. A cluster of anomalous events can be seen in the image around 9.6° and -5.7° in the x- and y-directions, respectively.	81
5.5	Time series measurement of TES electron measurements taken using a 2 keV electron beam. The inset shows a measurement event with estimated 190 eV energy.	82
5.6	Electron spectra measured using TES 24 at varying beam energies. The number of counts has been normalised by the peak amplitude with a energy bin width of 1 eV.	84
5.7	Average rate of electron measurement events plotted versus applied beam current.	86
5.8	a) Average TES shape due to different measured event energies, measured at 0.1 R_n TES bias point. b) Maximum pulse height in (a) plotted against calculated energy. c) Variation of TES response shape with TES bias voltage. The TES bias point is shown as a fraction of the normal state resistance, R_n	86

5.9	a) Voltage-current and b) voltage-Joule power relations of TES 24 measured at varying temperatures, all taken on the same day.	87
5.10	Measured power plateau values plotted against nominal bath temperatures at which these measurements were taken. The datapoints have been colour-coded based on the number of days passed since the initial cooldown of the cryostat to 4 K. The plotted lines were fitted for each set of measurements taken in the same day using Eqn. 5.6.	88
5.11	Comparison between power plateau measurements of TES 24 in Fig. 5.2 and Fig. 5.9 over time from the initial cooldown for each set of measurements.	88
5.12	Power spectral density of TES 24 measured at 130 mK, $0.25 R_n$ on several days following initial cooldown of the cryostat. The grey line shows the fitted roll-off of a TES with 1.0 ms τ_{eff}	89
5.13	a) Measured electron spectra taken at beam energies spanning 300 eV to 2000 eV. The spectra have been normalised by total area and energy bin widths of 2 eV have been used. b) Ratio between measured energy of the high energy peak and the applied beam energy. The measured peak energy was calculated by applying a Gaussian fit. c) Full-width at half maximum of the fitted high-energy peak plotted against beam energy. The horizontal line at 20 eV is the predicted FWHM resolution limit determined using Eqn. 5.2.	91
5.14	a) Comparison between 1 keV beam energy spectra in Fig. 5.6 and Fig. 5.13 with 1 eV energy bin sizes. b) and c) show the low and high energy regions of the same spectrum. The red dashed line in (c) shows a fitted Gaussian distribution, centred at 890 eV with a 52 eV FWHM.	93
5.15	Equivalent to Fig. 5.14 but with 2 keV beam energy. The red dashed line in (c) shows a fitted Gaussian distribution, centred at 1690 eV with a 44 eV FWHM.	93
5.16	a) Average pulse shapes based on calculated event energy. All pulses were measured using TES 24 at 130 mK nominal bath temperature and at $0.25 R_n$ b) Relation between the maximum pulse height in (a) and calculated event energy.	94
5.17	Measured electron count rate versus beam current collated from a range of beam energies between 0.3 and 2 keV.	94
5.18	Dark time series measurements of the TES 24 and TES 12. The y-axis shows that readout output voltage, before conversion to TES current.	96

5.19	TES voltage-current (a), voltage-resistance (b) and noise spectral densities (c) of TES 12 and TES 24. These measurements were all taken at 130 mK bath temperature.	97
5.20	Calculated Joule heating of TES 12 against applied voltage bias, measured at 130 mK across several days from the initial cryostat cooling to 4 K. . . .	98
5.21	Current noise spectral density of TES 12, measured at 130 mK and $0.25 R_n$, across several days from the initial cryostat cooling to 4 K.	98
5.22	a) Measured electron energy spectrum of 500 eV electron beam scattered off a graphite target. Different bias voltages were applied to the graphite. b) The low energy range of the spectrum in (a).	99
5.23	Total scattered electron distribution of graphite foil measured by [106] using a 500 eV beam.	99
5.24	Map of TES electron detection events plotted against applied electron beam deflection angle. The spot size is proportional to the measured electron energy. The spot colour is determined by the bias applied to the graphite target during the measurement.	100
5.25	a-b) Averaged TES electron detection responses at different event energies plotted on two separate axes for clarity. c) Maximum pulse height in (a) and (b) plotted against measured energy.	101
5.26	a) Voltage-current and b) voltage-resistance measurements of TES 24 performed at 130 mK. c) TES Joule heating against applied bias, measured on several days after initial cooldown to 4 K.	103
5.27	Noise spectral densities of TES 24 measured on several days after initial cooldown to 4 K. Spectra were taken at 130 mK bath temperature and $0.25 R_n$. 104	
5.28	a) Measured electron energy spectra of a 1 keV beam scattered off a graphite target. -20 V, 0 V and 20 V biases were applied to the target. b) Low energy region of the spectrum in (a).	105
5.29	a) Total scattered electron distribution of graphite foil measured from reference [106] using a 1 keV beam. b) - f) Measured electron energy spectra using various beam energies. The beam energy used is shown by the vertical line.	106
5.30	Low energy regions of the spectrum in Fig. 5.29	107
5.31	Electron beam energy plotted against the resulting highest energy electron events measured in Fig. 5.29.	108

5.32	a - b) Averaged TES electron detection responses at different event energies plotted on two separate axes for clarity. c) Maximum pulse heights in (a-b) plotted against event energy. d) Average responses of three different event energies, normalised to the same max amplitude.	109
5.33	a) Electron count rate plotted against beam current. The colour scale shows the time elapsed since the first electron measurement. b) Histograms of number of electron counts plotted against the corresponding x- and y- beam deflection angles. Block colour represents the applied beam current with the blocks stacked sequentially in time from earliest at the bottom and latest at the top.	110
5.34	Noise spectral densities of TES 24 measured on several days after initial cooldown to 4 K. Spectra were taken at 130 mK bath temperature and $0.25 R_n$.	112
5.35	a) Map of the change in TES current from equilibrium, measured at different electron beam angles. The beam was rastered across the plotted range. The TES current is shown on a colour scale from black to yellow. A number of electron detection events are visible in the centre of the scan. b) Plot of electron detection events against beam deflection angle, compiled over a number of scans of a narrow angular region. The spot size is proportion to the measured event energy.	112
5.36	Measured electron count rate plotted against the applied beam current at 1 keV beam energy.	114
5.37	a) Comparison between measured electron energy spectra with 1 keV beam energy in the previous set of measurements (Fig. 5.29 in Section 5.3.2) and in this set Section 5.3.3. Low (b) and high (c) energy regions of the spectrum in (a). The spectra have been normalised by area and have 1 eV energy bin sizes.	114
6.1	a) A suspended Mo/Au TES representative of the design of the $10 \times 10 \mu\text{m}$ device reported here. The inset shows an enhanced depth of field image of a different device with a backing plate pillar visible underneath, for reference. b) Diagram of device and backing plate positions in relation to bias plate and ground.	118
6.2	a) Voltage-current relation of TES 7 measured at 120 mK. b) TES power flow to bath plotted against TES bias voltage measured. Measurements taken at applied plate biases from 0 to 20 V at intervals of 1 V have been overlaid. The differences between measurements are not visible at this scale.	120

- 6.3 a) TES power flow to bath plotted against plate bias voltage from 0 to 20 V, measured at the normal-state resistance ($R_n/2$) TES bias voltage. The error bars were calculated using a standard deviation of the measured temperature variation during each measurement. b) The data in (a) plotted against bath temperature with the V_{plate} colour scale showing the applied plate bias. . . . 120
- 6.4 a) TES response measured at 0 and 20 V applied plate bias. The bottom inset provides the difference from subtracting the 0 V and 20 V measurements. The red line shows the fitted response using a single exponential decay constant. b) The maximum difference between two exponential decays with time constants differing by $\Delta\tau_{eff}$ calculated using Eqn. 6.5 for the exponential fit in (a). 122
- 6.5 a) TES current measured at varying plate bias, V_{plate} with the corresponding current noise spectral densities (NSD) plotted beneath. Plate biases of 5 V, peak-to-peak was applied with 8.2 Hz. b) Repeat of (a) with 5.2 Hz plate bias frequency. c) Asymmetric V_{plate} at 3.1 Hz between -4 and 1 V peak voltages. d) Measurement with no plate bias applied. 124
- 6.6 Same measurements as Fig. 6.5 at 8.2 Hz plate bias frequency from an unbiased superconducting TES (a) and normal state TES (b). The TES readout voltage has been plotted instead of current as the conversion from readout voltage to current is not defined at zero applied bias after correcting for stray resistance. 125
- 6.7 Measured TES bias voltage and sinusoidally varying plate bias at 8.2 Hz plotted on same axes. The corresponding voltage noise spectrum is shown below. 126
- 6.8 a) Voltage-current relation of TES 7 measured at 120 mK with dynamic resistance, R_d , labelled at 34 nV bias. b) Measured TES current at $V_{TES} = 34$ nV with 8.2 Hz plate bias. 127
- 6.9 a) Measured TES current at +34 nV TES bias with varying plate bias. b) Corresponding noise spectral density and c) phase spectrum of the measurement in (a). d-f) Repeat of (a-c) at -34 nV TES bias. 128
- 7.1 a) X-ray spectrometer (XPS) sample holder geometry relative to incident electron and argon ion beams. b) 3D model and c) photograph of the aluminium sample holder designed to position two samples normal to the incident electron beam. The positions of the samples are shown by the red squares in (b), these samples were held in place by clamps screwed into the sample holder. 133

7.2	Absolute drain currents measured from 2.0 keV electron beams on gold (Au), niobium (Nb), titanium (Ti), highly-oriented pyrolytic graphite (HOPG) and the Faraday cup (FC). These measurements were taken with zero applied bias to the sample holder (left) and with 2×9 V batteries (right).	135
7.3	Mean drain currents measured in the Faraday cup at varied electron energies and sample holder biases. The error bars denote one standard deviation range across multiple measurements.	135
7.4	Relative electron absorption efficiencies measured relative to the Faraday cup for different sample materials with the sample holder a) unbiased and b) biased using 2×9 V batteries.	136
7.5	Relative electron absorption efficiencies separated by absorber material. . .	137
7.6	Simplified cross-section view of an example device showing device layers and electrical contacts to the TES and absorber.	140
7.7	Mask drawings of several TES device designs with increasing TES length, horizontally, and increasing absorber area, vertically. The imaged devices correspond to the following device IDs in Table 7.2: a) A4, b) D4, c) L8, d) L6, e) L3, f) B4, g) G4, h) J3.	141
7.8	3D model of a designed electron calorimeter TES. The vertical-scale has been increased to show the ordering and overlap of the contact layers. . . .	141
7.9	Mask drawings of Chip 1 (left) with the Nb grounding layer and Chip 2 without this layer. The colour scheme of this figure follows Fig. 7.7.	142
7.10	Mask drawings of the full 2-inch wafer showing the six device chips surrounded by a set of resolution and test features including two test chips. Each test chip contains 3 completed devices and 3 devices not suspended but on the bulk substrate.	143
7.11	Microscope images of partially processed devices prior to deep reactive-ion etching.	144
7.12	Photographs of a) the top and b) the bottom of the gold-plated device module for mounting the TES and SQUID chips. c) shows the top of the module with the lid in place.	145
7.13	Resistance-temperature dependence of a 150 m Ω TES with labelled transitions. 146	
7.14	Resistance-temperature measurements of three TES bilayers with a) 50 m Ω , b) 100 m Ω and c) 150 m Ω resistances and different applied currents. Each set of measurements shows the resistances measured during heating and cooling. The shaded areas show the data between the 10th and 90th percentiles within 2 mK of the measurement.	147

7.15	The same measurements as in Fig. 7.14 taken for two devices from the test chips in fully processed wafer.	147
7.16	Comparison between resistance-temperature measurements from the initial set of devices, initial devices with heat treatment (HT) and devices from the test chip, separated by TES resistance and applied current. The shading is equivalent to Fig. 7.14 and Fig. 7.15. All measurements were taken while cooling the devices.	149
8.1	TES energy resolution limit plotted against transition temperature and TES saturation energy. The values have been calculated for a device with $n = 2$	157
8.2	Maximum count rate of a 1000 mm ² area TES array at varying device areal densities. The shaded red region delineates the maximum measurement rate of concentric hemispherical analysers (CHAs) with the gradient onset representing the start of nonlinear detector response to high count rates.	161
8.3	a) Example sidecar TES geometry with absorber beside the superconducting TES film, on an island suspended by narrow legs. b) Membrane-suspended TES with the absorber above the TES. c) Position-sensitive TES with two TES films either side of the absorber.	163
8.4	Direct X-ray photoelectron measurement using an array of TESs without electron optics	165
8.5	Hybrid electron spectrometer design where photoelectrons are collected, coarsely dispersed by energy and decelerated prior to measurement by the TES.	167
8.6	TES bolometric array integrated with a concentric hemispherical analyser.	168

List of tables

3.1	Predicted TES performance with the given example set of device parameters where all symbols are as defined in the text. Collection time is the time needed to measure 10^6 particles at the given count rate and array size. . . .	52
4.1	Summary of the devices used for TES electron measurement experiments .	69
7.1	Layer thickness of device components. The ordering of elements in the superconducting bilayer and absorber represent the order of deposition in these structures with the first element being at the bottom.	139
7.2	List of designed TESs with predicted properties at 250 mK transition temperature, 100 mK bath temperature. The response times τ_{eff} , saturation energies E_{sat} and energy resolutions ΔE were calculated from the device properties shown assuming $n = 2$ and $\alpha = 100$ in the small-signal limit.	151
9.1	Predicted TES performance capabilities for arrays designed for high-resolution and high count rate measurements. The energy resolutions (ΔE have been calculated using Eqn. 2.39 and multiplied by a factor of 1.5 for the resolution-optimised array, and 1.75 for the rate-optimised array, to account for sub-optimal performance. The larger factor in the rate optimised array allows for resolution degradation due to the use of multiplexed readout. The count rates have been estimated assuming an average rate of one event every 10 effective time constants ($10\tau_{\text{eff}}$). The saturation energies (E_{sat}) have been chosen to encompass the range of electron energies generated by an Al $K\alpha$ X-ray source.	179

Chapter 1

Introduction

1.1 Overview

Electron spectroscopy encompasses a range of analytical techniques that are vitally important in surface science. In general, these techniques involve measuring the energy of electrons emitted from a sample's surface to probe the properties of the surface itself. As such, the ability to perform these measurements is intrinsically linked to the capabilities of the electron detectors used.

Currently, electron spectrometers perform energy-resolved measurements by filtering the electrons collected by the instrument, allowing only a narrow energy band through to the detector at a time, with the width of this energy band determining the resolution of the measurement. A range of electron energies can be measured by sweeping this energy band across the energy range of interest. However, instruments using this form of energy filtering to provide energy-resolved measurement possess a fundamental inefficiency as the vast majority of electrons collected by the instrument will have energies outside the narrow pass-band, and therefore be discarded. Overcoming this limitation requires an entirely different approach to measuring electron energies, where the detector itself is capable of identifying individual electrons whilst resolving their energies with high accuracy.

Transition-edge sensors (TESs) could be such a detector as they possess inherent, single-particle energy sensitivity. In principle, TESs can achieve orders of magnitude greater count rates over existing electron spectrometers whilst providing high-resolution energy measurement. Despite the potential advantages of TES electron spectroscopy, these devices have not been considered for this application before. Therefore, a preliminary investigation was carried out into the capabilities of TESs as electron spectrometers, the aim of which was to determine if TESs are capable of electron detection and energy measurement, and if

so, whether the capabilities of this type of detector are advantageous over existing electron spectrometers.

1.2 Introduction to Electron Spectroscopy

The field of electron spectroscopy encompasses a range of analytical techniques, widely used in both scientific and industrial research applications. Fundamentally, electron spectroscopy involves the measurement of the kinetic energy distribution of electrons emitted from a sample to understand the elemental, chemical, electronic and structural nature of the sample itself. Electron emission can be initiated using photons, such as in X-ray photoelectron spectroscopy (XPS), or by an incident electron beam, as in Auger electron spectroscopy (AES). In the case of electron energy-loss spectroscopy (EELS), electrons being measured are from the incident beam itself with the magnitude of energy lost in the sample being of interest.

These techniques can be extended to more extreme energy ranges or to consider different aspects of the electron-sample interactions, creating families of related techniques. In particular, XPS has produced a number of related methods including ultraviolet photoelectron spectroscopy (UPS) and angle-resolved photoelectron spectroscopy (ARPES), both used for band structure measurements; and near-ambient pressure XPS (NAP-XPS) where the sample being measured is under an atmosphere greater than 1 mbar, typically between 1 and 10 mbar.

Electron spectroscopy techniques are surface-sensitive by nature of the short mean free path of electrons in solid matter, which is of the order of several nanometres for electrons below 5 keV [1]. As the electron elastic and inelastic mean free paths increase with energy above 100 eV, the electron energy being measured is related to the depth being probed. An example of this is hard X-ray photoelectron spectroscopy (HAXPES) which uses photon energies greater than 2 keV, compared to standard XPS which operates below 2 keV. The increased incident photon energy allows for electron ejection from deeper within the sample, providing information depth more than 10 nm below the sample's surface.

Extending this principle further leads to transmission-based methods such as transmission EELS which are no longer strictly surface sensitive. EELS instruments integrated with transmission electron microscopes use incident electron beams in the range of tens to hundreds of kiloelectronvolts that pass through a thin sample entirely and are measured afterwards. As a comparison, surface-sensitive reflection EELS (REELS) uses electron energies around 1 keV.

Despite the numerous differences, one common feature of all of these techniques lies in the electron analyser. While the design of the analysers are customised for the specific

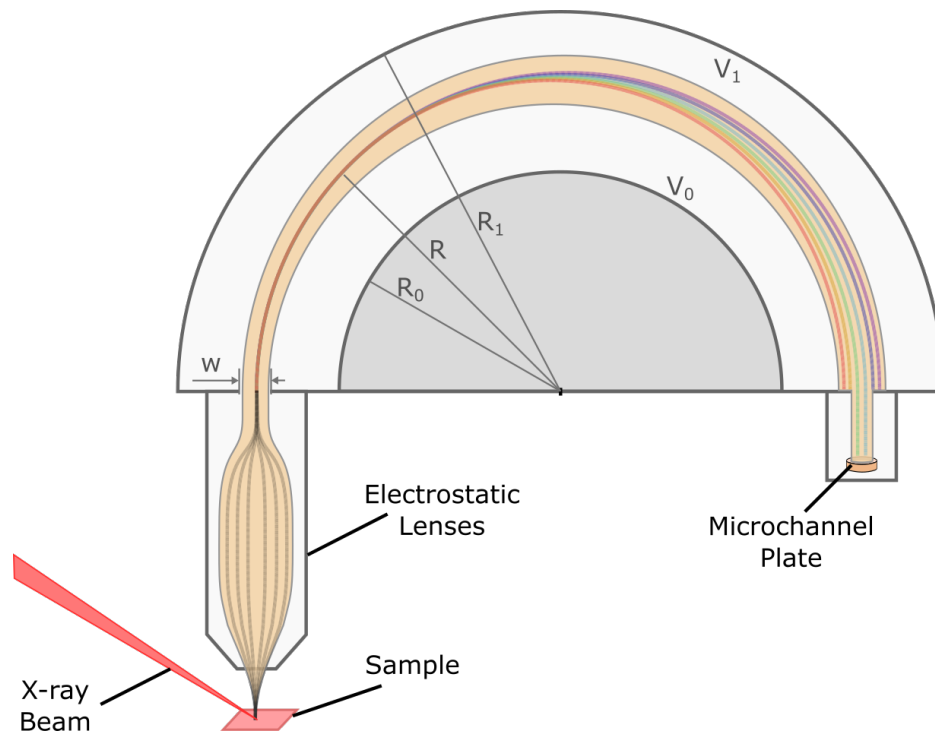


Fig. 1.1 Operating principle of a concentric hemispherical analyser.

application, the fundamental operating principle of modern electron spectrometers is the same: the collected electrons are dispersed by energy and then counted using energy-insensitive detectors. Electron dispersion can be performed in time, as in time-of-flight spectrometers but is most commonly performed in space, which is the principle of the widely-used concentric hemispherical analyser (CHA). Electron detection is often performed using electron multiplier arrays called microchannel plates (MCPs). Higher energy techniques such as transmission EELS do not require electron multiplication and instead can observe single electron events through scintillation or direct detection [2]. In either case, the detection method observes that an electron absorption event has occurred but not its energy. Energetic information is obtained by filtering a specific electron energy range through to the detector.

1.3 Concentric hemispherical analysers

Determining the suitability of TESs within the entire field of electron spectroscopy is a very large undertaking, especially as experimental electron detection using transition-edge sensors has not previously been demonstrated. Therefore, I will focus on comparing the capabilities of TESs to one of the most common types of electron spectrometer, the concentric hemispherical analyser.

Over the last few decades, CHAs have replaced cylindrical mirror analysers and become the electron analyser of choice for the vast majority of XPS instruments. The basic operating principle of the CHA is shown in Fig. 1.1; incident electrons are collected by an electrostatic or magnetic lens and sent between two concentric hemispheres of differing electric potentials. The electrons are deflected to the MCP detector array due to the electric field set up between the two hemispheres. Electrons entering the analyser halfway between the hemispheres tangential to the circle defined by the analyser radius R , with kinetic energy E_p , will follow a path between the two hemispheres and pass through the exit slit and reach the MCP. The relation between the pass energy, E_p and the applied hemispherical voltages is given by

$$E_p = \frac{e(V_0 - V_1)}{R_1/R_0 - R_0/R_1} \quad (1.1)$$

where V_0 and V_1 are the voltages of the inner and outer hemispheres, respectively. R_0 and R_1 are the hemisphere radii and e is the charge of an electron [3]. The energy resolution of a CHA is dependent on the angular distribution of electrons entering the hemispheres and the width of the entrance slit, w . The angular distribution is less significant for the energy resolution of modern instruments with the use of 2D imaging detectors. Neglecting angular distribution effects, the full-width at half maximum (FWHM) energy resolution approximately follows [3]

$$\Delta E = \frac{E_p w}{2R}. \quad (1.2)$$

A key feature of Eqn. 1.2 is that the energy resolution is linearly proportional to the electron energy entering the hemispheres. Therefore, to enhance energy resolution, electrons entering the CHA are decelerated by a known amount depending on the chosen pass energy and the portion of the electron spectrum to be measured. Electrons with energies below the pass energy must be accelerated rather than decelerated to be measured. XPS measurements are taken in fixed analyser transmission (FAT) mode where only electrons with energies near to or above a fixed pass energy enter the analyser. Incident electrons are decelerated and the electrons matching the pass energy travel through the analyser to the microchannel plate. Therefore, at any one time, only a narrow portion of the incident electron energy spectrum is observed; to measure across a spectral range, the deceleration potential must be swept across the energy range of interest. The advantage of FAT mode is the ability to achieve both uniform- and high- resolution measurement of electron energies across the spectrum. A major drawback of this technique is the reduced electron throughput.

The electron throughput of a CHA is defined by its transmission function which is dependent on the incident electron energy, lens settings and slits widths all of which can vary between and during measurements [4]. The transmission function of CHAs vary not just

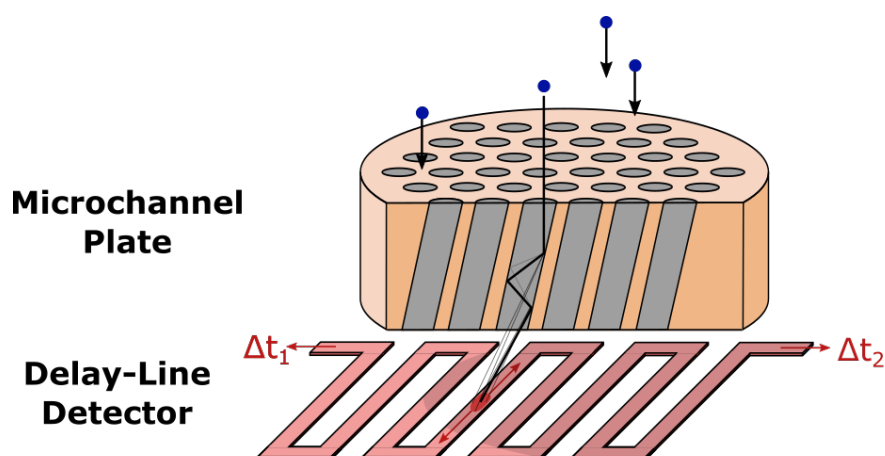


Fig. 1.2 Positional measurement of incident electrons using microchannel plate in combination with a delay-line detector.

with instrument design and settings but also with time meaning that CHAs require regular calibrations to perform quantitative measurements. The importance of this calibration is clearly demonstrated by the wide variety of transmission functions observed across XPS instruments in the inter-laboratory XPS intensity calibration study in [5].

The introduction of delay-line detectors (DLDs) to modern XPS instruments has greatly improved measurement capabilities by providing positional sensitivity across the microchannel plate. An MCP comprises an array of microchannels, each of which acts as an electron multiplier. A single electron striking entering a microchannel results in a shower of electrons escaping the MCP. These electrons strike the delay-line detector creating two charge pulses travelling in opposite directions along the DLD (see Fig. 1.2). The position of the electron interaction can be determined by comparing the times at which the two charge pulses are detected. Accurate, 2-dimensional localisation can be achieved by using two delay lines with orthogonal windings.

One way in which DLDs can be utilised is for 'snapshot' mode measurements. When performing electron measurements, a narrow but finite band of electron energies will pass through the exit slit and reach the MCP. These electron energies will be dispersed by energy and so positional information of an electron detection event conveys a degree of energy information also. By using DLDs, a spectral band of approximately 10% of the pass energy can be measured concurrently in snapshot mode, enhancing measurement rate without compromising resolution [6].

In conjunction with energy spectra, CHAs can be used to collect imaging or angle-resolved measurements. The optics at the CHA entrance are used to collect and accelerate electrons emitted from the sample but also to distribute these electrons across the entrance

slit to the hemispheres. The chosen distribution can be used to maximise signal intensity or energy resolution but can also be used to perform imaging or angle-resolved measurements by mapping electron distribution across the slit to electron emission location or emission angle from the sample.

1.4 Introduction to TESs

Over the last 25 years, transition-edge sensors have become the state-of-the-art energy detectors used in numerous applications including astronomic instrumentation, beamline X-ray spectroscopy, dark matter searches, single photon detection and neutrino measurements [7–13]. Despite the versatility of these detectors, surprisingly little attention has been paid to using transition-edge sensors in massive particle spectroscopy, in particular electron spectroscopy. TESs are superconducting devices that exploit the extreme resistance-temperature relation of a superconductor about its transition temperature to perform highly-sensitive energy measurements. In operation, TESs are cooled to below their superconducting transition temperature and are voltage-biased such that the Joule heating from the device maintains the TES temperature at a fixed point within its superconducting transition. The device temperature is fixed through a negative electrothermal feedback (ETF) loop wherein a change in heat flowing into or out of the detector is counterbalanced by a change in ohmic power dissipation. When absorbing incident particles, the additional thermal energy entering the TES is balanced by a reduction in Joule heating; the corresponding change in the device current can be measured to determine the magnitude of thermal energy absorbed.

TESs can be used for bolometric or calorimetric measurements, as illustrated in Fig. 1.3. Bolometers measure the total thermal power received due to the absorption of a large number of particles, with the particle arrival rate being greater than the detector's relaxation rate. As the bolometer is not sensitive to the individual particle energies but rather the overall absorbed power, these devices require prior filtering of the incident radiation by energy to perform spectroscopic measurements.

TES calorimeters operate in far lower particle flux regimes allowing the device to measure individual particles. The characteristic TES response to a particle absorption event is an exponentially decaying pulse in current. The size of this pulse can be related directly to the particle energy and so no prior energy filtering is required to measure particle energies.

The earliest demonstration of a transition-edge sensor was in 1941 with the bolometric measurement of infrared radiation using superconducting tantalum wire [14]. TES calorimetry was demonstrated in 1949 by measuring the incidence of alpha particles using a niobium nitride film [15]. The improved sensitivity available to TESs over thermistor bolometers and

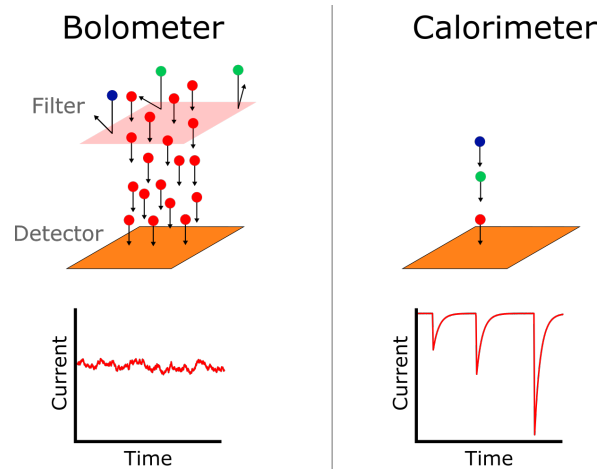


Fig. 1.3 Difference in TES response between bolometric and calorimetric measurements.

calorimeters was apparent and so a variety of TES applications were considered over the following decades, including infrared bolometry, nuclear particle detection, and molecular beam bolometry [16–21]. During this period, due to difficulties in performing low-noise current measurements, TESs were typically current-biased with the output signal being the voltage. Current-biased TESs suffer from major drawbacks such as thermal instability and difficulties in operating an array of current-biased TESs simultaneously, the result of which was that TESs found very few practical applications [22].

These difficulties were overcome in the early 1990s by integrating superconducting quantum interference device (SQUID) readout with TESs [23, 24]. SQUIDs are highly-sensitive magnetometers and so, by inductive-coupling to the TES circuit, can be used for low-noise current amplification of voltage-biased TESs. Unlike with current-biasing, voltage-biased TESs display a negative electrothermal feedback loop (ETF) and a self-regulated device temperature, providing stability against thermal runaway. The negative ETF loop improves TES response time by returning the TES to equilibrium temperature and resistance faster than through heat diffusion alone. The self-regulated device temperature allows for far easier simultaneous operation of TESs within an array as small fluctuations in both temperature no longer render devices inoperable. The introduction of series-array SQUID readout systems in particular provided low-noise, high-gain, wide-bandwidth amplification that could be directly connected to room-temperature electronics, greatly simplifying TES readout systems [25].

A key aspect of TES development in subsequent years was the progression to larger TES array sizes. Directly addressing small arrays of TESs numbering tens of devices is feasible but quickly becomes impractical for larger array sizes where cost, complexity and thermal

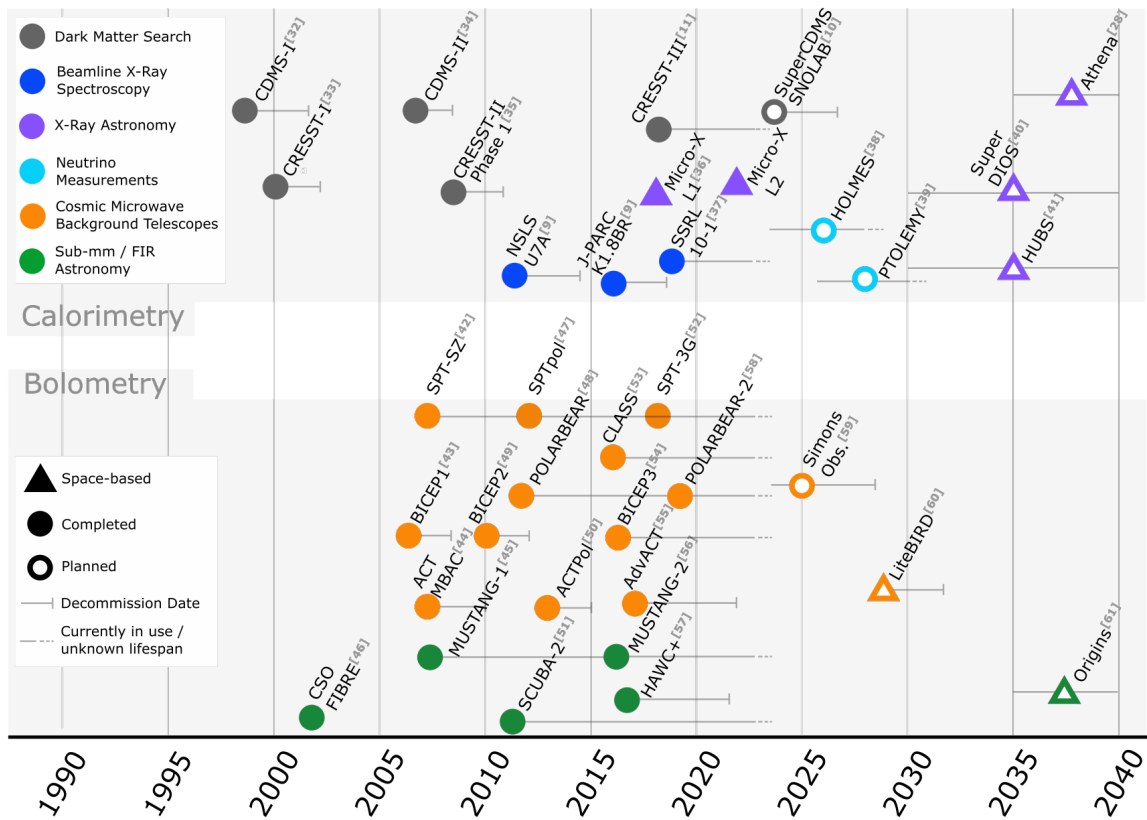


Fig. 1.4 Timeline of past and future projects utilising TES measurement across a range of applications.

loading issues become prohibitive. Therefore, multiplexed readout becomes necessary to increase array sizes further, by allowing readout of multiple devices over a single channel. Several TES multiplexing schemes have been implemented in recent decades including time-division, code-division, frequency-division and microwave-SQUID multiplexing, all with varying bandwidths, multiplexing factors and at different stages of maturity [26, 27]. Arrays of thousands of TESs have been developed using these multiplexing schemes and there is no theoretical upper bound on array size. However, multiplexed readout has its own drawbacks, notably with degraded noise performance. Reductions in energy resolution of 5 - 10% was measured in [28–31] across several multiplexing methods for TES X-ray calorimeters. For many applications, this noise degradation cost is far outweighed by the ability to improve measurement rates by several orders of magnitude.

1.5 TES Applications

TESs arrays have found a number of applications in astronomy, beamline spectroscopy, and fundamental physics research. The excellent sensitivity and energy resolutions of TESs make them the detector of choice for photon-starved applications or when ultra-low noise measurements are needed. These application requirements are reflected in the range of projects utilising TES arrays; a selection of such projects are shown in Fig. 1.4.

The majority of research into TES calorimetry has been focussed on X-ray measurement and dark matter detection, operating in the kiloelectronvolt energy range. The CDMS and CRESST projects are examples of direct-detection dark matter searches. Both projects use TESs to measure phonons produced by interactions with dark matter particles inside large target crystals.

TES X-ray calorimetry was originally developed for astronomical measurements but in recent years TES X-ray calorimetry has progressed towards synchrotron beamline spectroscopy experiments also. Several synchrotron beamlines have utilised TES arrays for a range of X-ray techniques including time-resolved absorption and emission spectroscopy, resonant inelastic X-ray scattering and more exotic measurements such as hadronic atom spectroscopy [9, 37, 62, 63].

The maturity of TES X-ray calorimeters is sufficiently advanced for the development of multiple X-ray space telescopes using TES arrays [28, 41, 40, 29]. The first demonstration of X-ray TESs in space was performed by the Micro-X sounding rocket in 2018, although failure of the attitude-control system prevented time on target for the spectrometer [36]. A second Micro-X flight took place in 2022, the results of which are yet to be published.

Research into TES calorimeters at optical and near-infrared wavelengths has been driven in recent years by quantum communication where single photon detectors with high detection-efficiency are of great importance [12, 13, 64]. At longer wavelengths, TESs are not currently able to effectively discriminate photons by energy. Instead, at far-infrared and microwave wavelengths, TESs operate through bolometric measurement with numerous bolometric TES arrays having been deployed for cosmic microwave background (CMB) and far-infrared astronomy. To date, these projects have been carried out in ground-based observatories across the world but space-based missions are being planned for the 2030s.

Beyond photon measurement, there have been a small number of investigations into massive particle measurement by TESs. TES massive particle measurement dates back nearly to the beginning of TES history with the first demonstration of alpha particle calorimetry in 1949 [15]. TES alpha particle spectroscopy has been considered in more recent years for the purposes of nuclear material detection, with the devices demonstrating measurement of 5.3 MeV alpha particles at 1.06 keV resolution [65]. The direct dark matter searches

spanning back to the 1990s have been also applying TESs with the goal of massive particle measurement. TESs were also briefly considered for use in mass spectrometry in the early 2000s where they demonstrated high particle sensitivity, independent of mass [66, 67].

Recently, TES electron measurement has been examined by a few groups but for applications unrelated to electron spectroscopy and none have yet demonstrated experimental results. The HOLMES and PTOLEMY projects are both developing TESs for electron energy measurement but as a means of indirectly measuring neutrino properties. HOLMES seeks to use TESs to measure the energy of electrons released from the radioactive decay of ^{163}Ho implanted within the TES absorber itself. This decay process emits an electron neutrino and so the electron kinetic energy can be used to bound the mass of the emitted neutrino. Currently, HOLMES has achieved an energy resolution of 4.2 eV calibrated at the 5.9 keV Mn $K\alpha$ X-ray peak [38]. The PTOLEMY project looks to measure the cosmic neutrino background by measuring the energy of electrons released from the capture of electron neutrinos by tritium [39]. The energy scales of the electrons measured by PTOLEMY are far lower than HOLMES, at several eV rather than keV.

Another project to measure low-energy electron using TESs has also recently begun, with the aim of characterising the energy distribution of secondary electrons produced by carbon ion beams for radiotherapy [68]. The measurement of these sub-keV electrons is planned to be performed using very small $1\times 1\ \mu\text{m}$ Ir TESs of 20 nm layer thickness. Complimentary measurements have been previously performed using TESs to measure the energy of the carbon ion beams themselves to improve dosimetry control in heavy-ion radiotherapy [69, 70].

The diversity of projects using TESs demonstrates the versatility of these detectors spanning massless, massive, charged, uncharged and hypothesised dark matter particles, across several orders of magnitude of energy. The lack of research into TESs for electron spectroscopy is a significant gap in the field given the importance and widespread use of electron spectroscopic techniques and the capabilities of TESs as highly-sensitive particle calorimeters. The energy range of interest to electron spectroscopy aligns precisely with that of X-ray spectroscopy where TES arrays have already been deployed for beamline measurements. The following section explores the possibilities that arise from using TESs as electron spectrometers by comparing the measurement method and performance of conventional electron spectrometers to TESs.

1.6 Comparison with CHAs

The combination of energy sensitivity and single particle detection offered by transition-edge sensors opens up a range of possibility when considering TESs for electron spectroscopy. However, identifying the areas in which TESs could provide the most benefit or how this technology could be incorporated into electron spectroscopy is not immediately apparent due to the fundamentally different measurement principles of TESs and existing electron spectrometers. As a first step, we can broadly compare the capabilities TESs and CHAs to understand the differing characteristics of each.

The primary feature to consider is energy resolution. The FWHM energy resolution of the CHA is approximated by Eqn. 1.2. Operated in FAT mode, the resolution is flat across the spectrum and scales linearly with pass energy. A typical XPS analyser with radius R of 200 mm, operating with fixed analyser transmission energy of 200 eV would be capable of providing energy resolutions between 0.1 and 5 eV, using Eqn. 1.2. The CHA energy resolution is dependent on the entrance slit width used, which typically can be varied from 0.1 to 5 mm. The relation between entrance slit width and energy resolution sets up a fundamental trade-off between increasing measurement rate and resolution in a CHA.

The FWHM energy resolution of a TES follows

$$\Delta E = 2\sqrt{2\log(2)}\sqrt{4k_B T_c E_{sat}}\sqrt{\frac{n}{2}}. \quad (1.3)$$

where T_c is the TES superconducting transition temperature, E_{sat} is the saturation energy of the device and n is a device parameter with a value between 2 and 4 that is characteristic of the thermal link between the TES and surrounding thermal bath. Further explanation of this equation is provided in Section 2.5.

The resolution of a TES is not dependent on electron optics but on the detector used and the resolution limit of a TES is not dependent on the energy of particle being measured, up to the TES saturation energy. Beyond the saturation energy, the TES can still perform energy measurement but with reduced sensitivity to the portion of absorbed energy exceeding the saturation energy. The resulting relation between energy resolution and saturation energy is mapped out in Fig. 1.5 across typical TES operating temperatures. The range of TES energy resolutions is comparable to that reached by CHAs, though to match the very best CHA resolutions, TESs require very low temperatures and low saturation energies.

As described previously, CHAs have an intrinsic trade-off between measurement rate and energy resolution. This relation is not present in TESs where energy resolution and count rate can be more easily decoupled. The maximum count rate of a TES calorimeter is determined

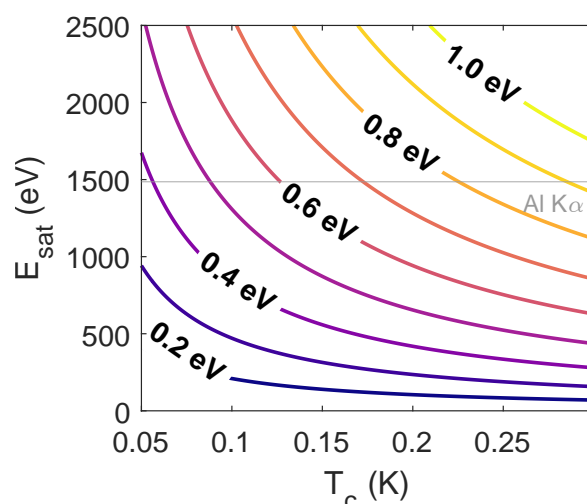


Fig. 1.5 TES energy resolution limit plotted against transition temperature and TES saturation energy. The values have been calculated for a device with $n = 2$.

by the TES response time, discussed in the Chapter 2, and is given by

$$\tau_{\text{eff}} = \frac{nC}{\alpha G}, \quad (1.4)$$

where τ_{eff} is the effective time constant, C is the TES heat capacity, G is the TES thermal conductance to the bath, α characterises the sharpness of the TES superconducting transition and n is a device parameter, characteristic of the TES thermal link as described previously. The TES heat capacity determines the device saturation energy but also the TES response time; larger heat capacities increase saturation energy, worsen energy resolution and lengthen the TES response time. To a good approximation, the observed energy resolution is not dependent on the TES thermal conductance and so the effective time constant can be set largely independent of the energy resolution by changing G .

The specific mechanism by which the TES response time places a limit on count rate is through pileup. Pileup occurs when the TES response to different particles overlaps in time, degrading the ability to measure the energy of either particle. For reference, X-ray calorimetry TESs operating at kiloelectronvolt energies, comparable to XPS and AES measurements, display response times between $100 \mu\text{s}$ and several milliseconds, though response times as low as $40 \mu\text{s}$ for 6 keV photons have been demonstrated [71–74]. The true limit to count rate will depend upon both the TES response time and the ability of the data analysis software to separate partially overlapping events. An important aspect of TES measurement rate capabilities is the parallelisation of measurement using arrays of multiplexed devices. A key

consideration is the combination of array size and TES response time that would be required for the measurement rate of a TES spectrometer to be comparable to a CHA.

As TESs are capable of single particle energy measurements, the available detection efficiency, or ratio of electrons emitted to electrons detected, of a TES spectrometer is far greater than that of a CHA. The most important source of detection inefficiency in a CHA is the requirement for energy filtering prior to detection. Assuming a range of 1000 eV is measured at a 1 eV resolution, this measurement would require at least 1000 steps in energy. At each step, electrons outside the pass energy range would be rejected and so the detection efficiency would be on the order of 0.1%. Detection efficiency is improved by taking snapshot spectra, dispersing the electrons across a 2D detector, but this capability mitigates the underlying inefficiency rather than solving it. In addition, MCPs are not uniformly efficient across the detector area meaning that when taking snapshot spectra, the measurement efficiency will vary across the spectral range. To perform quantitative XPS measurements, the measured portion of the spectrum is typically fully swept across the entire detector so each energy is measured with the same integral efficiency. Quantitative snapshot measurements can be performed but would require careful calibration of the MCP's detection efficiency as a function of position.

As TESs do not require prior energy filtering, the available detection efficiency is not limited and so the achievable measurement efficiency can be increased by orders of magnitude without increasing electron emission from the sample. This is especially important in areas such as XPS where high-intensity, collimated and monochromatic X-ray beams are difficult to produce and could damage the sample being measured. In addition, the TES sensitivity is uniform across particle energies provided the electron is absorbed, and so quantitative measurement and calibration is much simpler.

1.7 Thesis Outline

All of the characteristics of TES calorimetry suggest that TESs are an excellent prospect for electron spectroscopic measurement. However, there is a large span of possibility with regards to both TES spectrometer design and the detector requirements across the range of techniques within electron spectroscopy. As such, there is a need for systematic investigation into the application of TESs to the field of electron spectroscopy.

In this thesis, I present the first investigation into performing electron spectroscopy using TESs. As TES electron calorimetry has not been demonstrated before, there are foundational aspects to consider to determine the applicability of TESs to electron spectroscopy, each of which are examined in the following chapters. The questions that must be answered are

whether TES electron calorimetry can be performed at all and if so whether the combination of energy resolutions, energy ranges and measurement rates offered by TES spectrometers surpass the capabilities of existing electron spectrometers. Finally, is the question of how TESs could be practically integrated into electron spectroscopy measurements.

Chapter 2 provides the basic theory behind TES calorimetry and derives key TES properties such as energy resolution, response time and saturation energies. The response of TESs to energies approaching and beyond the saturation energies are qualitatively considered and methods of analysing such data are briefly outlined in Section 2.6.

Chapter 3 applies TES calorimetry theory to determine the capabilities of TESs in electron spectroscopy through the use of simulated TES electron measurements. I present the design of the TES measurement simulation software, the data analysis software and results from applying the simulation package to the TES measurement of X-ray photoelectron spectra. Fisher information analysis was used to determine the fundamental energy resolution limit of the simulated TESs and to compare this limit to that observed using the data analysis software; in this way, the basic detector capabilities and the performance of the data analysis software were both assessed. The results of these simulations were used to determine if TESs are competitive with CHAs and to establish the device requirements needed by a TES array to match or exceed the capabilities of CHAs performing the same XPS measurements.

Chapter 4 and **Chapter 5** present the first TES electron spectroscopic experiments. Chapter 4 describes the design and assembly of the experimental apparatus used to perform the first experimental TES electron measurements. The chapter provides an overview of the experimental system from the electron source used to the software used to synchronise TES measurements with the electron source. Chapter 5 provides the electron measurement results obtained using the experimental system described in Chapter 4. As electron calorimetry has not been demonstrated using TESs before, the purpose of these experiments were proof-of-principle measurements to determine the feasibility of TES electron calorimetry in the energy range of 0-2000 eV. These measurements were performed using pre-existing Mo/Au bilayer TESs that were repurposed for electron calorimetry tests. Two different experimental arrangements were tested, the first measured electrons directly from the electron source, characterising the measurement of a monochromatic electron beam. The second arrangement measured the electron spectrum scattered off a graphite target, representative of the usage of a TES in an surface science measurement.

The use of electric fields provides a method of controlling the energy range and position of charged particles reaching the detector array, and is an important aspect of any electron spectrometer. For this reason, in order to determine the potential role of TESs in electron spectroscopy, the sensitivity of TESs to applied electric fields must first be understood.

Chapter 6 describes measurements performed to establish the sensitivity of TESs to applied electric fields. The magnetic field sensitivity of TESs has been investigated previously in [75–77] but the potential effects of strong electric fields on TES behaviour has not been considered. In this chapter, measurements of the sensitivity of Mo/Au TESs to applied electric fields up to 90 kV/m are presented, both to static fields and low-frequency AC fields to determine the compatibility of integrating TESs with electron optic systems.

In **Chapter 7**, I present designs of bespoke electron-detecting TESs. The electron absorption properties of various candidate electron absorber materials were tested to identify TES electron absorbers suitable for the initial set of devices. Using the results of these absorption measurements in conjunction with findings from previous chapters, a set of devices were designed for electron spectroscopy and to further understand TES-electron interactions. To my knowledge, these devices are the first TESs to propose integrating electron optics into the detector itself; if successful this would be a powerful tool in both controlling and measuring the interaction of charged particles with the TES absorber. Prototype devices were fabricated and preliminary characterisation of the superconducting bilayers in these devices is provided in this chapter also.

Chapter 8 builds on the experience gained from previous chapters to examine the role TESs can play in electron spectroscopy, comparing the performance of these detectors with CHAs and considering the manner in which TESs could be incorporated into electron spectroscopic instruments with regards to energy-, time- and angle-resolved measurements.

Chapter 9 concludes the thesis by considering the most important aspects of the work performed in this project for the use of TESs beyond electron detection but to TES particle measurements in general. This chapter also highlights future areas of research raised by this thesis of interest to the TES community such as the use of electron optics to screen unwanted charged particles from the detector array. Such a system would be of use in space-based instrumentation where TESs performance is sensitivity to unwanted measurement of secondary electrons from cosmic ray strikes.

Chapter 2

TES Calorimetry Theory

2.1 Introduction

This chapter outlines the theoretical basis by which TESs are used as highly-sensitivity calorimeters and introduces the relevant equations describing their capabilities. The basic theory underlying calorimetry is introduced in Section 2.2 which is then extended to the specific case of TES theory in Section 2.3. The results of Section 2.3 are used to determine TES saturation energies and energy resolutions in Section 2.4 and Section 2.5, respectively. The chapter concludes in Section 2.6 by considering the deviation of TES response in the large-signal limit where the incident particle or photon energy is a significant fraction of the TES saturation energy.

2.2 Basic Calorimetry

Calorimetry operates on the principle that if the heat capacity of the calorimeter is known, the heat flow into or out of the calorimeter can be quantified through monitoring the calorimeter's temperature. For a particle calorimeter, the relevant source of heat entering the detector is the absorption and thermalisation of incident particles. The time-dependent temperature ($T(t)$) of a calorimeter can be calculated from

$$C \frac{dT(t)}{dt} = -P_b(t) + P_{in}(t), \quad (2.1)$$

where C is the calorimeter heat capacity, P_b the thermal power flow from the calorimeter to the surrounding thermal bath and P_{in} is the power absorbed by the calorimeter. In the case of

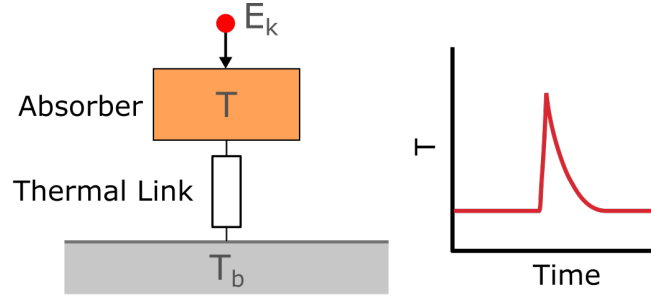


Fig. 2.1 Response of a thermal calorimeter to the absorption of a particle with energy E_k .

discrete particle absorption, neglecting the thermalisation time, P_{in} can be modelled as

$$P_{in} = E_k \delta(t - t_k), \quad (2.2)$$

where E_k is the particle energy, the arrival and absorption of which is described using a delta function at time t_k .

The heat flow to the bath is calculated as

$$P_b = G_b(T(t) - T_b), \quad (2.3)$$

where G_b is the thermal conductance between the calorimeter and the surrounding thermal bath. Inserting Eqn. 2.2 and Eqn. 2.3 into Eqn. 2.1, the temperature response of the calorimeter becomes

$$T(t) = \frac{E_k}{C} e^{-t/\tau} + T_b, \quad (2.4)$$

where the decay constant is $\tau = C/G_b$. The response of a calorimeter to an impulse of energy is an abrupt rise followed by an exponential decay in temperature, the area of which is proportional to the energy received, as shown in Fig. 2.1. The sensitivity and speed of a calorimeter are determined by its heat capacity and thermal conductance, but are wholly dependent on the ability to measure temperature accurately, precisely and quickly. Temperature measurement is central to calorimetry and the defining characteristic between different calorimetric techniques is the method by which temperature is monitored.

2.3 TES Calorimetry

Transition-edge sensors use the steep resistance-temperature dependence of a superconductor within its superconducting transition to perform precise power and energy measurements. TESs operate by voltage-biasing a superconductor that is held at its superconducting transition

temperature (T_c). External thermal power that enters the TES, such as from particle absorption events, will increase the temperature of the TES which will thereupon display a greater electrical resistance. By measuring the TES current during this time, the change in TES resistance and, therefore temperature, can be determined. In a voltage-biased TES, the electrical and thermal response of the TES to absorbed heat couple together to create an electrothermal feedback loop. This feedback loop acts to maintain the TES temperature within its superconducting-normal transition upon receiving additional heat by reducing the TES current and associated Joule heating.

TES behaviour can be described by two coupled differential equations describing the thermal and electrical response of the device. We will begin by considering the thermal response in isolation in Section 2.3.1 and then consider the complete TES response in Section 2.3.2.

2.3.1 Thermal Response

In order to consider the thermal differential equation in isolation, we must assume that the TES current is linearly proportional to temperature. In reality, the presence of a load resistance and inductive coupling to the readout circuit renders this assumption inaccurate but this simplified thermal model is still of use for deriving some basic TES properties.

Due to the non-zero electrical resistance of a TES in its superconducting transition, a voltage-biased TES will exhibit Joule heating of magnitude $P_J = I^2 R$, where I is the current passing through the TES and R is the TES resistance. The effect of this heating is to maintain the device temperature above that of the surrounding thermal bath. As such, the TES temperature follows

$$C \frac{dT(t)}{dt} = -P_b(t) + P_J(t) + P_{in}(t), \quad (2.5)$$

with P_{in} being equivalent to Eqn. 2.2 for calorimetric applications. C is the heat capacity of the TES, including both the superconductor and separate particle absorber, if present; in some TESs, the superconducting film also acts as the absorber.

In practice, TESs are connected to a thermal bath through a weak thermal link such as by suspending the TES on a thin membrane or on an island connected to the bath by narrow legs [8, 78]. The thermal power diffusion, P_b , is modelled using [79]

$$P_b(t) = K(T(t)^n - T_b^n), \quad (2.6)$$

where the parameter K depends upon the magnitude of thermal conductance between the device and the bath. This description of thermal conductance allows for a temperature gradient from the device to the bath. The geometry and nature of the thermal link determines the value of the thermal conductance exponent, n , typically lying between 2 and 4. This exponent is related to the dimensionality of phonon transport and phonon scattering mechanisms across the thermal link [80]. For example, TESs connected to the thermal bath in the few-mode ballistic phonon regime display $n \approx 2$, whereas $n = 4$ in the 3-dimensional radiative limit [81]. The thermal conductance, G_b is defined as

$$G_b \equiv \frac{dP_b}{dt} = nKT^{n-1}. \quad (2.7)$$

At equilibrium when $P_{in} = 0$, Eqn. 2.6 and P_J must balance exactly to maintain the TES temperature.

Solving Eqn. 2.5 in general requires knowledge of the $R(T, I)$ surface through the superconducting transition. Following the derivations in [82] and [83], the problem can be simplified in the small-signal limit where R and I are assumed to change linearly from their equilibrium values, R_0 and I_0 . The TES resistance can be approximated as

$$R(T) \approx R_0 + \alpha \frac{R_0}{T_0} \Delta T + \beta \frac{R_0}{I_0} \Delta I, \quad (2.8)$$

where we have introduced the TES equilibrium temperature T_0 and the parameters α and β . α defines the sharpness of the TES resistance-temperature dependence, following

$$\alpha \equiv \frac{T}{R(T)} \frac{\partial R(T)}{\partial T}, \quad (2.9)$$

whereas β characterises the TES resistance-current dependence:

$$\beta \equiv \frac{I}{R(T)} \frac{\partial R(T)}{\partial I}. \quad (2.10)$$

TES behaviour is heavily dependent on α whereas β is of lesser importance and so we will assume $\beta = 0$ for the time being.

Using Eqn. 2.8, P_J simplifies to

$$P_J = I^2 R \approx I_0^2 R_0 + 2I_0 R_0 \Delta I + \alpha \frac{P_{J,0}}{T_0} \Delta T, \quad (2.11)$$

and from the definition of G , P_b becomes

$$P_b(T) \approx P_{b,0} + G\Delta T. \quad (2.12)$$

Inserting Eqn. 2.2, Eqn. 2.11 and Eqn. 2.12 into Eqn. 2.5 provides

$$C \frac{d\Delta T(t)}{dt} = -G\Delta T + 2I_0 R_0 \Delta I + \frac{\alpha P_{J,0}}{T_0} \Delta T + E_k \delta(t - t_k) \quad (2.13)$$

where $\Delta T = T(t) - T_0$ and $\Delta I(t) = I(t) - I_0$. We are currently assuming that the TES current change is linearly proportional to temperature change through the relation

$$\Delta I = -\frac{V}{R_0^2} \frac{\partial R}{\partial T} \Delta T = \frac{\alpha I_0}{T_0} \Delta T, \quad (2.14)$$

where V is the TES bias voltage.

Inserting this relation into the thermal differential equation leads to

$$C \frac{d\Delta T(t)}{dt} = -G(1 + \mathcal{L}) \Delta T + E_k \delta(t - t_k) \quad (2.15)$$

where \mathcal{L} is the TES electrothermal feedback (ETF) loop gain,

$$\mathcal{L} \equiv \frac{\alpha P_{J,0}}{GT_0}. \quad (2.16)$$

In a voltage-biased TES, the electrothermal feedback loop acts to compensate for the additional heat by reducing current. The strength of the feedback loop is characterised by \mathcal{L} , where in Eqn. 2.15 it can be seen that the presence of \mathcal{L} allows for an additional pathway to reduce thermal energy in the TES.

The solution to Eqn. 2.15 is an exponential decay analogous to Eqn. 2.4,

$$\Delta T(t) = \frac{E_k}{C} e^{-t/\tau_{\text{eff}}} \quad (2.17)$$

where τ_{eff} is the effective TES time constant. The proportional current response is given by

$$\Delta I(t) = -\frac{\alpha I_0}{T_0} \frac{E_k}{C} e^{-t/\tau_{\text{eff}}}. \quad (2.18)$$

Fig. 2.2 depicts the resistance, temperature and current changes in a TES upon receiving an impulse of thermal energy.

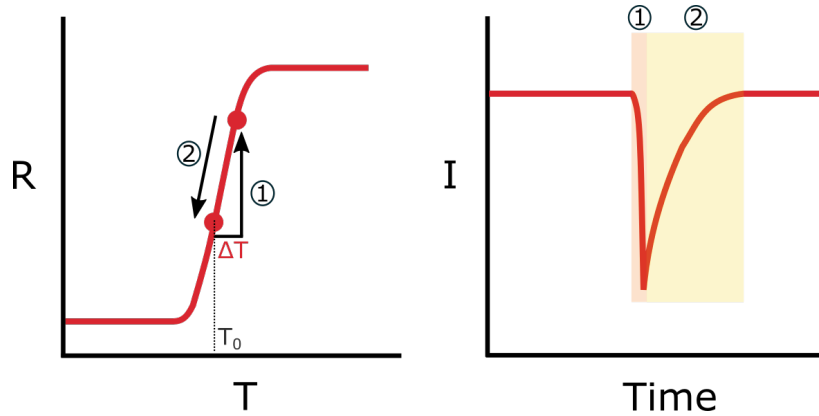


Fig. 2.2 TES calorimeter response to a particle absorption event in terms of TES resistance (left) and current (right). At time 1, the particle is absorbed with the TES response occurring over the region of 2.

The time constant τ_{eff} is modified from the thermal time constant $\tau = C/G$ by the ETF loop following

$$\tau_{\text{eff}} = \frac{\tau}{1 + \mathcal{L}} = \frac{\tau}{1 + \frac{\alpha}{n} \left(1 - \frac{T_b^n}{T^n}\right)}. \quad (2.19)$$

In the strong ETF limit such that $\alpha \gg n$ and under the condition that $T_b \ll T_0$, τ_{eff} simplifies to

$$\tau_{\text{eff}} = \frac{nC}{\alpha G}. \quad (2.20)$$

Typical values of α can range from 20 to over 100 meaning that the electrothermal feedback loop can reduce the TES response time by as much as a factor of 50.

The ETF loop is a critical aspect of TES behaviour beyond increasing the speed of the detectors. The negative ETF loop maintains the TES at the chosen operating temperature within its superconducting transition and so in an array of multiple devices of differing T_c , each device can be held at its own transition temperature by controlling the voltage bias of each TES. This capability is critical to operating arrays of TESs simultaneously. Before the introduction of superconducting quantum interference device (SQUID) readout systems, TESs were current-biased and so displayed positive ETF, where the temperature rise from radiation absorbed by would lead to a rise in voltage, increasing Joule heating in the superconducting film and potentially leading to thermal runaway. As such, the temperature of these devices could not be controlled independently of the bath temperature. When cooling an array of current-biased TESs on the same chip, due to variations in the TES transition temperatures, only a small subset of devices would be within its superconducting transition, and therefore usable, at a time [22].

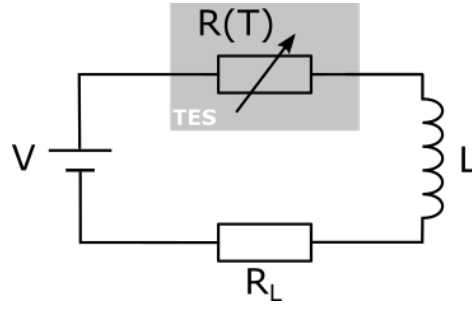


Fig. 2.3 TES bias circuit with TES resistance of $R(T)$, bias voltage V , load resistance of R_L and inductance L .

2.3.2 Electrothermal Response

In Section 2.3.1, we considered the behaviour of a TES in the absence of electrical components beyond the voltage source. However, a key aspect of any TES is the detector readout which, in modern TESs, is performed by series array SQUIDs. Series array SQUIDs provide low-noise, high-responsivity current-to-voltage conversion with extremely low-input impedance, that can be fed directly to room-temperature electronics. However, integrating TESs into SQUID readout circuits requires the use of inductive coupling, as shown by the simplified TES bias circuit in Fig. 2.3. The behaviour of a TES within the circuit in Fig. 2.3 is described by both Eqn. 2.5 and

$$L \frac{dI(t)}{dt} = V - IR_L - IR(T, I), \quad (2.21)$$

where L is inductance and R_L is the load resistance.

Following the same process as previously, we can linearise the TES resistance but this time without assuming $\beta = 0$ such that

$$R(T) \approx R_0 + \alpha \frac{R_0}{T_0} \Delta T + \beta \frac{R_0}{I_0} \Delta I \quad (2.22)$$

and

$$P_J \approx I_0^2 R_0 + 2I_0 R_0 \Delta I + \alpha \frac{P_{J,0}}{T_0} \Delta T + \beta \frac{P_{J,0}}{I_0} \Delta I. \quad (2.23)$$

The resulting linearised TES equations are

$$C \frac{d\Delta T(t)}{dt} = -G(1 - \mathcal{L}) \Delta T + I_0 R_0 (2 + \beta) \Delta I + E_k \delta(t - t_k) \quad (2.24)$$

and

$$L \frac{d\Delta I}{dt} = -(R_l + R_0(1 + \beta)) \Delta I - G \frac{\mathcal{L}}{I_0} \Delta T + \Delta V \quad (2.25)$$

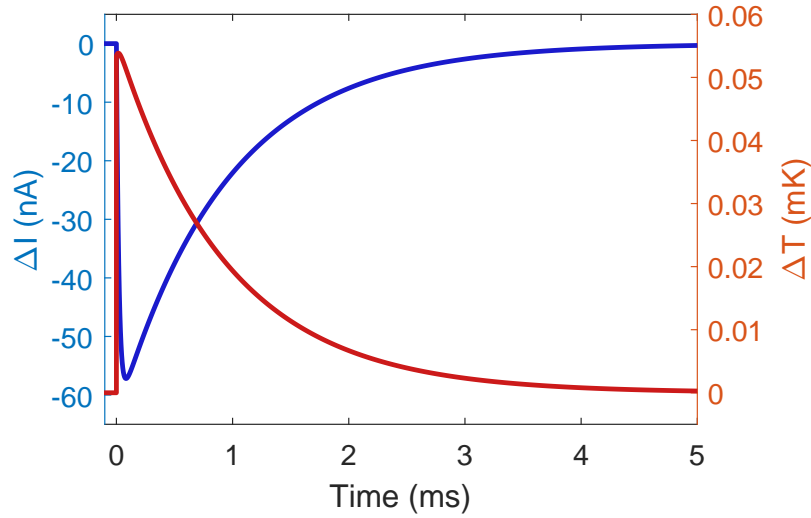


Fig. 2.4 TES temperature and current response to a thermal impulse at time zero numerically calculated from Eqn. 2.24 and Eqn. 2.25.

where the inclusion of $\Delta V = V(t) - V_0$ allows for bias voltage fluctuations. Analytical solutions to Eqn. 2.24 and Eqn. 2.25 are derived in [82] but Fig. 2.4 shows an example numerical solution with the characteristic exponentially decaying temperature and current response to the injection of heat at a time of zero. However, unlike in Section 2.3.1, the TES response is no longer fully characterised by a single exponential decay but instead is of the form

$$\Delta I(t) \propto e^{-t/\tau_{el}} - e^{-t/\tau_{eff}} \quad (2.26)$$

where the risetime is governed by the electrical time constant τ_{el} [82]. In the strong ETF limit, $\tau_{el} \rightarrow L/R$ and τ_{eff} reduces to Eqn. 2.20.

Another key TES parameter is the power-to-current responsivity, $s_I \equiv d\Delta I/dP_{in}$ given by [82]

$$s_I(\omega) = \frac{-1}{I_0 R_0} \left(\frac{R_L + R_0(1 + \beta)}{R_0 \mathcal{L}} + \left(1 - \frac{R_L}{R_0}\right) + i\omega \frac{L\tau}{R_0 \mathcal{L}} \left(\frac{1 - \mathcal{L}}{\tau} + \frac{R_L + R_0(1 + \beta)}{L} \right) - \frac{\omega^2 \tau L}{\mathcal{L} R_0} \right)^{-1} \quad (2.27)$$

where $\omega = 2\pi f$ is angular frequency. In the strong ETF limit and $R_L \ll R_0$, the zero-frequency responsivity simplifies to

$$s_I(0) = \frac{-1}{I_0(R_0 - R_L)}. \quad (2.28)$$

As a representative example, a TES with $I_0 = 1 \mu\text{A}$, and $R_0 - R_L = 50 \text{ m}\Omega$ would have a sensitivity of $s_I(0) = -20 \mu\text{A/pW}$. A very important practical consideration regarding TESs is that to achieve good sensor performance, the background noise levels must be suppressed to levels that are at least below particle energies being measured. The noise must be suppressed below the intrinsic detector noise itself to achieve optimal performance. For devices as sensitive as TESs, capable of resolving sub-eV particles, the design of the detector, readout system and surrounding apparatus must be carefully considered. For example, the TES must be connected to with superconducting wiring to prevent Joule heating external from the TES itself. The TES voltage bias must be capable of providing a stable voltage of the order of tens of nanovolts across a TES with milliohm resistance, with minimal external interference.

2.3.3 Energy Integral

In order to calibrate a TES, it is important to be able to relate the energy dissipated by the TES current response to the energy of the incident particle. The thermal energy compensated for by the reduction in TES current can be estimated using

$$E_{\text{ETF}} = \frac{-1}{s_I(0)} \int_0^\infty \Delta I(t) dt. \quad (2.29)$$

The TES current response in Section 2.3.2 reduces to Eqn. 2.18 in the strong ETF limit [83] and so, assuming $R_L \ll R_0$, the energy integral becomes

$$E_{\text{ETF}} = \frac{\mathcal{L}}{1 + \mathcal{L}} E_k = \frac{\left(1 - \frac{T_b^n}{T_0^n}\right)}{\frac{n}{\alpha} + \left(1 - \frac{T_b^n}{T_0^n}\right)} E_k \quad (2.30)$$

Importantly, $E_{\text{ETF}} \propto E_k$ and in the case of strong ETF and $T_c \gg T_b$, $E_{\text{ETF}} \rightarrow E_k$. For a TES with 200 mK transition temperature, 100 mK bath temperature, $\alpha = 50$ and $n = 2$, $E_{\text{ETF}} = 0.95E_k$. TESs operating in the strong ETF limit are able to accurately measure absorbed energies but to achieve the best absolute measurements of energy, the TES should be calibrated against known particle or photon sources, or the energy integral must be precisely calculated. This latter approach is not trivial, especially beyond the small-signal limit, as is discussed in Section 2.6 and it is far more practical to calibrate against known sources such as elemental X-ray emission energies, as are typically used within TES X-ray calorimetry.

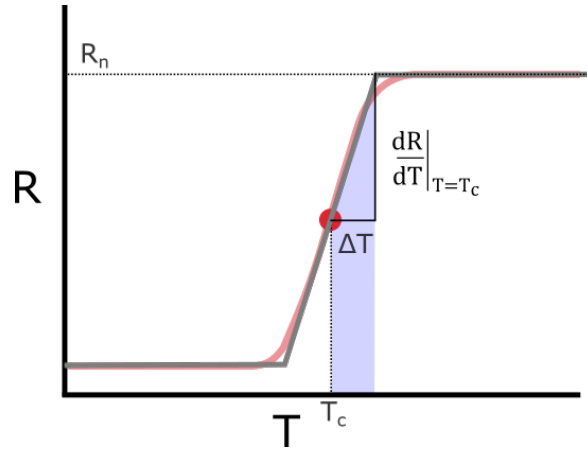


Fig. 2.5 Estimation of superconducting transition width in temperature assuming a linear resistance-temperature dependence. The normal state resistance (R_n) and central transition temperature (T_c at $R = R_n/2$) are marked. TES saturation energy can be estimated as $C\Delta T$ where C is the TES heat capacity.

2.4 Saturation Energy

TES saturation energy is defined by the minimum particle energy necessary to heat the TES into its normal state. This value can be approximated by [83]

$$E_{sat} \approx \frac{C}{\alpha} T_c, \quad (2.31)$$

where E_{sat} is the saturation energy. If the TES resistance-temperature dependence is assumed linear as in Fig. 2.5, the energy necessary to drive the TES from its operating temperature at T_c into its normal state follows Eqn. 2.31. In reality, precise calculation of a device's saturation energy requires knowledge of the TES $R(T, I)$ surface, and solving Eqn. 2.24 and Eqn. 2.25 beyond the small-signal limit. Additionally, the TES operating temperature can be set anywhere within the transition meaning that the saturation energy can be increased by biasing the TES at a temperature that is lower within its superconducting transition. However, as α is a function of temperature, the chosen TES operating temperature within its transition will impact the TES response shape. This is shown in Fig. 5.8 from Chapter 5, reproduced in Fig. 2.6 where several measured TES responses to absorbed electrons are shown, with different decay times dependent on the TES bias point. The biasing of the TES within the superconducting transition are represented by the fraction of the normal state resistance (R_n) displayed by the device.

As the TES reaches saturation, α tends to zero, resulting in a gradual reduction of ETF sensitivity. The result of this is not the inability to measure energies near to or exceeding

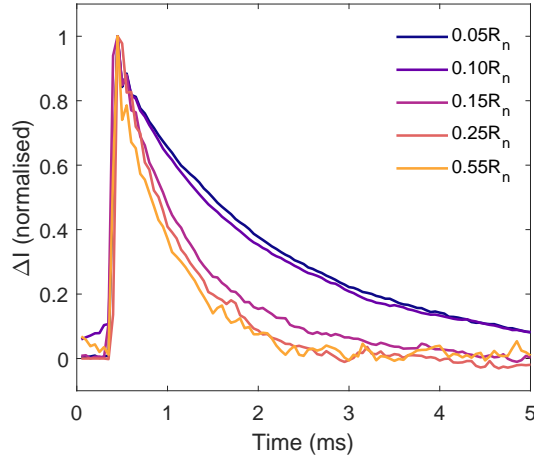


Fig. 2.6 Variation of measured TES response shapes with TES bias voltage. The TES bias point is shown as a fraction of the normal state resistance, R_n .

E_{sat} , but instead a gradual flattening and broadening of TES response at higher energies is observed, as shown in Fig. 2.7. This reduction in TES sensitivity around E_{sat} , as opposed to any precipitous sensitivity loss, means that precise calculation of the energy required for the TES to reach its normal state is unnecessary for many practical purpose and the approximation in Eqn. 2.32 is sufficient when considering saturation limits.

2.5 Energy Resolution

The primary types of noise relevant to TES measurement are phonon noise, Johnson noise and readout noise. Phonon noise is the most significant noise source for a well-designed TES and arises from statistical fluctuations in phonon distribution. Johnson noise is a related form of noise but applies to temperature-driven random fluctuations in electrical current across a resistor; for TES measurement, the relevant resistors are the TES itself and also the load resistor. When using SQUID readout systems, readout noise is a negligible source of noise in comparison to phonon and Johnson noise, though this is not necessarily true for multiplexed measurements.

The figure-of-merit defining the noise performance of a given bolometer or calorimeter is the noise-equivalent power (NEP). NEP is defined as the thermal power input into the detector equivalent to the observed noise power per unit readout bandwidth. The phonon noise NEP can be modelled as [84]

$$\text{NEP}_{\text{ph}}^2 = 4k_B T_0^2 G F(T_0, T_b), \quad (2.32)$$

where the parameter F is dependent on the nature of the thermal link between the TES and bath, typically taking values between 0.5 and 1 [82]. As NEP is input-referred, the filtering of the noise source by the TES must be accounted for when considering Johnson noise. following

$$\text{NEP}_J^2(\omega) = \frac{S_J(\omega)}{|S_I(\omega)|^2}, \quad (2.33)$$

where $S_J(\omega)$ is the current noise power spectral density for TES Johnson noise. This is not true for phonon noise as phonon noise enters the detector as thermal power fluctuations. The resulting Johnson noise NEP becomes [84, 85]

$$\text{NEP}_J^2(\omega) = 4k_B T_0 \frac{P}{\mathcal{L}^2} (1 + \omega^2 \tau^2), \quad (2.34)$$

using the thermal time constant $\tau = C/G$. Combining Eqn. 2.33 and Eqn. 2.34 following

$$\text{NEP}_{\text{Total}}^2 = \text{NEP}_{\text{ph}}^2 + \text{NEP}_J^2 \quad (2.35)$$

results in

$$\text{NEP}_{\text{Total}}^2(\omega) = 4k_B T_0^2 G \left(F + \frac{n}{\alpha^2} \frac{T_0^n}{T_0^n - T_b^n} (1 + \omega^2 \tau^2) \right). \quad (2.36)$$

Johnson noise from the load resistor can be neglected when $R_L \ll R_0$, otherwise it must be included into Eqn. 2.7 in addition to TES Johnson noise.

The typical method of analysing TES calorimetry data is through pulse height estimation using 'optimal filtering' [86, 87]. In optimal filtering, a filter template is calculated by minimising the least-squares difference between the observed and model pulse shapes in the frequency domain, in the presence of a given noise power spectrum. Under white noise conditions, the form of the filter reduces to the average measured pulse shape in the time domain. When the noise is not white, the filter applies weights to data's frequency spectrum to maximise signal-to-noise at each frequency independently. The full-width half maximum (FWHM) energy resolution obtained using optimal filtering for a calorimeter with stationary, Gaussian noise and a linear energy response is [88]

$$\Delta E = 2\sqrt{2\ln(2)} \left(\int_0^\infty \frac{4}{\text{NEP}_{\text{Total}}^2(f)} df \right)^{-1/2}. \quad (2.37)$$

Inserting Eqn. 2.36 into Eqn. 2.37 leads to

$$\Delta E = 2\sqrt{2\ln(2)} \sqrt{4k_B T_c^2 \frac{C}{\alpha} \sqrt{\frac{T_c^n}{T_c^n - T_b^n} \left(nF + \frac{n^2}{\alpha^2} \frac{T_c^n}{T_c^n - T_b^n} \right)}} \quad (2.38)$$

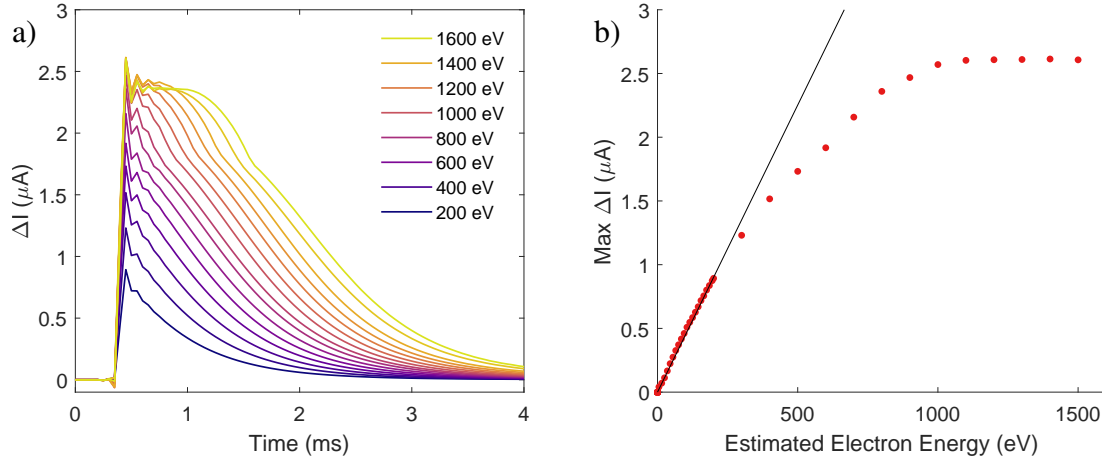


Fig. 2.7 a) Average TES pulse shapes grouped by measured event energy, from Section 5.3.2. b) TES event energy plotted against averaged maximum pulse current. In both plots, the event energy has been calculated from the area beneath the peak.

which reduces to

$$\begin{aligned}\Delta E &= 2\sqrt{2\ln(2)}\sqrt{4k_B T_c^2 \frac{C}{\alpha} \sqrt{\frac{n}{2}}} \\ &= 2\sqrt{2\ln(2)}\sqrt{4k_B T_c E_{\text{sat}} \sqrt{\frac{n}{2}}}\end{aligned}\quad (2.39)$$

under the conditions that $F = 0.5$, $T_c \gg T_b$ and $\alpha^2 \gg n^2$, typical for a TES in the strong ETF limit. For the purposes of consistency with the literature, the TES operating temperature T_0 in Eqn. 2.36 has been replaced with the nominal superconducting transition temperature, T_c .

From Eqn. 2.38 and Eqn. 2.39, it can be seen that TES energy resolution can be improved by reducing the TES saturation energy, the transition temperature or the thermal conduction exponent, n . The saturation energy is limited by the particle energies of interest for the chosen TES application. The TES transition temperature is limited by the practically reachable cryostat temperatures with TESs currently operating at tens to hundreds of millikelvin. The thermal conduction exponent is determined by the thermal link between the TES and bath, with values typically between 2 and 4.

2.6 Large-Signal Response

A result of the relation between TES energy resolution and saturation energy is that to achieve the best resolutions, the saturation energy must be set close to the maximum particle energy

to be measured. Based on the comparisons between TESs and existing electron spectrometers in Section 1.6, TES electron spectrometers will need to optimise for energy resolution and so will also require saturation energies as low as is practical which will mean that a portion of the measured particle energies will have energies lying outside the small-signal limit of the TES.

Beyond the small-signal limit, the TES behaves in a non-linear manner in response to absorbed energy, exemplified by the measurements in Fig. 2.7 from Chapter 5. This non-linearity can be examined in terms of pulse height or in terms of pulse area versus absorbed energy.

The height of the observed current pulse in a TES to an absorbed particle is linear with the particle energy in the small-signal limit. However, once the linear approximations applied in Eqn. 2.22 no longer hold, the TES response cannot be accurately modelled solely using an exponential rise and decay but instead will take on a form dependent on the path taken by the TES across the $R(T, I)$ surface during the pulse. As a result, the pulse shape varies based upon measured energy, as is visible in Fig. 2.7a, with the inflection at around $1.7 \mu\text{A}$ being most notable for this particular device. The ringing at the peak is a result of low-pass filtering during readout rather than a TES effect.

Peak area non-linearity arises when the area defined by the measured current pulse no longer scales linearly with energy as the proportion of energy exchanged directly with the bath becomes a function of the total absorbed energy. During a measurement event, as the TES temperature rises higher above T_0 , the feedback loop begins to saturate and α drops, approaching zero. When the feedback loop completely saturates, the pulse peak flattens and remains flat until the detector has returned to its transition temperature window. The pulse energy can still be estimated from the pulse area but the detector has lost temperature sensitivity and so will not display the occurrence of additional piled-up particles during this time. Provided the pulse width is much smaller than τ , the majority of the absorbed energy will be observed in the area of TES current pulse. It is predicted that by measuring the pulse width, the energy of an incident X-ray photon with energies several times greater than the TES saturation energy could be measured with comparable accuracy to a photon with less than the saturation energy by [89]. This has not been experimentally demonstrated yet but could provide a new manner in which TESs can be used provided the loss of sensitivity to additional particles when the TES is saturated is an acceptable compromise.

In theory, the non-linear peak height and area can be numerically modelled but this would require precise measurements of the circuit bias and resistances, most notably $R(T, I)$. Additionally, the specific effects arising from the TES geometry must be accounted for including the thermal conductance from the TES absorber to the superconducting structure

or even the particle absorption location within the absorber itself. A particularly difficult challenge to overcome is modelling the nature of non-stationary noise present within the large-signal regime. Non-stationary noise in a TES arises due to the relation between TES resistance and the observed noise spectral density at the output. The noise displayed by the TES at the measurement peak deviates significantly from the baseline noise. A result of these difficulties in accurately modelling and predicting large-signal TES behaviour is that TES calorimeters are typically calibrated against known energy sources, rather than the electrical circuit. [90–92].

TES calibration, or gain, curves are found by measuring the TES pulse shapes at known photon energies. The calculated gain curves are used to linearise TES pulse height against absorbed energy prior to optimal filtering. For example, when measuring X-ray photons in the non-linear regime, an energy resolution of 0.86 eV was achieved by [71] for the 1486 eV Al $K\alpha$ peak using this method. However, converting the TES current measurements into resistance before applying optimal filtering was found to both improve the linearity of the calibration curve and reduce non-stationary noise resulting in a resolution of 0.73 eV. The benefits of analysing TES resistance pulses was previously predicted in [93], where the authors argue that calculated TES resistance scales more linearly with energy but also that the magnitude of phonon noise remains uniform across the pulse, and so the observed total noise is more stationary. Results of simulations describing planned Athena X-ray telescope TESs also suggest improved performance using resistance-based analysis but in these cases, the large inductances used meant that directly converting the TES current to resistance did not improve linearity. Instead a proxy resistance-based measure was found that scaled with linearity with energy [94, 95].

When operating an array of identically designed TESs, the specific behaviour of each device will vary and must be characterised. For large array sizes numbering hundreds or thousands of pixels, the complexity of the analysis method and the level of pixel characterisation necessary for the method must be balanced against practical considerations, such as characterisation and computation time; this is especially true for real-time methods or space-based detector arrays where the available computation capabilities may be limited.

2.7 Conclusion

The basic principle behind TES calorimetry is qualitatively straightforward insofar as the thermal energy absorbed by a TES is compensated for by a reduction in Joule heating through an electrothermal feedback loop. The change in Joule heating is directly proportional to the absorbed energy and so can be used to quantify the absorbed energy. This behaviour has

been addressed within the small-signal limit in this chapter but it should be noted that the key equations regarding energy resolution and TES response remain as good approximations well into the large-signal regime approaching the TES saturation energy. These equations are also vitally important for predicting TES performance and for designing devices.

Quantitative analysis of large-signal TES calorimetry is difficult and so in practice, the scaling of TES pulses with energy is empirically calibrated using known energy standards, both for ease but also to extract the optimal energy resolutions from the detectors. The observed deviation from the predicted energy resolution for large-signal pulses is highly-dependent on detector linearity and noise stationarity. As a result, the chosen calibration and analysis method is of great importance for optimising TES energy resolution.

Chapter 3

TES Electron Spectroscopy Simulation

3.1 Introduction

The first question to ask when considering the application of transition-edge sensors to electron spectroscopy is whether this is a realistic proposal and if so, what potential benefits are available. To answer this question, I built a software package in MATLAB R2021a to simulate the detection and energy measurement of particle fluxes using TES calorimetry. The software package was used to investigate the potential role of TESs in electron spectroscopy, specifically X-ray photoelectron spectroscopy where improving detector technology could provide significant benefits. The purpose of this work was to find the set of detector requirements necessary for TES electron spectrometers to match the capabilities of existing electron spectrometers in XPS measurements, and therefore determine the viability of TES electron spectroscopy.

Section 3.2 outlines the design and function of the software package which was then applied in the context of XPS measurements in Section 3.3. I then apply Fisher information analysis to the simulated TES measurements to calculate the fundamental energy resolution lower limit as determined by TES properties (Section 3.4). Using these results, Section 3.5 details the detector requirements needed for TES X-ray photoelectron spectroscopy to be comparable to existing electron spectrometers.

3.2 Simulation Model

I created the software in two separate parts, reflecting the measurement and subsequent data analysis that would be performed in a TES electron spectroscopy experiment. The software package first generates time series datasets corresponding to TES measurement of an incident

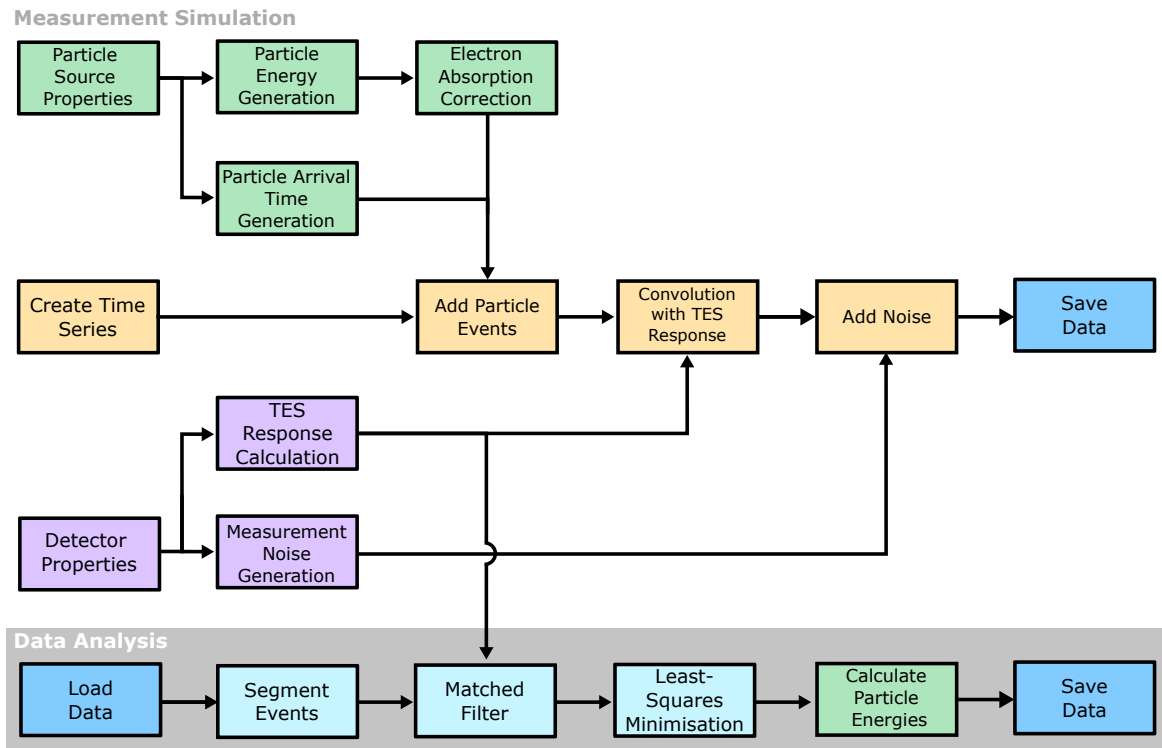


Fig. 3.1 Software block diagram showing the steps used to generate and analyse simulated TES measurement data. The green block represents the particle source properties including energy spectrum, purple blocks describe TES properties. Steps used in the construction of the simulated dataset are shown in orange, and data analysis is shown in blue.

particle flux. Analysis software then receives these datasets and calculates the spectrum of incident particle energies. As the original spectrum of particle energies is known, the ability of the detector and data analysis method to measure the particle spectrum can be investigated. Fig. 3.1 shows the structure of the data simulation and analysis software. The only connections between the two parts of the software are the simulated dataset and the shape of the TES response to an incident energy pulse.

3.2.1 Data Simulation

For each simulation, the properties of the TES detector and the particle source were first chosen. The data simulation software would then create an empty time series with a given duration and sampling frequency. A set of incident particles would be generated across the measurement period, as defined by the particle arrival time and energy. The software was made to generate particle arrival times using three types of distribution:

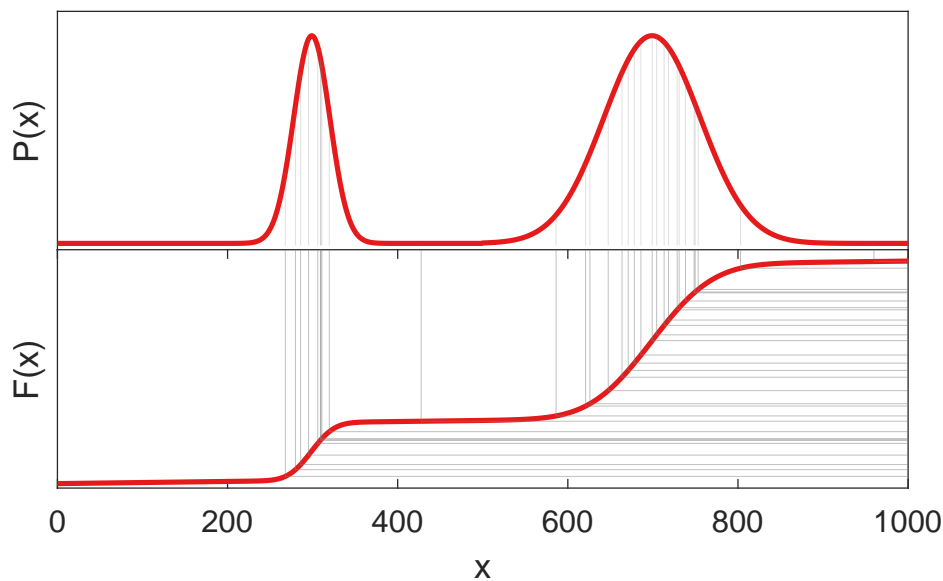


Fig. 3.2 Random sampling from probability density function $P(x)$ using inverse transform sampling. A set of uniform random numbers are represented as the horizontal lines intersecting $F(x)$, the cumulative distribution function of $P(x)$. The vertical lines represent the output after transformation by $F^{-1}(x)$.

- **Random** arrival times mimic the expected time distribution of electrons emitted from an electron gun. With a given mean particle flux, the set of particle arrival times were randomly generated with a uniform distribution across the time series.
- **Periodic** arrival time generation produces single particles separated by a given period. This mode was used to simulate measurements in the absence of particle pileup. As such, the number of particles simulated is only determined by the duration of the time series and the time period between particles.
- **Pulsed** particle sources simulate the behaviour of a pulsed electron beam by applying a pulsing mechanism on top of the random source. By setting a given pulse width and duration, periodic particle pulses would be generated with each pulse having a variable number of particles. The number of electrons in each pulse is dependent on the pulse width and particle flux chosen. For example, if a continuous electron flux of 1000 s^{-1} and a pulse width of 1 ms is chosen, each pulse will have an average of one electron but, statistically, only e^{-1} pulses will have exactly one electron.

The second value defining each particle is its energy. A key requirement for the software is to be able to generate particle energies sampled from a range of energy distributions such as Gaussian distributions or entire XPS spectra. In order to randomly sample energies

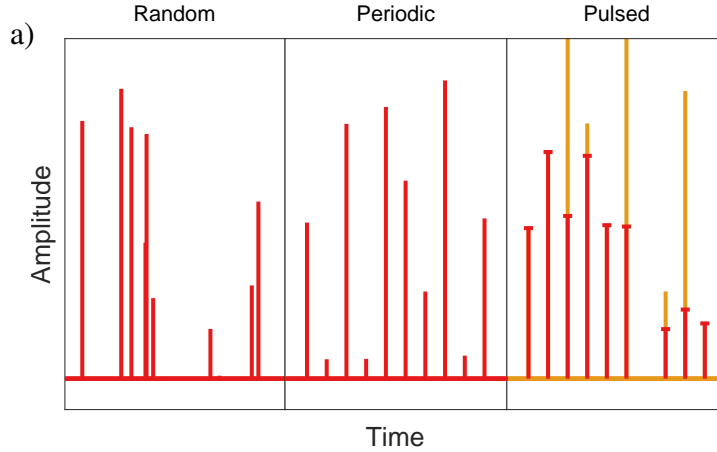


Fig. 3.3 Generated particle events inserted into a time series with randomly generated or periodic arrival times. The pulsed source shows periodic pulses with a given pulse duration therefore allowing multiple electrons per pulse. In this example, the pulse width is smaller than the sampling frequency and so the particles events are concurrent. The different electrons have been distinguished by colour.

from arbitrary probability density functions, particle energies were generated using inverse transform sampling. This method transforms uniform random numbers into random numbers sampled from a given probability density function, $P(x)$. As depicted in Fig. 3.2, inputting a set of uniform random numbers into $F^{-1}(x)$ outputs a set of numbers sampled from the distribution $P(x)$. $F^{-1}(x)$ is the inverse of the cumulative distribution function, $F(x) = P(X \leq x)$, where X is a random variable.

After generating the particle arrival times and energies, these events need to be placed into the time series and converted into TES measurement data. For every particle event, a single point is inserted into the time series with amplitude corresponding to the particle energy. If multiple particles are present with a time difference smaller than the sampling period, the amplitudes are added together. Examples of the resulting time series are shown in Fig. 3.3 with the two colours in the pulsed source plot representing the contribution of two separate particles arriving concurrently.

The particle event delta functions represent energy entering the detector but not the response of the TES to the incident energy. By convolving the time series in Fig. 3.3 with the TES response in Eqn. 2.18, reproduced below,

$$\Delta I(t) = -\frac{E_{abs}}{C} \frac{\alpha I_0}{T_c} e^{-t/\tau_{eff}}, \quad (3.1)$$

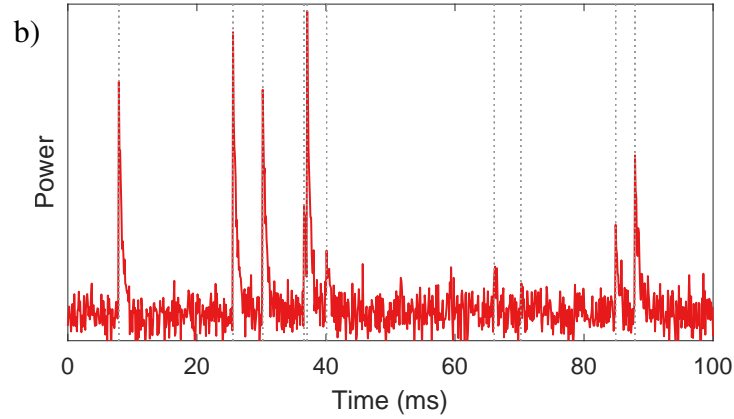


Fig. 3.4 Simulated TES measurement using the random arrival time particles and energies in Fig. 3.3. Dashed lines show the particle arrival times.

the time series was converted to TES measurement data in the absence of noise. As the relation between absorbed energy and current in Eqn. 3.1 is linear, the sign has no practical bearing on the analysis and so particle detection events have been simulated as positive exponential pulses rather than negative for simplicity of representation. Under the assumptions that the TES is linear, calibrated and not saturated, it is not necessary to define α , I and T in Eqn. 3.1 and so I will instead refer directly to energy. It should be noted that TESs monitor the change in current and so after conversion to energies, the TES measures power over time with the measured particle energy being the integrated area beneath the exponential pulse.

The final step of the data simulation software is to include measurement noise. Detailed treatment of TES noise is highly dependent on the detector geometry and so is beyond the scope of this simulation considering TES electron spectroscopy has not even been experimentally demonstrated, previously. Instead, a simplified model of TES noise has been used where the TES noise-equivalent power (NEP) has been assumed to follow Eqn. 2.36 under the condition that $\omega \ll 1/\tau$. Under this condition, the noise frequency dependence can be neglected and so becomes white. As such, the output power fluctuations, ΔP_{rms} , are related to NEP by

$$\Delta P_{\text{rms}} = \text{NEP} \sqrt{\Delta f_{ss}} \quad (3.2)$$

where Δf_{ss} is the single-sided output bandwidth. Assuming these noise fluctuations follow a zero-mean Gaussian distribution, ΔP_{rms} is equivalent to the noise standard deviation, σ . For a discretised time series with sampling period Δt , the output bandwidth is limited to half of the sampling frequency; as such,

$$\sigma = \frac{\text{NEP}}{\sqrt{2\Delta t}}. \quad (3.3)$$

With a given TES NEP, Gaussian white noise was sampled with standard deviation following Eqn. 3.3. A portion of the resulting time series is shown in Fig. 3.4 with particle arrival times and energies corresponding to the random source in Fig. 3.3.

The simulation software described to this point has been generic with regards to the particle being measured and has assumed complete energy absorption. As the software has been built to consider electron measurement, I included an optional modification to the simulated absorbed energies to account for incomplete electron energy absorption, as represented in Fig. 3.1. These electron absorption losses can occur through either photon or electron emission from the absorber; in the energy ranges being investigated, photon emission is infrequent enough to have negligible impact on the measurement, especially when using absorbers with low atomic mass elements. The loss mechanisms of significance are backscattered and secondary electron emission. The effects of electron absorption inefficiencies for TESs and mitigation methods are discussed in Chapter 8 but we will briefly examine secondary electron and backscatter losses here.

Secondary electron emission occurs when the primary incident electron ionises and releases electrons from the absorber. These secondaries typically have very low energies (<50 eV) and each primary electron can cause the emission of multiple secondaries. The Chung-Everhart model provides a good approximation of the secondary electron energy distribution from a metallic absorber [96]

$$f(E_s) = \frac{E_s - E_F - \Phi}{(E_s - E_F)^4} \quad (3.4)$$

where E_s is the secondary electron energy, E_F is the absorber Fermi energy and Φ is the work function. It should be noted that for incident electrons over 100 eV, the secondary electron energies are largely independent of the primary electron. When considering energies in terms of the vacuum level, $E_{vac} = E_F + \Phi$, Eqn. 3.4 becomes

$$f(E_s) = \frac{E_s - E_{vac}}{(E_s - E_{vac} + \Phi)^4}. \quad (3.5)$$

A plot of calculated secondary electron energy distributions (relative to E_{vac}) is provided in Fig. 3.5 with work functions of 3 eV and 5 eV. As can be seen, the vast majority of secondary electrons have energies below 20 eV. The average number of secondary electrons emitted by a primary electron depends on the primary electron energy, the absorber material, surface geometry and surface chemistry but typically ranges between 0.5 and 2 [97].

Unlike secondary emission, backscattered emission occurs when the primary incident electron is scattered out of the absorber. For flat samples of low atomic mass elements,

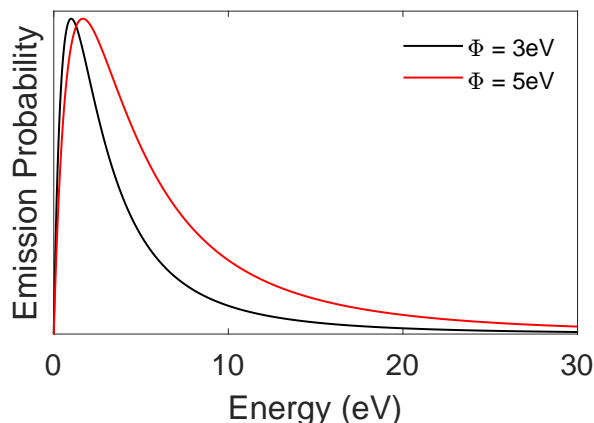


Fig. 3.5 Scaled secondary electron energy distributions relative to the vacuum level, calculated using Eqn. 3.5 using work functions of 3 eV (red line) and 5 eV (black line)

the probability of electron backscatter has been measured to range between 10 and 20% [98]. This probability can be reduced by optimising absorber geometry and material. The backscattered electron can carry any amount of energy up to the primary electron energy but the majority of backscattered electrons deposit little or no energy into the absorber [99]. These events would be observed by the TES as low energy events (<100 eV) and so would map high energy portions of the measured electron spectra to low the energy region. Backscatter losses have little detrimental impact on the peak shapes and energies but can distort the spectrum background. The low energy portion of the spectrum (<100 eV) is also of little interest in electron spectroscopy techniques such as XPS. Additionally, the energy distribution of backscattered electrons is more strongly connected with the absorber material than is the case with secondary electrons. Modelling backscatter losses requires assumptions about the absorber material without providing significant benefit to the conclusions that can be drawn from the simulation, therefore I have not included backscatter emission losses in the software, using only secondary electron emission.

Secondary electron losses were simulated by assigning secondary electrons with given energies to each primary electron event. The number of secondaries was randomly sampled from a Poisson distribution with a specified average secondary electron yield per primary electron. The energies of each secondary electron were generated in same manner as the primary electron energy but sampled from the Chung-Everhart distribution. The total secondary electron energy loss was then subtracted from the primary energy prior to placing the particle event in the time series. This method assumes a constant secondary electron yield regardless of primary electron energy; the yield actually rises to a maximum value at a primary energy between approximately 100 eV and 1000 eV depending on the material and surface chemistry. Therefore, the simulation overestimates the true incidence of secondary

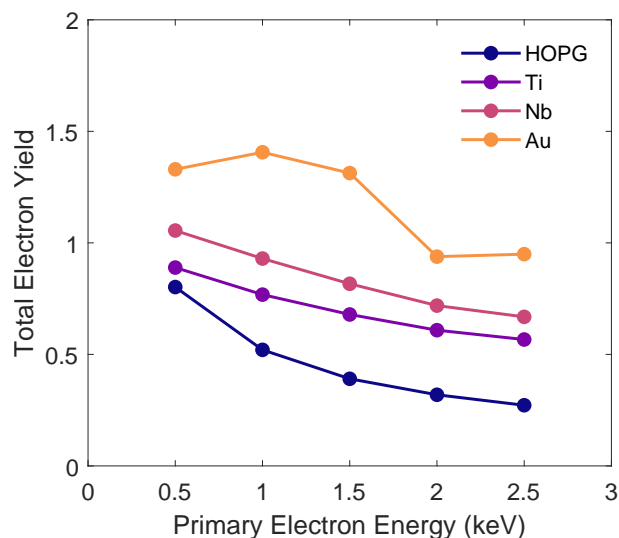


Fig. 3.6 Measurements of total electron yield emitted from highly-oriented pyrolytic graphite (HOPG), titanium, niobium and gold samples at various primary electron energies.

electrons for the purposes of simplicity. The dependence between secondary electron yield and primary electron energy is illustrated in Fig. 3.6; this figure summarises measurements I made of total electron yield (TEY) from various absorber samples; this measurement is described in more detail in Section 7.2. TEY represents the total number of electrons emitted from the absorption of a single primary electron. The observed yield of electrons with energies over 18 eV was below 0.1 for every measurement and so the measured yield is dominated by the secondary electrons. The peak yield for niobium, titanium and graphite (HOPG) occurred below 500 eV primary electron energy whereas for gold, the peak was observed at 1 keV.

3.2.2 Data Analysis

After simulating TES measurements of particle fluxes, the time series data were sent to the analysis software to identify particle measurements events and their corresponding energies. As shown in Fig. 3.1, the data analysis software receives only the measurement data and the TES response shape, as would be typical in an experimental measurement. The analysis software consists of three steps: coarse particle identification extracts segments of the time series containing particle events; the matched filter stage calculates the number of particles and their arrival times within each segment; the final step uses a least squares minimisation procedure to calculate the energies of these particles.

Coarse particle identification was achieved by applying two amplitude thresholds; an event threshold and a noise threshold. Whenever the signal exceeded the event threshold, a

particle event was recorded. The beginning and end times of each event are defined as the most recent times the signal crossed above the noise threshold, before and after the event threshold crossing. The left figure in Fig. 3.7 shows the application of this thresholding method where the data within the dashed lines was extracted as a particle measurement event.

Each extracted data segment can contain one or more particle events meaning the ideal model describing each data segment is a superposition of exponential decays with different arrival times and amplitudes. Due to the presence of particle pileup, the particle arrival times must be known as accurately as possible to accurately determine particle energies. If the arrival times of overlapping particle events are measured inaccurately, the calculated particle energies cannot be apportioned to each particle correctly. In order to be able to estimate particle arrival times with minimal ambiguity, I incorporated a matched filter step to maximise the signal-to-noise ratio of the dataset. The matched filter convolved each data segment with the time-reversed TES response provided by Eqn. 3.1, the result of which is shown in Fig. 3.7b. Under ideal, noiseless conditions, the number of particles in the segment would correspond to the number of local maxima but the presence of noise introduces additional local maxima that require exclusion. The prominence of the peak was used to distinguish between maxima arising from noise and from particle events, where prominence is defined as the minimum distance along the x-axis between a local maximum and a higher amplitude value (if present). Local maxima, arising from noise, display little prominence from the background whereas event maxima would be expected to result in much more pronounced peaks. A minimum prominence threshold was used to distinguish between noise and particle maxima. The number of particles within each segment was determined by the number of maxima exceeding the threshold, with the corresponding arrival times defined as the times of these maxima.

After extracting the data segments and identifying the number of particles within, the energy of each particle was determined by applying a least-squares minimisation model to every data segment individually. The ideal model describing the measured data in each segment is a superposition of exponential decay pulses distributed across the time series with varied maximum amplitudes. Applying this model to a data segment with N sampled points and N_p particle events, the signal μ at datapoint n is given by

$$\mu_n = \sum_{j=1}^{N_p} \frac{E_j}{\tau_{\text{eff}}} \exp\left(\frac{-(t_n - \phi_j)}{\tau_{\text{eff}}}\right) H(t_n, \phi_j), \quad (3.6)$$

where t_n is the datapoint time, ϕ_j is the arrival time of the j 'th particle and E_j is the corresponding particle energy. $H(t_n, \phi_j)$ is a step function with a value of 0 when $t_n < \phi_j$, and 1 when $t_n > \phi_j$. Let \mathbf{y} be the vector of signal amplitudes from the data segment comprised

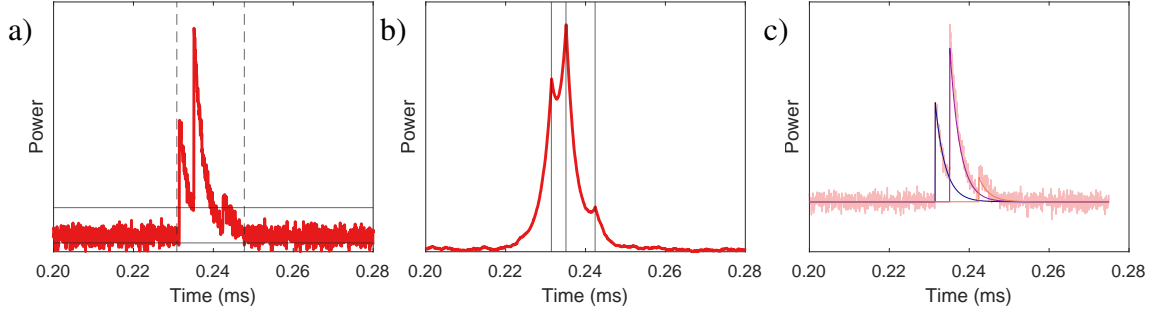


Fig. 3.7 a) Identification of a particle measurement event from a simulated TES measurement. The lower horizontal line represents the noise threshold and the upper line is the event threshold. The dashed vertical lines show the calculated data segment containing the event. b) Output of matched filter applied to (a) with vertical lines showing the identified particle arrival times. c) Calculated particle energies using a least-squares minimisation procedure overlaid onto the measurement data.

of n sampled datapoints, denoted y_n . If the measurement noise within \mathbf{y} is Gaussian, the probability of observing \mathbf{y} according to Eqn. 3.6 is

$$P(\mathbf{y}|\{E_j, \phi_j\}, \sigma) = (2\pi\sigma^2)^{-N/2} \exp\left(\sum_{n=1}^N \frac{-(y_n - \mu_n)^2}{2\sigma^2}\right). \quad (3.7)$$

The resulting log-likelihood function becomes

$$\begin{aligned} l(\{E_j\}|\mathbf{y}, \{\phi_j\}, \sigma) &= \ln(P(\mathbf{y}|\{E_j, \phi_j\}, \sigma)) \\ &= N \ln\left(\frac{1}{\sqrt{2\pi\sigma^2}}\right) + \frac{1}{2\sigma^2} \sum_{n=1}^N -(y_n - \mu_n)^2. \end{aligned} \quad (3.8)$$

The energy estimates, \tilde{E}_j , are the values that maximise the log-likelihood function such that

$$\left. \frac{\partial l}{\partial E_j} \right|_{E_j = \tilde{E}_j} = 0. \quad (3.9)$$

By applying this condition to Eqn. 3.8, it follows that

$$y_n = \sum_{j=1}^{N_p} \frac{\tilde{E}_j}{\tau_{\text{eff}}} x_{nj}, \quad (3.10)$$

where $x_{nj} = \exp\left(\frac{-(t_n - \phi_j)}{\tau_{\text{eff}}}\right) H(t_n, \phi_j)$. Eqn. 3.10 can be rewritten in matrix form,

$$\mathbf{y} = \frac{1}{\tau_{\text{eff}}} \mathbf{X} \mathbf{a}, \quad (3.11)$$

where \mathbf{y} is the vector of measured data, \mathbf{X} is the matrix populated by x_{ij} , and \mathbf{a} is the vector of particle energies. The set of energies can be estimated from Eqn. 3.11 by calculating the QR decomposition of \mathbf{X} . The final panel in Fig. 3.7 shows the application of this analysis procedure by plotting the separate particle arrival times calculated using the matched filter and energies of the data segment calculated from Eqn. 3.11.

3.3 X-ray Photoelectron Spectroscopy Simulation

Having demonstrated the simulation and the data analysis methods, I now show how the simulation software was used to understand the capabilities of TESs as electron spectrometers. Electron spectroscopy encompasses a number of techniques with a range of requirements and so we consider X-ray photoelectron spectroscopy specifically as it is a widely used technique in which improving detector technology would have a significant impact. I have applied the simulation software to the measurement of the XPS spectrum of silver using an Al $K\alpha$ X-ray source. Silver is commonly used as an XPS reference material due to the presence of two intense and narrow XPS peaks, Ag3d_{3/2} (1113 eV) and Ag3d_{5/2} (1118 eV) in close proximity. The spectrum used was obtained from SESSA (Simulation of Electron Spectra for Surface Analysis) and is shown in Fig. 3.8a [100]. By sampling electron energies from this energy distribution at a given flux, TES XPS measurement experiments were simulated. Fig. 3.8b shows the results of one such simulation using a TES with 100 μs response, sampled at 100 MHz for 1000 s. An average electron flux of 1000 s^{-1} was applied with random arrival times. The ideal line in black in Fig. 3.8b is the spectrum of input electron energies; this is the spectrum that would be measured in absence of measurement noise and analysis errors for the set of electrons simulated. The red line is the observed spectrum after applying the analysis method in Section 3.2.2 to the TES measurement data. Comparison between the two spectra shows accurate reconstruction of the source spectrum using TESs under the simulated conditions. The reduction in counts at low energies is due to the event threshold being set to 100 eV, thereby ignoring events with energies below this value. A small number electrons have been measured with energies below 100 eV due to pileup with higher energy electrons.

This simulation assumes ideal electron energy absorption. Assuming a gold absorber with work function of 4.8 eV [96], we can simulate the effect of secondary electron losses on the observed spectrum. Fig. 3.9 shows the results of this simulation under the same conditions as

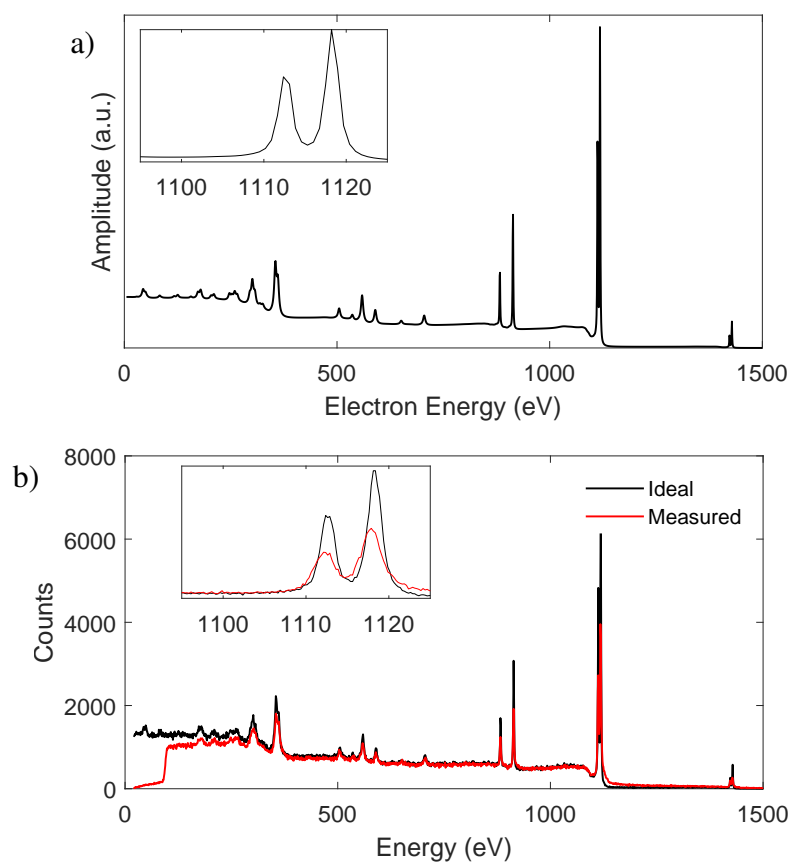


Fig. 3.8 a) Noise-free XPS spectrum of silver from SESSA simulation software [100]. b) Simulated measurement of XPS spectrum from (a) using a $100 \mu\text{s}$ response TES sampled at 10 MHz for 1000 s. The input electron rate was set at 1000 s^{-1} . The ideal line in black represents the observed spectrum in the case of where every electron energy is measured perfectly. The red measured line is the result after applying the data analysis method to the data. Reproduced from [101].

Fig. 3.8b but with an absorber with a secondary electron yield of 1. By including secondary electron losses, the observed XPS peaks display a low energy tail, broadening the peak but not shifting the peak energy observably. Given sufficiently long measurement times, an absorber displaying these levels of secondary losses would be capable of XPS measurements but consideration of the secondary electron spectrum from the absorber would be necessary for quantitative analyses.

These simulations demonstrate the efficacy of accurately measuring XPS spectra with TESs but also that the effect of secondary electron losses on the measured spectrum is notable and would require mitigation for any TES electron spectrometer. Such mitigation can be achieved through absorber design or electron optics as described in Chapter 8.

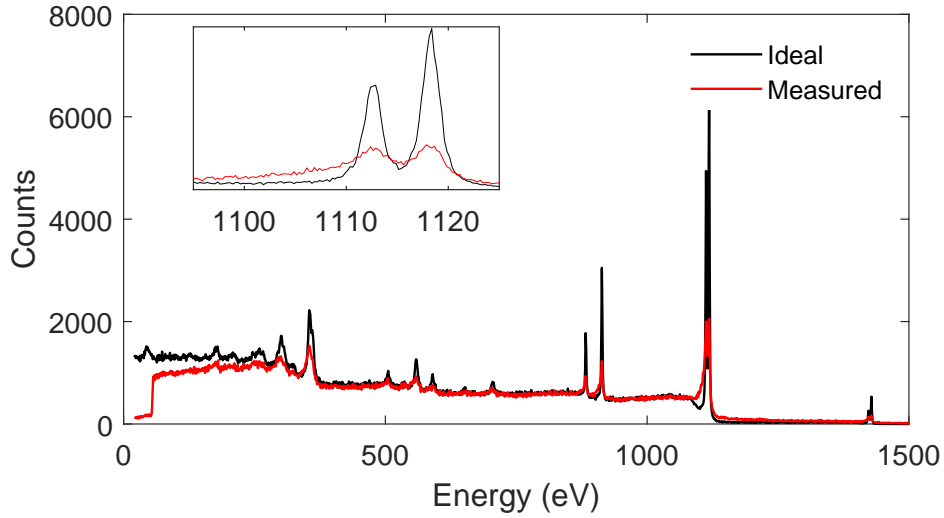


Fig. 3.9 Simulated measurement of the XPS spectrum of silver with the inclusion of secondary electron losses. The simulation was performed in the same manner as Fig. 3.8 but including secondary emission from an absorber with 4.8 eV work function.

3.4 Fisher Information

The energy resolution of a measurement system is fundamentally limited by the presence of noise, but can be further deteriorated by the chosen analysis method. An important question to answer is to what degree is the energy uncertainty in the measured spectrum fundamental due to noise, or an inefficiency from the analysis method. In this subsection, I apply Fisher information analysis to determine the contribution of the measurement noise and the analysis method software to the observed energy resolution from simulated measurement experiments. In doing so, we determine the detector's fundamental resolution limit but also can assess the effectiveness of the analysis software.

Consider a model with a parameter θ which outputs random variables X following the probability density function $P(X|\theta)$. Fisher information is a measure of the information contained within X with regards to the model parameter θ and is defined as [102]

$$I(\theta) = -\mathbb{E} \left[\left(\frac{\partial}{\partial \theta} l(\theta|x) \right)^2 \middle| \theta \right], \quad (3.12)$$

where $l(\theta|x)$ is the log-likelihood function of $P(X|\theta)$. Fisher information sets a lower limit on the certainty to which one can determine θ ; this limit is known as the Cramer-Rao bound [103] and is given by

$$\text{Var}(\tilde{\theta}) \geq \frac{1}{I(\theta)}. \quad (3.13)$$

It is important to note that the Cramer-Rao states the minimum variance to which we can possibly determine θ but it does not instruct on how to achieve this variance or even if it is practically possible. Eqn. 3.12 can be rewritten in the form of

$$I(\theta) = -\mathbb{E} \left[\frac{\partial^2}{\partial \theta^2} l(\theta|x) \middle| \theta \right], \quad (3.14)$$

whereby Fisher information can be understood in terms of the curvature of the log-likelihood function. The log-likelihood function is maximised when the estimate $\tilde{\theta}$ is equal to the true value of θ but the precision to which θ can be determined is dependent on curvature of the log-likelihood function about the maximum. Maxima with high curvature allow for precise localisation of the peak value and therefore a higher certainty estimate of θ .

Eqn. 3.14 can be shown to be equivalent to Eqn. 3.12 by rewriting $l(\theta|x)$ in terms of the likelihood function $\log L(\theta|x)$,

$$\begin{aligned} -\mathbb{E} \left[\frac{\partial^2}{\partial \theta^2} l(\theta|x) \middle| \theta \right] &= -\mathbb{E} \left[\frac{\partial}{\partial \theta} \left(\frac{1}{L(\theta|x)} \frac{\partial}{\partial \theta} L(\theta|x) \right) \middle| \theta \right] \\ &= -\mathbb{E} \left[\frac{-1}{L(\theta|x)^2} \left(\frac{\partial}{\partial \theta} L(\theta|x) \right)^2 \middle| \theta \right] - \\ &\quad \mathbb{E} \left[\frac{1}{L(\theta|x)} \frac{\partial^2}{\partial \theta^2} L(\theta|x) \middle| \theta \right]. \end{aligned} \quad (3.15)$$

The second term in Eqn. 3.15 is zero due to normalisation of the probability density function:

$$\begin{aligned} \mathbb{E} \left[\frac{1}{L(\theta|x)} \frac{\partial^2}{\partial \theta^2} L(\theta|x) \middle| \theta \right] &= \int \frac{\partial^2}{\partial \theta^2} L(\theta|x) dx \\ &= \frac{\partial^2}{\partial \theta^2} \int L(\theta|x) dx \\ &= 0. \end{aligned} \quad (3.16)$$

Converting the first term in Eqn. 3.15 back to $l(\theta|x)$ shows it is equal to the Fisher information

$$-\mathbb{E} \left[\frac{-1}{L(\theta|x)^2} \left(\frac{\partial}{\partial \theta} L(\theta|x) \right)^2 \middle| \theta \right] = \mathbb{E} \left[\left(\frac{\partial}{\partial \theta} l(\theta|x) \right)^2 \middle| \theta \right], \quad (3.17)$$

thereby showing that the two forms of Fisher information in Eqn. 3.12 and Eqn. 3.14 are equivalent.

The Cramer-Rao bound of the simulation model energy resolution was calculated by considering a time series of N measurements with a single particle event of energy E arriving

at the start of the time series such that

$$\mu_n = \frac{E}{\tau_{\text{eff}}} \exp\left(\frac{-t_n}{\tau_{\text{eff}}}\right) \quad (3.18)$$

and

$$l(E|\mathbf{y}, \sigma) = N \ln\left(\frac{1}{\sqrt{2\pi}\sigma^2}\right) + \frac{1}{2\sigma^2} \sum_{i=1}^n -(y_n - \mu_n)^2. \quad (3.19)$$

Applying Eqn. 3.18 and Eqn. 3.19 to Eqn. 3.14 provides the expression for Fisher information

$$I(E) = \frac{1}{\sigma^2 \tau_{\text{eff}}^2} \sum_{n=1}^N \exp\left(\frac{-2t_n}{\tau_{\text{eff}}}\right). \quad (3.20)$$

If the sampled measurements are taken periodically at Δt intervals, Eqn. 3.20 can be written as

$$I(E) = \frac{1}{\sigma^2 \tau_{\text{eff}}^2} \sum_{n=1}^N \exp\left(\frac{-2n\Delta t}{\tau_{\text{eff}}}\right). \quad (3.21)$$

This equation corresponds to a geometric series and so can be simplified using standard geometric series summation to

$$I(E) = \frac{1}{\sigma^2 \tau_{\text{eff}}^2} \frac{\exp\left(\frac{-2\Delta t}{\tau_{\text{eff}}}\right)^N - 1}{\exp\left(\frac{-2\Delta t}{\tau_{\text{eff}}}\right) - 1}. \quad (3.22)$$

Under the condition of sufficiently long measurement time such that $N\Delta t \gg \tau_{\text{eff}}$, the Fisher information expression reduces to

$$I(E) = \left[\sigma^2 \tau_{\text{eff}}^2 \left(1 - \exp\left(\frac{-2\Delta t}{\tau_{\text{eff}}}\right) \right) \right]^{-1}. \quad (3.23)$$

In the case of Gaussian white noise, the noise standard deviation σ can be rewritten in terms of noise-equivalent power (NEP). Using Eqn. 3.3 and Eqn. 3.23, the Cramer-Rao energy resolution limit becomes

$$\Delta E = 2\sqrt{2\log(2)} \frac{\text{NEP}}{\sqrt{2\Delta t}} \tau_{\text{eff}} \sqrt{1 - \exp\left(\frac{-2\Delta t}{\tau_{\text{eff}}}\right)}, \quad (3.24)$$

where the factor of $2\sqrt{2\log(2)}$ converts from standard deviation to full width at half maximum. In the limit of $\Delta t \rightarrow 0$, Eqn. 3.24 tends to

$$\Delta E \geq 2\sqrt{2\log 2} \text{NEP} \sqrt{\tau_{\text{eff}}}, \quad (3.25)$$

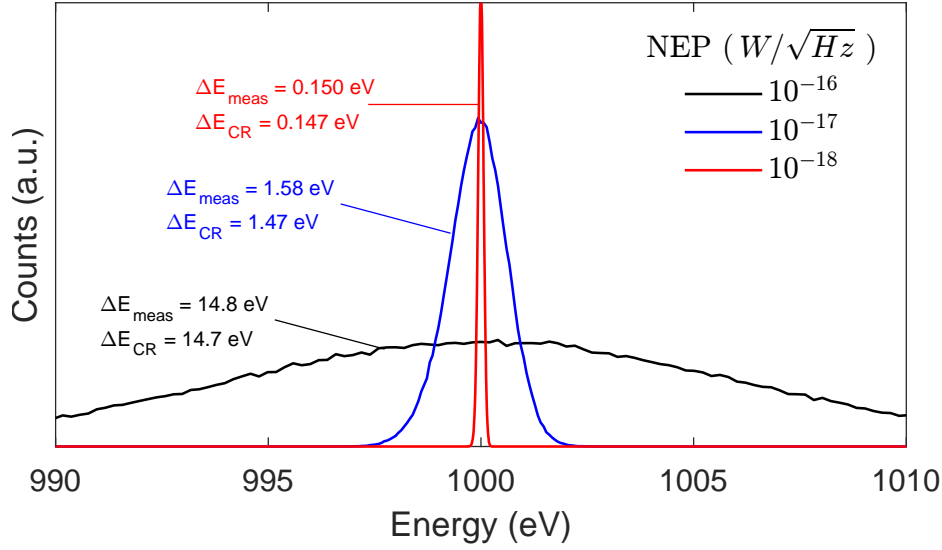


Fig. 3.10 Measured energy spectra of monoenergetic 1000 eV electrons at different simulated noise-equivalent powers (NEPs). Each simulation was performed with a detector response time of $100 \mu\text{s}$ at a 100 MHz sampling frequency measuring 5×10^5 electrons. The observed energy resolutions are compared (ΔE_{meas}) with the Cramer-Rao lower bound (ΔE_{CR}) calculated from Eqn. 3.26. Reproduced from [101].

providing the final expression for energy resolution calculated from Fisher information analysis. Using Eqn. 3.1, we can rewrite Eqn. 3.25 as

$$\Delta E \geq 2\sqrt{2\log(2)}\sqrt{4k_B T_c E_{\text{sat}} \frac{n}{2}}. \quad (3.26)$$

This result agrees with the result under white noise conditions in [88] and differs from the energy resolution of Eqn. 2.39 by a factor of $\sqrt[4]{n/2}$ under non-white noise conditions. When $n = 2$, the two equations match exactly.

With the fundamental resolution limit in hand, we can now compare Eqn. 3.25 with observed energy resolutions from simulated TES measurements. Fig. 3.10 shows the analysed particle energies from a simulation of monoenergetic 1 keV particles for NEPs of 10^{-16} , 10^{-17} and $10^{-18} \text{ W}/\sqrt{\text{Hz}}$. Each simulation utilised TESs with $100 \mu\text{s}$ decay time measured at a sampling frequency of 100 MHz. To prevent pileup, a periodic source was used with every particle spaced $10 \tau_{\text{eff}}$ apart in time. A total of 5×10^5 particles were generated in each simulation. The FWHM of each measurement peak, (ΔE_{meas}) was calculated and compared to the Cramer-Rao limit (ΔE_{CR}) calculated from Eqn. 3.25 in Fig. 3.10. The results show the analysis method provides near optimal energy resolution. In the absence of pileup, the

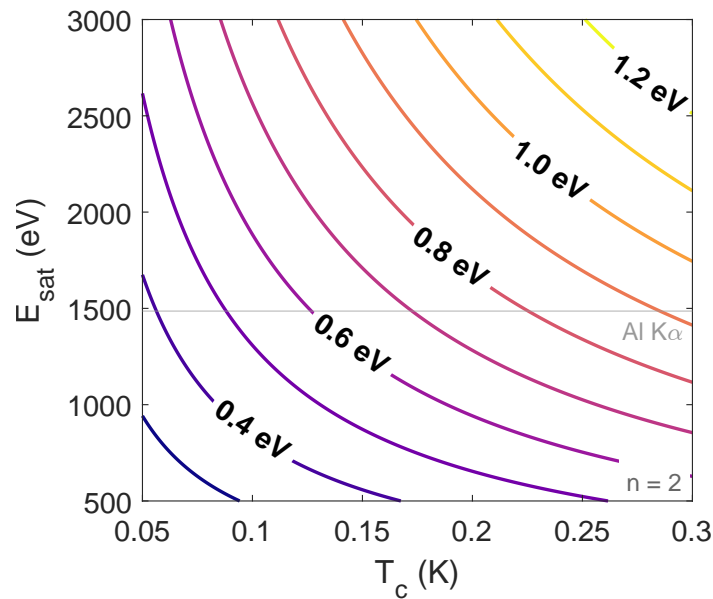


Fig. 3.11 TES energy resolution limit across a range of transition temperatures and saturation energies. For reference, the aluminium $K\alpha$ energy has also been shown.

data analysis method provides results that are reflective of the fundamental device behaviour within the range of parameters measured.

3.5 TES Electron Spectrometer Requirements

This section uses the simulation software to determine the TES detector requirements necessary to be comparable to concentric hemispherical analysers (CHAs) currently used in XPS measurements. The two key figures of merit to consider are energy resolution and count rate.

As discussed in Chapter 1, the operating principles of TESs and CHAs are fundamentally different and comparisons between the two technologies are dependent on the specific measurement circumstances. CHAs have an intrinsic balance between energy resolution and count rate that can be changed during operation. The energy resolution of a CHA can typically range from 0.1 eV to 5 eV dependent on the apparatus settings. In comparison, TESs have a fixed energy resolution that is dependent on the detector design and so cannot be changed during operation. Using Eqn. 3.26, Fig. 3.11 plots the relation between TES energy resolution, transition temperature, T_c , and saturation energy, E_{sat} . We can see that the TES energy resolution resides within the range achievable using CHAs but cannot match the best resolutions whilst maintaining sufficient saturation energies; the question of interest is whether TESs can provide a combination of energy resolution and count rate that cannot be achieved using CHAs.

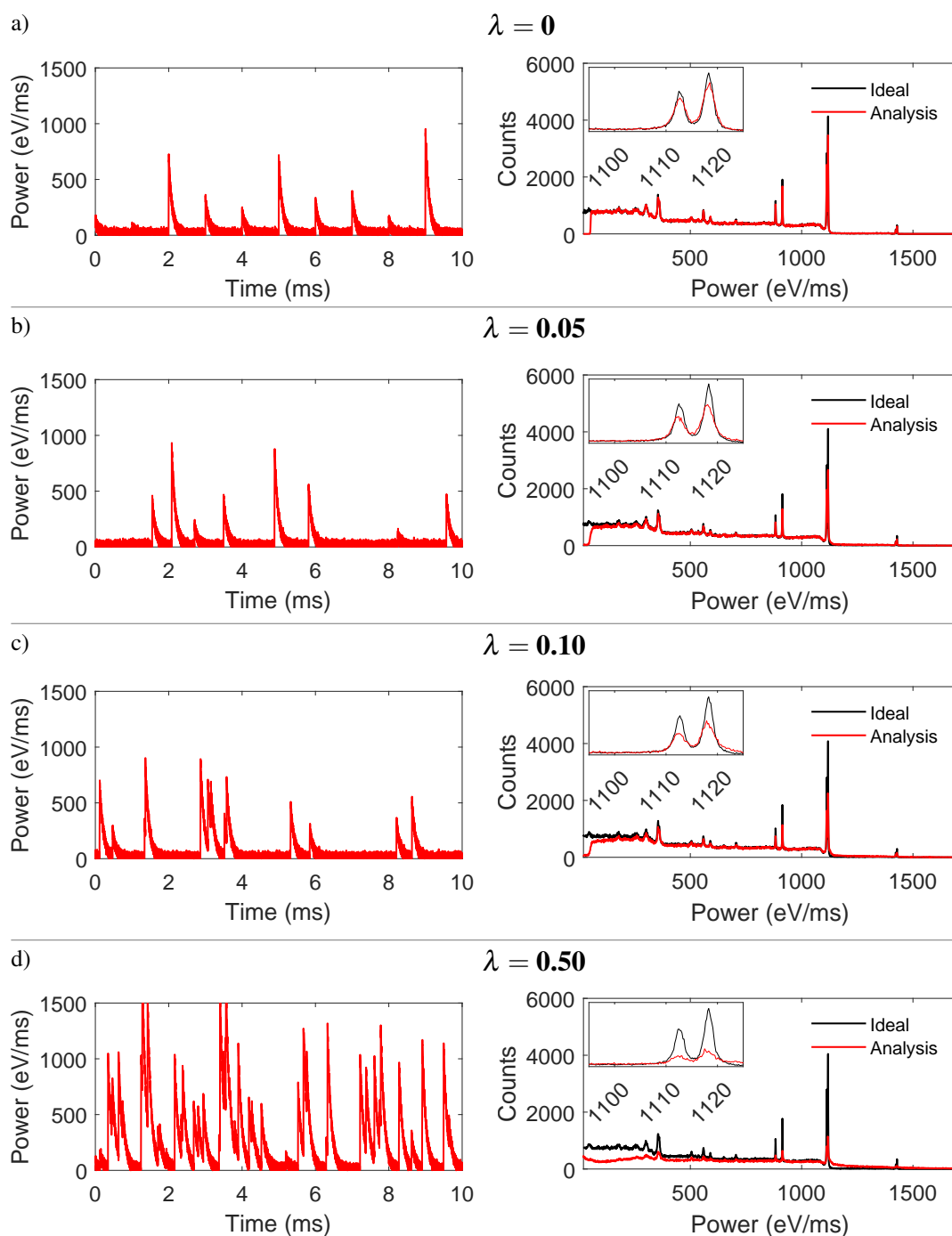


Fig. 3.12 Effect of different pileup rates (λ) on the measured XPS spectrum of silver. Every simulation was performed with a $100 \mu\text{s}$ response time TES sampled at 20 MHz measuring 5.75×10^5 electrons. $\lambda = 0$ was simulated using periodic electron arrivals spaced at $10\tau_{\text{eff}}$ λ of (b) 0.05, (c) 0.1 and (d) 0.5 were simulated using random particle arrival times with mean fluxes of arrival rates of 500 s^{-1} , 1000 s^{-1} , 5000 s^{-1} , respectively. Partially reproduced from [101].

The optimal electron count rate is determined by pileup, with the detrimental effects of pileup on the measured spectrum being dependent on the shape of the spectrum itself. For example, if the source electron spectrum was a single narrow Gaussian of energy E , high incidences of pileup, where overlapping particle events cannot be distinguished, would result in a measured spectrum of a multiple Gaussians with peak energies of multiples of E . The effect of pileup on a spectrum as structured as the XPS spectrum of silver is vastly different. As such, a systematic treatment of the effects of pileup is not straightforward but we can use the simulation software to empirically determine the best balance between high count rate and pileup for the purpose of XPS measurement.

Fig. 3.12 shows simulations with four different incidence rates of pileup. The parameter determining the degree of pileup is $\lambda = k\tau_{\text{eff}}$ where k is the electron arrival rate. λ is equivalent to the expected number of electrons arriving within the TES response time. The simulation without pileup (Fig. 3.12a) was performed using periodic particle arrival times with a $10\tau_{\text{eff}}$ spacing. Each simulation was performed with a $100\mu\text{s}$ TES sampled at 20 MHz measuring 5.75×10^5 electrons. The effect of pileup can be seen as a reduction in the ability to distinguish low energy electrons, resulting in an overestimate of higher energy electrons, especially higher than 1000 eV.

At pileup rates of $\lambda = 0.10$ or below, the TES was able to accurately measure the XPS spectrum but beyond this pileup rate, the observed spectrum is heavily distorted. $\lambda = 0.10$ provides the balance between high count rates and accurate measurements with the most significant pileup deterioration occurring at energies below 200 eV. This portion of the spectrum is of little practical interest in XPS applications and so this pileup rate has little detrimental impact of the measurement unless quantitative compositional data is required which would require a lower electron flux or implementing pileup rejection to ignore overlapping particle events.

In the case where electrons have random arrival times, the proportion of overlapping events can be calculated using Poisson statistics and so we can assess the effect of pileup rejection on count rate. As the TES response is an infinitely extending exponential decay, in order to assess pileup rates, a cut-off time is required after which the event is considered complete. The choice of cut-off time is inherently a trade-off between count rate and energy resolution, due to the diminishing ability to calculate the energies of overlapping particle events as the degree of overlap increases. For the purposes of the following analysis, non-overlapping events have been defined as being separated by at least $3\tau_{\text{eff}}$.

The probability of n events occurring in an interval of duration t is

$$P(n) = \frac{(kt)^n e^{-kt}}{n!}. \quad (3.27)$$

Table 3.1 Predicted TES performance with the given example set of device parameters where all symbols are as defined in the text. Collection time is the time needed to measure 10^6 particles at the given count rate and array size.

C (pJ/K)	G_0 (pW/K)	n	α	T_c (K)	Array Size
0.20	50	2	100	0.20	10
τ_{eff} (μs)	E_{sat} (eV)	ΔE (eV)	λ	Count Rate (s^{-1})	Coll. Time (min)
120	2500	1.0	0.1	830	2.0

For a specific particle absorption event, the probability that no particles have been absorbed within time t before and after is therefore e^{-2kt} . For non-overlapping events, separated by at least $3\tau_{\text{eff}}$, the proportion of events remaining after pileup rejection would be $e^{-6k\tau_{\text{eff}}}$. When $\lambda = 0.1$, 55% of particles are non-overlapping, corresponding to a greater count rate than $\lambda = 0.05$ without pileup rejection. As such, we can approximately state that the time required to measure a spectrum with pileup rejection to be double that without pileup rejection at $\lambda = 0.1$. In practice, the ability of a pileup rejection procedure at improving the quality of the data will be limited by the ability of the procedure to distinguish near simultaneous events as two separate events rather than a single one. Analysing the dataset for Fig. 3.12c showed that 11 % of incident electrons were unidentified due to their proximity to another event with all unidentified pileup events occurring at time differences of $2\tau_{\text{eff}}$ or less.

We can now use the simulation results to determine the device requirements for TES spectrometers under XPS measurement conditions. A typical CHA would be capable of measuring the spectrum in Fig. 3.12 with 10^6 counts in several minutes. A single TES with a $100\mu\text{s}$ response would require 17 minutes with a pileup rate of 0.1 and approximately double that time if including pileup rejection. Currently, TES X-ray calorimeters operating in the energy range investigated here display response times of hundreds of microseconds and so a single conventional TES calorimeter cannot currently match the count rate of a CHA. However, small arrays of tens of TESs would be able to match and exceed the count rate capabilities of CHAs. An array of 10 TESs with $120\mu\text{s}$ response times would only require 2 minutes to measure 10^6 particles with a pileup factor of 0.1. If we target an energy resolution of 1 eV and transition temperature of 200 mK, Eqn. 3.26 limits the saturation energy to a maximum of 2610 eV, significantly greater than the upper energy limit of 1487 eV when using an Al $K\alpha$ X-ray source.

Table 3.1 uses the results from this section to provide an example set of TES device parameters for electron spectroscopy and the predicted performance capability of a set of such devices. This set of devices would have comparable energy resolution and measurement rate to existing electron spectrometers when performing full spectrum measurements.

3.6 Conclusions

The chapter has described the design, testing and usage of a TES calorimetry software package to investigate the feasibility of using TESs in electron spectroscopy, specifically XPS. The key result from this chapter is that TESs are viable electron spectroscopy detectors but the advantages they offer lie within the desired trade-off between count rate and energy resolution.

The energy resolutions achievable using TESs lie within the range of concentric hemispherical analysers but TESs cannot currently match the best resolutions reached by hemispherical analysers without using very low temperatures and saturation energies. However, for any application where a balance between measurement rate and resolution is necessary, TESs have a significant advantage. TESs provide a route to improve measurement rates over CHAs by operating arrays of tens, hundreds or thousands of detectors simultaneously. This opens the door to orders of magnitude increases in measurement rates whilst maintaining sub-eV energy resolutions.

When designing TESs for electrons spectroscopy, these detectors will have to maximise energy resolution and so the saturation energy must be comparable with maximum electron energy to be measured. This will result in responses from the TES that are no longer described accurately by small-signal assumptions and will require more sophisticated analysis procedures, such as those discussed in Section 2.6.

Regarding the software package itself, and simulation and data analysis method were effective as tools to determine the requirements for TES electron spectroscopy. Fisher information analysis provided the fundamental achievable resolution limit for the simulated detectors but also showed the energy analysis method implemented operated near the resolution limit for non-overlapping events. The natural progression for the software package would be to incorporate more detailed TES physics regarding non-linear response shapes and non-white noise spectra. Such a tool would be particularly useful for the development of TES spectrometers by predicting the performance of different TES device designs.

Chapter 4

Electron Measurement System

4.1 Introduction

In this chapter, I describe the experimental apparatus used to perform what is to my knowledge the first TES electron spectroscopic measurements. The measurement system was designed to achieve three goals: demonstrate electron detection using TESs, measure electrons with energies spanning 0 - 2000 eV, and finally to demonstrate simultaneous measurement of a spectrum of electron energies. Two different experimental configurations were used: a direct beam configuration where the electron source was aimed directly at the TES chip and a scattered beam configuration where electrons were measured by the TES after being scattered off of a graphite target. The direct measurements were used to demonstrate the ability to measure electron energies using TESs and the scattered electron configuration was built to be able to measure electron spectra with improved noise performance.

Section 4.2 provides an overview of the full experimental system, after which, specific aspects of the system are presented. Section 4.3 outlines the choice of electron source used and the integration of the cryostat into the experimental system. Section 4.4 describes the electron beam pathway from the room-temperature source to the cryogenic TESs, in both the direct and scattered beam configurations. The TES measurement apparatus used to perform electron measurements is provided in Section 4.5. Finally, the software used to control the experimental system is outlined in Section 4.6.

4.2 Overview

The TES electron measurements were performed using a closed-cycle adiabatic demagnetisation refrigerator (CC-ADR). The cryostat consisted of four stages with base temperatures of

45 K, 4 K, 1 K and 100 mK. Pulse tube cooling maintained the temperature of the 4 K stage; the ADR provided the additional cooling required for the 1 K and 100 mK stages to reach their respective temperatures.

The electron beam was generated from a commercially sourced electron gun (SPECS EQ22), mounted onto the cryostat in the configuration shown in Fig. 4.1. The electron beam passed through windows in the vacuum jacket, 45 K and 4 K heat shields before reaching the 100 mK TES module. Two different configurations were tested with the TES module either directly in line with the electron beam, or out of line-of-sight. In the latter configuration, the electron beam was aimed at a graphite target and scattered electrons were measured.

In order to reduce thermal loading and confine stray electrons, tubes were mounted on the 45 K and 4 K stages with the internal surface painted black with colloidal graphite paint (Aquadag Graphite, Agar Scientific Ltd). These tubes were also capped with apertures and 1500 grade copper mesh (G243C, Agar Scientific Ltd) to further reduce infrared loading into the cryostat. Infrared loading both reduces the hold time of the 100 mK stage and, if the photons impinge on the TESs directly, provide a source of measurement noise. The additional thermal energy entering the TES can change the operating point of the device within the superconducting transition and sufficiently high degrees of thermal loading can entirely saturate the detectors.

The TES module consisted of a device chip with 30 TESs inductively coupled to a superconducting quantum interference device (SQUID) readout system. Mo/Au bilayer TESs with 200 mK transition temperatures were tested. These devices and the surrounding TES module were designed and fabricated as part of a previous PhD project investigating the physics of TESs [77]. As such, they were not originally designed for electron calorimetry but were repurposed to meet these ends.

Fig. 4.2 shows the cryostat used with the mounted electron source (a) and the 4 K stage with the TES device module affixed to the 100 mK stage (b)

4.3 Electron Source

When considering electron sources appropriate for the planned measurement, there were a number of parameters to consider such as the energy range, linewidth, beam current, operating pressure and stability over time. An additional complication of key importance is the thermal output of the source and whether this can be mitigated to prevent saturating the detector with infrared radiation. For this application, we required a source capable of producing electrons between 0 and 2 keV energies with narrow linewidths and extremely low beam current densities ($<1 \text{ nA/m}^2$) to allow for measurement of individual electrons.

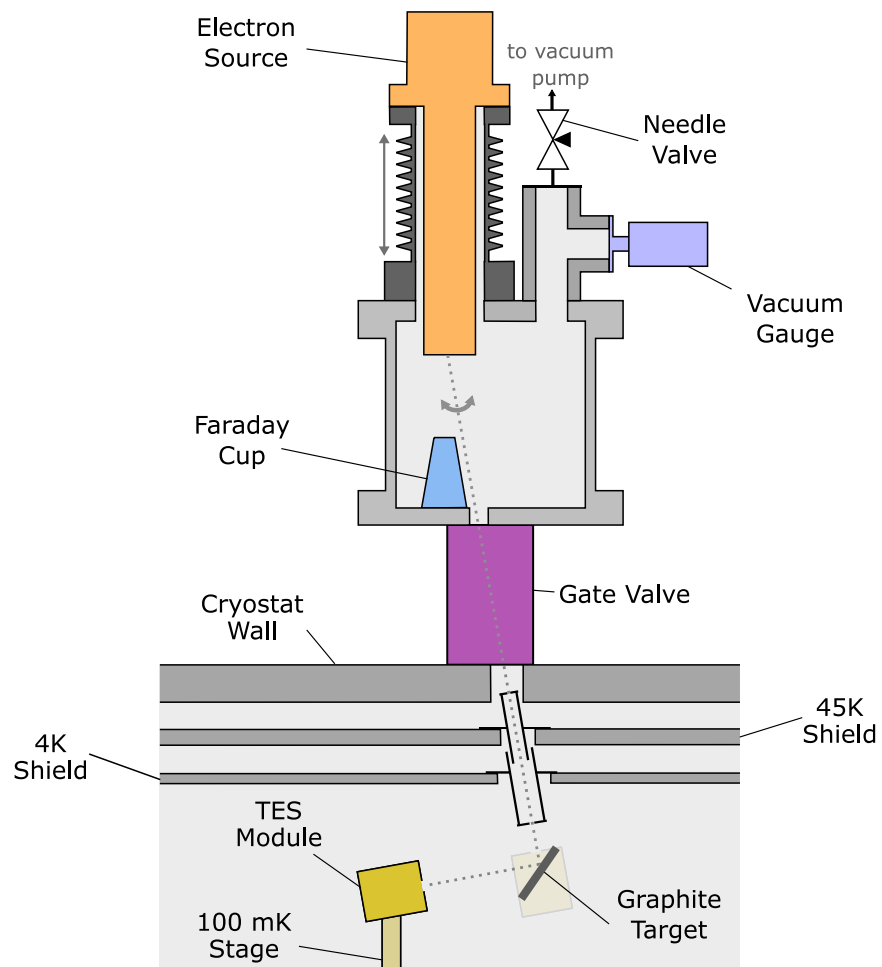


Fig. 4.1 TES electron measurement experiment in the scattered electron measurement beam configuration.

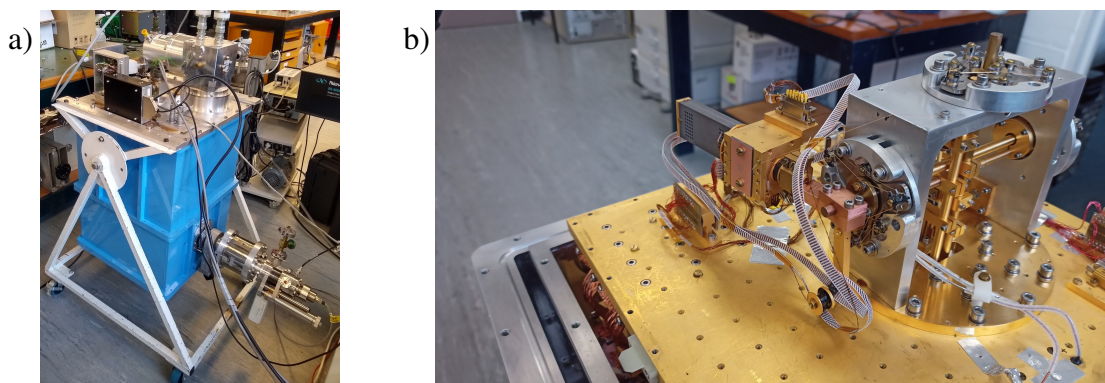


Fig. 4.2 a) CC-ADR cryostat with mounted electron source used for electron measurement experiments. b) 4 K stage with TES module mounted to 100 mK stage in the direct beam configuration.

Electron sources can be separated into two categories, thermionic and field emission sources. In thermionic sources, electrons are emitted from a sharp heated filament and then accelerated and focussed into a beam. Common filaments are tungsten and lanthanum hexaboride with filament temperatures of around 2800 and 1800 K respectively. Field emission sources apply high-strength electric fields to a sharp emitter tip to exploit the Schottky effect and allow quantum tunneling of electrons out of the tip. Field emission sources can be further divided into Schottky field emission guns (FEGs) and cold FEGs. Cold FEG filaments operate at room temperature, relying almost entirely on the applied electric field strength to extract electrons. Schottky FEGs have less field enhancement than cold FEGs and so utilise a combination of a heated filament and field emission to achieve the desired emission rate. The advantages of FEGs over thermionic emitters are increased current densities, longer filament lifetimes and reduced beam spread (both spatially and energetically). The key disadvantages are cost and the requirement for UHV conditions (10^{-9} mbar).

When comparing between the different source types for this experiment, the most important factors are the operating vacuum pressure, energy linewidth and infrared emission from the source. The CC-ADR cryostat used heavily relied on cryopumping to achieve UHV conditions meaning the pressure increases quickly away from the cold stages, rising over 10^{-7} mbar at the position of the electron source. Therefore, implementing a FEG system would require implementing differential pumping on the electron source or designing a custom electron source mounted to the 4 K stage, operating at cryogenic temperatures. The alternative, thermionic sources, can operate at 10^{-6} mbar and so, despite the wider beam energy spreads approaching 1 eV and increased thermal emission from the filament, thermionic sources were the most practical option.

Of the commercially available thermionic electron sources, the EQ22 source from SPECS was the best suited for our experiment. The EQ22 can create electron beams up to 5000 eV with beam currents spanning nanoamps to hundreds of microamps and energy FWHM around 0.7 eV. Additionally, the source has integrated x- and y- beam deflection allowing aiming and scanning the beam across chosen areas. The tungsten filament requires heating to 2500 K but the thermal loading from the filament can be greatly reduced by deflecting the beam away from the filament line-of-sight.

The next problem that was addressed was the manner in which the source was mounted onto the cryostat. The chosen arrangement is shown in Fig. 4.1 where the electron source was mounted onto a chamber outside the cryostat. The electron source has been positioned off-centre from the cryostat window by a 10° angle, requiring the electron beam to be deflected away from the filament line-of-sight to enter the cryostat. The insertion depth

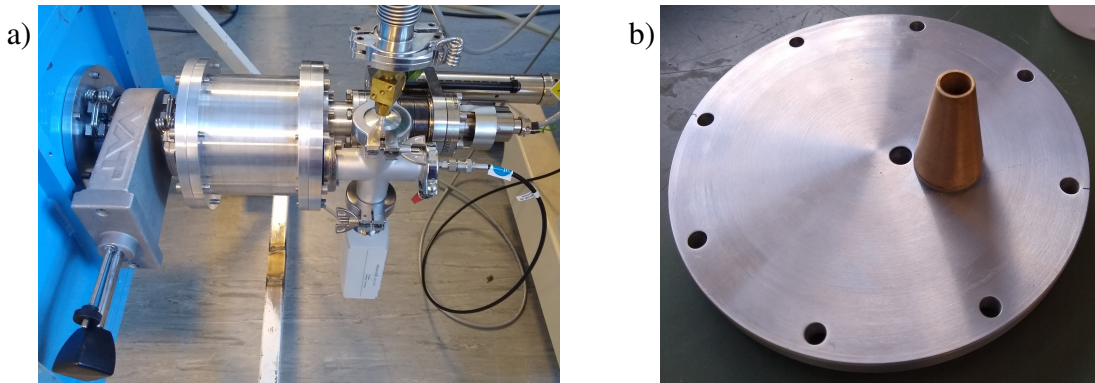


Fig. 4.3 a) Electron source assembly mounted onto the cryostat vacuum jacket. b) Faraday cup and aperture into cryostat.

of the electron source into the chamber was controlled through the use of bellows so the alignment can be adjusted in operation. The electron source was isolated from the cryostat by a gate valve and needle valve to allow for venting of the cryostat while maintaining electron source vacuum. The purpose of the needle valve was to be able to equilibrate the cryostat and electron source pressures controllably, prior to opening the gate valve.

The Faraday cup was positioned directly in front of the electron source for the purpose of measuring electron beam current prior to deflecting the beam into the cryostat. The beam current through the Faraday cup was measured using a Keithley 6485/E picoammeter. Photographs of the mounted electron source assembly and the Faraday cup are provided in Fig. 4.3a and b, respectively.

4.4 Electron Beam Pathway

When considering the beam pathway from the source to the TES module, there are three requirements that need to be met: the electron beam must be aligned to the target, the infrared thermal loading on the TESs must be minimised, and stray electrons must also be given a pathway to ground. If this last point is not met, the accumulating charge could deflect the electron beam off the desired path or high-voltage static discharge could damage the TES readout electronics, primarily the SQUIDs. To meet these requirements, modifications were made to the cryostat heat shields and the TES module.

4.4.1 Heat Shield Modifications

The two most important sources of infrared radiation entering the cryostat are from the room-temperature electron source chamber and the high-temperature electron source filament. The

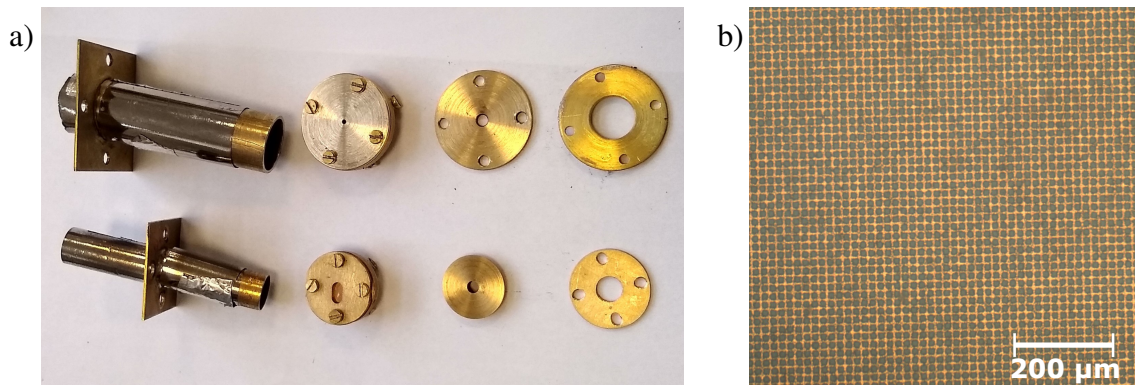


Fig. 4.4 a) 4 K (top) and 45 K (bottom) brass tubes and aperture assemblies for confining stray electrons and reducing infrared radiation entering the cryostat. b) Optical microscope image of 1500 lines per inch copper mesh.

high-temperature filament radiation was mitigated by mounting the source off-axis from the cryostat aperture, leaving the 300 K infrared radiation from the cryostat chamber as the primary source of thermal loading. The 300 K radiation power received by the TESs can be reduced blocking radiation using narrow apertures, dispersing the radiation using diffraction or by deflecting the beam away from this infrared radiation, as was done with the filament radiation, but each of these solutions have corresponding trade-offs.

The use of apertures to block radiation creates a balance between the ability to align the electron beam and amount of infrared reduction achievable. For narrow apertures, beam alignment is further complicated by the varying temperatures of different parts of the cryostat from the room temperature vacuum jacket and electron source chamber, the 45 K window, 4 K stage and 100 mK TES module. All of these components will undergo differing amounts of thermal contraction that would need to be accounted for to maintain beam alignment.

The ideal solution to the infrared loading problem would be to deflect the beam out of line-sight of the 300 K window as was done for the electron source. This deflection can be achieved using high-voltage deflector plates but the difficulties in modifying the experimental apparatus with appropriate high-voltage wiring was found to be impractical within the scope of this project. An alternative would be the use of magnetic field deflection but the key issue with this proposal was the resulting resistive heating. The currents necessary to achieve the required deflection angles would result in excessive Joule heating on the 4 K stage.

Therefore, the chosen solution was to use a combination of narrow apertures and mesh grids to reduce the IR radiation sufficiently to perform electron measurement. The meshes used were 1500 lines per inch copper grids with an open area of 55 % and approximately $10\ \mu\text{m}$ hole width. These meshes blocked incident radiation and dispersed the transmitted

radiation by diffraction. Over 70 % of 300 K black-body radiance occurs at wavelengths over $10\ \mu\text{m}$ and so the radiation exiting the mesh was diffused over a wide area by diffraction.

The meshes and apertures were affixed to two brass tubes mounted on the 45 and 4 K heat shields as shown in Fig. 4.1. The inside surfaces of both tubes were painted with colloidal graphite paint to act as a matte infrared absorbing surface whilst maintaining electrical conductivity at cryogenic temperatures. One end of both of these tubes was capped with narrow apertures of differing sizes and the mesh grids (see Fig. 4.4). The narrower 8 mm internal diameter tube is the 45 K tube whereas the wider 14 mm internal diameter tube was mounted onto the 4 K heat shield. The radiation entering the cryostat first passed through the 45 K aperture and dispersed by a single layer of mesh. The dispersed radiation was absorbed by or reflected off the matte black surface on the inside of the tube. The remaining radiation then entered the 4 K tube and exited after passing another layer of mesh and the 4 K aperture. The 4 K mesh was removed for later scattered electron measurements as it was observed to not be required.

Different combinations of apertures sizes in Fig. 4.4 were used at different stages of the project; the widest apertures shown, of 6 mm and 10 mm diameters, for the 4 K and 45 K tubes respectively, were used primarily to determine the rough beam alignment of the system. By measuring the beam current absorbed through the apertures or the TES module, the beam position could be determined. This procedure is discussed further in Section 4.6. As knowledge of the beam position relative to the TES array and aperture locations improved, the aperture sizes used were reduced in steps to minimise thermal loading on the TES. The smallest aperture shown in Fig. 4.4 of 1 mm diameter was only used in scattered electron measurements.

4.4.2 Magnetic Shielding

Of the apertures shown in Fig. 4.4, the elongated, asymmetric 45 K aperture is notably different. I designed the shape of this aperture as a compromise between magnetic field deflection and blocking IR radiation. The geometry of the cryostat necessitates mounting the electron source horizontally in relation to the target, introducing the complication of magnetic field deflection.

Ambient magnetic fields ranging from $30\ \mu\text{T}$ to $40\ \mu\text{T}$ were measured in the vicinity of the cryostat. These fields are sufficient to deflect the electron beam by centimetres at the energies and path lengths considered here. Magnetic field deflection was mitigated by wrapping the electron source chamber and brass tubes with magnetic shielding foil (Metglas 2705M, Hitachi Metals Inc.). This foil was observed to reduce the magnetic field within the electron source chamber from $39\ \mu\text{T}$ to $6\ \mu\text{T}$. The modified 45 K aperture was introduced to

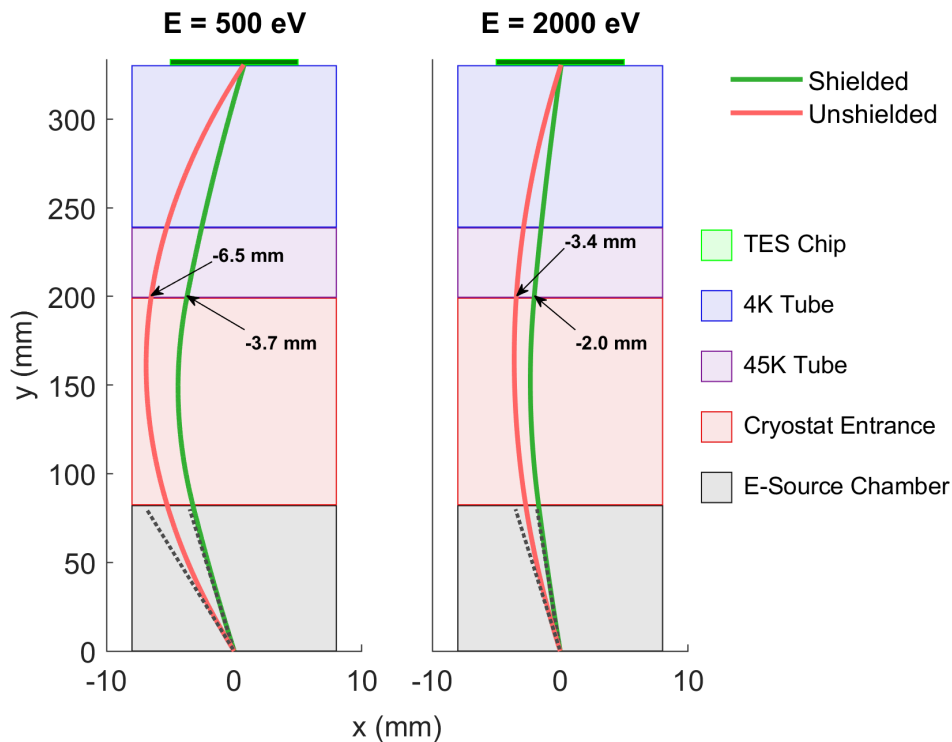


Fig. 4.5 Estimated electron beam deflection due to ambient magnetic fields. The coloured regions represent different components the beam passes through from the tip of the electron source to the devices. The cryostat entrance includes both the gate valve and cryostat vacuum jacket window. Beam paths were calculated under magnetic fields of $40 \mu\text{T}$ and shielding was assumed to reduce the magnetic field by a factor of 5 in each region except for the cryostat entrance which was left unshielded. Labelled distances show the separation between the beam path and the central axis at the entrance aperture of the 45 K tube.

accommodate the remaining observed beam deflection. The diagram in Fig. 4.5 demonstrates how this 4 mm wide aperture on the 45 K windows allows a wider range of deflected electrons to reach the TES target.

4.4.3 TES Module Modifications

The apparatus described in the previous sections helped navigate the electron beam into the cryostat whilst screening IR radiation. However, the TES module had to also be modified to allow electrons to reach the detectors themselves. As mentioned in Section 4.2, the module and devices were designed and manufactured as part of a separate PhD project [77], and so had to be adapted for electron measurement experiments. The lid of the device module and the clamping of the TES chip were redesigned to allow electrons to reach the TESs

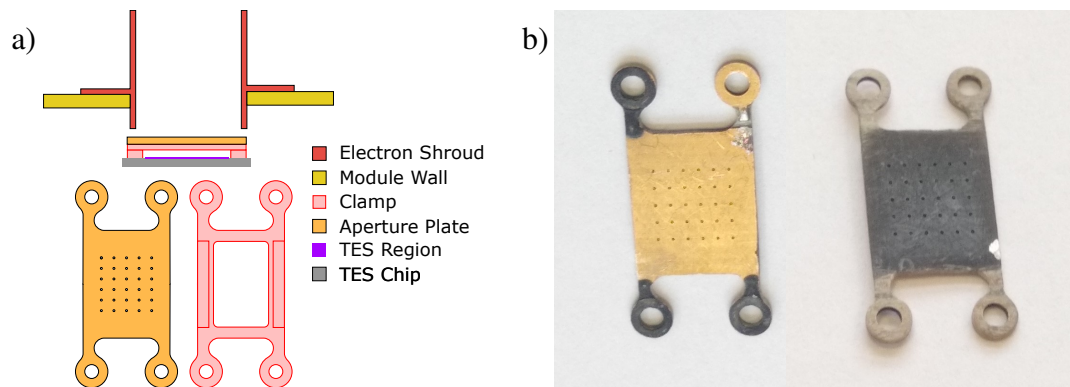


Fig. 4.6 a) TES module entrance and device clamping. b) Front and rear faces of the TES aperture plate with an array of 30 $200\ \mu\text{m}$ holes.

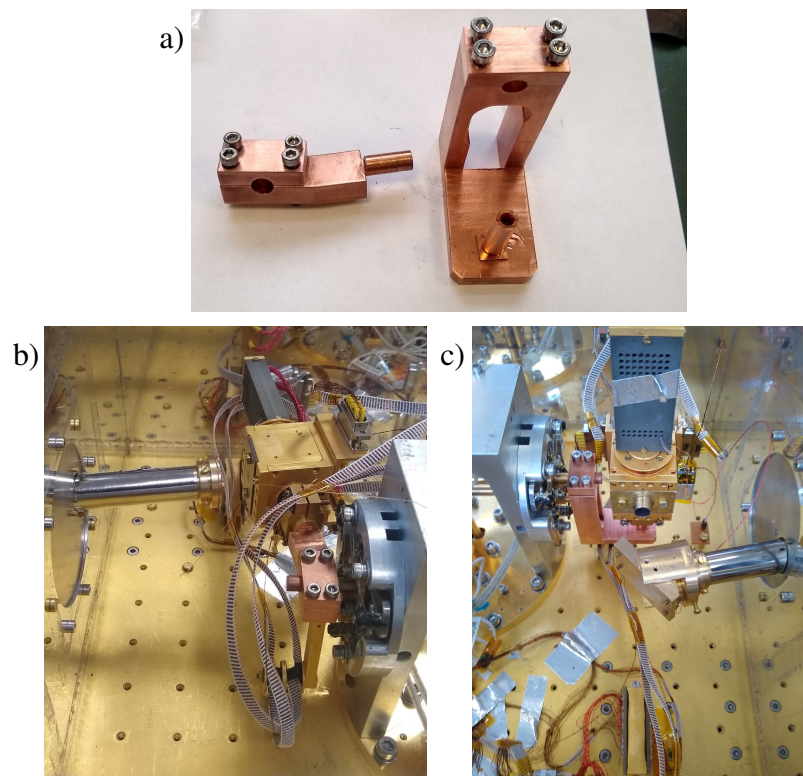


Fig. 4.7 a) Two TES module arms used to mount the module on the 100 mK stage for direct and scattered beam experimental configurations shown in b) and c), respectively.

(Fig. 4.6); the module was reoriented and repositioned into the path of the electron beam using the arms shown in Fig. 4.7, and TES ground connections were included to prevent charge accumulation, as described in the following subsection.

To allow electrons to enter the device module, the previous module lid was removed and replaced with a cylindrical brass shroud extending both into and outside the module. The purpose of the shroud was to confine and absorb stray electrons, preventing their entry into the cryostat chamber, or into the device module but away from the TES chip. The internal surface of the cylinder was painted with conductive black paint to aid in the absorption of stray electrons.

However, opening the module lid would greatly increase the thermal load on the TES as the incident IR radiation that would be reflected off the lid would now enter the module and be absorbed. Therefore, a gold-plated aperture plate was mounted above the TES chip to reflect a portion of this radiation away. The plate contained an array of $200\ \mu\text{m}$ apertures, positioned above the TESs to allow electrons to the devices. The aperture plate was affixed to fibreglass clamps holding the TES chip in place to ensure alignment between the apertures and the devices and the reverse face of the aperture plate was painted with conductive black paint to absorb and ground scattered electrons from the TES. Fig. 4.6 shows a diagram of the TES module modifications and photographs of the front and back faces of the aperture array.

The ability to apply a negative bias to the aperture plate was also designed for, but was not utilised. By connecting a bias wire to the gold plated surface, up to $-20\ \text{V}$ can be applied to the plate to reject incoming low-energy electrons and enhance electron absorption in the TES.

While the modifications to the module lid were the same for both scattered and direct beam measurements, an important component that differed between these two configurations was the arm mounting the TES to the $100\ \text{mK}$ stage. The two arms used are shown in Fig. 4.7 with the direct configuration shown in (b) and the indirect configuration in (c). The module arms were fabricated from copper and were designed to hold the box in the path of the electron beam. Ideally the arms would have been gold-coated to aid thermal contact, provide high IR reflectivity and prevent surface oxidation. However, this was not achievable in the time of the project and so the bare copper components was used.

Both the direct and scattered experimental configurations were successful in allowing for TES electron measurement, though greater degrees of infrared loading was observed in the direct beam configuration, as would be expected. The observed infrared loading is described in more detail in Chapter 5.

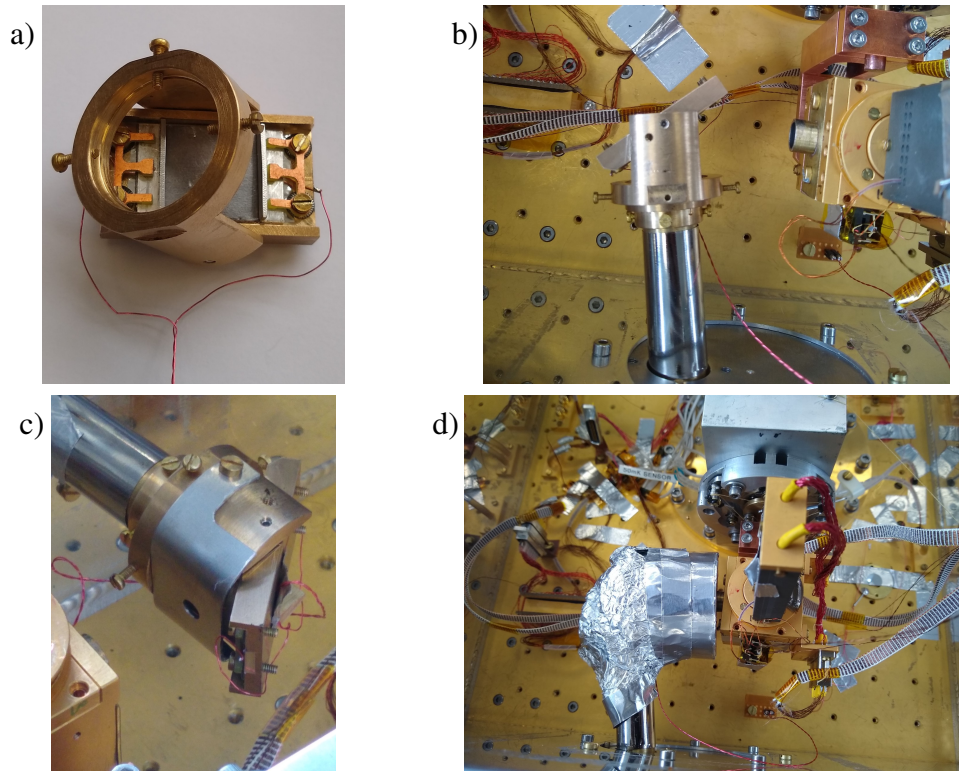


Fig. 4.8 a) Graphite target holder with graphite foil clamped in place and connected to two bias wires. b) Graphite target mounted onto 4 K tube and positioned in front of TES module. c) Collimator aperture fixed onto the target holder to block off-axis electrons reaching the detectors. d) Fully-assembled graphite target, surrounded by an aluminium cup and foil to contain scattered electrons.

4.4.4 Graphite Target Fixture

The final component of the scattered electron configuration, the graphite target, is discussed in this section. Graphite was chosen as the electron scattering target for its combination of low secondary electron yield (SEY) and infrared-absorbing properties. The low SEY means the scattered electron energy distribution is less dominated by electrons under 20 eV, allowing a greater proportion of higher electron energies to be measured.

A graphite target holder was designed to position 0.254 mm thick graphite foil (99.8 % purity, Alfa Aesar) relative to the incident electron beam. The foil was clamped down onto a rotatable stage such that the angle between the beam and the graphite surface could be controlled (Fig. 4.8a). This target holder was mounted onto the 4 K tube in front of the 4 K aperture, eliminating the possibility of the graphite target moving relative to the 4 K aperture during cooling (Fig. 4.8b). An additional collimating aperture was affixed to the target holder to further screen infrared radiation and prevent stray, off-axis electrons reaching the TES

chip (Fig. 4.8c). The entire target holder was then encapsulated in an aluminium cup to block electrons from entering the cryostat chamber. This cup overlapped with but did not touch the protruding shroud from the module lid. Aluminium foil was used to cover the back of the aluminium cup to prevent electrons escaping in that direction (Fig. 4.8d). For each measurement, the graphite was rotated such that the plane of the foil was 60° to the incident beam.

It should be noted that the scattered electron energy spectrum varies with emission angle with a very broad angular distribution of scattered electrons, spanning the entire half-space above the target. For these proof-of-principle measurements, as long as the electron beam was aligned such that it passed through the 4 K aperture and reached the graphite target, scattered electrons would be emitted in the direction of the TES module and measured. As the target to aim the electron beam at was now a point rather than a detector array spanning 5×5 mm, for the scattered electron measurements, the 1 mm aperture shown in Fig. 4.4 could be used without blocking detectors. The infrared loading in the scattered electron measurements was further reduced due to the increased path length and reflection off the IR-absorbing graphite target. Therefore, the copper mesh on the 4 K aperture was removed without observed change to the thermal loading.

The graphite sample holder was designed to clamp the target in place with a pair of bias wires to be able to apply a bias between -20 V and $+20$ V to see if the effect of the bias on the scattered electron energy distribution would be apparent through TES measurement. The graphite was electrically isolated from the sample holder by a layer of insulating Mylar tape. The graphite was held in place using two copper-plated polymer clamps. The copper-plated surface was grounded through the screws used to connect the clamps to the sample holder. Two L-shaped brackets were positioned in front of the exposed insulating polymer to prevent charging. The bias wires were clamped between these brackets and the graphite foil (see Fig. 4.8a). This arrangement functioned at isolating the graphite but gradual charging of the clamps was observed. The polymer clamps were therefore removed and the graphite was clamped and grounded directly to the sample holder.

4.5 TES Measurement System

Having described the experimental apparatus used to send electrons at the TESs, we now consider the system used to measure these electrons. The device chip mounted in the TES module contained 30 Mo/Au bilayer TESs with 40 and 120 nm layer thicknesses, respectively. Each device was suspended on 200 nm thick Si_xN_y islands by four $50 \mu\text{m}$ long, $1.41 \mu\text{m}$ wide legs Si_xN_y . Some devices had 200 nm thick gold bars patterned on the surface with

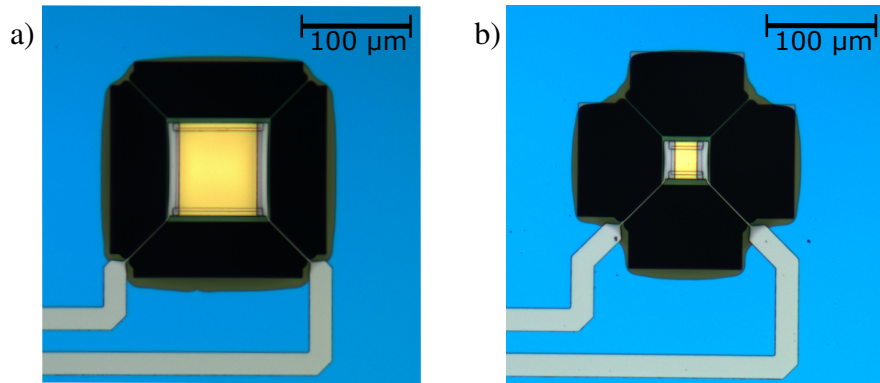


Fig. 4.9 Microscope images of a) 70 μm and b) 20 μm width Mo/Au TESs without gold bars, suspended on four silicon nitride legs.

the aim to reduce device noise. The device areas, number of gold bars and geometry of the bars varied across the TES array; Fig. 4.9 show images of two of the devices on the chip with varying geometries. Further details of the device designs and fabrication methods are reported in [77].

The TES bias and readout circuitry were built prior to this project but, for completeness, I will briefly describe their function here. The circuit diagram of the TES bias and readout systems are given in Fig. 4.10. The bias circuit on the left of the diagram was used to apply stable voltage biases of the order of tens of nanovolts across the TES whose normal state resistances ranged between 50 and 100 $\text{m}\Omega$. A bias voltage of $2V_A$ was applied across a chain of bias resistors, each with R_{bias} resistance. The TES was biased by connecting the device in parallel to one of these resistors. The TES current, I_{TES} , was measured using two-stage superconducting quantum interference device (SQUID) amplification. The SQUID output was measured using room temperature readout electronics with the voltage output, V_{out} , proportional to I_{TES} .

The first-stage DC SQUID has been denoted SQ1 in Fig. 4.10. SQ1 was connected to a single TES; as four SQ1 SQUIDS were available for use within the device module, one of four TESs could be read at a time during any cooldown. The TES in operation was inductively coupled to a current-biased SQ1. The output of the first-stage SQUID was then coupled to a series array of DC SQUIDS (SSA) (simplified to a single SQUID in Fig. 4.10 for the purposes of clarity). The purpose of the SSA is to provide wide bandwidth, high-gain amplification of the SQ1 signal with impedance-matching to the room-temperature preamplifier [104].

The overall readout circuit was operated as a null-type detector using a flux-locked feedback loop. The output of the SSA was used to cancel the flux entering SQ1, making V_{out} linear with respect to I_{TES} . A second feedback loop was available to lock the SSA. This

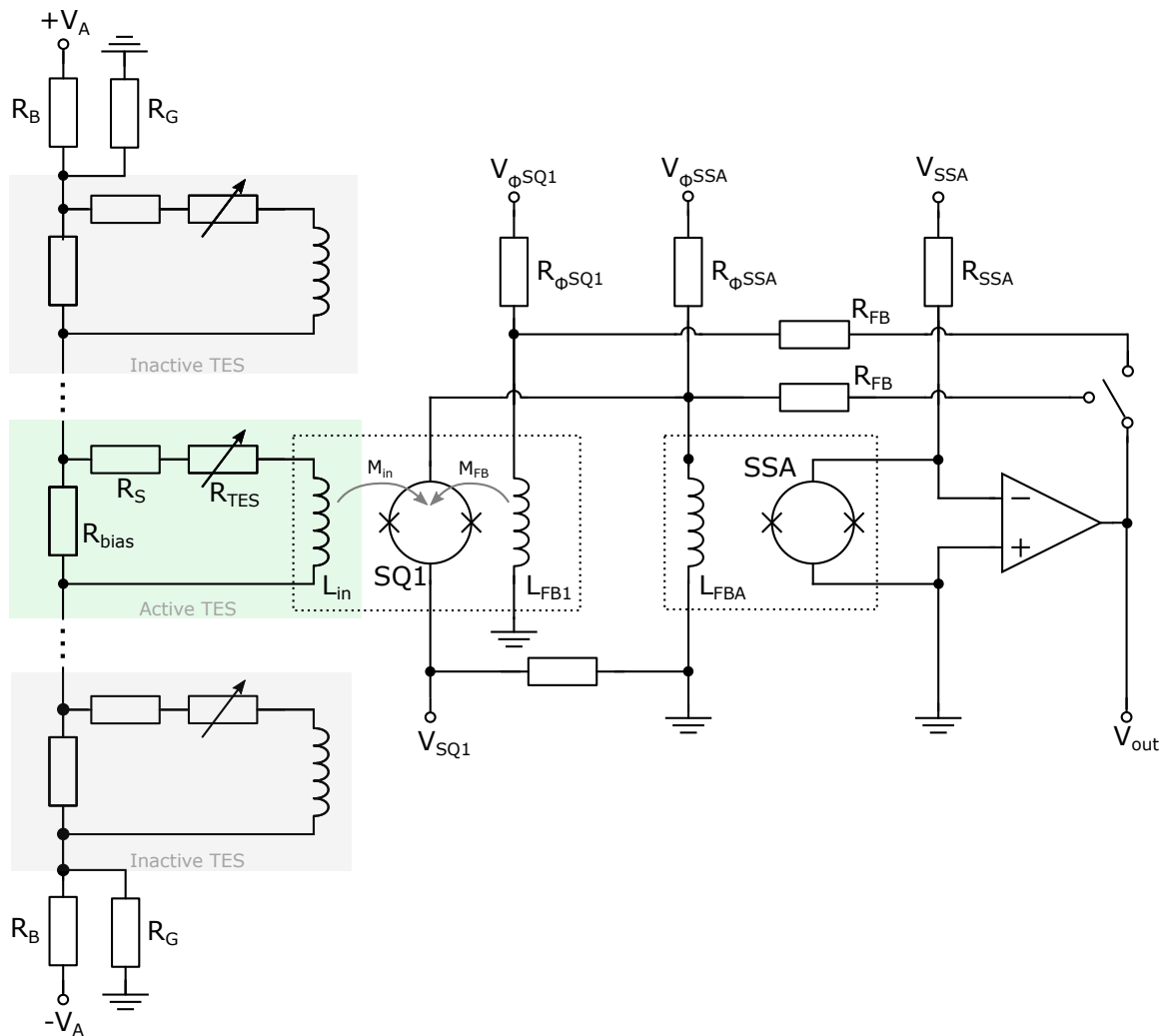


Fig. 4.10 Circuit diagram of the TES bias and two-stage SQUID amplifications.

was used to determine the bias point of SQ1 that maximises responsivity. Control of the SQUID and TES voltage biases was performed manually, using custom-made electronics, whilst the amplified readout signal was recorded by a PC data acquisition card, operated using LabVIEW.

The TES current during operation can be calculated from the recorded V_{out} using

$$I_{TES} = \frac{V_{out}}{M_{ratio}R_{FB}} \quad (4.1)$$

Table 4.1 Summary of the devices used for TES electron measurement experiments

ID Number	TES Length (μm)	Number of Bars (μm)	Response Time (ms)
2	70	0	0.41
3	40	0	0.22
12	40	1	0.53
17	100	2	0.56
24	100	3	0.58

where M_{ratio} is the mutual inductance ratio between the two SQUID stages ($M_{\text{in}}/M_{\text{FB}}$). With the TES current known, the voltage across the TES can be determined using

$$V_{\text{TES}} = \frac{R_{\text{bias}} V_{\text{mult}} V_{\text{A}} - I_{\text{TES}} (R_{\text{bias}} R_{\text{S}} + R_{\text{bias}} R_{\text{B}} + R_{\text{B}} R_{\text{S}})}{R_{\text{L}} + R_{\text{B}}}, \quad (4.2)$$

where R_{S} accounts for stray resistance. The multiplicative factor, V_{mult} , accounts for the symmetric bias of $\pm V_{\text{A}}$ with a measured value of 1.992.

When using Eqn. 4.2, the measured voltage offsets in V_{out} and V_{A} were corrected for and magnitude of stray resistance, R_{S} , calculated. The voltage offsets can be calculated using the requirement that, when in the normal state, the TES follows ohmic behaviour with an extrapolated current of zero when no bias is applied. The stray resistance offset was determined by requiring that the TES displays zero resistance when superconducting, such that the gradient of V_{TES} against I_{TES} is infinite. Prior to measuring electrons, the I-V relation of the TES was measured across a range of bias voltages in order to determine these parameters.

One modification to the existing TES measurement system was made to prevent the charging of the TES being tested and risking static discharge to the SQUIDS. The modification made was grounding the TESs using two symmetric connections at either end of the bias resistor chain, shown in Fig. 4.10. These lines were grounded to the cryostat vacuum jacket at the external electrical feedthrough of readout signal. The resistances to ground (R_{G}) were primarily due to the low-temperature wiring, approximately 50Ω . R_{G} is orders of magnitude greater than the $15 \text{ m}\Omega$ resistances of each bias resistor and so the inclusion of these ground connections had no observable impact on the readout performance. Over the course of the electron measurements in Chapter 5, no charging or damage to the readout system was observed from electron measurement.

Of the 30 devices on the chip, a subset of 5 devices were tested in electron detection experiments. A summary of these devices is provided in Table 4.1. These devices were

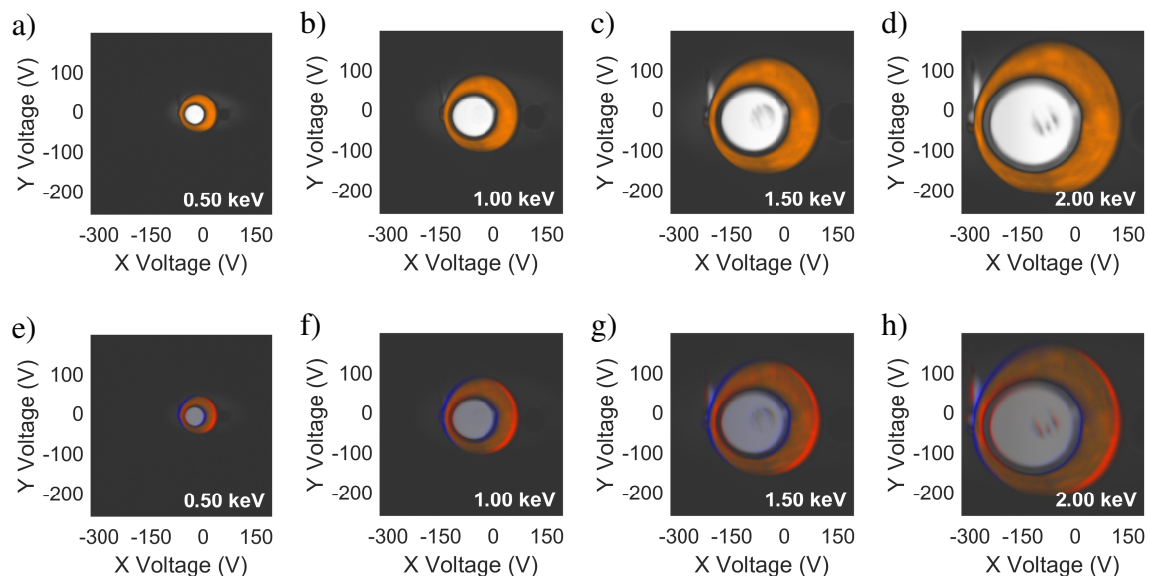


Fig. 4.11 a) - d) Beam current images of the Faraday cup measured at different electron beam energies. White regions represent net electron absorption, orange colours show net electron emission and black shows no net current measurement. e) - h) Beam current images from a) - d) with superimposed differences between current measurements with and without magnetic shielding around the electron source chamber. Blue colours show an absolute decrease in current measurement by adding shielding and red shows absolute current increase. The images all display the cup appearing to shift to the right after adding shielding to the chamber.

primarily chosen due to their size and corresponding heat capacity. Devices smaller than $40\ \mu\text{m}$ widths were observed to either be saturated by incident infrared radiation in the direct beam configuration, or have under $500\ \text{eV}$ saturation energies during scattered electron measurements. For direct beam measurements, the devices were also chosen to span a range of positions on the device chip in case of a small misalignment between the box and the $4\ \text{K}$ aperture.

4.6 Software

In this section, I describe the software used to control the EQ22 electron source and monitor the TES readout. I wrote LabVIEW software to operate the electron source, record beam currents, scan the beam current across a specified region and synchronise the TES measurement times with the beam scan times. By doing this, the beam angles corresponding to TES measurement events were determined.

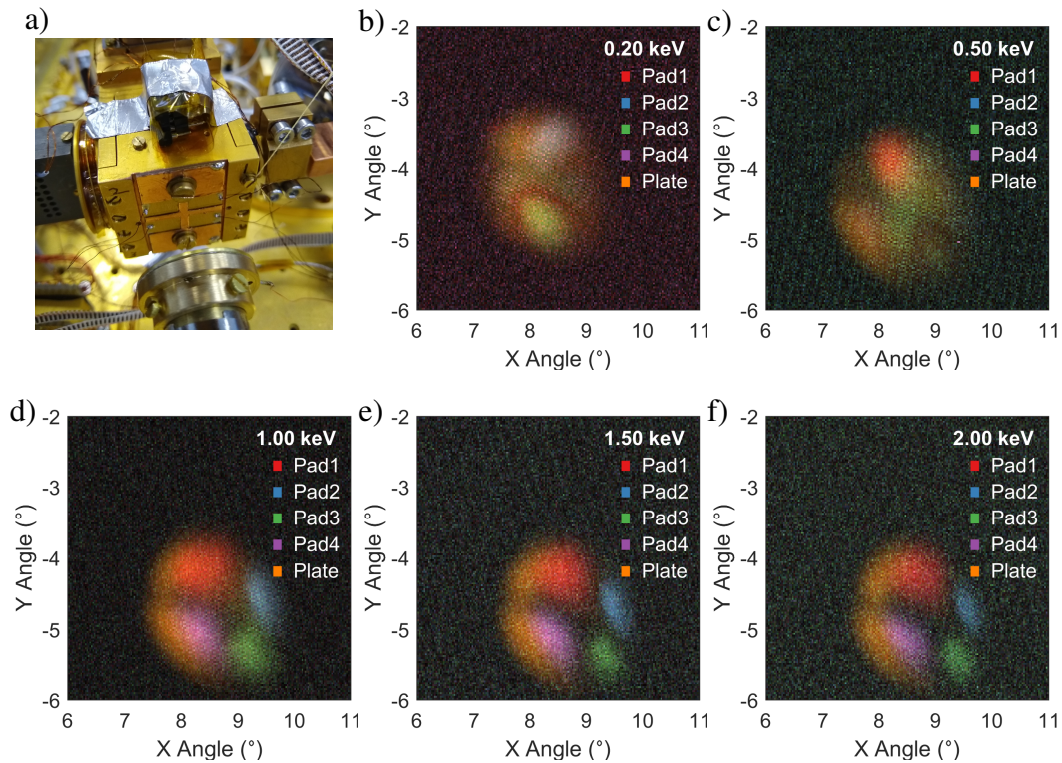


Fig. 4.12 a) Custom box lid with four copper pads, each with its own electrical connection for current measurement. b) - f) Beam current images at different beam energies measured through the four pads and the 4 K aperture (labelled as plate).

The SPECS EQ22 electron source was controlled using a combination of analogue input and a serial connection, using the Virtual Instrument Software Architecture (VISA) API. Instructions controlling beam energy, focus, and Wehnelt voltage (determining the beam current), were sent to the electron source using the VISA channel, as these parameters only needed to be set once at the beginning of the scan. The beam deflection was controlled by two ± 10 V analogue inputs to the EQ22 electron source power unit. These inputs control the x- and y- beam deflection voltages between -650 and 650 V each. Analogue control of the beam deflection was chosen to allow more reliable and faster changes to the deflection angle. In parallel to controlling the electron source, the LabVIEW Virtual Instrument (VI) monitored the beam current absorbed by the Faraday Cup by recording the analogue output from the Keithley 6485/E picoammeter.

I used the software to image the Faraday cup in order to test the computer-controlled operation of the electron source. Applying the minimum and maximum x- and y- deflection voltages, beam dwell time and number of measurement points, the software defined a grid of x- and y- deflection voltages and rastered the beam across the grid, holding for the given

dwell time at each point. By synchronising polling of the picoammeter with the time of each deflection angle, a 2D image of the Faraday cup can be built, measured by beam current. Fig. 4.11a to d shows four such measurements performed at different beam energies. The aperture into the cryostat, to the right of the cup, is also faintly visible, due to the background of scattered electrons absorbed by the Faraday cup when the beam is not incident on it. The apparent size of the cup scales with beam energy as the deflection angle of the beam is linearly proportional to the electron energy at a given deflection voltage. As each scan uses the same range of voltages, a wider scan area was rastered across for low energy electrons than high energy electrons. The black to white colours of each image represent net beam absorption whereas black to orange represents net electron emission due to secondary emission yields greater than 1 from the sloped cup surface. Fig. 4.11e-h shows how the image shifts when wrapping the magnetic shielding, discussed in Section 4.4.2, around the electron source chamber *in-situ*. The blue regions show where the absolute signal drops by applying shielding whereas red regions show an increase in absolute signal. The image can be observed to shift to the right by shielding the chamber, as expected. The darker region within the cup itself is where the current wire is held in place through the base of the cup, creating a small region preferentially scattering electrons out of the cup.

This same imaging method can also be performed through any ungrounded conductive surface within the cryostat. Therefore, I utilised this technique to aid in aligning the electron beam to the TES module. Fig. 4.12a shows a photograph of a custom module lid with four separate copper pads, each with an individual feedthrough out of the cryostat. By measuring the beam current passing through each pad alongside beam angle, the location of the TES module can be determined during a cooldown. Fig. 4.12b-f shows such measurements, plotting beam current against beam angle in each channel. The fifth channel labelled plate is the current measured through the 10 mm 4 K aperture of the mounted on the tube. This aperture was insulated from the brass tube and the current through it was measured in the same manner as the four copper pads.

This method of locating the electron beam position using separate current measurement channels was found to be very useful for determining beam position within the cryostat and was also incorporated into the design of the bespoke electron detecting TES chips in Chapter 7.

The final portion of the LabVIEW software I wrote was to synchronise TES data collection with the electron beam scan. Due to software compatibility issues, the TES data recording had to be performed by a separate PC to the electron source controlling computer. The TES measurement software was previously designed to collect the output voltage from the TES readout for a given duration at a specified sampling frequency when run. I modified

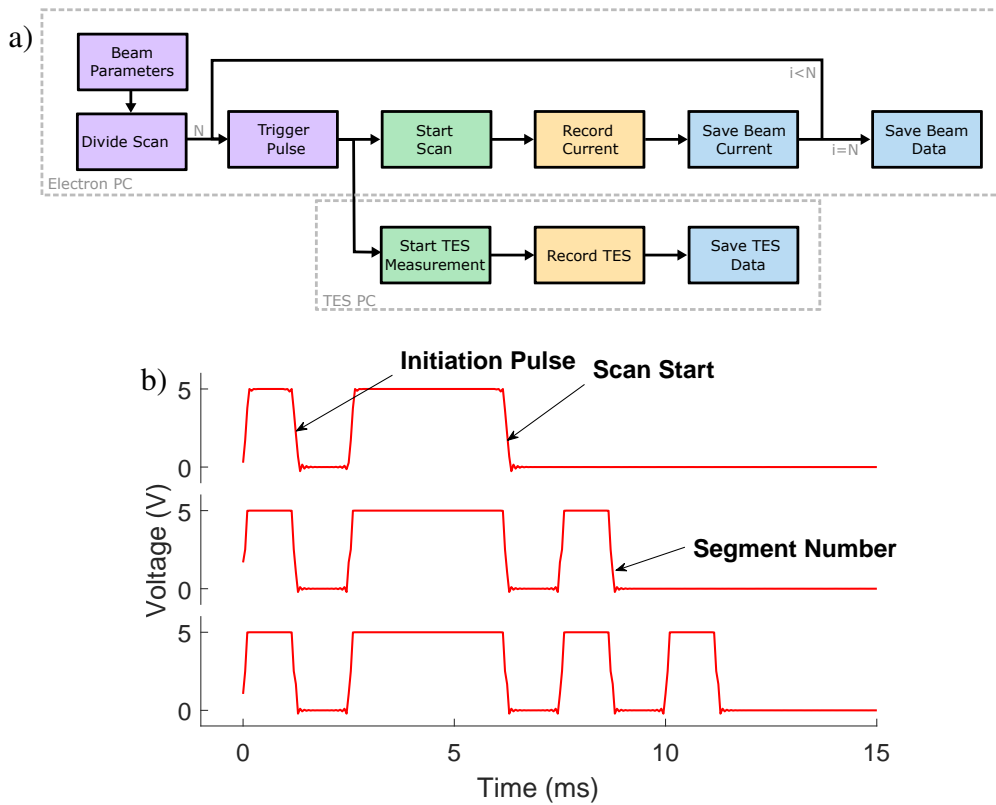


Fig. 4.13 a) Software block diagram of the synchronised beam scan and TES data collection procedure. b) Measurements of different initiation pulses as recorded by the TES measurement PC.

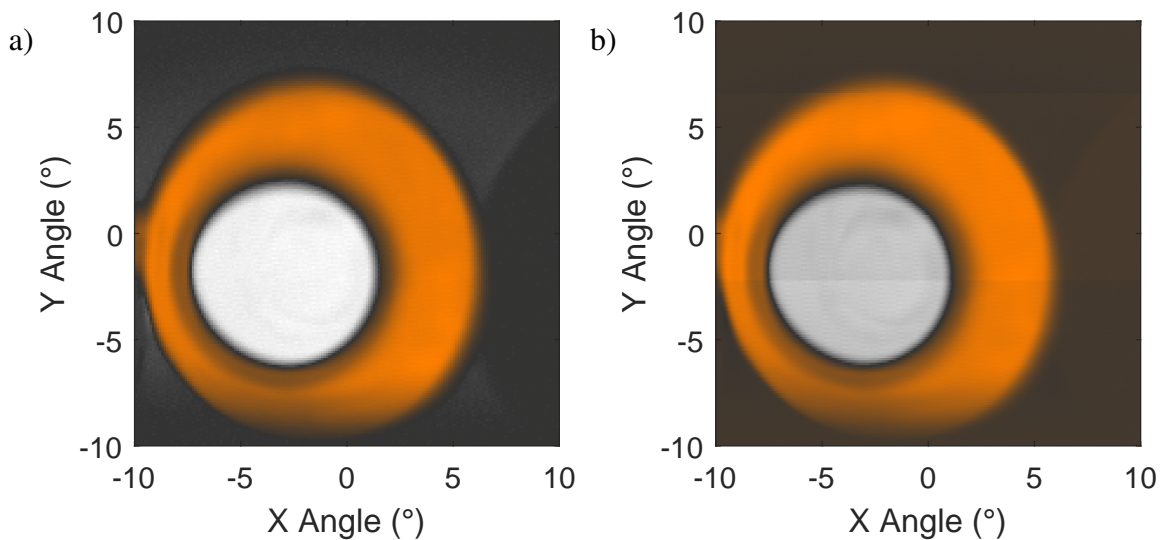


Fig. 4.14 a) Beam current images of the Faraday cup as recorded by a) the electron source controlling PC and b) TES measurement PC. Both images were recorded simultaneously with the image divided into 20 second recording segments.

this software to initiate recording upon receiving a trigger pulse from the electron source PC. This same trigger pulse initiates the electron beam scan. In this way, the beam scan and TES measurement were synchronised such that beam angles can be correlated to TES measurement events.

A limitation of the TES data collection system was the buffer size of the data acquisition card limiting the length of measurements to approximately 30 seconds at 20 kHz frequency. To enable longer measurements, the software was changed into divide the beam scans into multiple 20 second segments, with each segment recorded separately as shown diagrammatically in Fig. 4.13a. Each segment was initiated with the trigger pulse and upon completing each 20 second segment, the beam was returned to the Faraday cup and the beam current measured. In order to know which beam scan segment was being recorded, the trigger pulse numerically denoted which segment it initiated (Fig. 4.13b). The trigger pulse was recorded and used to check the start time of the measurement and the segment number

The synchronisation procedure was tested by connecting the analogue output of the picoammeter to both the electron source PC and the TES measurement PC. The Faraday cup was scanned in the same manner as Fig. 4.11 but using the segmented scan and trigger initiations. The images from both PCs were recorded and reconstructed (Fig. 4.14). The TES recording PC image was reconstructed by interpolating the beam angle depending on the recording time after the trigger pulse. The agreement between these two images verifies the implementation of the software with precision limited by the electron beam width.

4.7 Conclusions

This chapter has outlined the apparatus and software that was successfully used to carry out the first TES electron spectroscopic measurements, described in Chapter 5. The key challenge in designing this experiment was in reducing infrared radiation from the electron source without preventing electrons reaching the TESs. We were able to sufficiently screen infrared radiation to allow TES operation using a combination of narrow apertures, infrared-absorbing graphite paint and fine copper mesh. The use of the mesh was necessary to reduce infrared loading on the TESs but does introduce an additional surface that electrons are able to scatter off on the path between the source and detector. This compromise was acceptable for the planned proof-of-principle measurements but would not be ideal in further electron spectroscopy experiments.

The challenge of blocking infrared radiation would be present in the design of any TES electron spectrometer measuring a room-temperature sample. As there is no material that can block IR radiation whilst allowing electrons to pass without scattering, the ideal solution to

this challenge would exploit electron optics, such as high-voltage deflector plates or magnetic lens, to separate IR radiation from the incident electrons.

Chapter 5

Experimental TES Electron Calorimetry

5.1 Introduction

In this chapter, I present the first TES electron spectroscopy measurements using the apparatus described in Chapter 4. These measurements were designed to determine whether electron detection using TESs is possible and if so, to then determine the calorimetric measurement capabilities of TESs measuring electron energies in the range of 0 to 2000 eV. Finally, these TESs were used to measure the energy spectrum of a monoenergetic electron beam scattered from a graphite target in an experiment representative of the proposed role of TESs as electron spectrometers.

Initial experiments used the direct beam configuration where the electron beam was aimed directly at the TES module, the results of which are discussed in Section 5.2. The experiment was then reconfigured for scattered beam measurements where the beam was aimed at a target and the scattered electrons were measured (Section 5.3). Each subsection presents results taken during the same cryostat cooldown, referring to the period of time the cryostat was held at cryogenic temperatures. Experimental changes and improvements were made between cooldowns meaning that each subsection represents a set of measurements performed using the same experimental setup.

5.2 Direct Beam Experiments

5.2.1 Initial Measurements

The initial electron experiments had three objectives: to check beam alignment, to see whether electrons could be detected at all using this measurement system and, if so, to determine the ability of the detector to resolve electron energies.

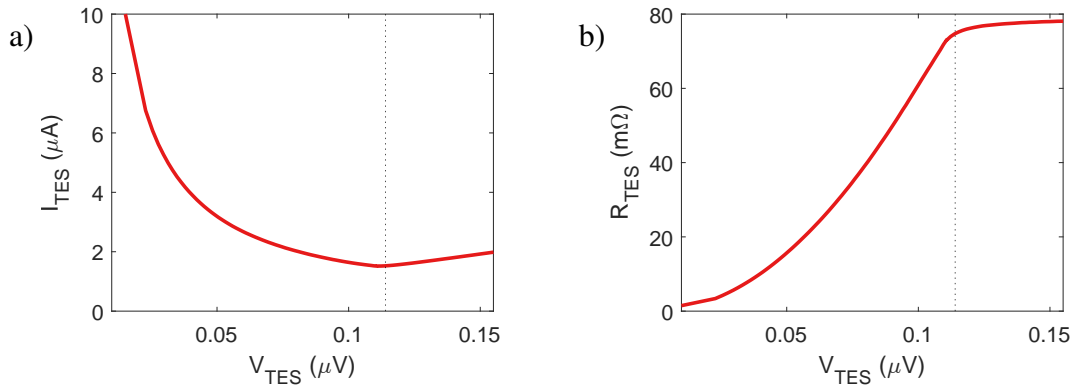


Fig. 5.1 a) Voltage-current relation of a $100\ \mu\text{m}$ square, voltage-biased Mo/Au bilayer TES. Measurement was performed at 120 mK. b) Voltage-resistance corresponding to the measurement in (a).

The measurements were achieved using the apparatus described in Chapter 4 with the slotted 45 K aperture and 4 mm diameter 4 K apertures, both shown in Fig. 4.4. The TES used for electron measurements is designated as TES 24. This TES was a $100\ \mu\text{m}$ square Mo/Au bilayer device, with three normal gold bars patterned on the surface and a transition temperature of 200 mK. This device was also the largest on the chip and so possessed the largest saturation power.

Fig. 5.1 shows the voltage-current and voltage-resistance relations of TES 24 measured at 120 mK. These measurements were taken by reducing V_{TES} from $0.15\ \mu\text{V}$ to $0\ \mu\text{V}$, wherein the TES transitioned from ohmic behaviour to superconducting behaviour.

An important characteristic of any TES is the heat flow between the detector and the thermal bath. In its superconducting transition, TESs display a power plateau due to an electrothermal feedback loop. This power plateau is the result of the negative electrothermal feedback of a voltage-biased TES that maintains the TES operating temperature by balancing power flow to the bath, P_{bath} , with the TES Joule heating. Due to this equilibrium, P_{bath} can be calculated from the TES voltage-current relation. Fig. 5.2 shows the observed P_{bath} over the course of several weeks. The label shows the number of days that have passed since the cooldown of the cryostat to 4 K.

Over the course of multiple weeks, this power plateau rose significantly in value, approaching a power of nearly 200 fW. This rise in power was due to an increase in current required to maintain the TES at its transition temperature. A likely explanation for this effect is that the bath temperature slowly fell across measurements. The falling bath temperatures would require increased Joule heating to maintain the TES at its superconducting transition and P_{bath} would increase over time.

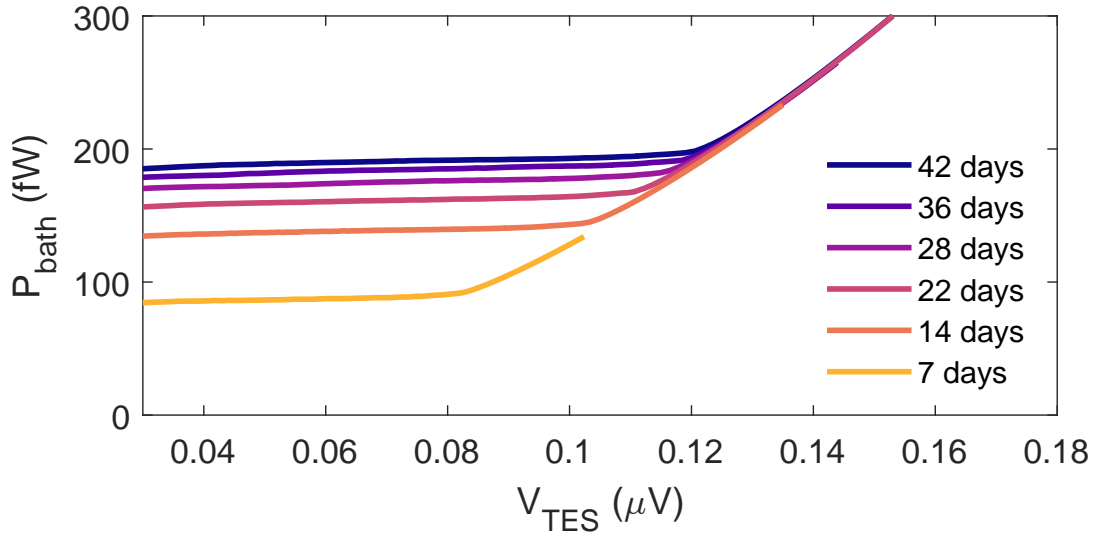


Fig. 5.2 Power flow of TES 24 from the TES to the thermal bath. Each measurement was taken on different days following initial cooldown of the cryostat to 4 K. All data were taken at a nominal bath temperature of 120 mK.

An alternative explanation is that the direct infrared loading on the TES dropped over several weeks. Black-body radiation incident on the TES can heat the device and create a temperature gradient between the TES and bath without applied current. Therefore, the current needed to heat the device to its transition temperature would be reduced. If the direct infrared loading on the TES then decreased, an increase in P_{bath} would be observed in the same way as if the bath temperature had dropped.

In either scenario, a component must be present in the apparatus that is decreasing in temperature over weeks, suggesting poor heat-sinking to the bath. The slowly cooling component, while problematic for precise energy measurements, did not prevent electron measurement and so I continued to use this experimental setup to search for electron events using TES 24.

The noise-power spectral density (NSD) of the TES measurement noise is shown in Fig. 5.3. The spectrum shows the characteristic TES response with a roll-off at 100 Hz alongside 50 Hz electrical noise. The shown current noise fit was calculated using

$$\Delta I_N(f) = \frac{\Delta I_N(0)}{\sqrt{1 + (2\pi f)^2 \tau_{\text{eff}}^2}} \quad (5.1)$$

where $\Delta I_N(f)$ is the frequency-dependent current noise and τ_{eff} is the TES effective time constant.

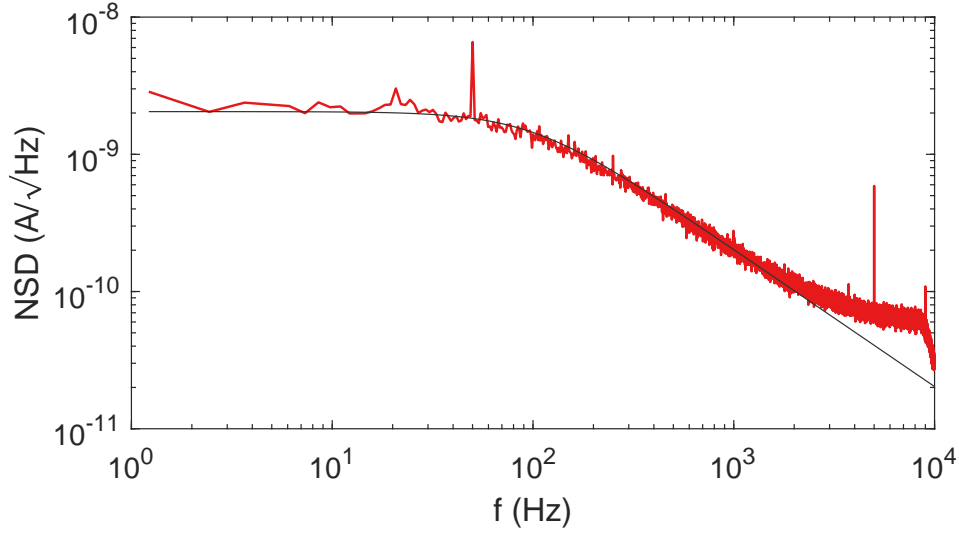


Fig. 5.3 Current noise spectral density (NSD) of TES 24 measured at 120 mK. The black line shows the fitted roll-off for a TES with 1.6 ms τ_{eff} .

TES noise spectra can be used to estimate the TES energy resolution limit using

$$\Delta E_{\text{abs}} = 2\sqrt{2\log(2)} \text{NEP}(0) \sqrt{\tau_{\text{eff}}}, \quad (5.2)$$

where $\text{NEP}(0)$ is the noise equivalent power at zero frequency and τ_{eff} is the TES effective response time (see Eqn. 3.25 and Section 2.5). $\text{NEP}(0)$ can be estimated using the zero frequency TES responsivity, $s_I(0)$,

$$\text{NEP}(0) = \frac{\Delta I_N(0)}{s_I(0)} \approx \Delta I_N(0) I_0 (R_0 - R_L) \quad (5.3)$$

where I_0 and R_0 are the TES current and resistance respectively and R_L is the value of the load resistor (see Section 2.3.2). Using Fig. 5.3, $\text{NEP}(0)$ was calculated at $5 \times 10^{-17} \text{ W}/\sqrt{\text{Hz}}$ and $\tau_{\text{eff}} = 1.6 \text{ ms}$, with values of $I_0 = 4.5 \mu\text{A}$, $R_0 = 7.5 \text{ m}\Omega$ and $R_L = 2.2 \text{ m}\Omega$. The calculated resolution is therefore $\Delta E_{\text{abs}} = 30 \text{ eV}$. This resolution limit was not intrinsic to the detector but was instead photon noise limited due incident black-body radiation on the TES; future measurements with reduced infrared loading displayed smaller noise-equivalent powers using the same device.

The first step to performing electron measurement experiments was to find the electron deflection angles, as applied by the deflector plates in the source, needed to send electrons to the TES. To do this, the electron beam was rastered across a specified angular range. Whilst the beam was scanned, the TES current was recorded. By synchronising the TES current

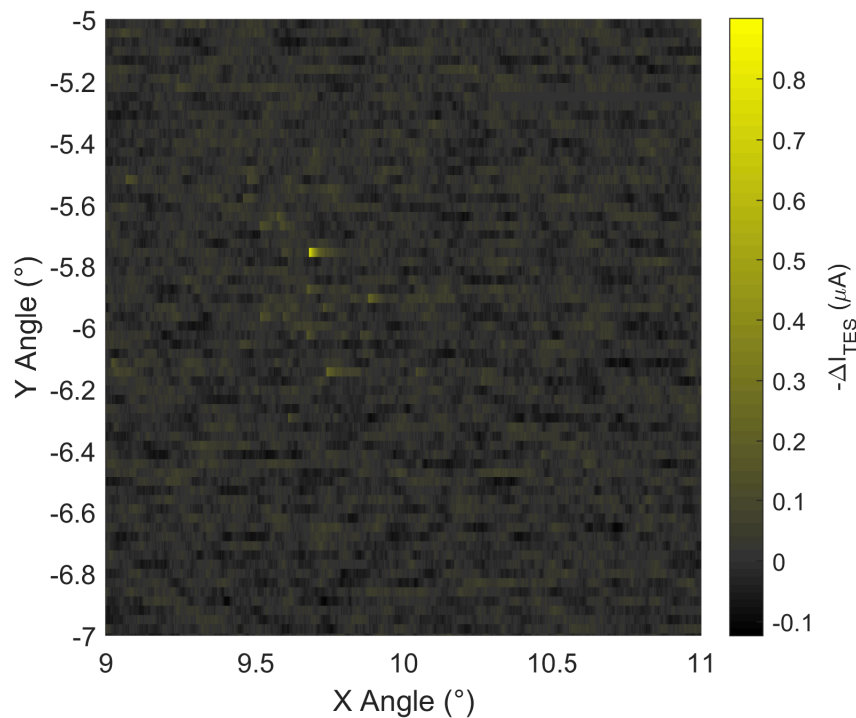


Fig. 5.4 Change in TES current from equilibrium, measured at different electron beam angles. The beam was scanned left to right in rows from -7° to -5° in the y-direction. The TES current is shown on a colour scale from black to yellow. A cluster of anomalous events can be seen in the image around 9.6° and -5.7° in the x- and y-directions, respectively.

with the beam scan, the electron beam angle from the source was correlated to the TES measurement time, in the manner described in Section 4.6. In this way, a map of beam angles versus TES current can be made; such a map is provided in Fig. 5.4. A cluster of events can be seen in this figure around 9.6° in the x-direction and -5.7° in the y-direction, where TES current is represented by pixel colour.

Aiming the electron beam at this region reliably resulted in observed TES current pulses. These events were not observed with electron source aimed in other directions or when turned off. The 20 second time series shown in Fig. 5.5 is an example of the observed TES current measurements with a 2 keV, 0.25 nA electron beam aimed at this region. The inset shows a single event with the characteristic TES exponential decay.

Fig. 5.4 and Fig. 5.5 demonstrate TES electron measurement, an excellent result for the initial measurements, successfully demonstrating the operation of the experimental scheme. It is very likely that the pulses observed in Fig. 5.5 correspond to individual electron events based upon the energies (or a small number of concurrent, low-energy electrons) due to the

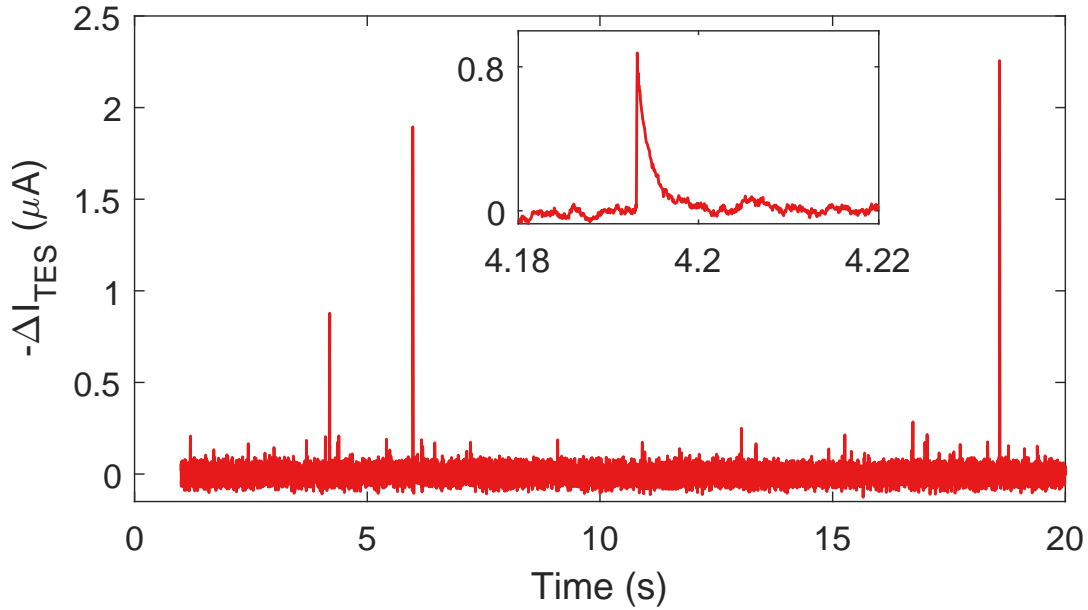


Fig. 5.5 Time series measurement of TES electron measurements taken using a 2 keV electron beam. The inset shows a measurement event with estimated 190 eV energy.

discrete nature of the pulses observed and the range of pulse amplitudes down to the noise floor.

To determine the energies of these electron events, each observed electron event was located within the time series data and the event energy was calculated following a similar procedure to that used in Section 3.2.2. The difference between the procedure in Section 3.2.2 and the analysis performed in this chapter is the manner by which the peak energy was calculated. Previously, the pulse shapes were fitted using a known form of TES response that scales in amplitude based on event energy. This simplification is valid in the small-signal limit beyond which, the TES response shape is non-linearly dependent on energy. Typically in X-ray calorimetry, the response shapes would be calibrated at known X-ray photon energies [105]. As these electron measurements are the first of their kind, I instead determined event energies by integrating the area beneath the peak. This approach is more susceptible to noise error than fitting the response, but allows for calculating event energies into the non-linear regime without prior knowledge of the TES response shapes. Knowing the TES bias voltage, the event energy can be calculated as

$$E_{\text{abs}} = \int_{t_1}^{t_2} -\Delta I_{\text{TES}}(t) V_{\text{TES}} dt, \quad (5.4)$$

where E_{abs} is the energy absorbed by the TES electrothermal feedback (ETF) loop, $\Delta I_{\text{TES}}(t)$ is the change in TES current from equilibrium and V_{TES} is the TES voltage bias. Detection events were found using the method described in Section 3.2.2 with the event start and end times, t_1 and t_2 , were found by locating the latest time before and first time after the event where $\Delta I_{\text{TES}}(t)$ crosses zero.

The main underlying assumption in Eqn. 5.4 is that the entirety of the absorbed energy is accounted for by the reduction in Joule heating. This assumption is correct in the limit of strong electrothermal feedback, such that the effective time constant τ_{eff} is significantly smaller than the thermal time constant τ in the absence of electrothermal feedback. However, the measurements performed here are not at the strong electrothermal feedback limit and a non-negligible portion of thermal energy will have diffused from the TES to the bath and not been measured. The magnitude of energy lost can be estimated as discussed in Section 2.3.3, using

$$E_{\text{ETF}} = \frac{\left(1 - \frac{T_b^n}{T_c^n}\right)}{\left(1 - \frac{T_b^n}{T_c^n}\right) + \frac{n}{\alpha}} E_{\text{abs}} \quad (5.5)$$

where $T_b = 120$ mK is the bath temperature, $T_c = 200$ mK is the TES transition temperature. α characterises the sharpness of the superconducting transition and n is the dimensionality of thermal conductance between the TES and bath. For this device, using $\alpha = 30$ and $n = 2$, we expect an underestimate of 10%. However, the magnitude of this underestimate cannot be precisely determined as the bath temperature for these measurements may have varied, as indicated by the drifting values of P_{bath} . The presence of this energy underestimate is not significant for the purposes of these proof-of-principle experiments as it is systematic to all electron observations, and could be calibrated for by measuring electrons of known energies, as would be typical for X-ray measurements.

Using this experimental apparatus, multiple electron energy spectra were observed at a range of applied beam energies, shown in Fig. 5.6. These measurements were all taken over four days, between 21 and 25 days since the original cooldown and at a fixed TES bias voltage of 34 nV, corresponding to approximately $0.10 R_n$ (normal state resistance). However, due to the observed bath temperature drift, the position of the bias within the TES transition will have shifted over this time frame, modifying the TES response shape and noise between different days.

For each beam energy, the observed spectra were largely the same with most electrons having energies below 100 eV and a few higher energy electrons. The most likely explanation for these measurement is that the direct electron beam path to the TES was blocked. Instead, what was measured appears to be a mixture of high-energy secondary electrons and

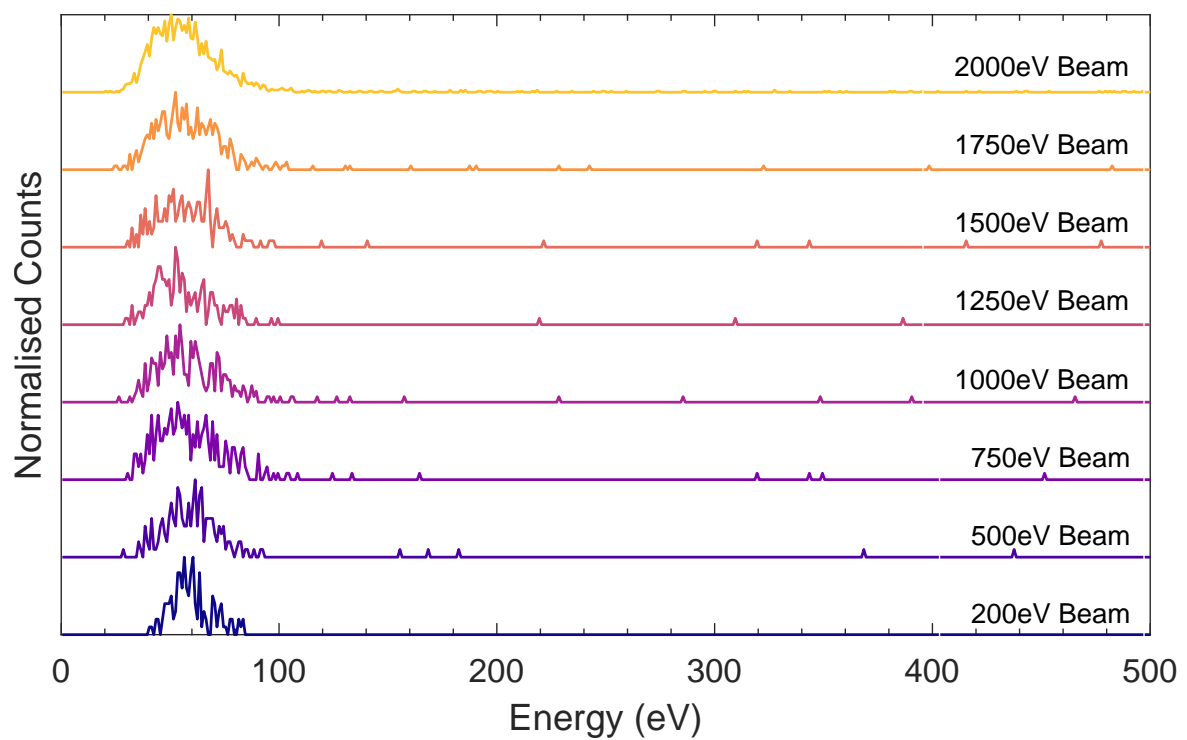


Fig. 5.6 Electron spectra measured using TES 24 at varying beam energies. The number of counts has been normalised by the peak amplitude with a energy bin width of 1 eV.

inelastically scattered primary electrons. However, it is interesting to note that the minimum electron energy observed was 40 eV, larger than noise-limited energy resolution of 30 eV and the modal secondary electron energy, expected to be approximately between 10 eV and 20 eV. The reason for this discrepancy is unknown, but in later measurements, lower energy electrons were measurable within more noisy data. This suggests that the lack of low energy electrons in these measurements was due to these electrons not reaching the TES rather than an artifact of the data analysis.

Further evidence that the direct path from the electron source to the TES was blocked is provided by comparing the beam current to the rate of TES electron events observed, shown in Fig. 5.7, all taken with a 2 keV beam energy. A linear relation is observed between count rate and beam current with an approximate rate of 1 event per second when using a 0.6 nA beam current. The TES area was $100\ \mu\text{m} \times 100\ \mu\text{m}$, and so the incident electron flux density would be $10^8\ \text{m}^{-2}\text{s}^{-1}$ or $16\ \text{pA}/\text{m}^2$. Assuming the electron beam spot size is 5 mm diameter at the target, with uniformly distributed electrons, and 1 % of electrons pass through the cryostat apertures to reach the device module, the flux density would be still be $300\ \text{nA}/\text{m}^2$ at 0.6 nA beam current. The scale of this difference implies that the electrons being measured must have been scattered multiple times prior to reaching the TES. Based on previous beam alignment measurements, the electron beam was likely entering the 4 K chamber but the TES itself was not directly aligned with both the 4 K and 45 K apertures.

Despite not directly measuring the electron beam, the TES response to electrons in the energy range observed can still be determined. In total, around 5500 events were measured in this series of measurements. I grouped these events based on the calculated energies into bins of 10 eV and averaged the observed TES response. A selection of these average pulse shapes are provided in Fig. 5.8a. Fig. 5.8b shows linear relation between the maximum pulse height versus the measured electron energy from 0 to 1000 eV. The distribution of pulse heights broadens at higher energies due to a fewer number of events observed with these energies, meaning that the scatter in Fig. 5.8b increases with energy. A very low bias point was initially chosen to provide a large saturation energy and a long response time to any observed electron events, allowing for these events to be observed as easily as possible. However, increasing the bias point to the steeper resistance-temperature gradient of the superconducting transition increases the sensitivity of the detector, reducing response time and improving energy resolution at the cost of reduced saturation energy. The change in response time is clearly shown in Fig. 5.8c, decreasing from 1.70 ms at $0.05 R_n$ to 0.65 ms at $0.55 R_n$.

This initial set of measurements show that TES electron detection and calorimetry is possible. Electron events of varying energies were consistently observed. However, the low

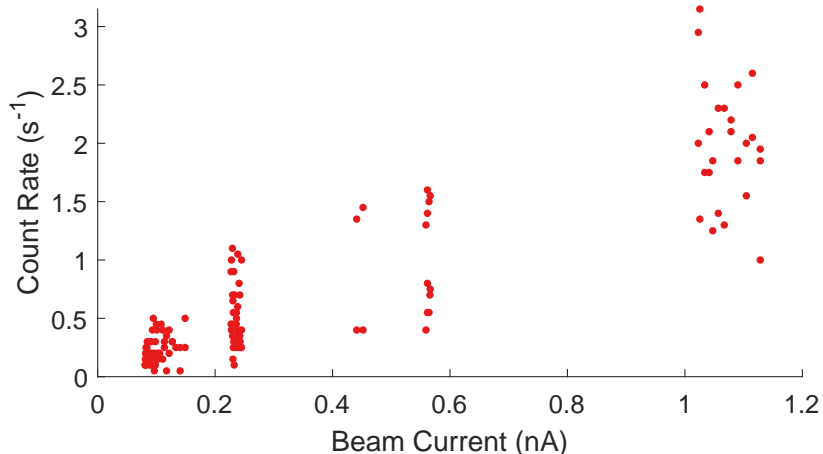


Fig. 5.7 Average rate of electron measurement events plotted versus applied beam current.

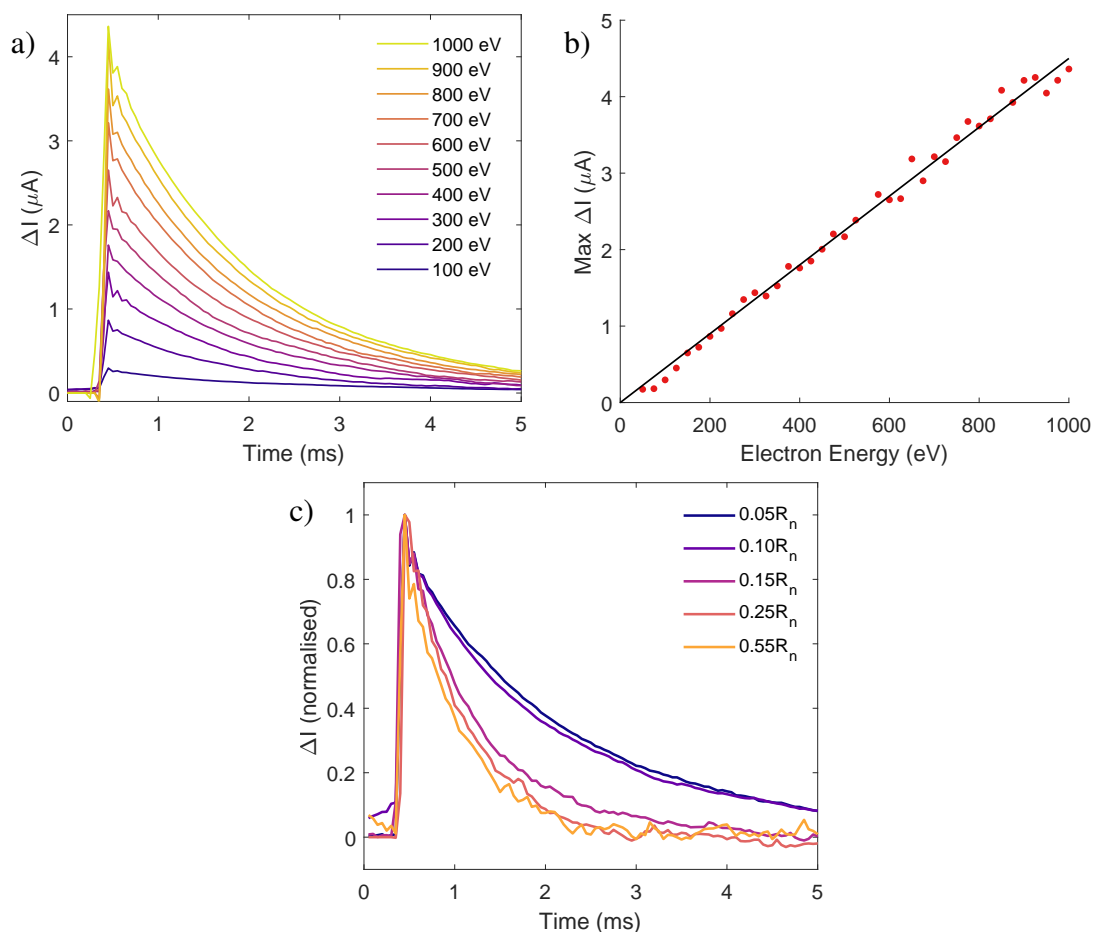


Fig. 5.8 a) Average TES shape due to different measured event energies, measured at $0.1 R_n$ TES bias point. b) Maximum pulse height in (a) plotted against calculated energy. c) Variation of TES response shape with TES bias voltage. The TES bias point is shown as a fraction of the normal state resistance, R_n .

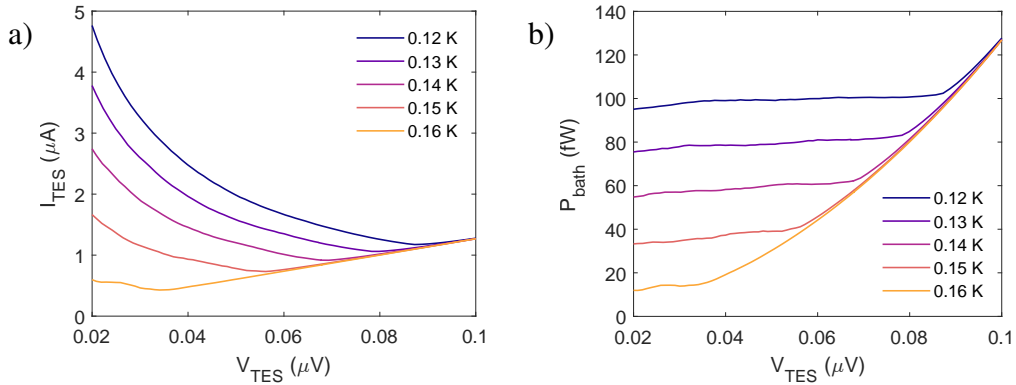


Fig. 5.9 a) Voltage-current and b) voltage-Joule power relations of TES 24 measured at varying temperatures, all taken on the same day.

number of high-energy electrons suggests that the electrons measured did not arrive directly from the source but were instead scattered. In addition, the TES or bath was observed to slowly cool across several weeks, thereby changing TES behaviour between measurements. The following set of measurements was designed to fix these two issues.

5.2.2 Realigned Measurements

Based on the results of the previous measurements, two changes were made to the experimental apparatus to try to improve alignment and prevent the change in P_{bath} observed over several weeks.

The heat sinking of the aperture array was identified as the most likely component that could have been gradually cooling over time. The thermal conductance bottleneck for this component was between the aperture array and the metal screws holding the array in place. The aperture array was designed to be able to be biased independently and so an insulating region separated the metal of the aperture array from the screws. This insulating region was bridged using Loctite Ablestik 285 thermally conductive epoxy for the measurements in this and following subsections. The aperture array was grounded for the previous set of measurements by a wire connection and remained grounded for the following measurements.

Based on the beam angles at which TES electron detection events were observed, the misalignment was likely due to the position of the device module rather than the cryostat window apertures and electron source. The TES array used covers 5×5 mm in area and so to maximise the chance of a TES being aligned with the electron source, the devices connected to the readout circuitry were distributed across the chip. All of the TESs connected for measurement were changed with the exception of TES 24.

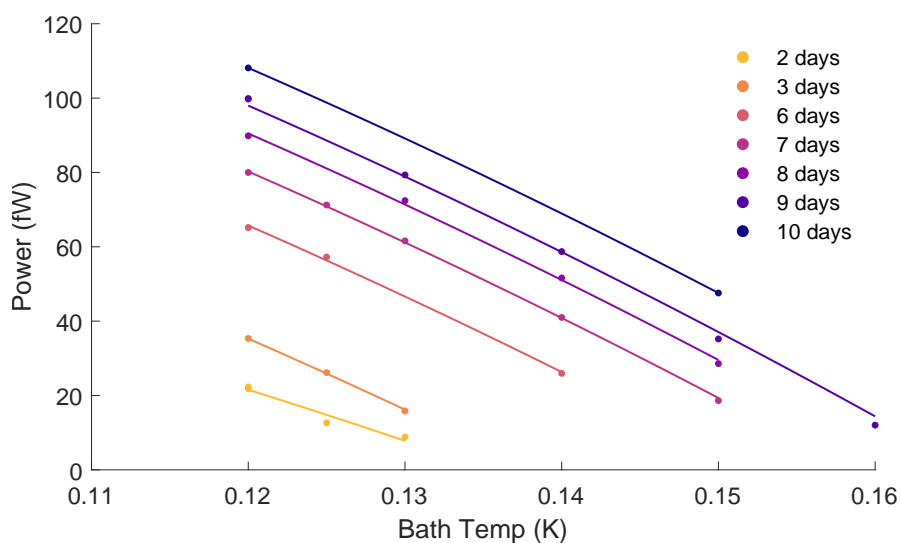


Fig. 5.10 Measured power plateau values plotted against nominal bath temperatures at which these measurements were taken. The datapoints have been colour-coded based on the number of days passed since the initial cooldown of the cryostat to 4 K. The plotted lines were fitted for each set of measurements taken in the same day using Eqn. 5.6.

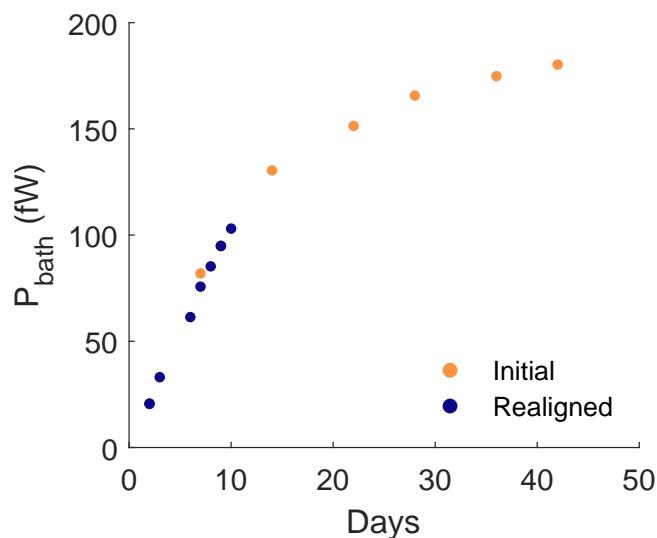


Fig. 5.11 Comparison between power plateau measurements of TES 24 in Fig. 5.2 and Fig. 5.9 over time from the initial cooldown for each set of measurements.

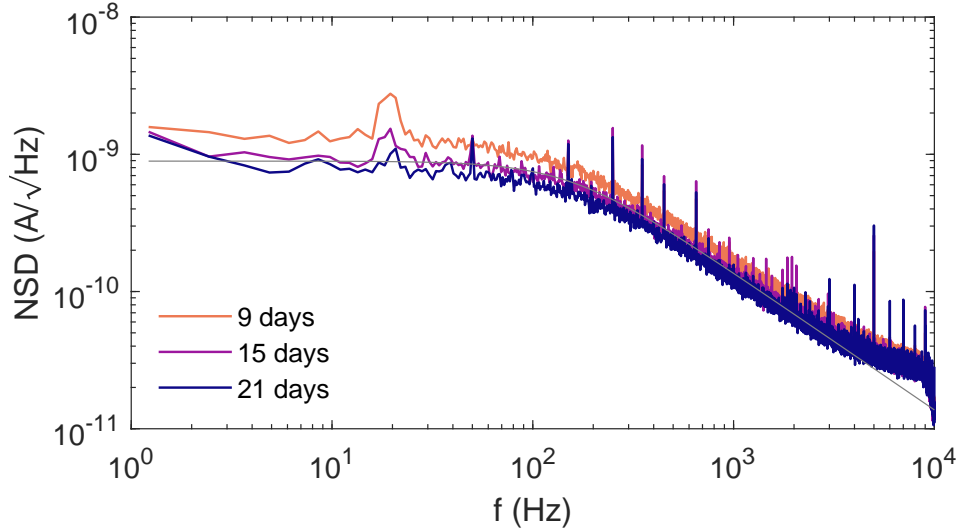


Fig. 5.12 Power spectral density of TES 24 measured at 130 mK, $0.25 R_n$ on several days following initial cooldown of the cryostat. The grey line shows the fitted roll-off of a TES with 1.0 ms τ_{eff} .

After implementing these changes and cooling the devices to 100 mK, only TES 24 was able to observe electrons on scanning the electron beam across the cryostat aperture and so this device was exclusively used for this set of measurements also. Fig. 5.9 shows a summary of the voltage-current relation of TES 24 over multiple nominal bath temperatures. These measurements show the TES to be superconducting up to 160 mK device module temperature; however, the cooling observed in Fig. 5.2 was also present during this set of measurements and so the true temperature on the TES chip is unknown. This cooling is shown in Fig. 5.10. In this figure, the average value of the power plateaus visible in Fig. 5.9 have been plotted against the nominal bath temperature. The representative value for each power plateau was calculated across the voltage range where the TES resistance spans $0.25 - 0.5 R_n$. Each coloured measurement set was taken on the same day with the number of days elapsed from the initial cooldown shown in the legend. The plotted lines have been fitted to datapoints following the relation

$$P_{\text{bath}} = K(T_c^n - T_b^n) \quad (5.6)$$

where T_b is the nominal bath temperature and K is the thermal conductance to the bath. These measurements clearly show an increase in the P_{bath} over the course of several days, as observed in Fig. 5.2. The drift in P_{bath} between the initial and these realigned measurements is compared in Fig. 5.11. Improving the heat-sinking of the TES aperture made no appreciable change to this cooling effect.

The noise power of the detector was also observed to drop over several days as shown in Fig. 5.12, likely to the temperature drift that occurred during this time. The value of $\text{NEP}(0)$ from Fig. 5.12 of $4 \times 10^{-17} \text{ W}/\sqrt{\text{Hz}}$ is comparable to the value of $5 \times 10^{-17} \text{ W}/\sqrt{\text{Hz}}$ previously observed in Fig. 5.3.

In the measurements presented in Section 5.2.1, a fixed voltage bias was chosen but the presence of a slow temperature drift meant that the chosen bias point had drifted within the TES superconducting transition over time. To prevent this from occurring in subsequent experiments, on each day of measurement, the TES voltage-current relation was measured and the bias voltage corresponding to $0.25 R_n$ was found. All subsequent measurements were performed at $0.25 R_n$ bias voltage in both direct beam and scattered beam measurements. These measurements were also performed at 130 mK rather than the previous used bath temperature of 120 mK. The purpose for this change was to increase the length of time the adiabatic demagnetisation refrigerator (ADR) could maintain the fixed bath temperature. At 130 mK, three to four hours of continuous electron measurements could be performed each day.

Using these measurement conditions, electrons were sent to the TES with beam energies between 300 and 2000 eV. The measurements presented in this subsection were taken over 11 days, with a total of 23,000 electron events observed. Fig. 5.13 collates the electron energies measured during these experiments. The observed distribution of electron energies measured was significantly different to the previous set of measurements. A large number of low energy secondary electrons and what appears to be primary electrons were measured across all beam energies. This is to be expected from the experimental setup because the copper mesh will have produced secondary and inelastically scattered electrons. The ratio between the primary and secondary electron peaks appears largely similar between 600 and 1400 eV but the higher and lower beam energies show a greater proportion of secondary electrons.

The primary electron peak is also consistently lower in energy than the incident electron beam. To quantify this difference, I fitted these peaks with Gaussian distributions to calculate the peak energy and FWHM. Fig. 5.13b compares the ratio between the measured peak energy and the beam energy. The ratio is constant up to 1000 eV with a systematic 10% error followed by a non-linear portion likely due to the TES becoming saturated. This result clearly demonstrates the ability of a TES to perform electron calorimetry across several orders of magnitude of electron energies.

Fig. 5.13c shows the observed FWHM of these peaks with the horizontal line at 20 eV representing the minimum FWHM that would be observed due to the TES energy resolution, given a monoenergetic electron source. This value was estimated using Fig. 5.12. Three different factors will have contributed to the observed peaks being broader than the TES

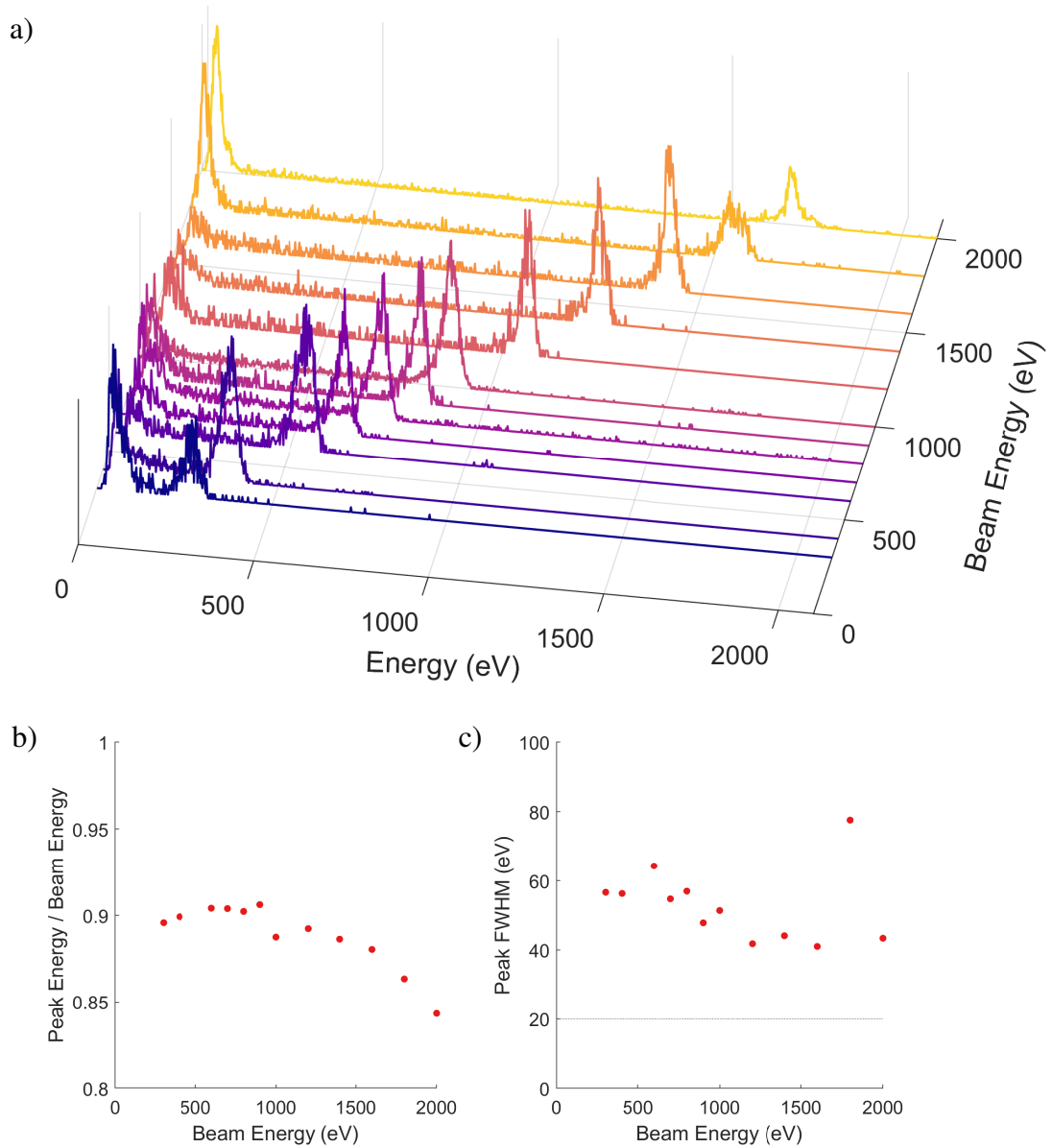


Fig. 5.13 a) Measured electron spectra taken at beam energies spanning 300 eV to 2000 eV. The spectra have been normalised by total area and energy bin widths of 2 eV have been used. b) Ratio between measured energy of the high energy peak and the applied beam energy. The measured peak energy was calculated by applying a Gaussian fit. c) Full-width at half maximum of the fitted high-energy peak plotted against beam energy. The horizontal line at 20 eV is the predicted FWHM resolution limit determined using Eqn. 5.2.

resolution limit. Firstly, the high-energy electrons would possess a range of energies, especially if inelastically scattered prior to reaching the detector. Second is inefficient electron energy absorption by the TES. The emission of secondary and backscattered electrons would result in a range of electron energies being measured even if a monochromatic source was used. Finally, the errors in the analysis method would further broaden the measured energy distribution.

A number of events were also observed with apparent energies beyond the beam energy. These events are the result of pileup which has not been successfully identified by the data analysis method.

It should be highlighted that the spectra in Fig. 5.13 have been constructed by identifying 23,000 separate electron detection events and calculating the energies of these events based on the calculated TES responsivity. The number of electron events necessary to construct an energy spectrum necessitates the use of automated software to identify electron events and calculate their energies. It is highly encouraging that this practical demonstration of the data analysis method shows a clear ability to receive experimental TES data and return physically relevant electron energy spectra with the observed electron energies scaling as would be expected with the applied beam energy.

Fig. 5.14 and Fig. 5.15 compares the 1000 and 2000 eV spectra measured in this and the previous subsections. Other than the high-energy, primary electron peak, the most notable difference between these measurements is the shifting of the low energy peak to lower energies. For the realigned measurements, the minimum observed energy is likely due to the data analysis failing to identify electron events within the noise floor.

As in Fig. 5.8, the pulse shapes of different electron energies are shown in Fig. 5.16. The onset of the non-linear relation between pulse height and event energy is clearly observable above 500 eV. The much earlier onset of non-linear behaviour is due to a combination of factors. The bath temperature in these measurements has been increased from 120 mK to 130 mK to maintain sufficient hold times. This in combination with the fact that the TES was now being operated at $0.25 R_n$ instead of $0.1 R_n$, and the additional thermal loading on the TES is the cause of the reduced saturation energy. At low energies, fitting a single exponential decay shows a decay constant of 1.05 ms.

In addition to the differences in the measured energy spectra and TES response, the maximum count rates observed for this set of experiments was also a factor of 50 greater than in Section 5.2.1 for a given beam current (Fig. 5.17). The data used to produce Fig. 5.17 includes a number of beam energies. No single beam energy was measured using a sufficiently wide range of beam currents to make the relation between beam current and count rate clear

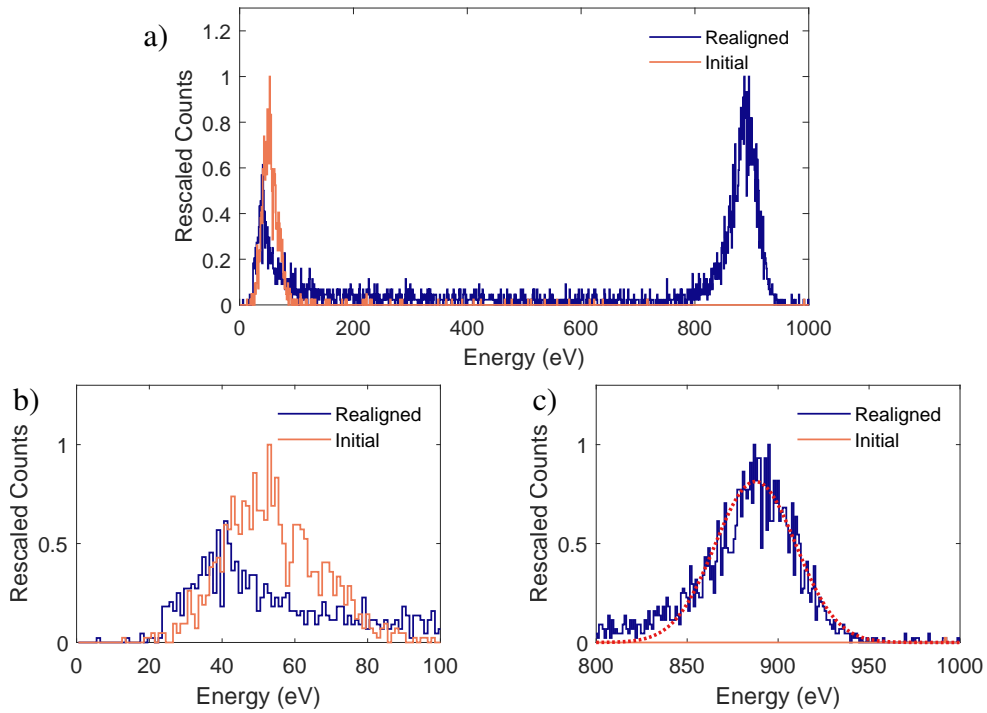


Fig. 5.14 a) Comparison between 1 keV beam energy spectra in Fig. 5.6 and Fig. 5.13 with 1 eV energy bin sizes. b) and c) show the low and high energy regions of the same spectrum. The red dashed line in (c) shows a fitted Gaussian distribution, centred at 890 eV with a 52 eV FWHM.

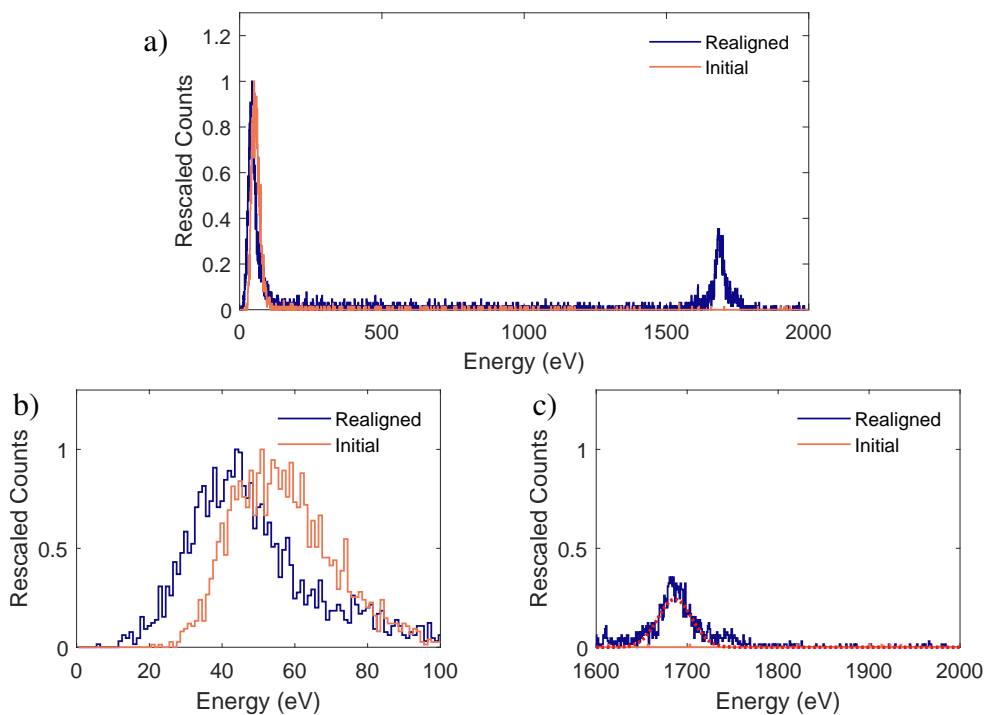


Fig. 5.15 Equivalent to Fig. 5.14 but with 2 keV beam energy. The red dashed line in (c) shows a fitted Gaussian distribution, centred at 1690 eV with a 44 eV FWHM.

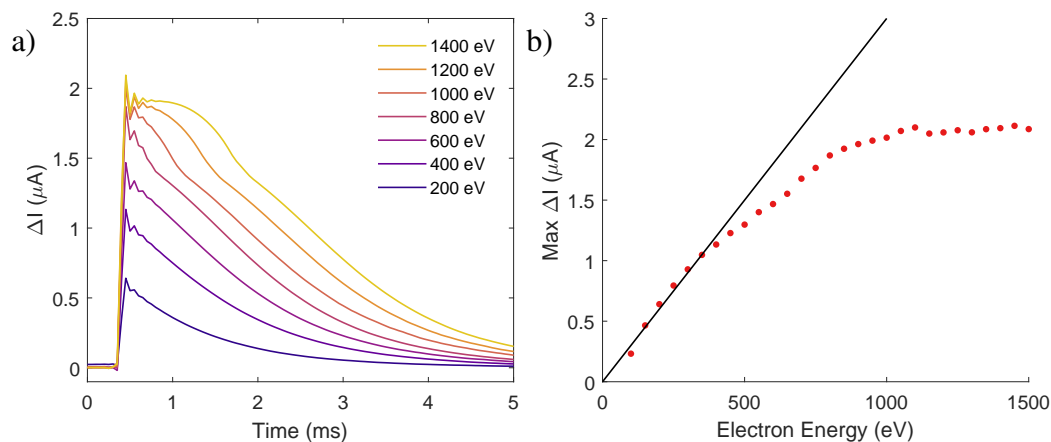


Fig. 5.16 a) Average pulse shapes based on calculated event energy. All pulses were measured using TES 24 at 130 mK nominal bath temperature and at $0.25 R_n$ b) Relation between the maximum pulse height in (a) and calculated event energy.

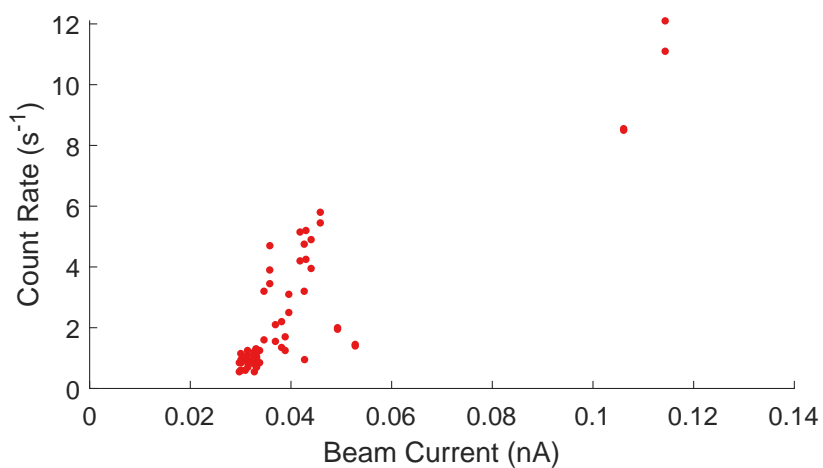


Fig. 5.17 Measured electron count rate versus beam current collated from a range of beam energies between 0.3 and 2 keV.

but collating many different datasets shows the expected linear relation between count rate and beam current.

This set of measurements clearly demonstrates TES electron calorimetry up to 2 keV. Therefore, future experiments were designed to build on this result by improving TES energy resolution. The energy resolutions of these measurements were limited by infrared loading on the detectors and so to improve TES performance, the incident radiation power was reduced. One method of reducing the infrared loading is to narrow the apertures between the electron source and the TES but doing so would make aligning the electron beam through the aperture to the TES prohibitively difficult. An excellent option would be to remove the TES module from line-of-sight to the electron source and electrostatically deflect the electrons to the TES, but implementing this solution was not practical within this project. Instead, I adapted the experiment toward the detection of electrons scattered off a target. In doing so, the measured electron spectrum would be representative of the usage of a TESs as electron spectrometers whilst removing the detectors from the electron beam line-of-sight.

5.3 Scattered Beam Experiments

5.3.1 Initial Measurements

The TES was removed from direct line-of-sight of the electron source to implement the scattered beam experimental setup described in Chapter 4. The scattered beam measurements were assembled as described in Section 4.4.4 with a graphite target mounted in front of the 4 K cryostat aperture and the device module repositioned to face the graphite target. The graphite target was electrically isolated from the target holder with a dedicated bias wire connected, allowing the graphite to be biased relative to the cryostat ground. For the initial measurements, the same aperture sizes as the direct beam experiments were used. One component that was not in place for this set of experiments was the collimating aperture shown in Fig. 4.8 that blocked off-axis electrons reaching the TES from the graphite target.

On cooling the devices to 100 mK, the readout channel to which TES 24 was connected displayed unusual semi-periodic noise, shown in Fig. 5.18. The source of this noise was not identified but it was linked to the readout channel rather than the TES. For this set of experiments, TES 12 was therefore tested instead of TES 24. TES 12 was a smaller, 40 μm device with a single normal metal gold bar patterned on the surface. Therefore, this device displayed a much lower saturation energy, but improved energy resolution. The TES voltage-current, voltage-resistance and noise spectra for TES 12 and 24 are shown in Fig. 5.19. Of

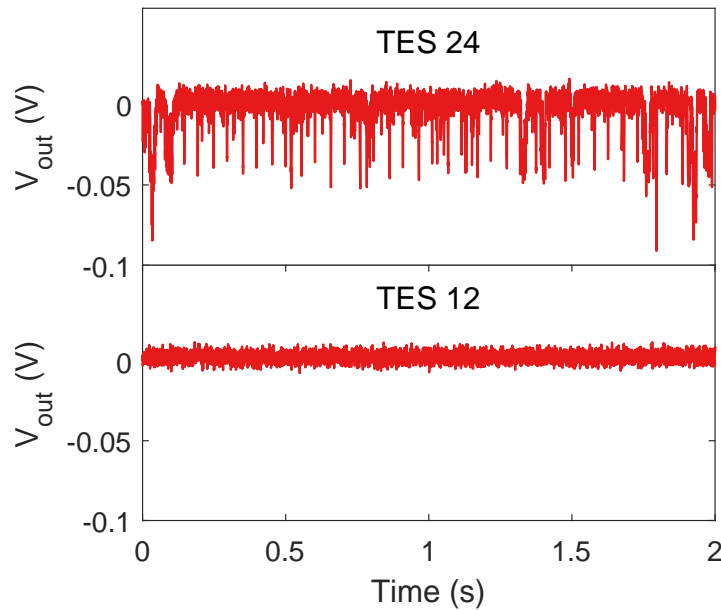


Fig. 5.18 Dark time series measurements of the TES 24 and TES 12. The y-axis shows that readout output voltage, before conversion to TES current.

particular note is that the low frequency current noise of TES 24 was reduced by a factor of two compared to Fig. 5.12, despite the additional noise displayed by the readout.

An important question to answer is whether the temperature drift of previous measurements was resolved by the new experimental setup. Fig. 5.20 and Fig. 5.21 clearly shows that there was a small amount of cooling between the first and second day of measurement after which, the device temperature for TES 12 remained very consistent with no significant difference in the noise spectra or power plateaus over the time span of measurements. The poorly heat sinked component present in Section 5.2 was not identified, but moving to the scattered electron configuration eliminated the problem.

Due to its small size TES 12 was observed to strongly saturate when measuring electrons above 500 eV. Therefore, the measurements taken for this set of measurements were all at 500 eV beam energy, but with biases between -20 and 20 V applied to the graphite target. The reasoning for applying this bias is that a positive voltage on the graphite would suppress the emission of low energy secondary electrons, allowing for a greater proportion of higher energy electrons to be observed. The measured energy spectra are shown in Fig. 5.22.

The measurements show a very small number of electrons above 50 eV energy and that applying the voltage bias had little effect on the secondary electron peak. For comparison, Fig. 5.23 shows the total scattered electron spectrum of highly-oriented pyrolytic graphite measured in [106] using a cylindrical mirror analyser. As the spectrum in [106] was measured over a broad range of emission angles with the beam normal to the sample, it cannot be

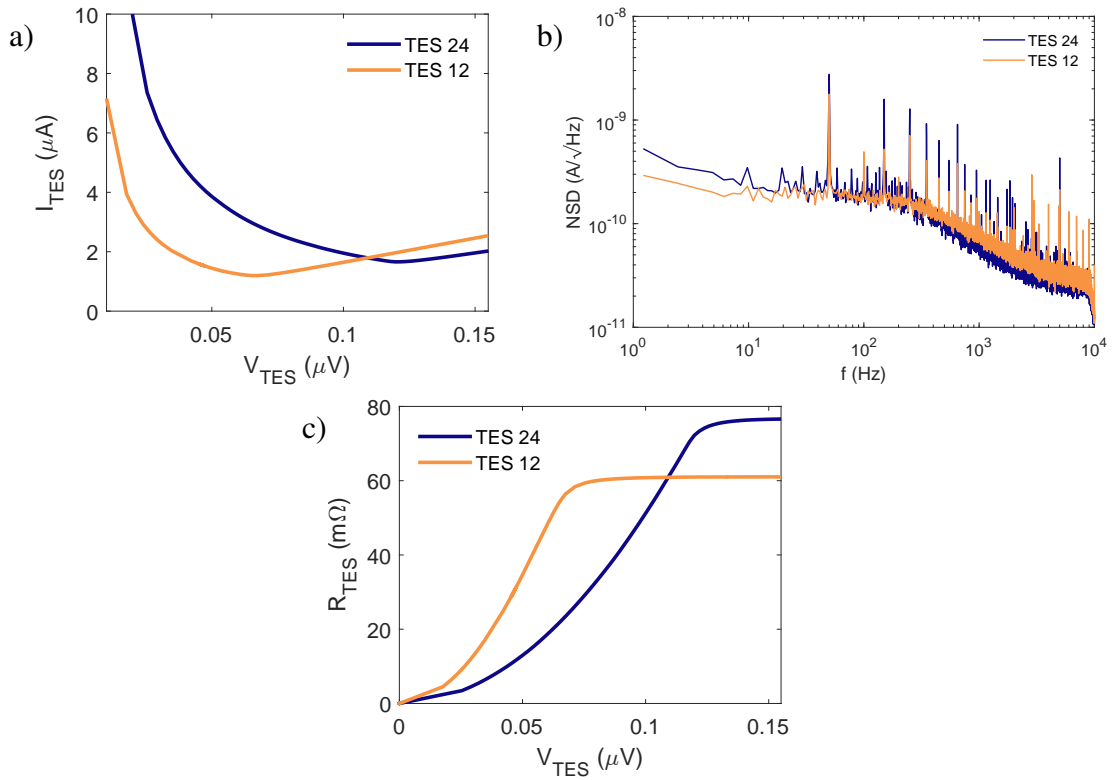


Fig. 5.19 TES voltage-current (a), voltage-resistance (b) and noise spectral densities (c) of TES 12 and TES 24. These measurements were all taken at 130 mK bath temperature.

quantitatively compared to our measurements but it provides good qualitative information on what we would expect to observe. At low energies, a very sharp, low energy secondary electron peak at 2 eV was observed in [106] that cannot be seen in Fig. 5.22, likely due to the energy resolution limit of the TES measurement being 3.5 eV (calculated from Fig. 5.21). Additionally, magnetic fields of $10 \mu\text{T}$ would be sufficient to deflect these low energy electrons away from the TES. The secondary electron peak occupies a similar energy range but very few electrons with energies over 50 eV were measured in Fig. 5.22. We would expect a low, mostly flat background of electron energies between 50 and 500 eV, and a small elastic peak which was not observed. One possible explanation is that the measured spectrum was dominated by secondary electrons emitted from the copper meshes, graphite surface and TES aperture array. Of the 32,000 electrons measured only 900 electrons had energies over 50 eV and so high-energy features that may have been present were not resolved. The 500 eV peak would also be broadened by the detector energy resolution, secondary emission from the TES surface and any inelastic scattering events prior to reaching the TES. It is important to note that in this case, while we have used high-purity graphite foil, the cryostat has no *in-situ* method of cleaning the surface and relies heavily on cryopumping to achieve UHV

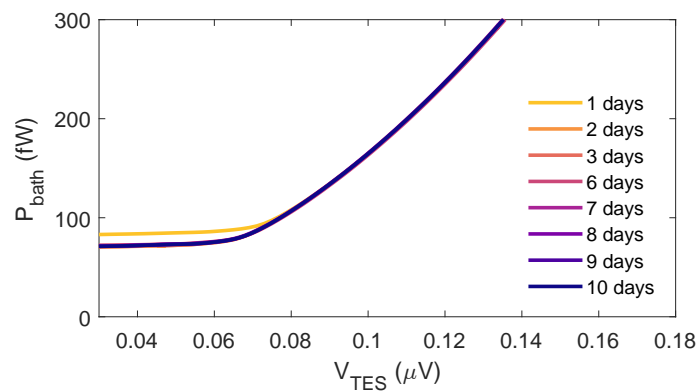


Fig. 5.20 Calculated Joule heating of TES 12 against applied voltage bias, measured at 130 mK across several days from the initial cryostat cooling to 4 K.

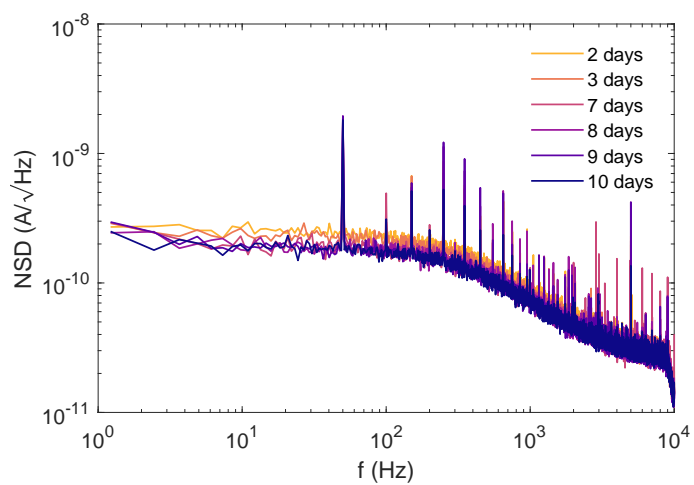


Fig. 5.21 Current noise spectral density of TES 12, measured at 130 mK and $0.25 R_n$, across several days from the initial cryostat cooling to 4 K.

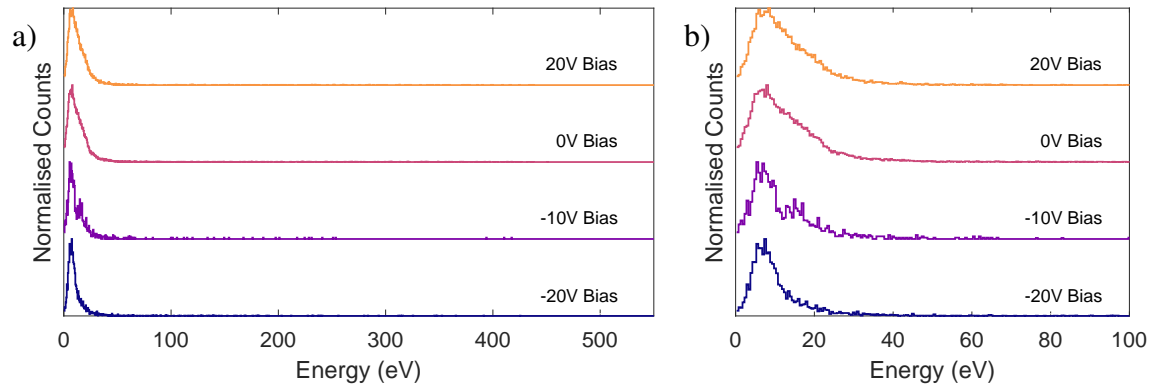


Fig. 5.22 a) Measured electron energy spectrum of 500 eV electron beam scattered off a graphite target. Different bias voltages were applied to the graphite. b) The low energy range of the spectrum in (a).

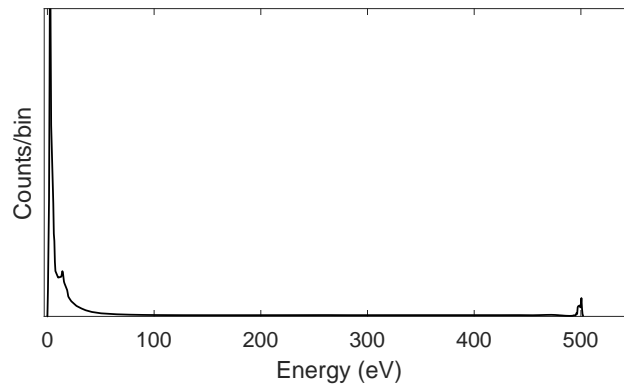


Fig. 5.23 Total scattered electron distribution of graphite foil measured by [106] using a 500 eV beam.

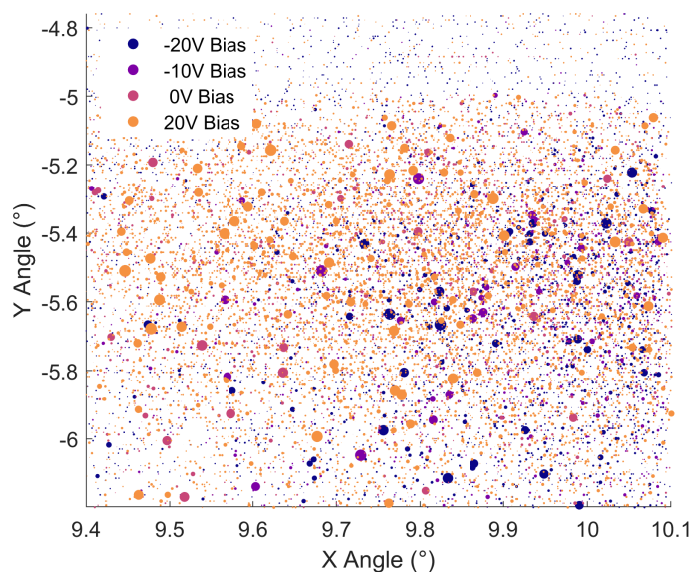


Fig. 5.24 Map of TES electron detection events plotted against applied electron beam deflection angle. The spot size is proportional to the measured electron energy. The spot colour is determined by the bias applied to the graphite target during the measurement.

conditions. As such, the graphite surface will unavoidably be coated with various deposits, primarily carbon, oxygen, nitrogen and hydrogen.

While applying a bias to the target had little effect on the electron spectrum, it does appear that the secondary electron peak may be made up of two overlapping distributions and applying a negative bias to the target suppressed the higher energy distribution. These two distributions are most clearly shown by the double peak in Fig. 5.22b around 10 and 15 eV. The energies of these peaks do not correspond to the sharp 2 eV peak in Fig. 5.23 and so the observed energy distribution is not expected to be solely due to scattering off the graphite.

The reduction in events above 15 eV with decreasing bias voltage was unexpected in two ways. Firstly, if the electric field between the TES and target was uniform, secondary electrons emitted from the negatively biased target would be accelerated towards the TES. The reason why this was not observed could be due to the fact that the electric field around the target was not uniform, due to the grounded mount and aperture in proximity to the target. The second unexpected feature is that the high energy tail appears to drop in number of counts with larger negative bias but not necessarily dropping in energy. If this observation is true and not an artifact of shot noise, it suggests that applying a negative bias deflected some of these higher energy electrons away from the TES rather than decelerating them.

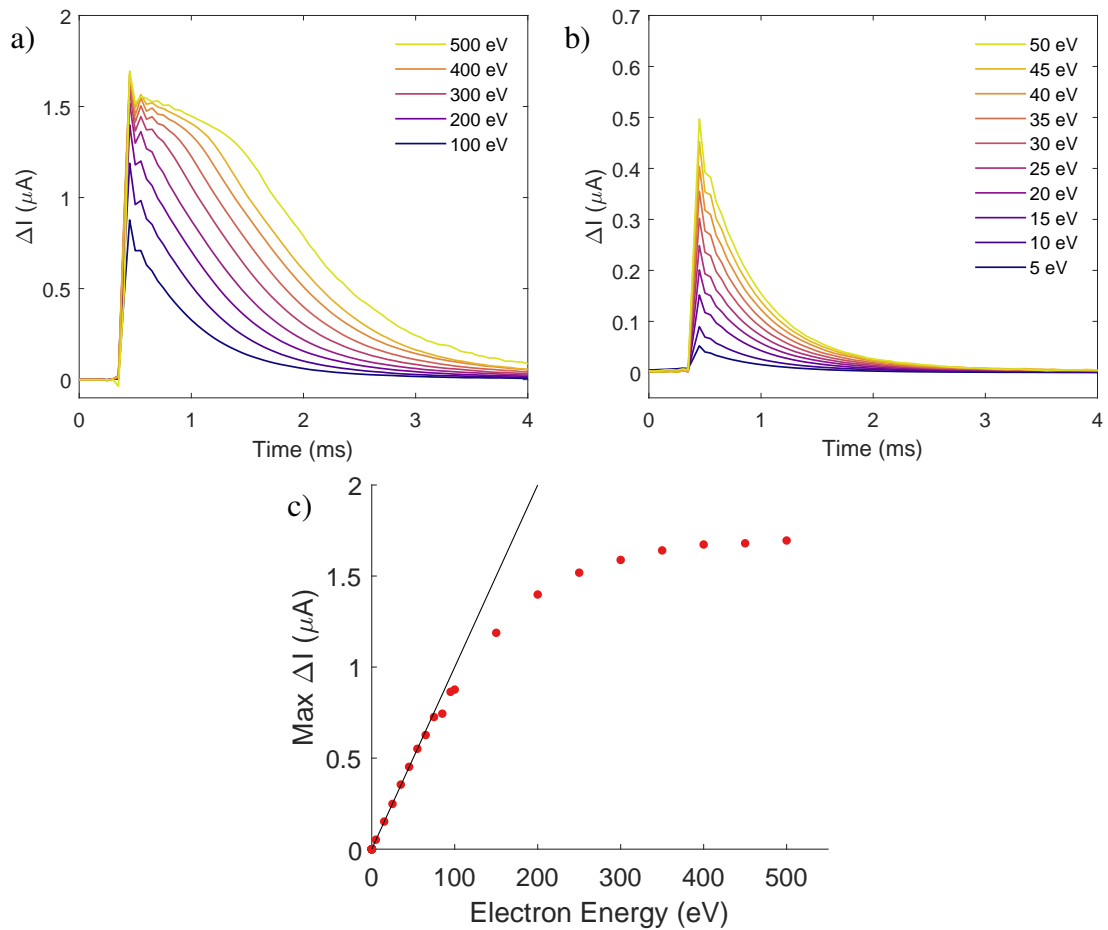


Fig. 5.25 a-b) Averaged TES electron detection responses at different event energies plotted on two separate axes for clarity. c) Maximum pulse height in (a) and (b) plotted against measured energy.

To further investigate the effect of bias on the electron measurements, the angular distribution of electron events based on the beam angle from the source has been plotted in Fig. 5.24. All of these measurements were taken by rastering the beam across the plotted angular region. Each individual spot represents a TES measurement with the size of the spot being proportional to the measured event energy. The 4 K aperture directly in front of the graphite target is expected to correspond to 0.7° of deflection angle. The spot size of 500 eV electrons at this distance from the source is not accurately known; Fig. 4.12 suggest this value was several millimetres at the device module, further increasing the angular range of the beam that would result in an electron striking the graphite. Additionally, due to the presence of mesh on both the 45 K and 4 K apertures, scattering off of these meshes would introduce additional dispersion of the electrons beyond the plotted beam angles, leading to a wider angular distribution of events observed.

The chosen region in Fig. 5.24 overlaps with the top of slotted 45 K aperture, shown by the flat boundary at -5° Y angle above which only sparse secondary electron events were observed, presumably scattered from gas in the electron source chamber. A notable difference in the angular distribution between +20 V and -20 V graphite bias is that the high energy events at positive target bias are favoured at smaller X angles in comparison with the negative bias. The electric field in the vicinity of the graphite target will have been non-uniform with respect to the beam path, due to the target surface being angled at 60° to the incident beam, and the presence of the grounded target holder and apertures in proximity to the graphite surface. Therefore, an angular relation between deflection angle and target bias is not unexpected, though quantifying the relation would be difficult.

Fig. 5.25 shows the averaged TES responses to different event energies. Saturation at 500 eV is clearly evident with the linear regime between pulse height and energy occurring up to 100 eV. Using the noise spectrum in Fig. 5.21, and $\tau_{\text{eff}} = 0.60$ ms, the energy resolution of this detector is be estimated at 3.5 eV, an excellent result for a TES adapted for proof-of-principle electron calorimetry experiments.

These measurements successfully demonstrate TES electron spectroscopy but with two major limitations. The first being the low saturation energy of the detector being used. At electron energies below 500 eV, aiming the electron beam through both 45 K and 4 K apertures becomes increasingly difficult due to the ambient magnetic field. Secondly, the measured electrons remain dominated by secondary electrons that are not produced from the graphite target. If these electrons had been emitted by the graphite, applying a voltage bias to the target would have notably changed the energy of the secondary electron peak. Therefore, the next set of measurements was designed around reducing these secondary electrons.

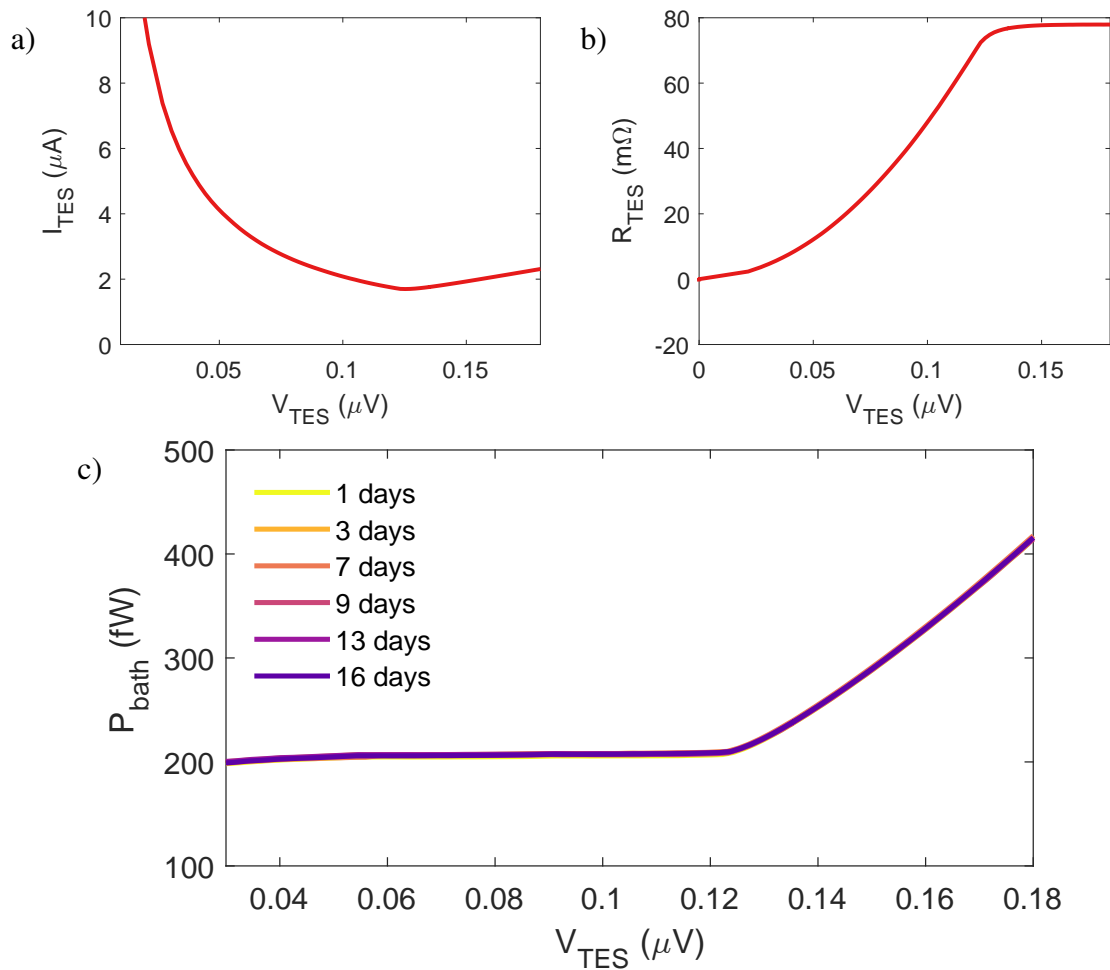


Fig. 5.26 a) Voltage-current and b) voltage-resistance measurements of TES 24 performed at 130 mK. c) TES Joule heating against applied bias, measured on several days after initial cooldown to 4 K.

5.3.2 Reduced Secondary Electron Measurements

In order to reduce the measurements of secondary electrons emitted from surfaces other than the graphite target, the mesh on 4 K aperture was removed entirely because the reduced thermal loading made it no longer necessary to use. The collimating aperture, shown in Fig. 4.8c, was made and mounted to the target holder to block any stray secondary electrons from the target holder itself reaching the TES. The same devices were connected to the readout but the readout channels of TES 12 and TES 24 were swapped to allow measurement of TES 24 without the additional noise observed previously. For this set of measurements, TES 24 was used due to its greater saturation energy.

As shown in Fig. 5.26, the measured TES power plateau remained constant across measurements at 200 fW, larger than the maximum plateau of 180 fW in the initial direct

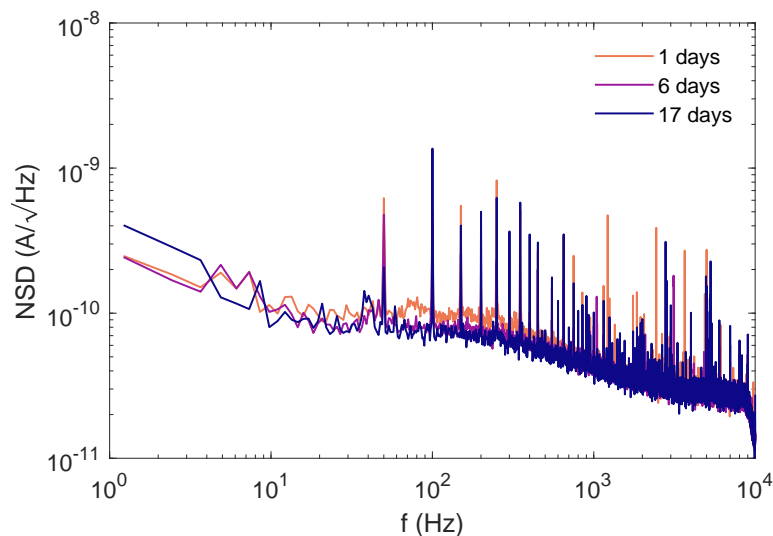


Fig. 5.27 Noise spectral densities of TES 24 measured on several days after initial cooldown to 4 K. Spectra were taken at 130 mK bath temperature and $0.25 R_n$.

beam measurements. This measurement is encouraging as it shows that the TES behaviour remained very consistent over the course of weeks with reduced thermal loading compared to the direct beam measurements. The noise spectral densities in Fig. 5.27 have also reduced by a factor of five compared to direct beam measurements, although the 50 Hz noise and harmonics remain at similar magnitudes than previously measured for this device, with some pink noise apparent at low frequencies. With this level of noise, the minimum energy resolution that can be achieved is predicted to be 4 eV, far better than the previous measurements using TES 24 in Section 5.2 of 30 eV.

Using TES 24, the energy spectrum of the scattered 1 keV beam was measured at different graphite bias voltages. These results are given in Fig. 5.28. The histogram amplitudes have been scaled by the total number of counts to allow comparison between the spectra. A number of high energy electrons were observed in each measurement, ranging up to nearly 1000 eV. For -20 V bias, 54% of all counts were above 100 eV, this value was 49% at 0 V and 55% for +20 V. For comparison, in Section 5.3.1, this number was 2% across all biases.

The differing proportions indicate that applying a bias, positive or negative, did screen a portion of low energy electrons. A positive bias on the graphite should suppress secondary electron emission while a negative bias may have prevented secondary electrons from the entrance aperture reaching the TES. However, as the energy distribution below 20 V did not notably change on applying a positive bias, the majority of low energy electrons do not appear to have been emitted from the target itself.

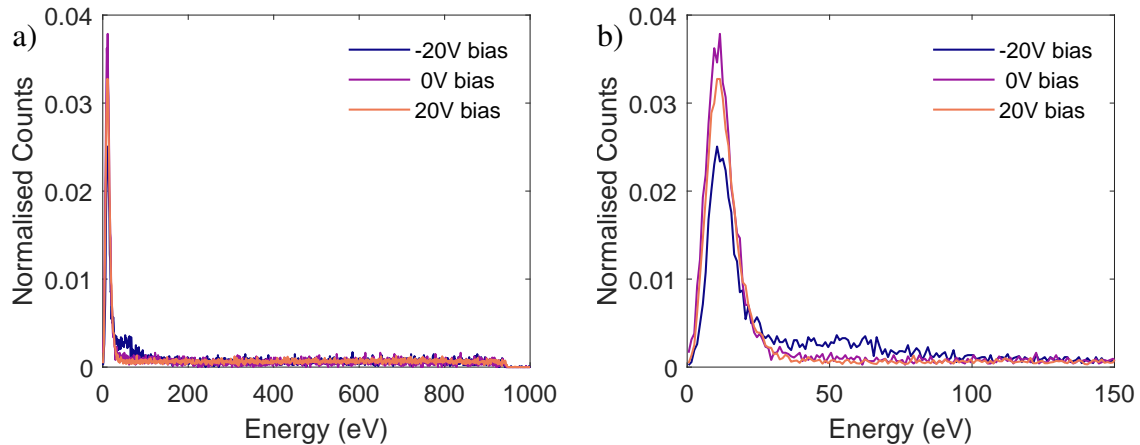


Fig. 5.28 a) Measured electron energy spectra of a 1 keV beam scattered off a graphite target. -20 V, 0 V and 20 V biases were applied to the target. b) Low energy region of the spectrum in (a).

Instead of looking at a single beam energy and changing the target bias, we now look at the measured spectra from a range of beam energies between 750 eV and 2000 eV with an unbiased graphite target. Fig. 5.29 and Fig. 5.30 provide the results from these measurements. The panel in Fig. 5.29a and Fig. 5.30a is the predicted spectrum referenced from [106], previously referenced in Fig. 5.23. The spectra measured by the TES is quite consistent with the reference spectrum, the notable differences being at low and high energies. The lack of the sharp, low energy secondary electron peak, typical of crystalline graphite, is likely a result of the TES energy resolution and contamination of the graphite surface with adsorbents. While the expected background of electrons between the secondary electrons and the elastic peak was measured, the elastic peak is not visible.

Fig. 5.31 compares the difference between the high-energy limit of the measured electrons and the beam energy. As would be expected, at higher energies, the difference broadens as the detector saturates. This saturation is clearly shown by looking at the average TES response shapes (Fig. 5.32), where significant saturation can be seen above 1 keV.

Resolving any indication of the elastic peak at the given level of noise requires more electron measurements. The simplest method to improve electron measurement rate is to increase beam current. However, the observed relation between beam current and count rate for these measurements was found to be quite complex as shown in Fig. 5.33a. The colour scale in this figure shows the time elapsed from the first measurement in minutes. Increasing the beam current did increase the count rate but over time, this count rate dropped as did the beam current. The beam current for the electron source was controlled by the voltage on the wehnelt electrode. At a fixed wehnelt voltage, the current was regularly observed to slowly

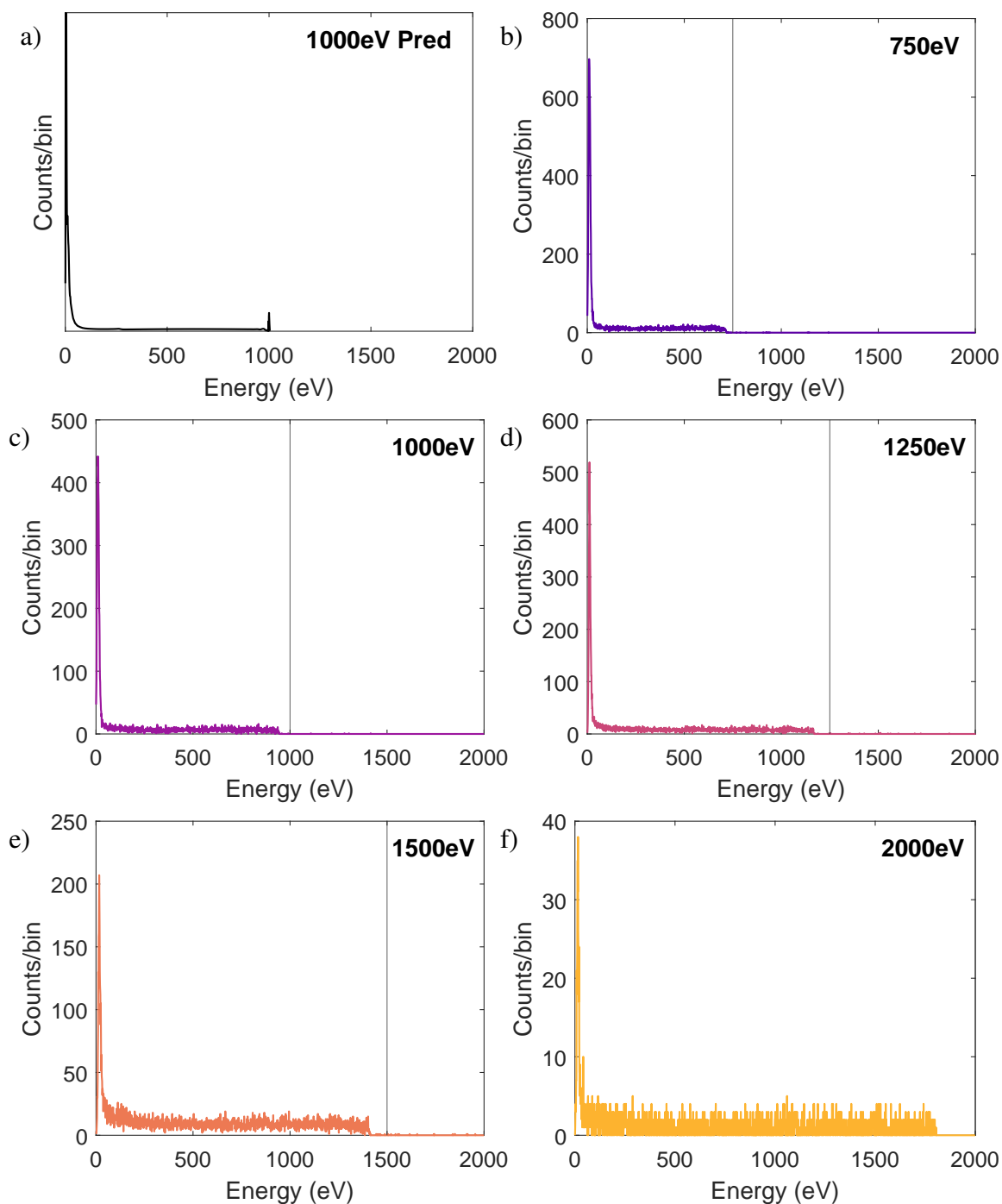


Fig. 5.29 a) Total scattered electron distribution of graphite foil measured from reference [106] using a 1 keV beam. b) - f) Measured electron energy spectra using various beam energies. The beam energy used is shown by the vertical line.

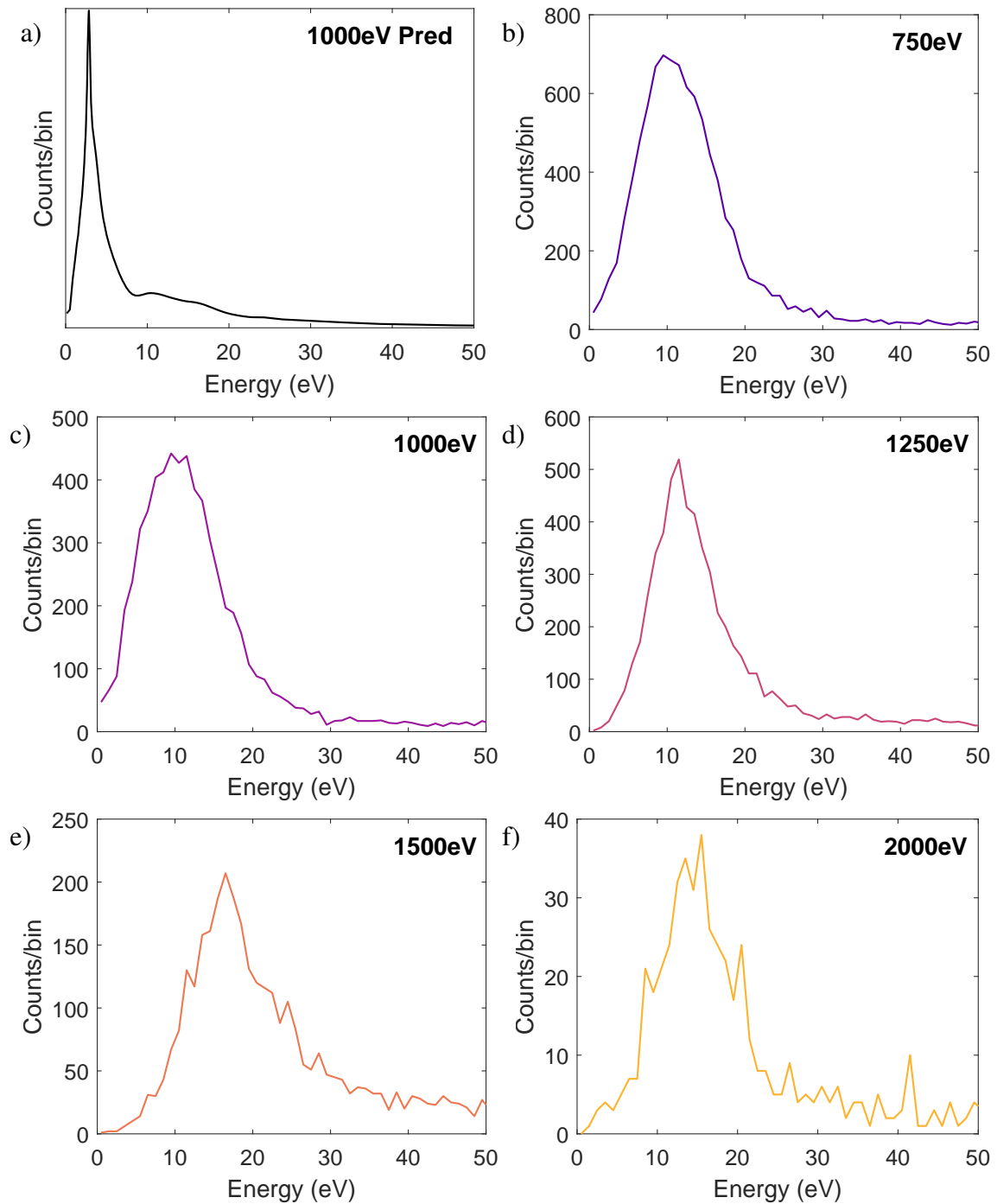


Fig. 5.30 Low energy regions of the spectrum in Fig. 5.29

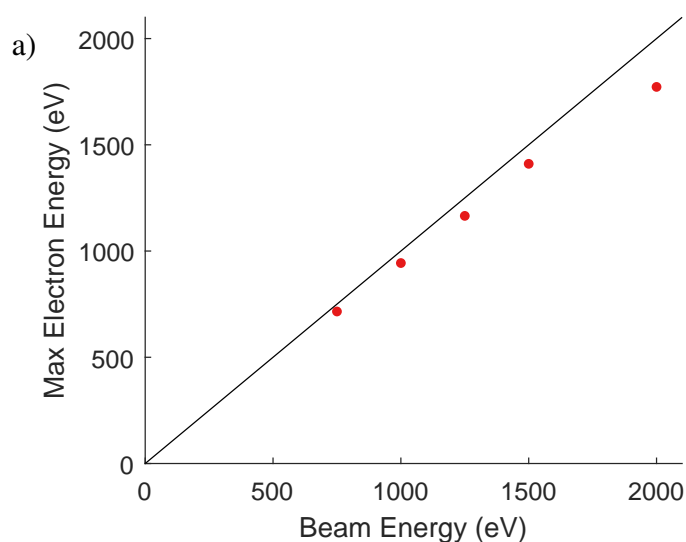


Fig. 5.31 Electron beam energy plotted against the resulting highest energy electron events measured in Fig. 5.29.

drift down over time, as shown in Fig. 5.33a, but the corresponding drop in count rate was greater than would be expected based solely upon beam current.

Fig. 5.33b shows the distribution of electron detection events by deflection angle at different beam currents. The electron beam was rastered across the angular range shown in the plots in these measurements. The measurements have been stacked sequentially in time with the earliest measurements at the bottom of each bar and the latest at the top. The colour of each portion of the bar corresponds to the beam current applied for those measurements. The y-deflection angles show no obvious change between the applied beam current and the y-angle distribution of events. However, the x-deflection angles clearly show that high current measurements favour larger angles compared to low currents. The measurements in Fig. 5.33b show the changing x-angle distribution of electron events when increasing the beam current followed by the distribution returning to the low-current distribution by reducing the beam current. Such a shift is indicative of something in the path of the beam charging under high current illumination and then discharging. The electric field from the charged object would be sufficient to deflect the electron beam, requiring adjustment in the beam deflection angle to compensate. The charged object must also be between the electron source and the target for it to have influence on the incident beam angle; after scattering, electron deflection angles will be largely uncorrelated to a small angular change of the incident beam, provided the beam strikes the graphite target. The only components with insulating materials between the source and the target are the clamps holding the graphite in place. These clamps must press against the graphite but not be in electrical contact so

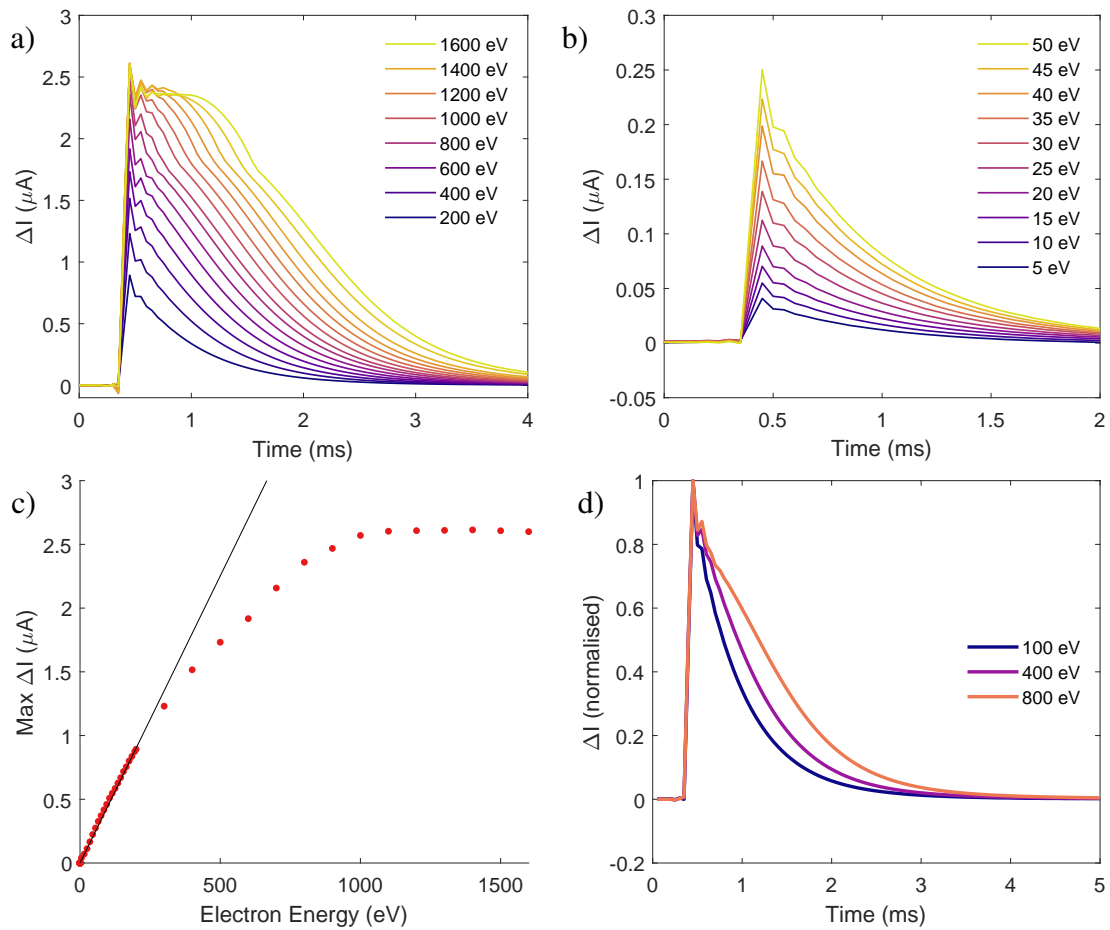


Fig. 5.32 a - b) Averaged TES electron detection responses at different event energies plotted on two separate axes for clarity. c) Maximum pulse heights in (a-b) plotted against event energy. d) Average responses of three different event energies, normalised to the same max amplitude.

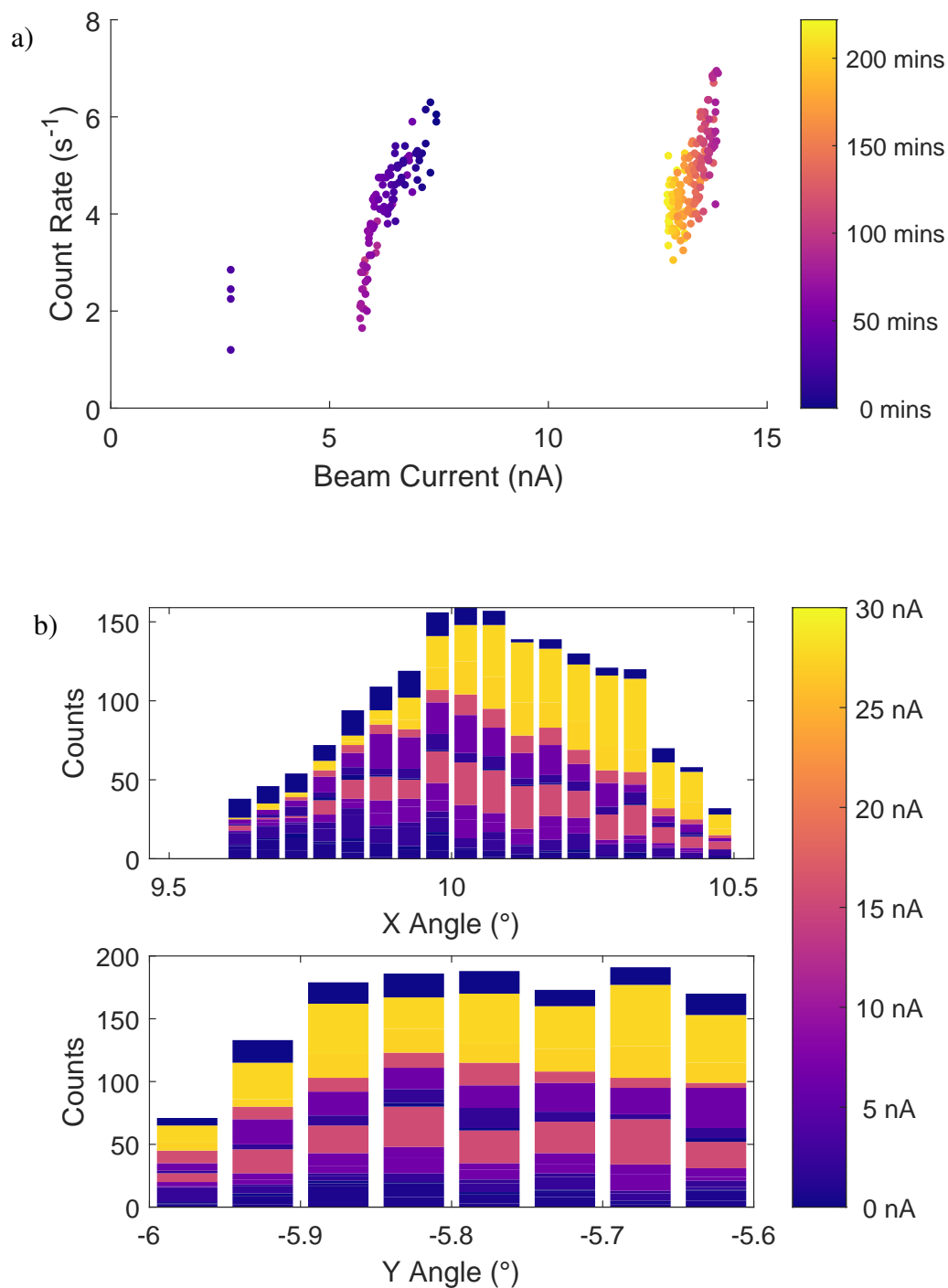


Fig. 5.33 a) Electron count rate plotted against beam current. The colour scale shows the time elapsed since the first electron measurement. b) Histograms of number of electron counts plotted against the corresponding x- and y- beam deflection angles. Block colour represents the applied beam current with the blocks stacked sequentially in time from earliest at the bottom and latest at the top.

as to not ground the graphite, allowing the target to be separately biased. These clamps, shown in Fig. 4.8b were polymer with a grounded copper layer on top. However, the sides of the clamp were exposed and insulating. Two L-shaped aluminium brackets were placed in front of the clamps to block these regions but it is possible for electrons to still reach the exposed insulator after multiple scattering events. At high currents, it is possible for the clamps to accumulate charge and deflect the incident electron beam. Therefore, this clamping arrangement was removed in the next set of measurements with no further charging effects observed.

5.3.3 Grounded Target Measurements

Due to the possible charging of the clamps holding the graphite in place, these clamps were replaced with fully metal ones. The use of these metal clamps meant that the graphite was now grounded to the target holder and could not be biased separately. The primary purpose of biasing the graphite was to reduce secondary emission, allowing for a greater proportion of higher energy electrons to be measured. Instead of biasing the target, for this set of measurements, a bias was instead applied to the TES aperture array. By applying -20 V to the aperture array, electrons with energies below 20 eV would be screened and prevented from reaching the TES. An additional benefit of this bias would be to suppress secondary electron emission from the TES surface, thereby improving electron energy absorption efficiency. Along with these changes, the 4K cryostat window aperture was reduced in diameter from 4 mm to 1 mm, to reduce infrared thermal loading on the TES. The same set of TESs were connected to the readout.

On cooling to 100 mK, it was observed that applying a bias to the TES aperture increased the temperature of the device module. The cause for this was a short on the order of $1\text{ G}\Omega$, between the TES aperture array and ground. This short would cause several nanowatts of heating on applying a bias, sufficient to warm the devices. Therefore, the TES aperture bias was not able to be used. The observation that electrically biased components dissipate a prohibitive amount of heat into the TES if they possess resistances on the order of $\text{G}\Omega$ is highly-relevant to the possible integration of electron optics into the TES itself, discussed in Chapter 6 and Chapter 7. Integrating electron optics into the TES absorber could prove an excellent method of controlling electron-TES interactions but care must be taken that these structures display minimal Joule heating.

Reducing the 4 K aperture from 4 mm to 1 mm had no observable impact on the thermal loading. Fig. 5.34 shows a collection of noise spectra observed during this set of measurements; the observed noise power was in fact greater than in Fig. 5.27, comparable with Fig. 5.21. One possible explanation for the increased noise in Fig. 5.34 is that the alignment

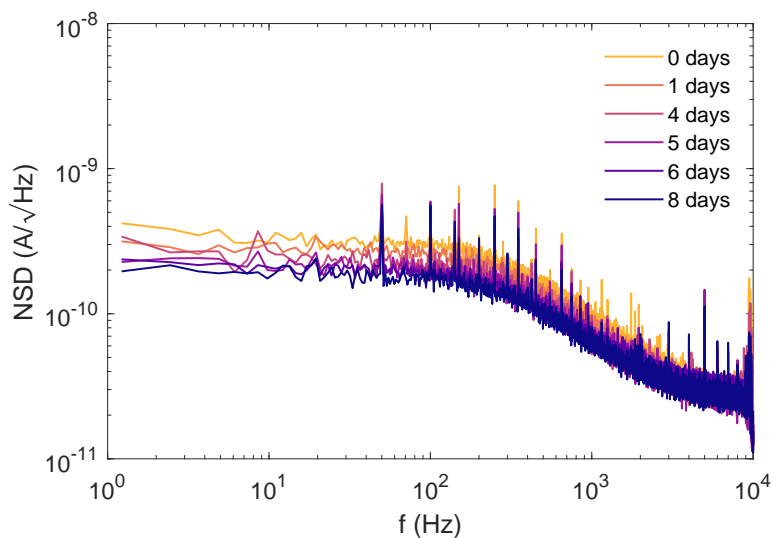


Fig. 5.34 Noise spectral densities of TES 24 measured on several days after initial cooldown to 4 K. Spectra were taken at 130 mK bath temperature and $0.25 R_n$.

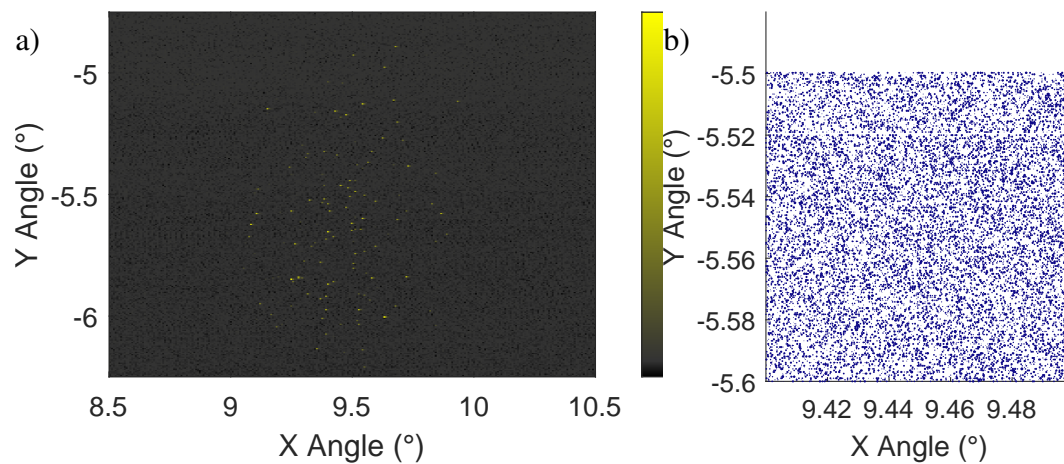


Fig. 5.35 a) Map of the change in TES current from equilibrium, measured at different electron beam angles. The beam was rastered across the plotted range. The TES current is shown on a colour scale from black to yellow. A number of electron detection events are visible in the centre of the scan. b) Plot of electron detection events against beam deflection angle, compiled over a number of scans of a narrow angular region. The spot size is proportion to the measured event energy.

between the graphite targets, 4 K and 45 K apertures was not correct in Section 5.3.2 and so the thermal loading on the TES was reduced. To check this, we can compare beam angles that resulted in electron detection events in Fig. 5.33b and Fig. 5.35.

In Fig. 5.35a, a 1 keV electron beam was rastered across the range shown and the TES current measured. The range of TES measurements lie between 9 and 10° in the x-direction and -6 and -5° in the y-direction. This range is comparable to the angles shown in Fig. 5.4 and Fig. 5.24; it does not match with Fig. 5.33b from the previous subsection. In Fig. 5.33b, the electron detection events were observed between 9.5 and 10.5° . To investigate this further, the electron beam was rastered across a small angular range where no electrons were observed in Fig. 5.35b. The distribution of events measured at these beam angles is shown in Fig. 5.35b; the electrons are qualitatively observed to be quite uniformly distributed in both energy and angle. The count rate of electrons in this region (plotted in Fig. 5.36) was observed to be an order of magnitude greater than for the measurements in the previous subsection (Fig. 5.33). These results all imply that the electron source, 45 K and 4 K apertures were not in correct alignment in Section 5.3.2. The magnitude of the angular difference observed indicates that many, if not all, electrons that were measured had scattered off the 45 K mesh or inside surface of the 45 K aperture prior to reaching the graphite target.

Given the greater available measurement rate, this set of measurements focussed on measuring the energy spectrum of 1 keV electrons scattered off the grounded graphite target with a large number of counts, comparing the result with that of Fig. 5.29. In total, 89,000 separate electron events were detected in this set of measurements, producing the spectrum in Fig. 5.37. This spectrum matches the 1 keV spectrum in the Fig. 5.29 closely, with the exception of the low energy electrons. A smaller proportion of secondary electrons were observed in the latter measurements, possibly due to the improved beam alignment. The distribution of secondary electrons has also shifted to slightly higher energies.

On the other side of the spectrum, no elastic peak is visible, instead the counts smoothly tail away at 950 eV. There are several factors that explain why the elastic peak was not resolved in these measurements, though determining the relative importance of each requires further work. The TES energy resolution at these energies is a major consideration. While the measured noise spectrum places a lower resolution limit of 3 eV, this does not account for errors in the analysis and importantly saturation in the detector. Fig. 5.32 shows the TES saturating around 1000 eV, therefore providing diminished energy sensitivity and degraded resolution. In addition to the TES energy sensitivity is incomplete electron energy absorption due to the emission of secondary electrons. The surface of the TES was gold which was measured to emit over 1 secondary electron per 1 keV incident electron in Section 7.2.3. These secondary electron losses would have further broadened the elastic peak towards lower

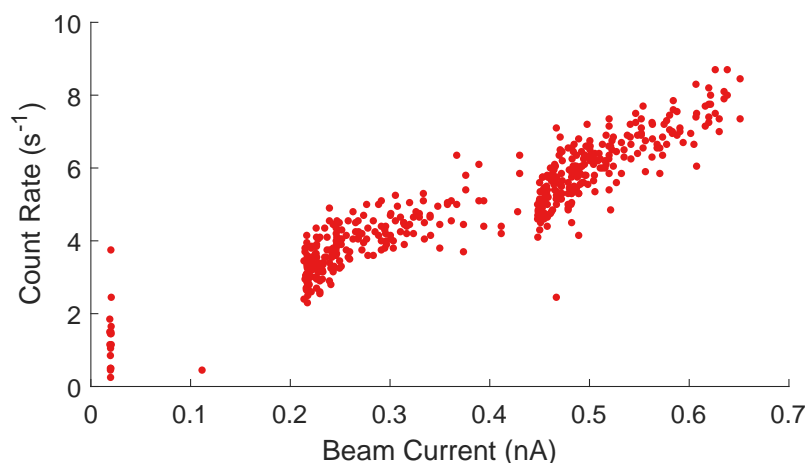


Fig. 5.36 Measured electron count rate plotted against the applied beam current at 1 keV beam energy.

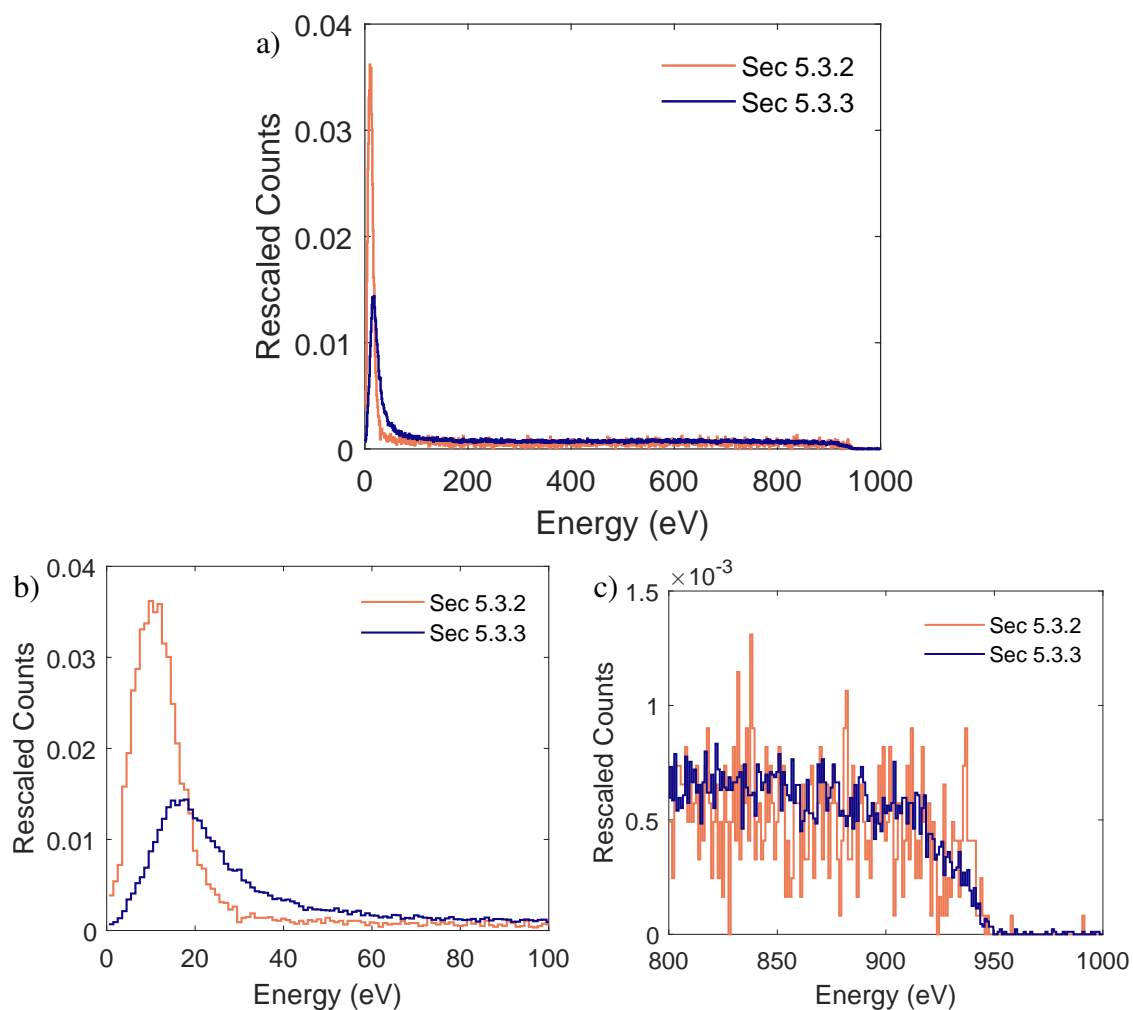


Fig. 5.37 a) Comparison between measured electron energy spectra with 1 keV beam energy in the previous set of measurements (Fig. 5.29 in Section 5.3.2) and in this set Section 5.3.3. Low (b) and high (c) energy regions of the spectrum in (a). The spectra have been normalised by area and have 1 eV energy bin sizes.

energies. The final factor to consider is the ratio between the elastic peak height and the inelastic background. This ratio is dependent on the material used, especially the surface chemistry, in addition to the incident electron angle and the angle between the target surface and the detector. Predicting the relative magnitude of the elastic peak above the background in these experiments would have to be done by simulating electron interactions with the graphite target.

5.4 Conclusions

These results presented in this chapter conclusively demonstrate both TES electron calorimetry and spectroscopy for the first time. Individual electron detection events were routinely observed by TESs in both direct beam and scattered measurements using TESs that were not originally designed for electron measurements but for infrared bolometry. These devices were successfully used to measure electron energy spectra spanning three orders of magnitude with energy resolutions below 4 eV, as determined by the observed measurement noise.

These spectra were extracted from the measured TES data using data analysis software based upon the software in Section 3.2.2. This software was used to identify and determine the energy of tens of thousands of electron events using experimental data in the presence of intrinsic detector noise and infrared loading on the TES. The strong correlation between the observed electron energies and the applied beam energy across different experiments and experimental configurations gives confidence in the analysis method and shows the experimental and analytical methods used provide an excellent platform for further investigation into TES electron calorimetry.

The experimental measurements presented here prove the principle of TES electron spectroscopy and can be built on by using bespoke electron-detecting TESs, as well as modifying the experiment to better separate the measured electrons from incident black-body radiation. The use of electron optics to deflect electrons towards a TES that is positioned out of line-of-sight from room-temperature components is the ideal method of blocking this black-body radiation; one possibility being placing a pair of deflector plates within the 4 K chamber to deflect the electron off-axis, either directly to the TES or at a sample target before measuring the resulting scattered electrons.

An important question that remains to be answered is the degree to which incomplete energy absorption by the TES was present in these measurements. As the detectors possessed a smooth gold surface, secondary electron emission will have had a significant impact on the measured energies. It is difficult to quantitatively determine this effect with the data at hand due to the sensitivity of secondary electron emission to the surface chemistry, but this energy

loss mechanism will have reduced the observed energy of an incident electron by an amount between 0 and 100 eV, taking into account the possibility for multiple secondaries emitted by a single primary electron. This inefficiency is not fundamental to the measured technique; it can be minimised, or even eliminated by improving the TES electron absorber design and applying electric fields to suppress emission, both of which are discussed in later chapters.

Chapter 6

TES Electric Field Sensitivity

6.1 Introduction

The sensitivity of transition-edge sensors to strong electric fields is of great importance when considering these devices for the measurement of charged particles. For example, DC fields can be used to greatly enhance energy absorption efficiency of incident electrons by suppressing the emission of secondary electrons from the absorber material. Additionally, electrostatic deflection can be used to redirect electrons, allowing for electrons emitted from a non-cryogenic source to be sent to a TES with minimal infrared loading. Applied electric fields can also precisely shift the energy of incident electrons into the optimal energy sensitivity range of the detector. As well as being able to enhance absorption efficiency, strong DC electric fields also provide a method to screen charged particles from the TES. This screening of charged particles would be valuable in blocking low-energy electrons in electron spectroscopy, but has applications beyond charged particle measurements. For example, secondary electrons from cosmic ray events are a considerable source of measurement noise in space-based measurements which could be mitigated by screening the incident charged particles from the detector [107].

In each of these cases, it is critically important to understand the sensitivity of TESs to applied electric fields. The sensitivity of TESs to magnetic fields has been studied previously [75–77] but little attention has been paid to electric fields. While we expect that applying DC electric fields will have little effect upon the superconducting components themselves, the electric fields could affect TES operation by coupling to two-level systems in the substrate, for example. TESs are fabricated on disordered membranes such as silicon nitride due to their low thermal conductances. However, these materials contain a large density of two-level systems (TLSs) contributing greatly to the observed heat capacities and thermal conductances [108–110]. Electric fields can couple to the polarisable portions of these TLSs,

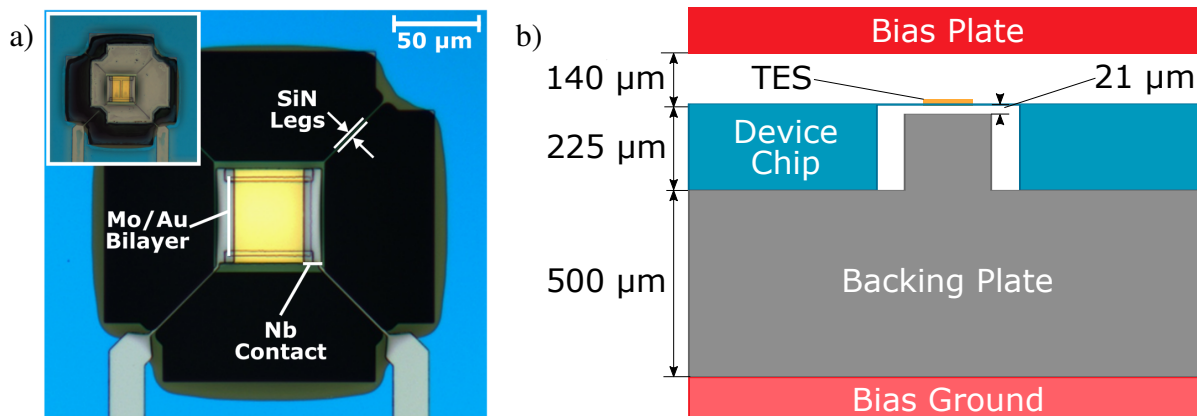


Fig. 6.1 a) A suspended Mo/Au TES representative of the design of the $10 \times 10 \mu\text{m}$ device reported here. The inset shows an enhanced depth of field image of a different device with a backing plate pillar visible underneath, for reference. b) Diagram of device and backing plate positions in relation to bias plate and ground.

providing a mechanism by which DC fields can change these key TES parameters. Therefore, I investigated the electric field sensitivity of Mo/Au bilayer TESs to determine whether the application of static electric fields observably alters the behaviour of these devices at field strengths up to 90 kV/m .

6.2 Apparatus

The measurements of TES electric field sensitivity were performed using the same set of Mo/Au bilayer devices described in Chapter 4. The device tested was a square $10 \mu\text{m}$ bilayer with no normal metal gold bars, denoted TES 7 in [77]. Fig. 6.1a shows a representative image of a $40 \mu\text{m}$ Mo/Au device without normal metal bars for reference. The measurements were performed using the same device module as in Chapter 4. Electric fields were applied to the device using a modified version of the clamping arrangement shown in Fig. 4.6a where, instead of an aperture plate positioned above the clamps, a copper bias plate was attached to the underside of the TES clamp. By attaching the plate to the clamp directly, the plate was held parallel at a fixed distance of $140 \mu\text{m}$ from the TES layer. The surface of the device module upon which the TES chip was clamped was used as the electrical ground. This arrangement is shown in Fig. 6.1b. The module lid was fully closed and the cryostat window was blocked to reduce infrared loading.

Between the device chip and the ground was a silicon backing plate with pillars extending up into each device well, $21 \mu\text{m}$ below the device layer. The pillars were capped with 300 nm of niobium. The inset of Fig. 6.1a shows an example of one of these pillars in position

beneath the device. The fabrication and design of the backing chip and pillars are described in [77], where they were used as a magnetic shield, attenuating the perpendicular component magnetic field strength at the TES, and as an infrared reflective backstop to enhance IR absorption efficiency. For these electric field sensitivity measurements, the backing chip acted to enhance the electric field strength experienced by the TES. Modelling the system as a parallel-plate capacitor with the gap partially filled by a dielectric material, the electric field present at the TES layer is

$$E = V \frac{\epsilon_2}{\epsilon_1 d_2 + \epsilon_2 d_1}, \quad (6.1)$$

where V is the applied plate bias, ϵ_1 and ϵ_2 are the permittivities of vacuum and silicon, and $d_1 = 704 \mu\text{m}$ and $d_2 = 161 \mu\text{m}$ were the distances from the top of the backing plate pillar to the bias plate and bias ground, respectively. The maximum voltage applied to the bias plate (V_{plate}) was +20 V. Using Eqn. 6.1, at 20 V plate bias and relative permittivity of 11.5 for low-temperature silicon, the field strength experienced by the TES is calculated to be 90 kV/m.

Two sets of measurements were performed, one establishing upper bound electric field sensitivity limits upon static electric fields (Section 6.3), the second investigating the effects of applying low-frequency sinusoidally varying electric fields (Section 6.4).

6.3 Static Field Measurements

6.3.1 TES I-V

The voltage-current relation of the $10 \mu\text{m}$ TES (TES 7) was characterised with applied plate voltages from 0 to 20 V in intervals of 1 V. These measurements were performed at a fixed bath temperature of 120 mK, the results of which are overlaid in Fig. 6.2a. In each case, the device entered its superconducting transition around 50 nV as the bias voltage V_{TES} was reduced. At TES bias voltages above 50 nV, the TES displayed ohmic behaviour, with rapidly falling resistance below 50 nV. As the device was in thermal equilibrium at each bias voltage, the Joule heating in the TES must have been balanced by the heat flow to the bath, P_b , and so

$$P_b = K(T_c^n - T_b^n) \quad (6.2)$$

where K is a measure of the thermal conductance between the device and the bath, T_c is the superconducting transition temperature, T_b is the bath temperature and n is a constant determined by the dimensionality of the thermal link between the TES and the bath. Fig. 6.2b

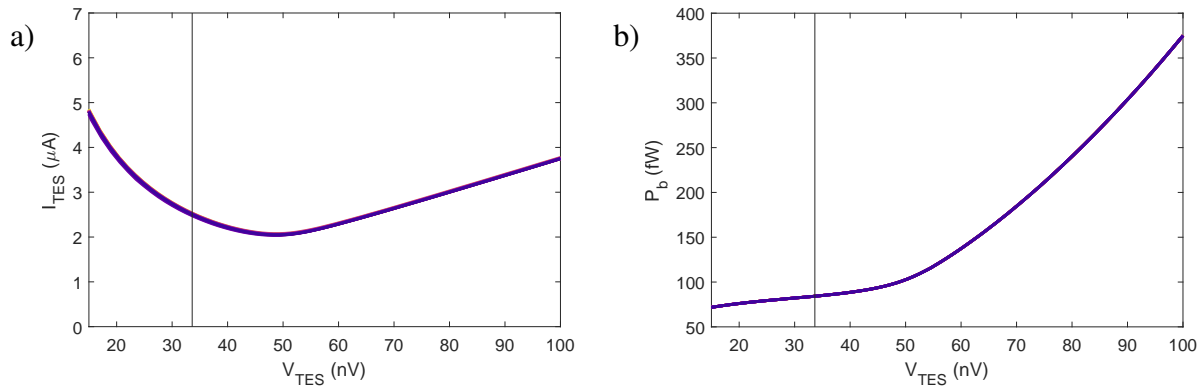


Fig. 6.2 a) Voltage-current relation of TES 7 measured at 120 mK. b) TES power flow to bath plotted against TES bias voltage measured. Measurements taken at applied plate biases from 0 to 20 V at intervals of 1 V have been overlaid. The differences between measurements are not visible at this scale.

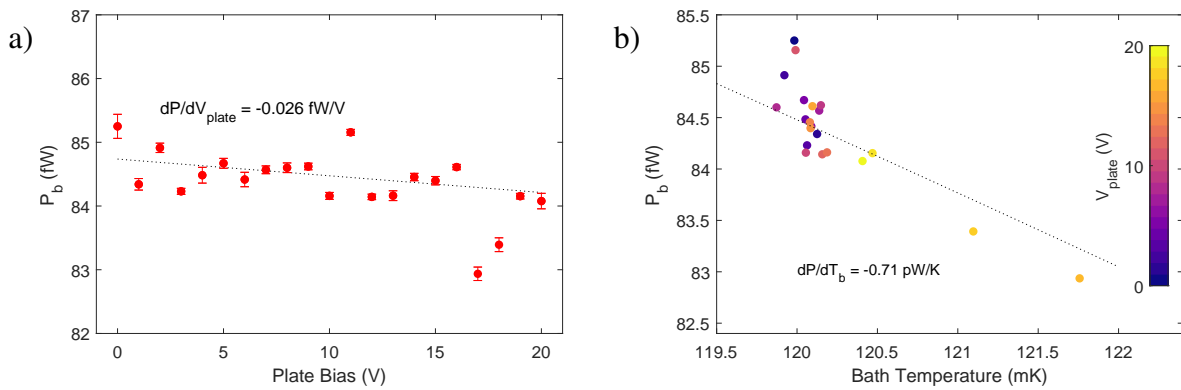


Fig. 6.3 a) TES power flow to bath plotted against plate bias voltage from 0 to 20 V, measured at the normal-state resistance ($R_n/2$) TES bias voltage. The error bars were calculated using a standard deviation of the measured temperature variation during each measurement. b) The data in (a) plotted against bath temperature with the V_{plate} colour scale showing the applied plate bias.

shows that there is no apparent effect of the applied electric field on P_b across the electric field strengths tested.

Fig. 6.3a investigates the relation between P_b with the applied field by plotting these two properties at a fixed TES bias point, represented by the vertical line in Fig. 6.2. The data show a weak negative correlation between the two variables, but also makes apparent two anomalously low values of P_b at 17 and 18 V plate bias.

The cause for these low values can be seen in Fig. 6.3b where the data in Fig. 6.3a has been replotted against bath temperature. The colour of each point has been scaled according to the plate bias. The dashed line shows the expected trend of P_b and T_b using Eqn. 6.2 and measured values of $K = 5.4 \text{ pW/K}^n$, $n = 2.4$ and $T_c = 0.20 \text{ K}$ for this device. The two values above 121 mK are the anomalous results at 17 and 18 V, indicating that the low values of P_b are the result of temperature drift rather than the applied field. For these two measurements, the ADR was reaching the end of its 120 mK hold time and so the temperature began to slowly rise.

Excluding the two anomalous measurements, the least squares linear fit of the data in Fig. 6.3a gives a gradient of -0.026 fW/V . The standard error of this fit is $\pm 0.012 \text{ fW/V}$ showing that the negative correlation is relatively small compared to the variations between measurements and that the TES is less sensitive to static electric fields up to 90 kV/m than to sub-millikelvin temperature fluctuations. The comparable size of the fitted gradient with the corresponding standard error and the correlation between P_b and the bath temperature, even when excluding the anomalous results, means that no significant correlation between the applied field and P_b was observed in these measurements. However, a better test of electric field sensitivity could well be observed in a cryostat with tighter temperature tolerances.

The results from Fig. 6.2 and Fig. 6.3 show the resilience of the TES to the applied electric field on the TES current-voltage relation. While no significant effects were observed, these results can still be used to place an upper bound limit on the dependence of the TES thermal conductivity, G on the applied electric field. The thermal conductivity depends on K by the relation

$$G = \frac{dP_b}{dT_c} = nKT_c^{n-1}, \quad (6.3)$$

using the same terms as in Eqn. 6.2. To calculate the thermal conductance sensitivity limits, I have assumed a linear dependence of electric field strength on K . The upper bound sensitivity of G to the applied field is $(dG/dE) = 1 \times 10^{-19} \text{ (W/K)/(V/m)}$. This value can be rewritten as a proportional change in G of $G^{-1}(dG/dE) = -0.07 \text{ (MV/m)}^{-1}$. For context, with this sensitivity, a 1000 V charged plate could be placed within centimetres of the TES with minimal effect on the thermal conductance.

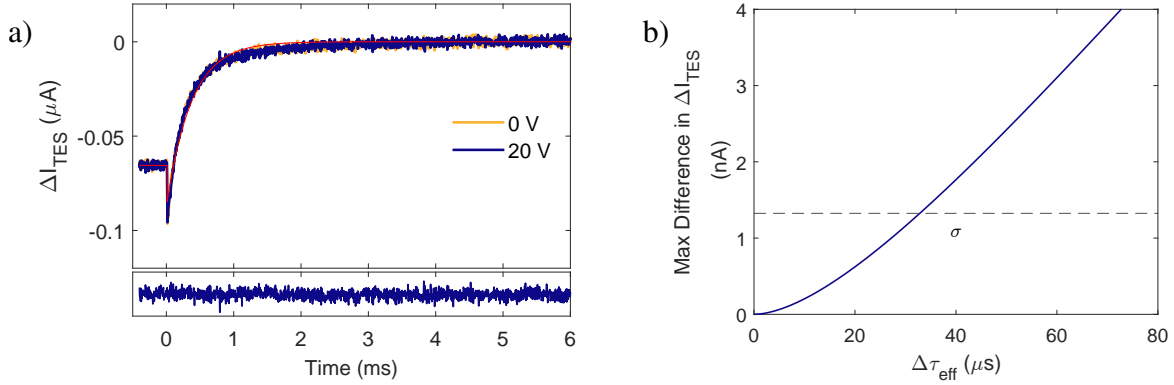


Fig. 6.4 a) TES response measured at 0 and 20 V applied plate bias. The bottom inset provides the difference from subtracting the 0 V and 20 V measurements. The red line shows the fitted response using a single exponential decay constant. b) The maximum difference between two exponential decays with time constants differing by $\Delta\tau_{\text{eff}}$ calculated using Eqn. 6.5 for the exponential fit in (a).

6.3.2 TES Response

With limits placed on the sensitivity of thermal conductance to static electric fields, we will now consider the effects of static electric fields on response time. TES response time was measured at 0 and 20 V plate biases with a 200 kHz sampling frequency.

Upon applying a 1 nV voltage step to the TES bias, the TES current dropped to its new equilibrium along an exponential decay with an decay constant of

$$\tau_{\text{eff}} = \frac{nC}{\alpha G}, \quad (6.4)$$

where τ_{eff} is the effective time constant and C is the TES heat capacity. Coupling between TLSs and the applied electric field is expected to impact the TES heat capacity and thermal conductance. The measurements in the previous subsection placed limits on thermal conductance sensitivity. As a result, measuring the TES response time allows us to investigate any relation between the TES heat capacity and the applied field.

The measured responses are plotted in Fig. 6.4a along with the difference obtained by subtracting the two responses shown. There is no observable difference between the two measurements indicating that the applied electric field has very little effect on the TES effective time constant.

The TES responses at 0 V and 20 V plate bias were fitted with exponential decays with a single decay constant by least-squares minimisation. The fitted decay constants were calculated to be 0.370 ms and 0.368 ms for the 0 V and 20 V measurement respectively. The 0 V fit is shown as the red line in Fig. 6.4a. The standard error of these fits are ± 0.002 ms,

highlighting the similarity in the responses. Comparing the fitted response to the measurement, a single decay constant does not fully match the observed response after around $500 \mu\text{s}$. Therefore, the single exponential decay model in Eqn. 6.4 does not fully characterise the TES response and additional uncertainty will be present in the estimates of τ_{eff} that has not been accounted for.

Of interest is the possible change in τ_{eff} upon applying an electric field. If the observed time constant τ_{eff} is assumed to differ at 0 and 20 V applied biases, the deviation in current between the two time response measurements, represented by $\overline{\Delta I}$, is

$$\overline{\Delta I} = A \left(\exp\left(\frac{-t}{\tau_{\text{eff}}}\right) - \exp\left(\frac{-t}{\tau_{\text{eff}} + \Delta\tau}\right) \right) \quad (6.5)$$

with the difference in response times represented as $\Delta\tau$, for a pulse starting at $t = 0$ with maximum amplitude A . As no shift in TES response was observed, the magnitude of $\Delta\tau$ must be constrained by the measurement noise. A conservative estimate of this constraint would be to require that $\overline{\Delta I}$ be smaller than the observed RMS noise in the measurement. $\overline{\Delta I}$ reaches its maximum value at

$$t_m = \frac{-\tau_{\text{eff}}(\tau_{\text{eff}} + \Delta\tau)}{\Delta\tau} \log\left(\frac{\tau_{\text{eff}}}{\tau_{\text{eff}} + \Delta\tau}\right). \quad (6.6)$$

Fig. 6.4b shows the maximum deviation calculated using Eqn. 6.5 and Eqn. 6.6 between two exponential decays of the form fitted in Fig. 6.4a when modifying one decay constant by $\Delta\tau_{\text{eff}}$. The dashed horizontal line labelled σ represents the RMS noise level in the TES response measurements. The maximum deviation between the two exponential responses in Fig. 6.4a within the noise floor is $33 \mu\text{s}$, corresponding to a 9% uncertainty in τ_{eff} . The true value for this sensitivity of τ_{eff} to the applied field is likely much smaller than this conservative estimate.

The sensitivity constraint on τ_{eff} is an order of magnitude less restricting than that placed on the thermal conductivity using Fig. 6.3 and so can be largely attributed to a possible change in heat capacity, following Eqn. 6.4. Once more, assuming C varies linearly with applied field strength, a 9% change in heat capacity by applying 20 V plate bias sets an upper bound of $C^{-1}(dC/dE) = \pm 1.0 (\text{MV/m})^{-1}$ on the sensitivity of TES heat capacity to applied electric fields.

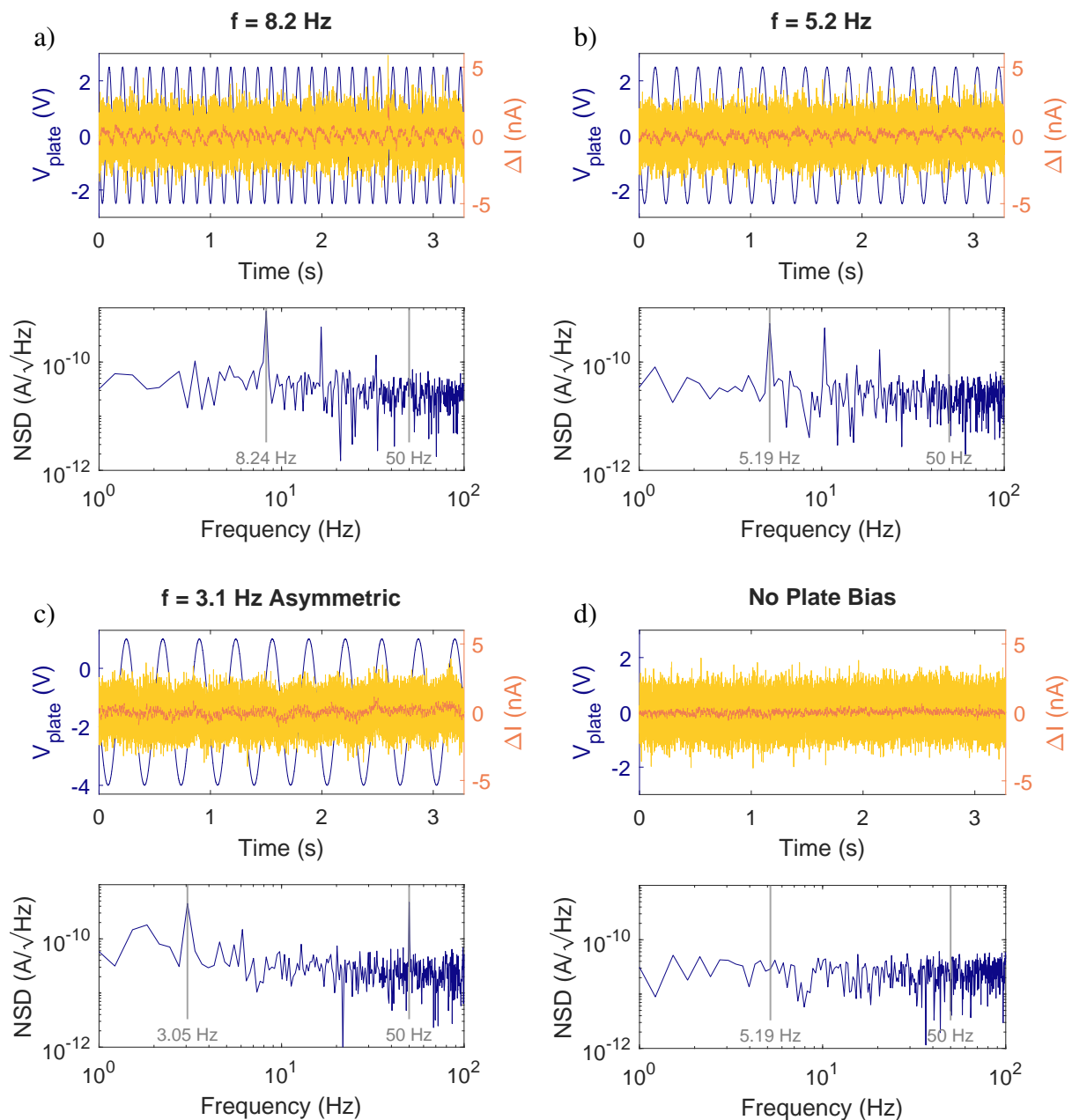


Fig. 6.5 a) TES current measured at varying plate bias, V_{plate} with the corresponding current noise spectral densities (NSD) plotted beneath. Plate biases of 5 V, peak-to-peak was applied with 8.2 Hz. b) Repeat of (a) with 5.2 Hz plate bias frequency. c) Asymmetric V_{plate} at 3.1 Hz between -4 and 1 V peak voltages. d) Measurement with no plate bias applied.

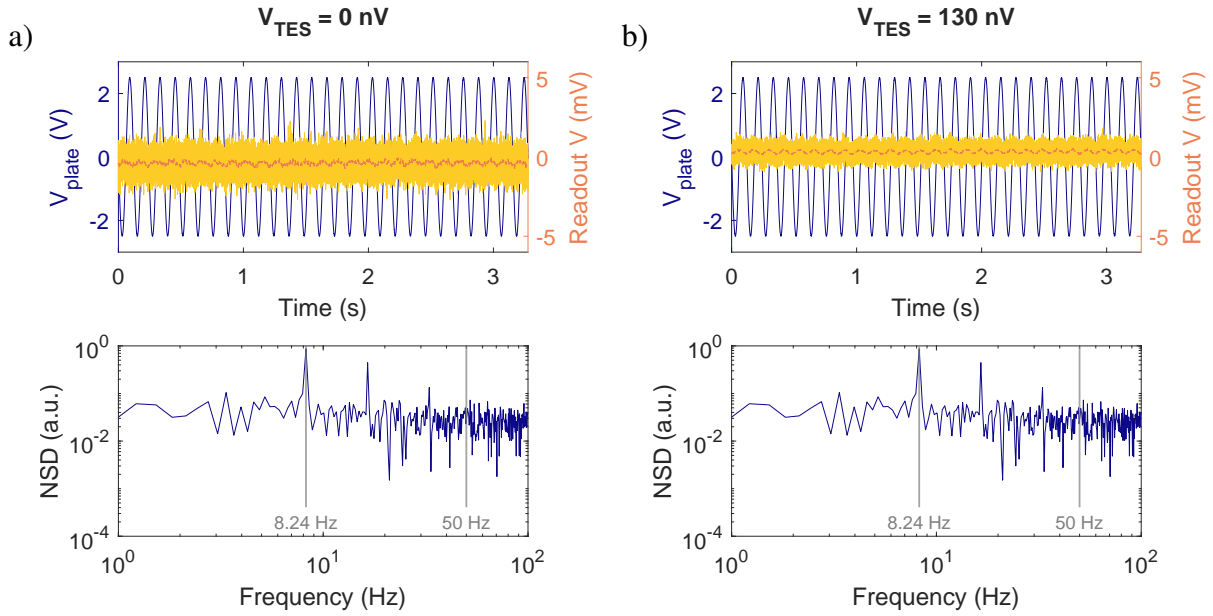


Fig. 6.6 Same measurements as Fig. 6.5 at 8.2 Hz plate bias frequency from an unbiased superconducting TES (a) and normal state TES (b). The TES readout voltage has been plotted instead of current as the conversion from readout voltage to current is not defined at zero applied bias after correcting for stray resistance.

6.4 Dynamic Field Measurements

With the absence of any significant effect on the TES by applying static electric fields, the effect of dynamic fields was then measured. Sinusoidally varying plate biases were applied to the TES whilst measuring the TES current and bias voltages. The sinusoid frequencies were chosen to provide a discrete number of cycles within each measurement period to mitigate spectral leakage when examining the Fourier transform of the signal.

Fig. 6.5a-c shows current measurements of TES 7 at various plate bias frequencies. The TES current, shown in yellow, was sampled at 20 kHz with the 100-point moving average of this current data plotted in orange and the applied plate bias in blue. The averaged data clearly shows small sinusoidal variations with frequencies corresponding to V_{plate} . Below the time series plots are the corresponding noise spectra with the measured sinusoidal peak frequency labelled. Removing the bias on the plate removes the sinusoidal variation, as seen in Fig. 6.5d.

Fig. 6.5 shows that applying an AC bias has a measurable, albeit small, effect on the TES with clear sinusoidal current variations matching the applied field frequency. The measurements do not show the mechanism of this coupling, however. To determine the coupling mechanism, further measurements were made with the TES being fully superconducting by

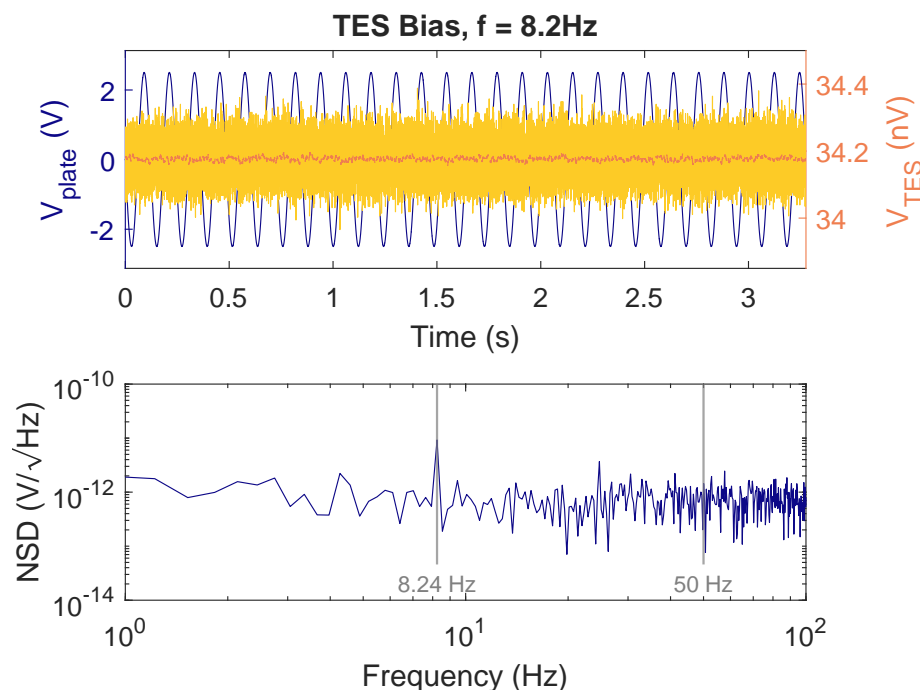


Fig. 6.7 Measured TES bias voltage and sinusoidally varying plate bias at 8.2 Hz plotted on same axes. The corresponding voltage noise spectrum is shown below.

applying no TES bias (Fig. 6.6a) and the TES being normal (Fig. 6.6b). AC coupling to the TES was present in both of these measurements, indicating that the effect is unrelated to the operation of the detector.

Measuring the TES bias voltage, rather than current, whilst applying varying plate bias also showed small sinusoidal variations, as seen in Fig. 6.7. This implies that coupling between the electric field and the TES bias circuit is the cause of the variations in the measured TES current. Further evidence for this hypothesis can be obtained by considering the dynamic resistance of the TES at this bias voltage. Fig. 6.8a shows that at 34 nV TES bias, the dynamic resistance of TES 7 was $-16 \text{ m}\Omega$. A segment of the current variation in Fig. 6.5 is shown in Fig. 6.8b where the peak-to-peak amplitude can be estimated at 1.4 nA. Using the dynamic resistance of the TES, this current variation would correspond to a voltage fluctuation of 22 fV which qualitatively matches with the observed V_{TES} fluctuations in Fig. 6.7.

If the TES bias voltage coupling is the predominant mechanism at play, the phase of the sinusoidal current component would be expected to reverse when reversing the polarity of the TES bias. If the coupling is within the readout circuit, this phase reversal would not be expected occur. Fig. 6.9 shows the TES current measurement with positive and negative TES bias. The phase flips at the frequency of interest, indicating that the predominant coupling is

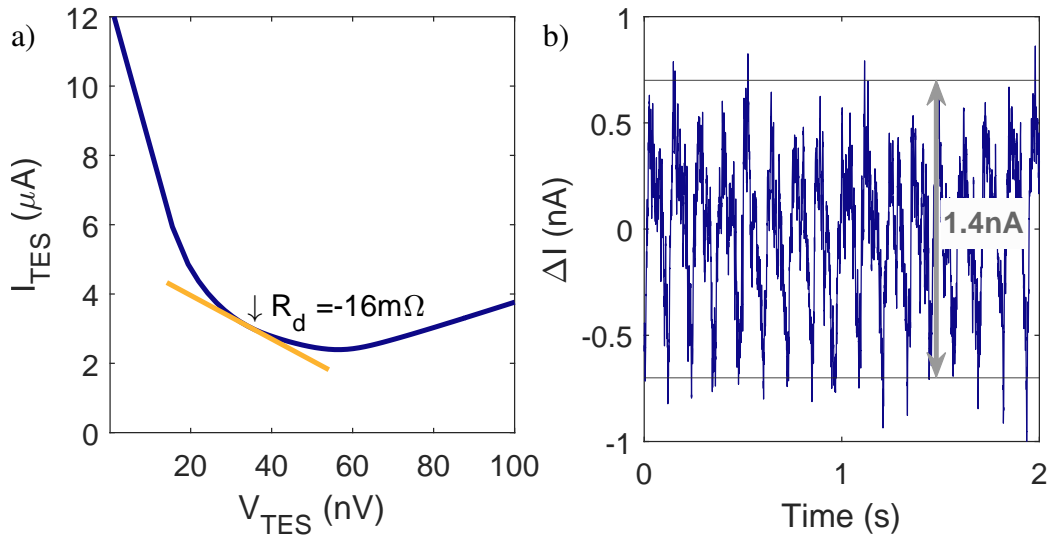


Fig. 6.8 a) Voltage-current relation of TES 7 measured at 120 mK with dynamic resistance, R_d , labelled at 34 nV bias. b) Measured TES current at $V_{\text{TES}} = 34$ nV with 8.2 Hz plate bias.

to the TES bias line. These measurements show that AC plate bias with frequencies below 10 Hz can couple with the TES bias supply, likely due to capacitive coupling due to the low frequencies used. The sinusoidal variation in V_{TES} was less than 1% and within the noise floor of the measurement.

6.5 Conclusions

For the first time, I have experimentally tested the low sensitivity of the Mo/Au TESs to static electric field strengths up to 90 kV/m. This result shows that using TESs in high electric field environments is feasible without changing device performance. This result allows for greater versatility when designing TES spectrometers for both measuring or screening charged particles. The lack of sensitivity also allows for integrating electron optics directly into the TES design by creating absorbers with separate biasing from the superconducting structure, to provide more control of the interaction between the charged particles and the device.

Low-frequency AC fields were observed to weakly couple to the TES bias circuit, most likely through capacitive interactions. This coupling is dependent on the device chip layout and the wiring to both the TES and bias plate. The observed coupling was very small with 22 fV variations in TES bias at 5 V plate bias at 8 Hz frequency but this coupling would likely become a significant consideration if operating TESs within higher frequency AC fields.

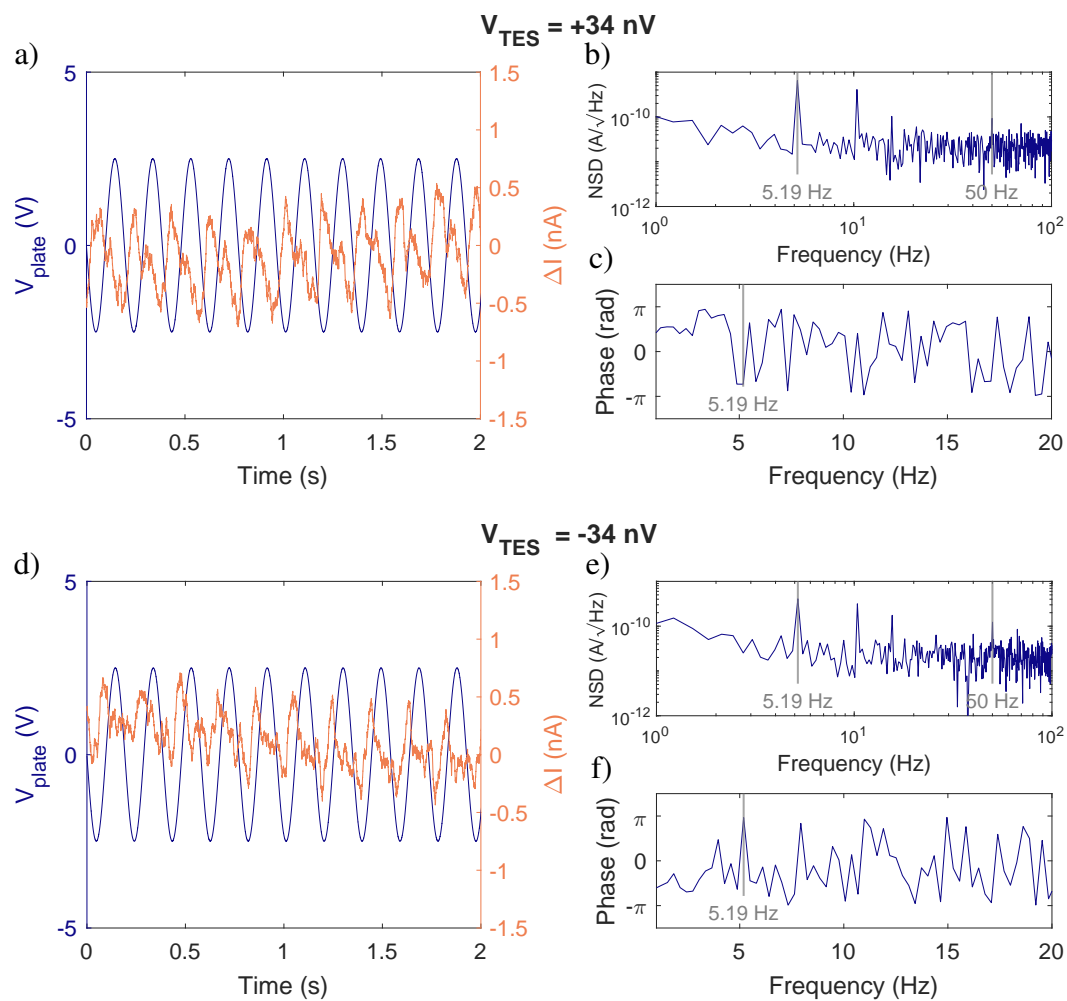


Fig. 6.9 a) Measured TES current at +34 nV TES bias with varying plate bias. b) Corresponding noise spectral density and c) phase spectrum of the measurement in (a). d-f) Repeat of (a-c) at -34 nV TES bias.

Chapter 7

Electron Calorimetry TES Design

7.1 Introduction

In Section 5, a set of proof-of-principle measurements successfully demonstrated TES electron measurement by adapting a set of detectors not originally designed for particle calorimetry. This chapter builds upon this work by creating designs for an initial set of TESs designed specifically for TES electron calorimetry.

As this is the first investigation into TES electron spectroscopy, there is a considerable scope of possible TES device designs that can be explored, not just in regards to detector performance such as energy range and resolution, but also device geometry and material choices. The closest comparison to TES electron spectrometers are TES X-ray calorimeters developed for astronomical and synchrotron beamline measurements. These detectors operate with similar resolution and energy range requirements, spanning photon energies up to several keV. However, TES X-ray calorimeters must balance absorber design with the TES saturation energy, determined by the device's heat capacity. The absorber design is constrained by the requirement that it has sufficient stopping power to efficiently absorb incident X-ray photons, whilst providing a heat capacity suitable for the chosen application.

Unlike X-rays, electrons display very short mean free path of electrons in solid matter; thin films of the order of 100 nm are sufficient to absorb electrons of 2 keV, regardless of the material choice [111]. This allows for far more flexibility in absorber designs compared to TES X-ray calorimeters to the extent that the superconducting film itself could be used as the absorbing structure. The disadvantage of the low electron mean free path is that as electrons cannot penetrate far within the absorber, energy losses from backscattered or secondary electrons escaping from the absorber surface becomes a much more significant consideration than for X-ray calorimetry.

A possible method of improving electron energy absorption efficiency is through the use of electron optics. The resilience of TESs to static electron fields observed in Chapter 6 suggests that incorporating electron optics into the devices themselves could prove an elegant method of improving electron absorption efficiency beyond the efficiency intrinsic to the absorber material.

As the electron-absorber interaction is of key importance, a set of candidate electron absorber materials were chosen based on their predicted absorption properties and compatibility with TES fabrication processes. The electron absorption efficiencies of these materials were tested, as described in Section 7.2, with the results of these measurements informing the TES material choices in the designed devices.

The first set of TES electron spectrometer device designs are presented in Section 7.3, a key aspect of these devices being an electron absorber electrically isolated from the superconducting structure. The separate electron absorber allows for optimising the absorption properties independent of the energy transducing capabilities of the superconductor. The absorber and superconducting structures were kept electrically separate to allow individual biasing of each. The *in-situ* control of TES absorber efficiency using electron optics means that these device designs provide a platform to demonstrate the viability of integrating electron optics into the devices and to investigate the interaction between absorbed electrons and the TES. From this platform, future design iterations can be performed with the goal of achieving devices meeting the requirements described in Chapter 3.

In addition to the electron absorber, the design of the superconducting thin film is also essential to the device performance. The design of these structures are described in Section 7.3 with Ti/Au superconducting bilayers chosen for their very sharp superconducting transitions. A set of test TES devices were fabricated to characterise the suitability of the superconducting transition of the deposited bilayer structures; the results of these characterisation measurements are provided in Section 7.4.

7.2 Electron Absorption Measurements

7.2.1 Candidate Materials

In order to begin designing the electron absorber, the first question that had to be answered was the choice of absorber material. There is an enormous scope of possible materials and so I created a list of requirements that must be met for the material to be appropriate for TES electron absorption. These material requirements are

- Electrical conductivity at cryogenic temperatures

- High thermal conductance to the superconducting film
- Display minimal electron absorption energy loss for incident electron energies up to 2 keV
- Compatible with existing TES fabrication methods

The material must be electrically conductive at cryogenic temperatures to prevent the absorber charging and decelerating subsequent electrons. This requirement limits the choice of candidate materials to metals and superconductors as the charge carriers in semiconductors are typically frozen out at cryogenic temperatures.

The electron absorbing structure must have high thermal conductances to the superconducting film to optimise the response time and energy resolution of the detector as well as to minimise differences in TES response to absorption events in different locations on the absorber. Superconductors cooled to below their transition temperature display poor thermal conductivity and so are less suitable than metals, though the low thermal conductivities can be mitigated by depositing a thin film of superconducting material on a metallic layer designed for fast thermalisation.

The primary electron energy loss mechanisms are backscattered and secondary electron emission. As a general rule, electron scattering cross-sections increase with atomic mass, thereby increasing the probability of backscattered or secondary electron emission. Therefore, the requirement of minimal energy loss confines the choice of candidate materials to low atomic mass elements.

The final requirement that the material be compatible with existing TES fabrication methods is a practical requirement as creating and testing a new fabrication route for an untested material is beyond the scope of this project.

In summary, the choice of candidate materials is limited to a metallic or possible superconducting material with low atomic mass elements that have previously been used within TES fabrication. This list of materials is exceedingly short, largely due to the final requirement, with titanium and aluminium being primary candidates. Niobium is also an acceptable material to test despite not being a low atomic mass element. Thin films of these three materials were deposited for electron absorption testing, as described in the following section.

In addition to aluminium, titanium and niobium, four more materials were chosen for testing. Gold was selected as it is a high atomic mass element and so acts as a comparison to other materials. Additionally, gold was the surface element in the Mo/Au TESs used in Section 5 and so these the electron absorption properties of gold are highly relevant to interpreting those measurements.

Carbon is the lowest atomic mass, practically usable solid with metallic properties and so was tested as it is expected to be the ideal absorber material. Carbon-based materials have not been used with TESs to my knowledge and therefore developing TESs based upon this material choice is not practical within this project. However, understanding the potential benefit of carbon absorbers is important to understand the outlook for TES electron measurement and for this reason, highly-oriented pyrolytic graphite (HOPG) and carbon nanotube forests were selected for testing. HOPG is an exceedingly pure, crystalline form of graphite and so provides the baseline with regards to graphitic carbon electron absorption properties. Carbon nanotube forests are of interest as their geometry allows for trapping electrons, reducing the probability of escape of primary or secondary electrons.

The final material selected for testing was titanium nitride. Titanium nitride was selected as it would be superconducting at the TES operating temperature, fulfilling the electrical conductivity requirements, and consists of low atomic mass elements. In addition, titanium nitride is not susceptible to oxidation changing the absorption properties of the surface, unlike elemental aluminium or titanium films.

200 nm films of niobium, gold, and titanium were deposited onto silicon substrates and tested whereas a bulk piece of HOPG was measured. The depositions were performed by the Quantum Sensors Group with experience with TES fabrication and so the deposited films are comparable with those to be used in completed TESs. Due to time constraints, aluminium, carbon nanotube forests and titanium nitride were not able to be tested.

7.2.2 Absorption Efficiency Measurement Apparatus

When considering electron absorption efficiency, it is first important to distinguish between particle absorption efficiency and energy absorption efficiency. It is entirely possible for an electron to enter the absorber, deposit a portion of its kinetic energy and then escape. As such, the energy absorption efficiency and particle absorption efficiency are related properties but not equivalent, and must be considered separately. The ideal method to determine both efficiencies would be to measure the entire electron energy spectrum emitted at all angles but performing this measurement would be highly impractical for the purposes of this project. Measuring net particle absorption efficiency alone can easily be performed by measuring the current passing through the absorber given a known beam current, but this gives no indication of the energy losses involved.

A compromise was chosen where the absorbed electrical current by the test sample was monitored, but a portion of energetic information was obtained by biasing the absorber. The absorbed current was measured when unbiased and when positively biased by one and two 9 V batteries. Applying the bias prevents emission of electrons from the absorber with

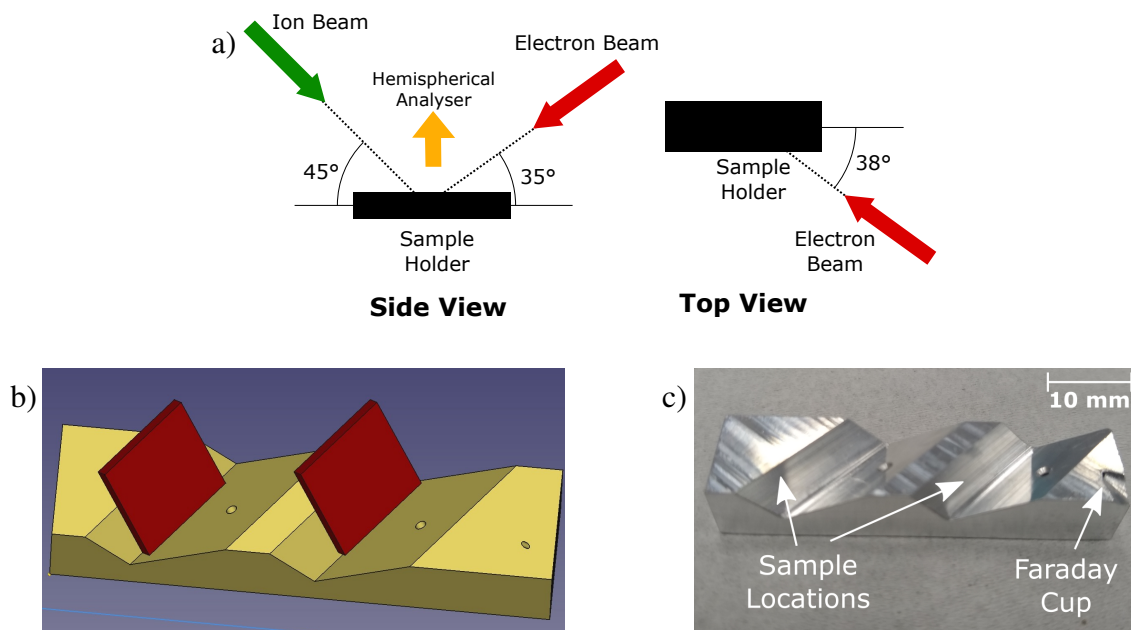


Fig. 7.1 a) X-ray spectrometer (XPS) sample holder geometry relative to incident electron and argon ion beams. b) 3D model and c) photograph of the aluminium sample holder designed to position two samples normal to the incident electron beam. The positions of the samples are shown by the red squares in (b), these samples were held in place by clamps screwed into the sample holder.

energies less than 9 eV and 18 eV energies. Comparing the absorption efficiencies at different biases reveals the relative proportions of low-energy emitted electrons. For simplicity of representation, the applied biases will be labelled as 0 V, 9 V and 18 V but in reality, the battery voltages were observed to drop across the measurements from 9.6 V and 19.2 V to 9.3 V and 16 V for the final measurements and so there is a significant variation of bias within the measurement set. It should be also noted that because the sample holder and samples were always kept in electrical contact, biasing the sample also biased the surrounding sample holder.

The material absorption efficiencies were measured at the National Physical Laboratory (NPL) using an Kratos Axis Ultra DLD X-ray Photoelectron Spectrometer. The instrument contained an argon ion sputter gun that can be used to clean the sample surface of contaminants and an electron beam to perform the absorption measurements. The drain current absorbed by the sample was measured using a Keithley 485 picoammeter.

Fig. 7.1a shows the relative position of the sample holder within the XPS instrument to the ion and electron beams. The incident electron beam was not normal to the sample surface when using the pre-existing flat sample holder. Therefore, I designed an custom aluminium sample holder to position multiple samples normal to the electron beam that was compatible

with the instrument. The 3D model of this sample holder is shown in Fig. 7.1b with two samples shown in position. The samples were held in place using aluminium clamps screwed into the sample holder. A Faraday cup was also included in the sample holder by drilling a narrow hole into the sample holder. The beam diameter was significantly smaller than the hole width and so the entire beam could easily be aimed into the cup. The Faraday cup was necessary as electron beam current would drift over time and vary across days, and so by aiming the electron beam at this cup, the total beam current was measured, *in-situ*.

When characterising an absorber, the material was first cleaned using the sputter gun. However, the sputter gun could not be used when the sample was in the custom holder due to the position of the ion gun and so the sample had to be laid flat and sputter cleaned. The sample was then repositioned onto the holder in atmosphere before being measured. As such, this procedure did not eliminate oxidised surfaces. The HOPG sample was not sputter-cleaned but was instead prepared by removing the top layer of graphite using tape, leaving a fully-cleaved top layer.

For each absorption measurement, the beam was first aimed at the Faraday cup and measured for 30 seconds, the beam was then repositioned to a sample material and held for at least 30 seconds before returning to the Faraday cup. This process was repeated for each measurement with the current recorded throughout. The measured currents are attributed to the absorber material but it should be noted that any electrons that escape the absorber and are collected by the sample holder would also be measured in the current and so there is a systematic overestimate inherent in the measurement procedure. As this overestimate is systematic across all measurements, it does not affect the process of identifying a suitable absorber material.

7.2.3 Absorption Efficiency Results

Fig. 7.2 plots a selection of current measurements of the Faraday cup (FC) and different absorber materials over time, when unbiased or biased using both batteries. The measurement shows a dramatic improvement in absorption by applying the positive bias. This change in current was not observed with the Faraday cup but the current did change from -10.0 nA to -10.2 nA indicating that the cup did not absorb the entirety of the beam when unbiased.

Fig. 7.3 shows the distribution of drain currents measured through the Faraday cup at different applied biases and beam energies. Each datapoint was obtained by averaging the current for the duration of the measurement. At each beam energy, the measured current was observed to change by 1-2% when applying a 9 V bias. However, increasing the bias further resulted in no significant change in current. Therefore, the majority of electrons reabsorbed by applying a bias had energies under 9 eV, though electrons that escape with over 18 eV

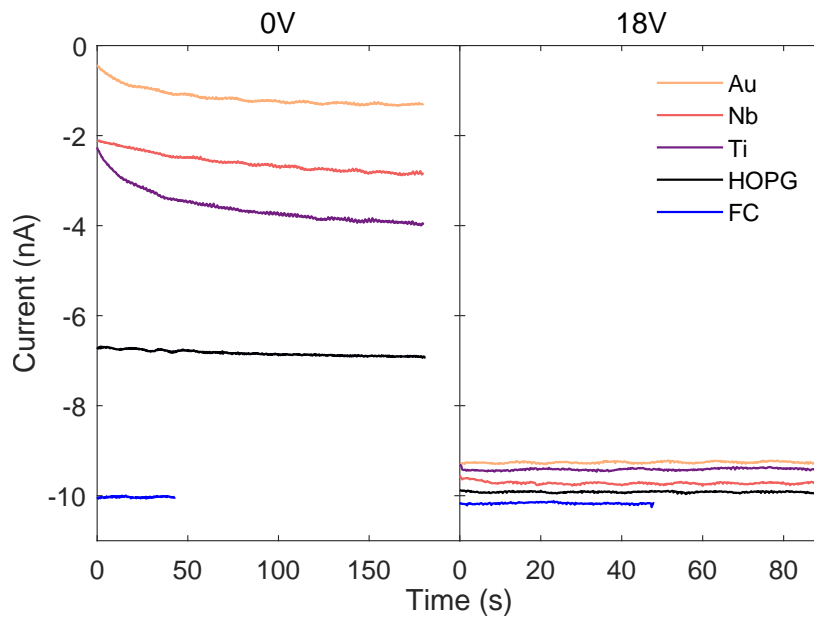


Fig. 7.2 Absolute drain currents measured from 2.0 keV electron beams on gold (Au), niobium (Nb), titanium (Ti), highly-oriented pyrolytic graphite (HOPG) and the Faraday cup (FC). These measurements were taken with zero applied bias to the sample holder (left) and with 2×9 V batteries (right).

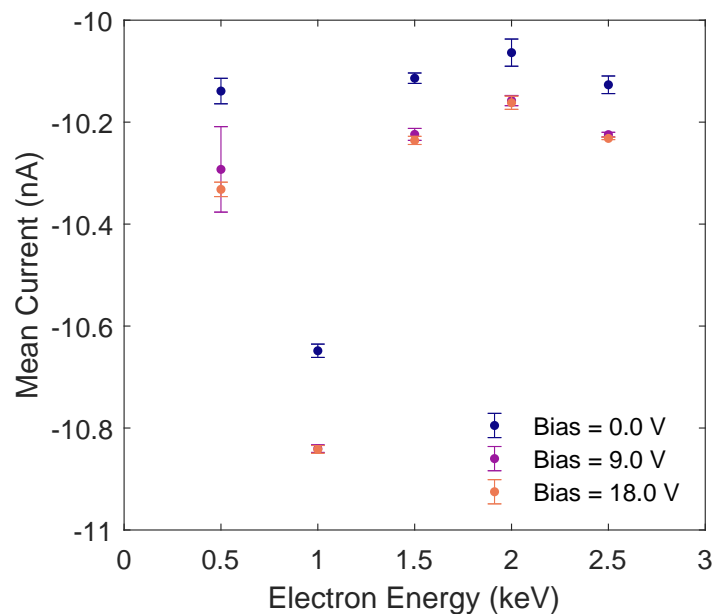


Fig. 7.3 Mean drain currents measured in the Faraday cup at varied electron energies and sample holder biases. The error bars denote one standard deviation range across multiple measurements.

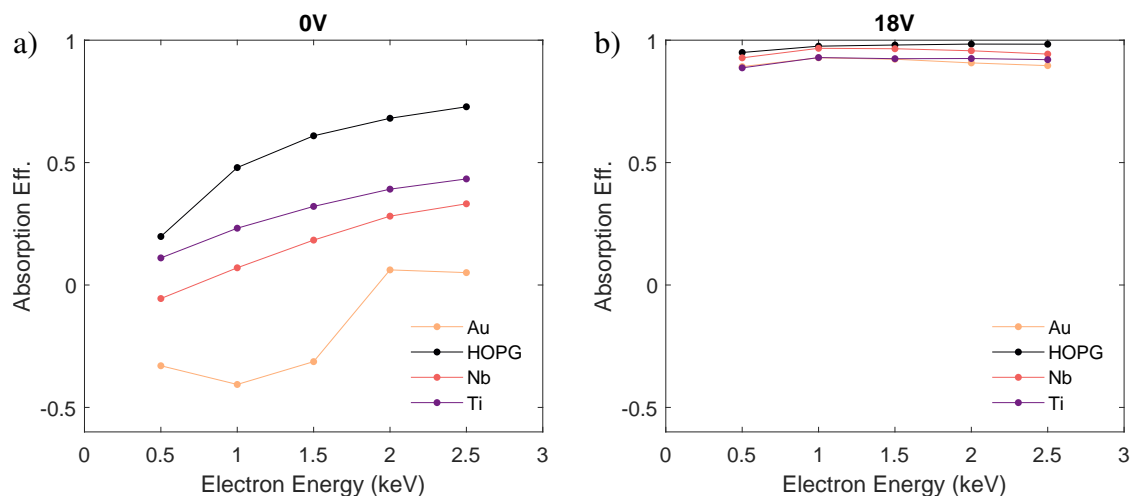


Fig. 7.4 Relative electron absorption efficiencies measured relative to the Faraday cup for different sample materials with the sample holder a) unbiased and b) biased using 2×9 V batteries.

energy would not be observed. For conciseness, the following absorption measurements will assume complete electron beam absorption by the Faraday cup and the measured currents absorbed by the samples will be normalised relative to the closest Faraday cup measurement in time.

A summary of the measured absorption efficiencies across various electron energies and materials is shown in Fig. 7.4. Each measurement shows the averaged drain current through the absorber after the current reached equilibrium. Negative absorption efficiencies show that the rate of secondary electron losses was greater than the electron absorption rate and so the net current through the sample holder was reversed.

Fig. 7.5 shows the effect of the applied bias upon each chosen absorber material. As expected, the graphite sample displayed the best absorption with titanium and niobium performing similarly well and gold being the poorest. However, these measurements also show that the ability to put a 20 V bias on the absorber dramatically improves the measurement efficiency across all energies tested and makes the choice of material far less important. Each material displayed over 90% particle absorption efficiency when biased, with HOPG showing 97% efficiency.

These measurements experimentally demonstrate that electron absorption efficiency is a vital factor to consider in electron calorimetric TESs. Of the materials tested, graphite is the ideal candidate absorber for the designed electron-detecting TESs but integrating a graphitic film into the TES would require developing and testing new TES processing routes. The electron absorption measurements show that using niobium or titanium would provide lesser

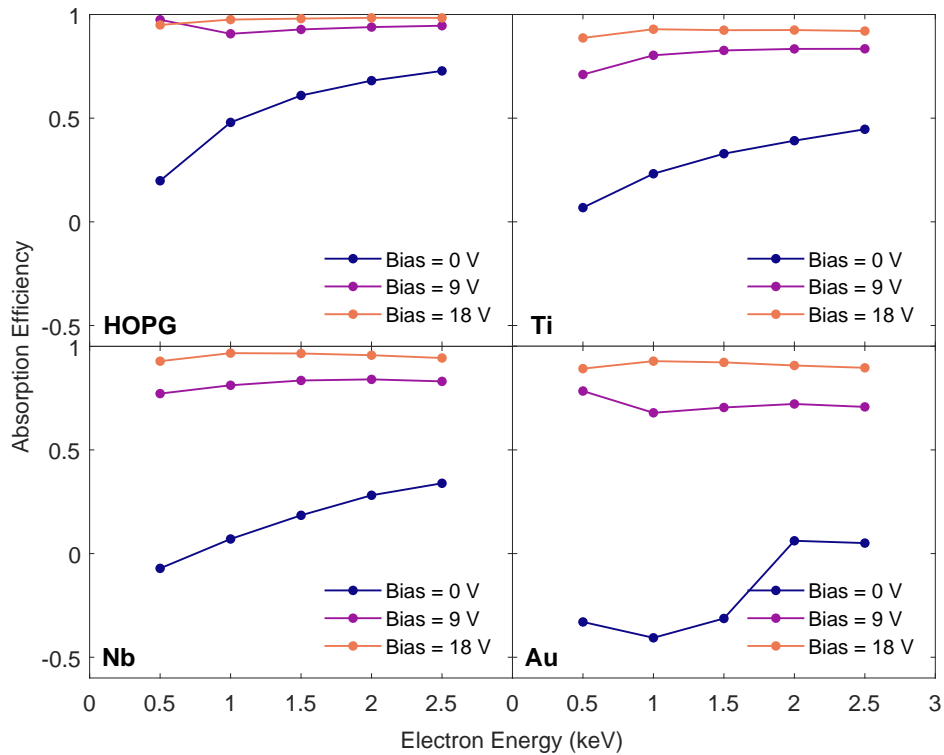


Fig. 7.5 Relative electron absorption efficiencies separated by absorber material.

but acceptable absorption efficiencies with the advantage that these materials are already compatible with existing TES fabrication methods. Titanium was chosen as the absorber material to proceed with, for these reasons.

7.3 TES Design

The aim for this first generation of bespoke TES electron spectrometers was to design a device capable of efficient electron absorption and high resolution energy measurement. These devices can then provide a platform to be improved upon in future device iterations, with the goal of meeting the device requirements laid out in Chapter 3.

Ti/Au bilayers were selected for the superconducting films with a target transition temperature of 200 mK, compatible with the 100 mK base temperature of the cryostat to be used alongside a dedicated titanium absorber electron absorber. Ti/Au bilayers have the likely advantage of sharper superconducting transitions over Mo/Au bilayers, represented by values of α around 100 compared to 20-30 for the Mo/Au devices used in Chapter 4 [112, 77]. Greater values of α provide improved energy resolution and response times due to more efficient electrothermal feedback. Ti/Au bilayers are an established material system for TESs

making it an excellent choice for these calorimeters. One disadvantage of these bilayers is the gold layer being the top-most layer of the device and so exposed to incident electrons. It is possible to invert the layers to provide Au/Ti devices and expose the titanium layer but fabrication of this bilayer would require additional testing for little benefit for these early devices.

The use of a bilayer superconductor is necessary to be able to control the transition temperature (T_c) of the superconductor through the proximity effect. The proximity effect arises when a superconductor is in contact with a second material, either non-superconducting or a superconductor with a lower T_c . In either scenario, Cooper pairs can diffuse a finite distance across the interface into the second material. This distance is characterised by the superconducting coherence length, typically on the order of tens or hundreds of nanometres, depending on the material [113]. The effect of this diffusion is to create a region of weakened superconductivity in the first material with suppressed transition temperature and a region with superconducting properties in the second material. In the case of a thin-film bilayer where the layer thicknesses are less than or comparable to the coherence lengths, the bilayer behaves like a uniform material with a T_c between the transition temperatures of the component layers (0 K for non-superconductors). The precise value of T_c for the entire bilayer can be tuned by adjusting the relative layer thicknesses of two layers. For the Ti/Au bilayer devices, TES layer thicknesses of 55 nm of Ti and 240 nm of Au were chosen. These layer thicknesses were calculated from the Usadel equations [114] and previous device testing, both performed by the Quantum Sensors Group to provide in a fully superconducting bilayer with a T_c of 200 mK. The initial bilayer areas were designed to be $50 \times 50 \mu\text{m}$ to provide stable devices with 50 m Ω normal state resistances.

As discussed in Section 7.2, the ability to bias the absorber can enormously improve electron absorption efficiency. As such, these devices were designed with separate absorbers, electrically isolated from the superconducting bilayer. The chosen electron absorber material was titanium but a pure titanium absorber would be problematic as titanium has a superconducting transition temperature of 390 mK. The heat capacity of a superconductor falls exponentially with temperature below the transition temperatures and so at 200 mK the absorber would contribute little to the total heat capacity of the device. This heat capacity determines the device's saturation energy and so using a pure Ti absorber would require a far more massive device than if a normal metal absorber was used. Therefore, a Au/Ti bilayer was selected for the absorber, with the gold providing the heat capacity and the titanium providing electron absorption efficiency. However, Au/Ti bilayers display the same proximity effect used in the Ti/Au bilayer to control T_c . Therefore, when determining the layer thicknesses of Au and Ti in the absorber, an additional consideration was choosing

Table 7.1 Layer thickness of device components. The ordering of elements in the superconducting bilayer and absorber represent the order of deposition in these structures with the first element being at the bottom.

	Layer Thickness (nm)	
Superconducting Bilayer	Ti	55
	Au	240
Absorber	Au	300
	Ti	65
Interconnects	Al	300
	Ti	200
Wiring	Nb	150
Substrate Membrane	Si_xN_y	200

layer thicknesses that ensure the absorber remains in its normal state when the TES bilayer is at its transition temperature. The chosen thicknesses were 65 nm of Ti with 300 nm of gold beneath. A table of layer thicknesses is provided in Table 7.1 as well as a cross-sectional view of an example TES design in Fig. 7.6.

With the absorber thicknesses and TES geometry chosen, the absorber areas were adjusted to provide the desired heat capacities. These heat capacities were chosen to span a range of saturation energies between 1 and 7 keV, with the low saturation energy devices displaying improved energy resolutions and non-linear energy dependence, and the larger devices being highly linear.

The initial device designs planned to use superconducting niobium leads in direct contact to both the TESs and absorbers, but Ti/Au TESs fabricated as part of a different project within the Quantum Sensors Group found that the direct TES to niobium contact resulted in inconsistent, broadened transitions with varying transition temperatures. Therefore, that project implemented titanium and aluminium interconnecting wires between the niobium and TESs with the hypothesis being that these interconnects prevent hydrogen diffusing from the niobium to the TES during fabrication, and altering the TES superconducting transition. The modifications were successful at preserving the TES transition and so I incorporated these contact designs for the electron calorimeters. However, introducing titanium and aluminium connections into the mask design raised concerns of forming superconducting regions of low critical current, of the order of several microamps, in the interconnects. The resistance-temperature dependence of a TES is the central aspect of the detector and so

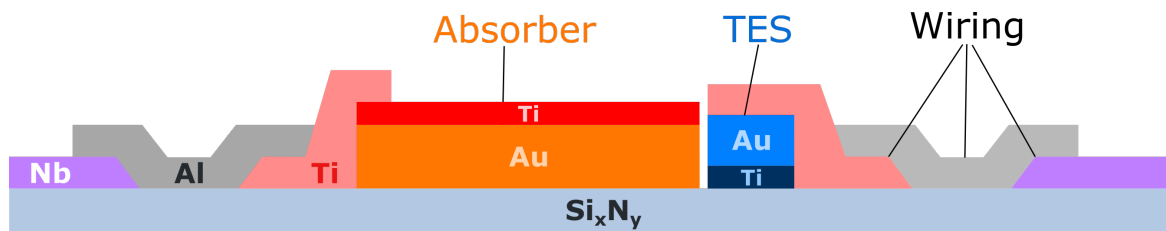


Fig. 7.6 Simplified cross-section view of an example device showing device layers and electrical contacts to the TES and absorber.

should not be overlapped by secondary effects such as the resistance changes from partially superconducting contacts. As the critical currents of the interconnects were predicted to be comparable with the operating current of the $50 \times 50 \mu\text{m}$ TES, a range of TES bilayer lengths were designed with dimensions of $50 \times 50 \mu\text{m}$, $100 \times 50 \mu\text{m}$ and $150 \times 50 \mu\text{m}$, thereby providing a range of devices with smaller operating currents.

The absorber and TES geometries were combined in multiple different combinations; a selection of the resulting device designs are shown in Fig. 7.7 spanning the range of TES and absorber sizes. The figure shows regions of multiple lithographic masks, drawn in KLayout defining the device layers. As with the previously tested Mo/Au devices, these TESs were designed to be suspended on four silicon nitride legs, all of $300 \mu\text{m}$ length with widths of 1.5 , 2.5 , 3.5 and $5 \mu\text{m}$ and 200nm thickness. High-aspect ratio silicon nitride legs reduce the dimensionality of the thermal conductance between the TES and bath, improving the TES energy resolution. The leg widths and lengths were chosen to provide a range of TES response times in the millisecond range.

An important aspect of the device design is the absorber being beside the superconducting film without electrical connection between the two. A consequence of this is that thermal conduction between the two structures is wholly dependent on diffusion through the substrate. The conductive link was therefore improved by partially wrapping the absorber around the superconducting film as visible in Fig. 7.7. Additionally, the gap between the absorber and superconductor was set at $5 \mu\text{m}$ in width to keep the diffusion length in the membrane as short as possible without risking any electrical contact due to alignment errors during fabrication.

A 3D model of a complete device is provided in Fig. 7.8 with the overlapping contact regions shown. The vertical thicknesses of the thin films have been enlarged for clarity.

Six separate device chips were defined on the lithographic masks with 16 devices for each chip. Two of these chips are shown in Fig. 7.9, following the same colour scheme as Fig. 7.7. On each chip, two devices were replaced with only absorber pads as controls in cases where direct current measurement of the incident electron beam through a large absorber is needed. Additionally, pads of the TES bilayer, absorber bilayer, niobium, aluminium and

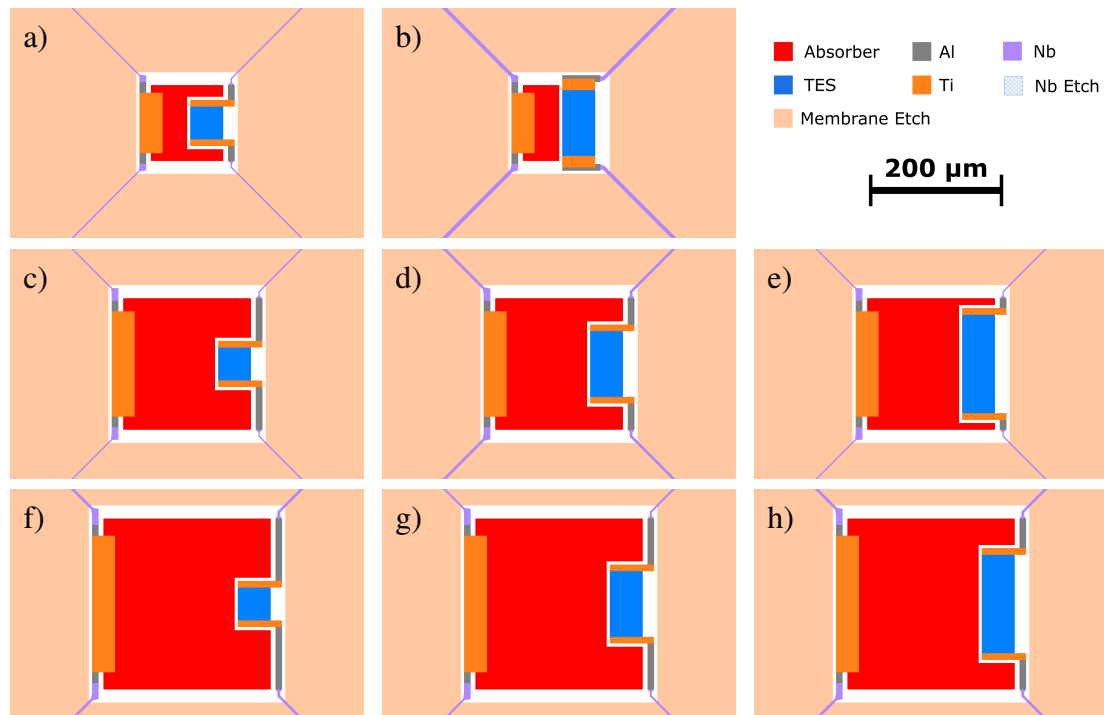


Fig. 7.7 Mask drawings of several TES device designs with increasing TES length, horizontally, and increasing absorber area, vertically. The imaged devices correspond to the following device IDs in Table 7.2: a) A4, b) D4, c) L8, d) L6, e) L3, f) B4, g) G4, h) J3.

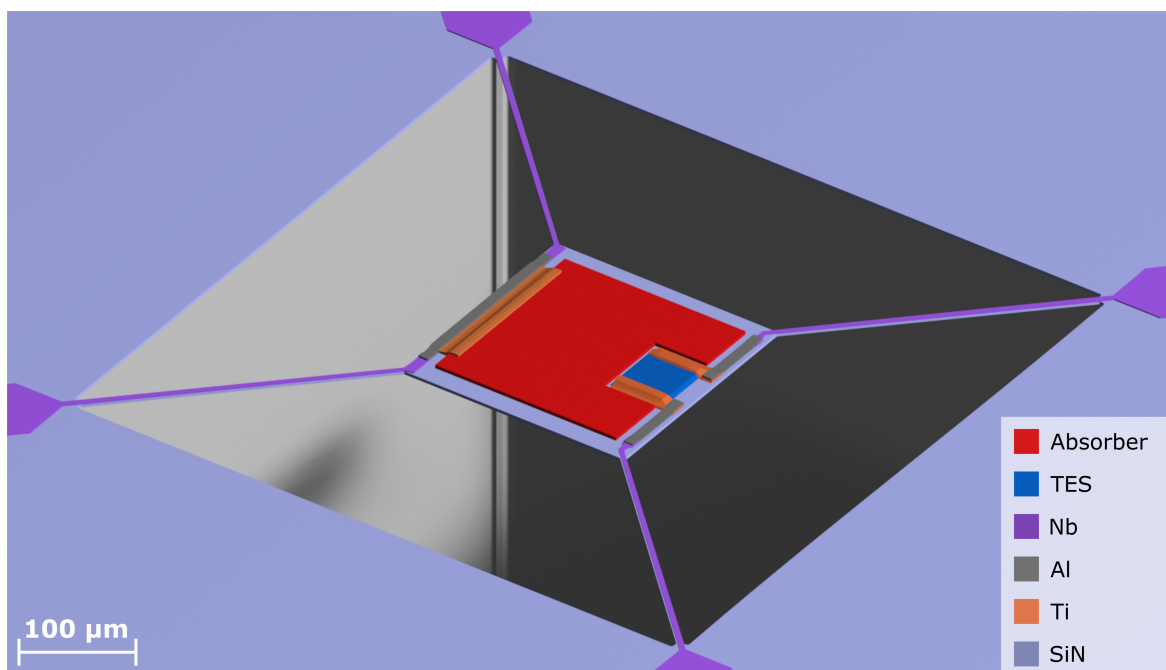


Fig. 7.8 3D model of a designed electron calorimeter TES. The vertical-scale has been increased to show the ordering and overlap of the contact layers.

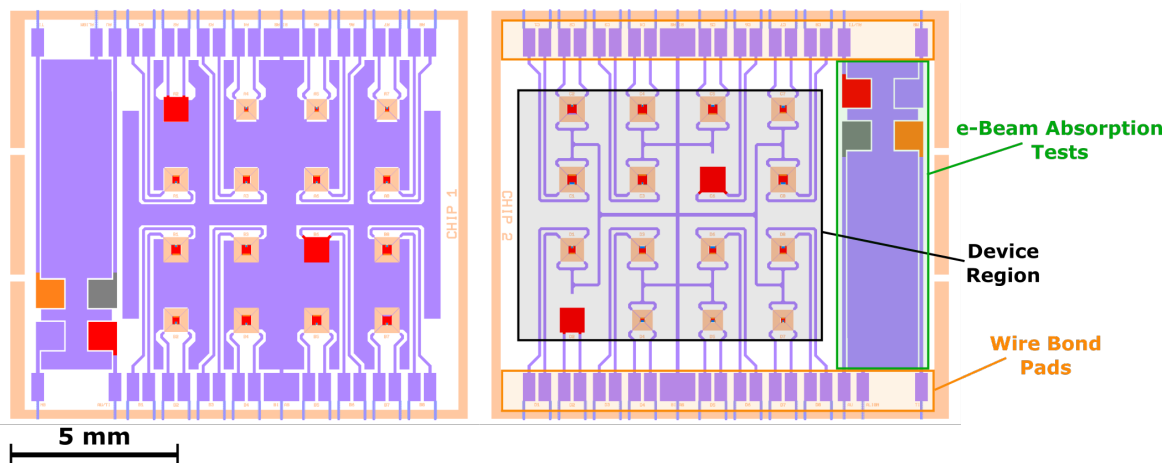


Fig. 7.9 Mask drawings of Chip 1 (left) with the Nb grounding layer and Chip 2 without this layer. The colour scheme of this figure follows Fig. 7.7.

titanium were all deposited on each chip with individual wire-bond connections available to each pad. These structures allow for easier identification of the electron beam position by measuring the current passing through each structure but also allow for *in-situ* electron absorption measurements for each material in a similar manner to Fig. 4.12. Half of the chips have niobium grounding layers covering the majority of the silicon nitride to compare any observable effects of the silicon nitride charging over time. Every absorber, and the grounding layer when present, are connected together with a pair of redundant bond pads present and so all of the absorbers would be biased and grounded together. From the results of Chapter 6, measuring the TES sensitivity to applied electric fields with and without the niobium grounding layer would be of interest to assess the presence of any capacitive coupling. Fig. 7.10 shows the finalised layout of the entire chip with test structures surrounding the device chips.

The table of the complete list of devices with predicted device properties is given at the end of this chapter in Table 7.2. These predictions were calculated for the transition temperature observed for fabricated test devices of 250 mK. The devices have also been separated by chip, as shown by different sections within the table. The devices were designed as combinations of three absorber sizes, three TES lengths and four Si_xN_y leg widths.

Fabrication of these devices using these masks was performed entirely by members of the group with extensive experience fabricating TESs. These devices were fabricated on 2-inch silicon wafers coated with 200 nm of Si_xN_y . The TES and absorber bilayers as well as the Nb, Ti and Al wiring were patterned using image-reversal lithography and deposited using DC magnetron sputtering physical vapour deposition. Reactive-ion etching (RIE) was

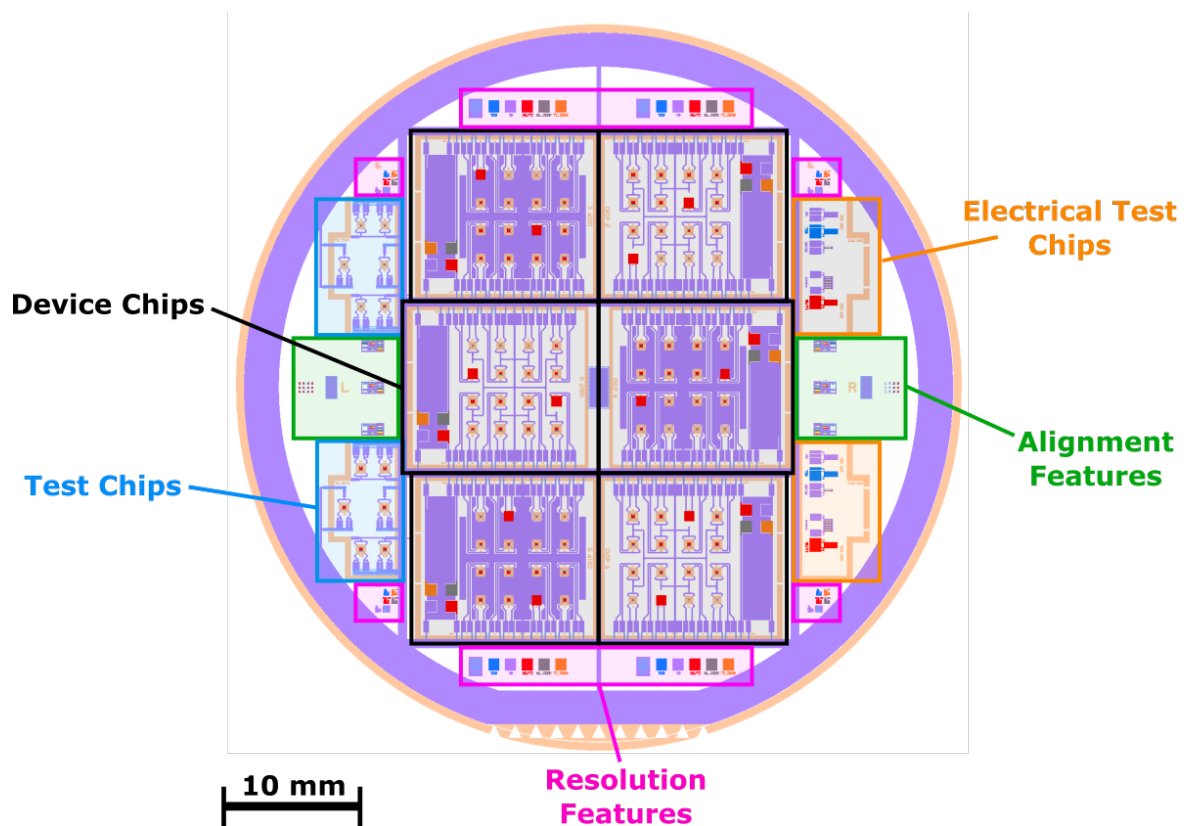


Fig. 7.10 Mask drawings of the full 2-inch wafer showing the six device chips surrounded by a set of resolution and test features including two test chips. Each test chip contains 3 completed devices and 3 devices not suspended but on the bulk substrate.

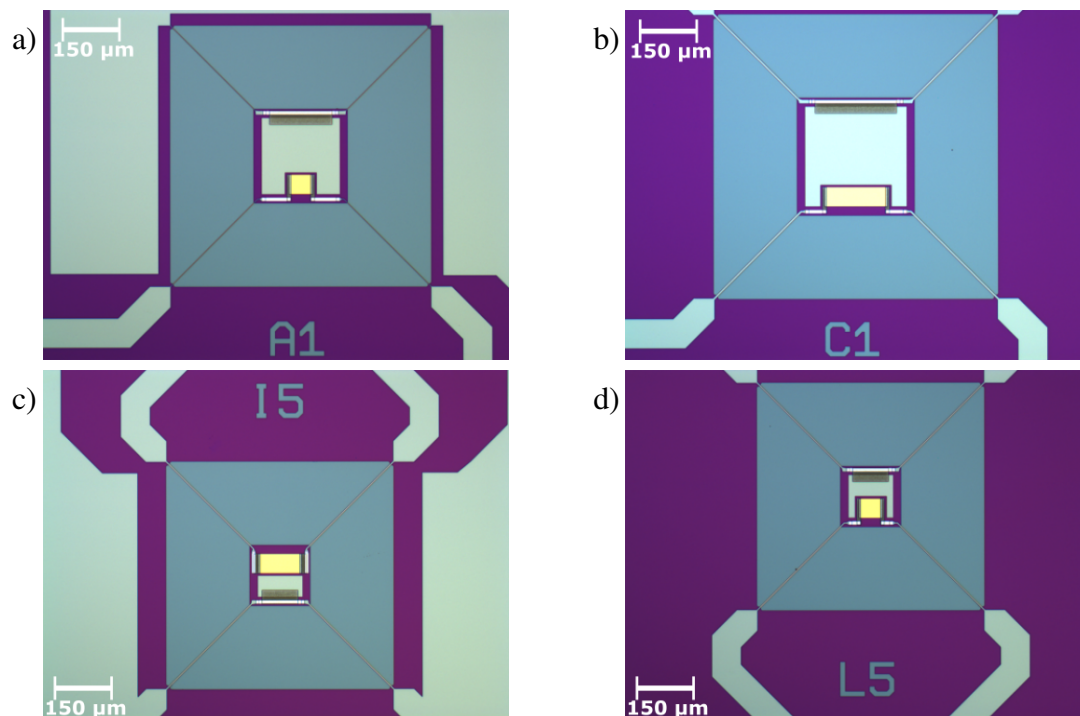


Fig. 7.11 Microscope images of partially processed devices prior to deep reactive-ion etching.

used to define the Si_xN_y with the substrate removal performed by deep reactive-ion etching (DRIE) from the underside of the wafer.

Microscope images of partially fabricated devices are shown in Fig. 7.11. These images were taken prior to DRIE and so the devices are not suspended at this stage. Unfortunately, this device wafer failed at the DRIE step, after which the device islands all detached from the chip. This failure mechanism is highly unusual, having not been before within the group, even when using far narrower and longer leg geometries. The specific cause is not currently known though over-etching is the likely reason. Two back-up wafers are currently partially fabricated.

Despite the failure of the initial device wafer, three devices on each test chip (see Fig. 7.10) were designed to not be suspended on these legs and so survived DRIE. These test devices have considerably larger thermal conductances than the suspended devices and cannot be used as detectors but the TES superconducting transition of these devices can be characterised. The results of these measurements are provided in Section 7.4.

Alongside the devices, the TES module for mounting the detector and SQUID chip was designed and built. Photographs of the module are shown in Fig. 7.12. One of the six device chips would be clamped in the centre of Fig. 7.12a with the lid placed above. The SQUID chip would be mounted in behind in Fig. 7.12b. The lid of the module contained a recessed

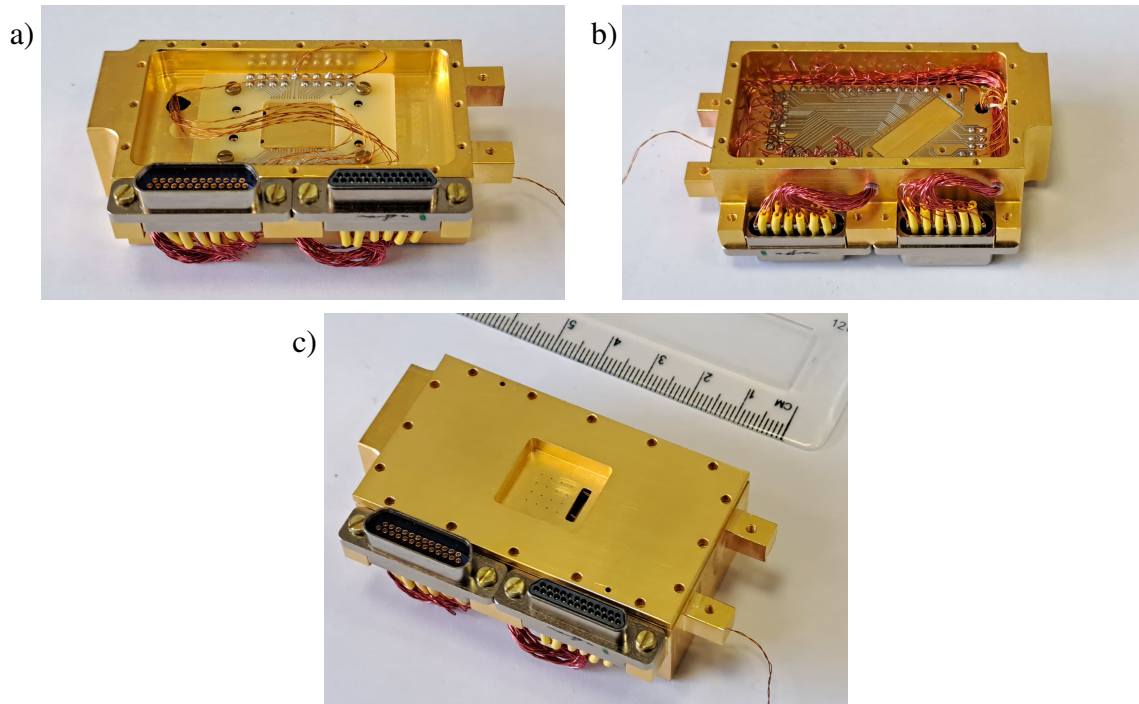


Fig. 7.12 Photographs of a) the top and b) the bottom of the gold-plated device module for mounting the TES and SQUID chips. c) shows the top of the module with the lid in place.

portion with a set of $200\ \mu\text{m}$ apertures aligned to the individual devices. The slot to the side of the aperture array is for the beam absorption test region on each chip. The apertures were recessed to minimise distance from the apertures to the TES to localise incident electrons as closely as possible to the devices. There is also the option to place an electrically insulating insert between the lid and the rest of the module allowing a bias to be applied to the lid to screen low energy electrons.

7.4 R-T Characterisation

I performed two sets of resistance-temperature measurements on electron calorimetric test devices, one on a set of superconducting bilayers made prior to full wafer fabrication to ensure the TESs function correctly with the additional contacts. The other set of measurements was performed on the test devices from the fully processed wafer that were not suspended by the DRIE step. These two sets will be referred to as the ‘Initial’ and ‘Test Chip’ devices.

The resistance measurements were performed in a three-stage pulse tube cooler, sorption cooler and dilution refrigerator capable of reaching base temperatures below 100 mK. Resistance measurements were performed while both cooling and warming the devices.

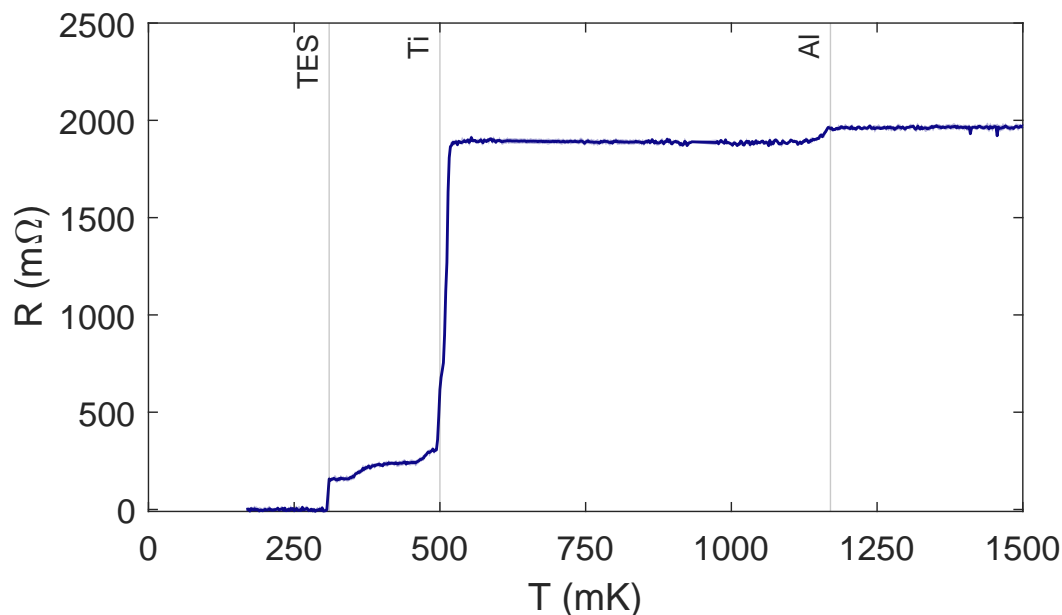


Fig. 7.13 Resistance-temperature dependence of a 150 mΩ TES with labelled transitions.

Fig. 7.13 plots the measured resistances whilst cooling a 100 mΩ device, from the initial set of devices with 0.3 μA of current passing through the bilayer. Superconducting transitions of the titanium and aluminium wires can be seen prior to the TES transition at 310 mK. A few extra nanometres of titanium were deposited on these devices during fabrication resulting in the increased TES transition temperature of 310 mK. Additional intermediate transitions were observed between the TES and Ti transitions; these are likely occurring in the contact region between the TES and the Ti wiring.

The resistance-temperature dependence of three devices in this set are provided in Fig. 7.14. In these figures, both the cooling and warming current measurements are provided. The measured TES resistances for each device was in very good agreement with the predictions of 50, 100 and 150 mΩ, and no hysteresis was observed at any applied current. In all instances, the intermediate transition critical temperatures reduce with increasing current. However, for the 50 mΩ device, these transitions occurred at a significantly lower temperature than the other devices; the cause for this difference is not apparent from these measurements alone.

The result of these initial checks is that the TES transition with the modified contacts remained consistent and sharp, and if produced closer to the target temperature, should be the lowest temperature transition in the device at applied currents up to 10 μA . This prediction was verified by the test chip devices produced from the full wafer (Fig. 7.15). These devices did not have the excess titanium thickness in the bilayer for the initial devices

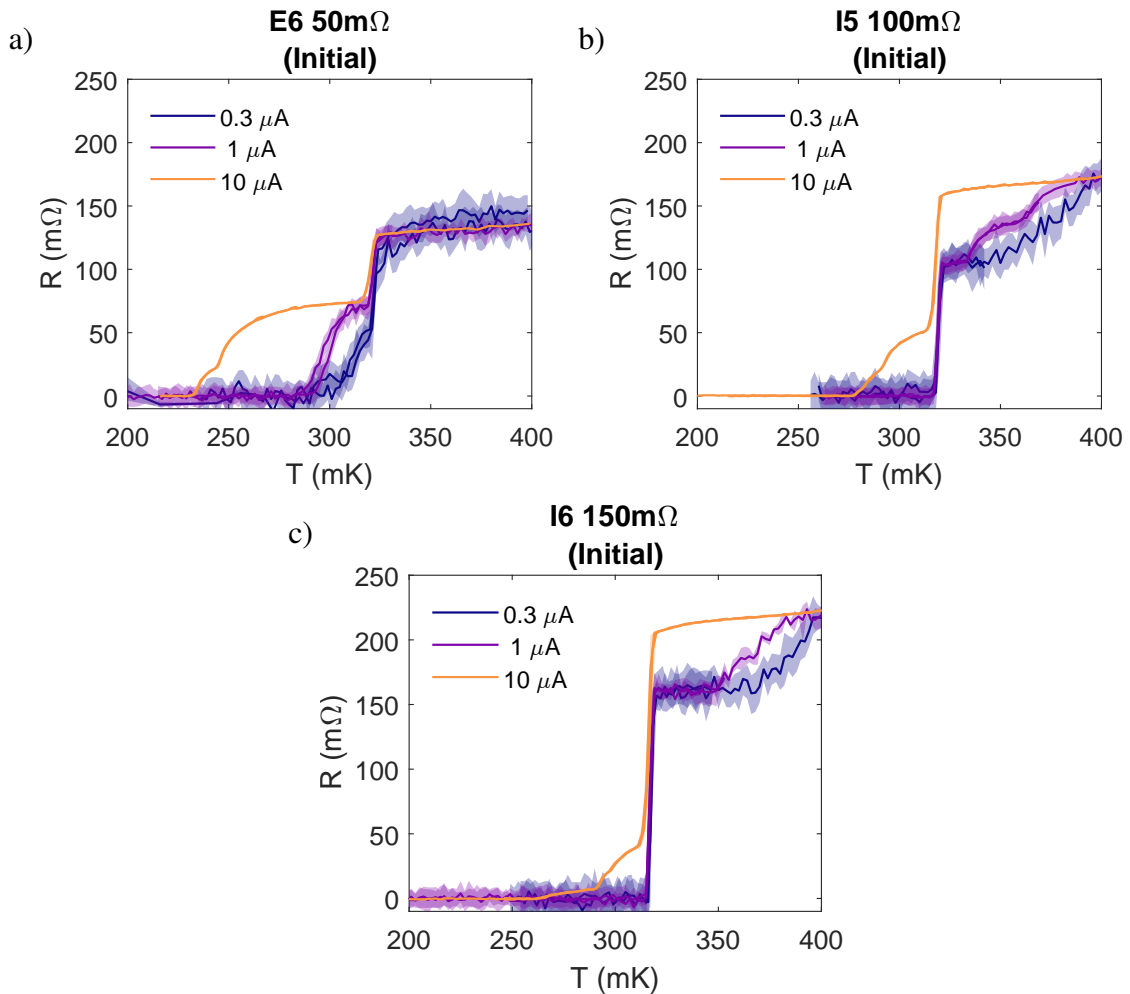


Fig. 7.14 Resistance-temperature measurements of three TES bilayers with a) 50 mΩ , b) 100 mΩ and c) 150 mΩ resistances and different applied currents. Each set of measurements shows the resistances measured during heating and cooling. The shaded areas show the data between the 10th and 90th percentiles within 2 mK of the measurement.

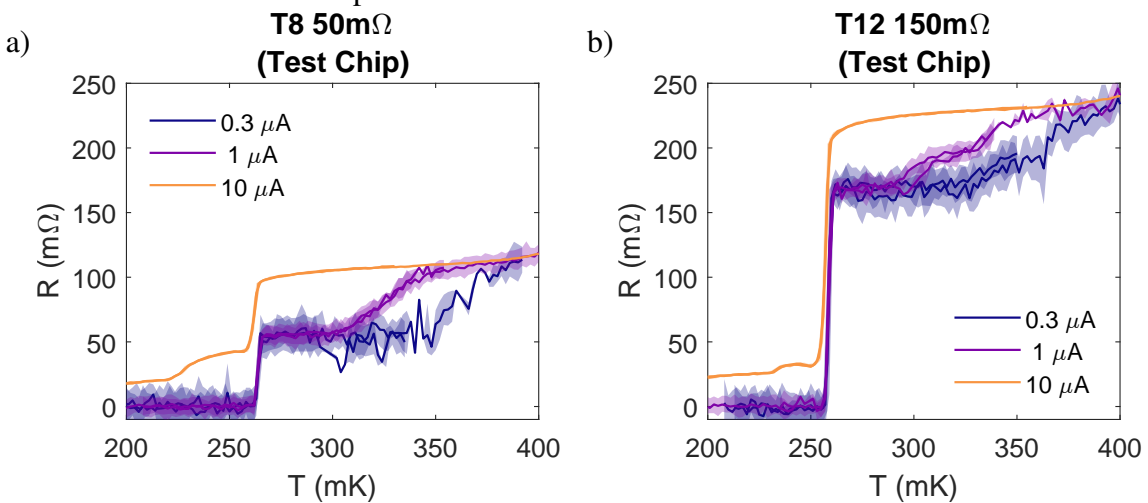


Fig. 7.15 The same measurements as in Fig. 7.14 taken for two devices from the test chips in fully processed wafer.

and so displayed reduced TES transition temperatures of 250 mK. At currents below $10 \mu\text{A}$, the test chip devices showed excellent superconducting transitions.

Fig. 7.16 collates the measurements from the initial and test chip devices for comparison. Included in these plots are measurements from a pair of devices from the initial set having undergone heat treatment. This heat treatment involved heating to 115°C in atmosphere for 1 hour to mimic the high temperature limit experienced by the devices during fabrication.

There is some variability between the transitions in this figure but in each set of devices, the TES transition remained consistent and narrow, and the effect of heat treatment appears to reduce the TES transition temperature by around 5 mK. It is difficult to assign explanations to the variations in the intermediate transitions with this limited dataset but the results of these measurements are encouraging when considering the use of this bilayer geometry for TES electron calorimetry. The intermediate transitions do not appear to be linked to the TES transition temperature and occur at temperatures above the TES transition temperature when using currents of $1 \mu\text{A}$ or below.

7.5 Conclusion

This chapter has presented the design and development of the first bespoke electron spectroscopy TESs, informed by the detector requirements from Section 3.5 and electron absorption efficiency measurements in Section 7.2. The designed devices span a range of geometries with predicted resolutions spanning from 0.8 to 1.9 eV FWHM at 250 mK and with saturation energies of 1.5 to 7.2 keV, shown in Table 7.2. The range of saturation energies allows for investigation into both the linear and non-linear response behaviour of the TES to electrons of different energies as being able to accurately identify electron energies in the non-linear response range near the TES saturation energy is an important aspect of optimising TES performance.

The materials selected for these electron-detecting TESs are expected to provide significant improvement over the Mo/Au TESs tested in Chapter 5. Based upon the measurements in Section 7.4, the Ti/Au TESs are predicted to have sharper superconducting transitions than the Mo/Au TESs and therefore display more efficient electrothermal feedback. The Au/Ti absorber will also display greatly improved electron absorption efficiency as shown by the difference in absorption efficiency measured between titanium and gold in Section 7.2.

The ability to independently bias the absorber in the TESs presented here is a particularly exciting prospect for TES electron spectroscopy. Measurements from Chapter 6 show that integrating electron optics into a TES is feasible but these devices are the first to practically implement this capability into the device design. Applying a bias to the absorber *in-situ*,

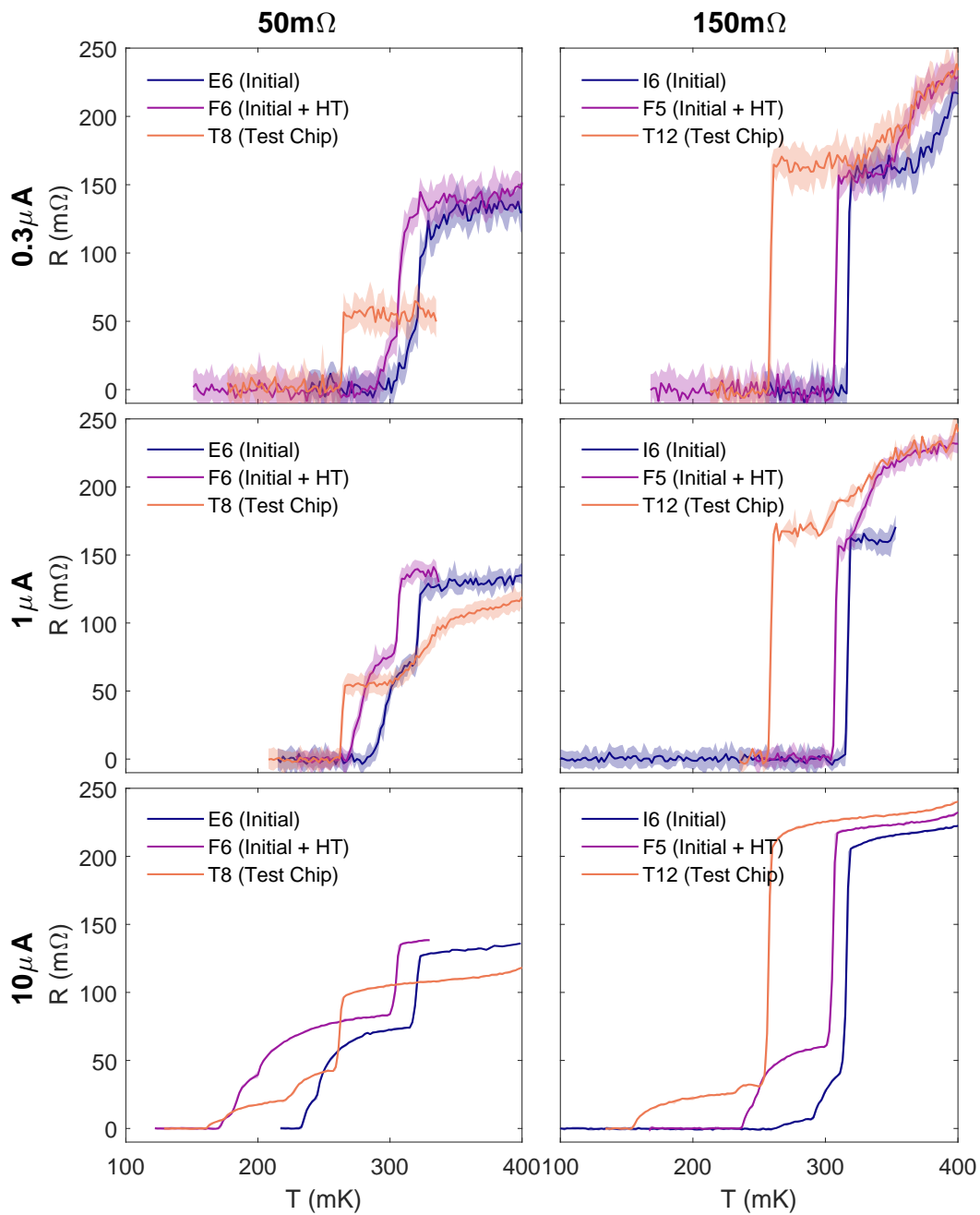


Fig. 7.16 Comparison between resistance-temperature measurements from the initial set of devices, initial devices with heat treatment (HT) and devices from the test chip, separated by TES resistance and applied current. The shading is equivalent to Fig. 7.14 and Fig. 7.15. All measurements were taken while cooling the devices.

would allow for control of the TES-electron interaction, either to enhance or reduce the electron energy absorption efficiency and is a promising tool both in electron measurement but also to any application where interaction between TESs and charged particles can be expected to occur.

An additional area of research would be to incorporate improved electron absorber materials into the TES device design, in particular carbon-based materials. Carbon nanotubes could also prove to be excellent electron absorbers but unfortunately this material, along with titanium nitride and aluminium could not be tested as part of the measurements of Section 7.2 due to COVID-19 lab shutdowns.

Table 7.2 List of designed TESs with predicted properties at 250 mK transition temperature, 100 mK bath temperature. The response times τ_{eff} , saturation energies E_{sat} and energy resolutions ΔE were calculated from the device properties shown assuming $n = 2$ and $\alpha = 100$ in the small-signal limit.

Device ID	Heat Capacity (pJ/K)	Thermal Conductance (pW/K)	TES Resistance (m Ω)	τ_{eff} (ms)	E_{sat} (keV)	ΔE (eV)
A1	0.3	0.5	50	15	4.2	1.4
A2	-	-	-	-	-	-
A3	0.3	1.1	50	6	4.2	1.4
A4	0.1	0.5	50	5	1.5	0.8
A5	0.1	1.1	50	2	1.5	0.8
A6	0.3	1.5	50	4	4.2	1.4
A7	0.1	1.5	50	2	1.5	0.8
A8	0.3	0.5	50	15	4.2	1.4
B1	0.6	0.5	50	25	7.2	1.9
B2	0.3	0.8	50	9	4.2	1.4
B3	0.6	1.1	50	11	7.2	1.9
B4	0.6	0.5	50	25	7.2	1.9
B5	0.6	0.8	50	15	7.2	1.9
B6	-	-	-	-	-	-
B7	0.6	1.5	50	8	7.2	1.9
B8	0.6	1.5	50	8	7.2	1.9
C1	0.6	1.5	150	8	7.2	1.9
C2	0.6	1.5	50	8	7.2	1.9
C3	0.6	1.1	50	11	7.2	1.9
C4	0.6	0.8	50	15	7.2	1.9
C5	0.6	0.5	100	25	7.2	1.9
C6	-	-	-	-	-	-
C7	0.3	0.8	100	9	4.2	1.4
C8	0.6	0.5	150	25	7.2	1.9
D1	0.3	0.5	50	15	4.2	1.4
D2	-	-	-	-	-	-
D3	0.3	1.5	150	4	4.2	1.4
D4	0.1	1.5	100	2	1.5	0.8
D5	0.1	1.5	100	2	1.5	0.8
D6	0.3	1.1	150	6	4.2	1.4
D7	0.1	0.5	50	5	1.5	0.8
D8	0.3	0.5	100	15	4.2	1.4

Device ID	Heat Capacity (pJ/K)	Thermal Conductance (pW/K)	TES Resistance (m Ω)	τ_{eff} (ms)	E_{sat} (keV)	ΔE (eV)
E1	-	-	-	-	-	-
E2	0.1	0.5	100	5	1.5	0.8
E3	0.3	0.5	100	15	4.2	1.4
E4	0.1	1.1	100	2	1.5	0.8
E5	0.1	1.5	50	2	1.5	0.8
E6	0.3	1.1	50	6	4.2	1.4
E7	0.3	0.5	50	15	4.2	1.4
E8	0.3	1.5	100	4	4.2	1.4
F1	0.6	0.5	50	25	7.2	1.9
F2	0.3	0.8	100	9	4.2	1.4
F3	0.6	1.1	100	11	7.2	1.9
F4	0.6	0.5	150	25	7.2	1.9
F5	0.6	0.8	150	15	7.2	1.9
F6	0.6	1.5	50	8	7.2	1.9
F7	0.6	1.5	150	8	7.2	1.9
F8	-	-	-	-	-	-
G1	0.6	1.5	100	8	7.2	1.9
G2	0.6	1.5	100	8	7.2	1.9
G3	0.6	1.1	100	11	7.2	1.9
G4	0.6	0.8	100	15	7.2	1.9
G5	0.6	0.5	100	25	7.2	1.9
G6	0.6	0.5	100	25	7.2	1.9
G7	0.3	0.8	100	9	4.2	1.4
G8	-	-	-	-	-	-
H1	-	-	-	-	-	-
H2	0.3	0.5	100	15	4.2	1.4
H3	0.3	1.5	100	4	4.2	1.4
H4	0.1	1.5	100	2	1.5	0.8
H5	0.1	1.1	100	2	1.5	0.8
H6	0.3	1.1	100	6	4.2	1.4
H7	0.1	0.5	100	5	1.5	0.8
H8	0.3	0.5	100	15	4.2	1.4

Device ID	Heat Capacity (pJ/K)	Thermal Conductance (pW/K)	TES Resistance (m Ω)	τ_{eff} (ms)	E_{sat} (keV)	ΔE (eV)
I1	0.3	0.5	150	15	4.2	1.4
I2	0.1	0.5	100	5	1.5	0.8
I3	0.3	1.1	150	6	4.2	1.4
I4	-	-	-	-	-	-
I5	0.1	1.1	100	2	1.5	0.8
I6	0.3	1.5	150	4	4.2	1.4
I7	0.1	1.5	100	2	1.5	0.8
I8	0.3	0.5	150	15	4.2	1.4
J1	0.6	0.5	150	25	7.2	1.9
J2	0.6	0.5	150	25	7.2	1.9
J3	0.6	1.1	150	11	7.2	1.9
J4	0.6	0.8	150	15	7.2	1.9
J5	-	-	-	-	-	-
J6	0.6	1.5	150	8	7.2	1.9
J7	0.6	1.5	150	8	7.2	1.9
J8	0.3	0.8	150	9	4.2	1.4
K1	0.3	0.8	150	9	4.2	1.4
K2	0.6	1.5	100	8	7.2	1.9
K3	0.6	1.5	50	8	7.2	1.9
K4	0.6	0.8	50	15	7.2	1.9
K5	-	-	-	-	-	-
K6	0.6	1.1	150	11	7.2	1.9
K7	0.6	0.5	150	25	7.2	1.9
K8	0.6	0.5	100	25	7.2	1.9
L1	0.3	0.5	150	15	4.2	1.4
L2	0.1	1.5	100	2	1.5	0.8
L3	0.3	1.5	150	4	4.2	1.4
L4	-	-	-	-	-	-
L5	0.1	1.1	50	2	1.5	0.8
L6	0.3	1.1	100	6	4.2	1.4
L7	0.1	0.5	50	5	1.5	0.8
L8	0.3	0.5	50	15	4.2	1.4

Chapter 8

Outlook for TES Electron Spectroscopy

8.1 Introduction

In this thesis, I have presented the detector requirements for TES X-ray photoelectron spectroscopy (Chapter 3), demonstrated TES electron spectroscopic measurement (Section 5), demonstrated the resilience of TESs to static electric fields (Chapter 6) and presented designs for the first set of TES electron spectrometers (Chapter 7). This chapter combines the findings of the previous chapters to determine in what way TESs could be applied to electron spectroscopic measurement most effectively. As there is a wide variety of electron spectroscopic techniques with different detector requirements, the focus of this chapter will be on comparing TESs to concentric hemispherical analysers (CHAs) used in X-ray photoelectron spectroscopy (XPS) in particular.

A key difference between TES calorimeters and electron detectors such as the microchannel plate (MCP) is the inherent energy resolution provided by TESs. The ability to both detect and discriminate particle energies means that any individual TES is capable of acting as an electron spectrometer in the absence of any electron optical system. However, electron optics in electron spectrometers such as the CHA play multiple roles beyond that required for energy resolved measurement; the optics collects a wide solid angle of emitted electrons and distributes these electrons to optimise for count rate, angle-resolved measurement or imaging. For these same reasons, it may be advantageous to use electron optics in conjunction with TES arrays with the additional benefit that these optics can remove the TES array from line-of-sight of a non-cryogenically cooled sample. As highlighted by the measurements in Chapter 5, black-body radiation from room-temperature components onto a TES is a large source of thermal loading and noise on the detector. Once optics are used in conjunction with TESs, the TES array becomes a component within a larger instrument, whose capabilities are dependent on the detector array and readout as well as the electron optical system. Therefore,

comparison between TESs and existing electron spectrometers requires the context of the type of measurement being performed, how the optics are configured to enable the chosen type of measurement and the performance capabilities of the detector array.

The chapter first discusses the general considerations relevant to the use of TESs in electron spectroscopy, such as device temperature, TES geometry and electron absorption efficiency in Section 8.2. The role of TESs within a larger spectrometer in conjunction with electron optics is examined in Section 8.3 by comparing three different TES spectrometer configurations with differing levels of reliance on optics. The chapter then concludes with a brief introduction to electron coincidence spectroscopy in Section 8.4. As every pixel in a TES array can act independently as its own energy-resolved spectrometer with time-resolved particle arrival times, TES measurement is naturally suited to coincidence spectroscopy; this section raises the potential of TESs in this field for further study.

8.2 Spectrometer Design Considerations

8.2.1 Temperature and Pressure

One of the primary considerations when designing a TES spectrometer is the transition temperature of the superconducting film, T_c . TES energy resolution is proportional to $\sqrt{T_c}$ and so TESs are operated at the lowest practically achievable temperatures, typically spanning between tens and hundreds of millikelvin. It is important to remember that the cryostat bath temperature (T_b) must be less than T_c for the detector to be usable, typically bath temperatures less than or equal to $T_c/2$ are used. Bath temperatures of 100 mK are easily reachable using adiabatic demagnetisation refrigerators (ADRs) but for specialist applications requiring the best resolutions, dilution refrigerators are capable of providing base temperatures of tens of millikelvin. As cryostat technology improves, it can be expected that the base temperatures available to TESs will continue to decrease, further improving TES energy resolutions.

With regards to pressures, electron spectroscopy requires ultra-high vacuum (UHV) conditions ($< 10^{-8}$ mbar) to minimise the probability of both elastic and inelastic scattering of electrons off gas molecules and to allow for the operation of equipment such as electron and ion sources. These pressure requirements are entirely compatible with TESs due to the cryogenic nature of these detectors. At cryogenic temperatures, UHV pressures are maintained through cryopumping where ambient gases condense on the low-temperature surfaces within the cryostat. An exception to these pressure requirements is near-ambient pressure XPS (NAP-XPS) where pressures of tens of millibar at the sample are used. However, differential pumping is used to quickly reduce the atmospheric pressure as the electron is

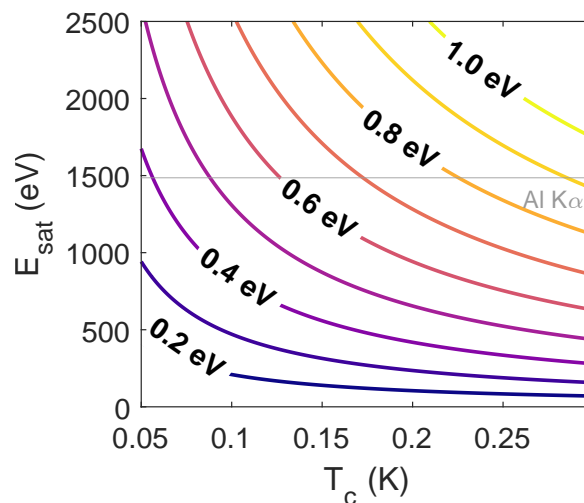


Fig. 8.1 TES energy resolution limit plotted against transition temperature and TES saturation energy. The values have been calculated for a device with $n = 2$.

collected by the spectrometer at which point the pressure requirements for a CHA and a TES electron spectrometers are equivalent.

8.2.2 Energy Resolution

A key result from Chapter 3 is that the energy resolution limit of a TES is comparable to the energy resolution of CHAs used in conventional XPS measurements. However, the resolution of the CHA can be traded-off against measurement rate *in-situ* which is not possible with TES arrays. Very high-resolution XPS measurements can achieve 0.1 eV resolutions which cannot currently be matched by TESs with saturation energies above 1000 eV. The advantage of a TES array instead lies in the ability to increase measurement rates by potentially several orders of magnitude whilst providing sub-eV energy resolution.

The FWHM energy resolution limit (ΔE) of a TES is given by

$$\Delta E = 2\sqrt{2\ln(2)}\sqrt{4k_B T_c E_{\text{sat}} \sqrt{\frac{n}{2}}}, \quad (8.1)$$

where k_B is the Boltzmann constant, E_{sat} is the saturation energy and n is a device parameter ranging between 2 and 4. This equation is discussed in Section 2.5 and the plot showing the relation between energy resolution, saturation energy and T_c from Section 2.5 has been reproduced in Fig. 8.1. As mentioned previously, TES energy resolution can be improved by reducing the operating temperature, within the bounds of current cryostat capabilities. Alternatively, the TES saturation energy can be reduced. The possibility of performing

high-resolution calorimetry far beyond the TES saturation energy has been proposed [89] but not yet demonstrated, and so for the purposes of this work, I will assume E_{sat} places an upper limit on TES energy sensitivity.

In an XPS measurement, the highest electron energy observed will be bounded by the X-ray photon energy, Al $K\alpha$ being a commonly used source at 1486.6 eV. At this saturation energy, the achievable TES resolutions span 0.4-1 eV as shown in Fig. 1.5. Achieving this resolution requires complete electron kinetic energy absorption efficiency, effective analysis of TES responses in the large-signal limit (Section 2.6) and minimal resolution degradation by readout multiplexing. The current state-of-the-art for TES X-ray calorimetry in this energy range is 0.86 eV resolution of Al $K\alpha$ photons by [71]. Assuming complete electron energy absorption, sub-eV resolution is possible with existing TES technology.

However, it is very possible that TES electron energy resolution can be further improved by exploiting the ability to controllably change the kinetic energies of electrons. The use of electrostatic lenses to precisely accelerate and decelerate electrons is central to the function of all electron analysers. Incorporating such systems with TES spectrometers would allow for the electrons incident on the TES array to be decelerated prior to detection. Therefore, the saturation energy of the detectors can be lower than the maximum electron energy emitted from the sample, improving the resolution of the TESs. The achievable energy resolutions can be lower than 0.1 eV for electrons with 50 eV operating at 100 mK. The chosen 50 eV energy is comparable to the pass energies used by CHAs, which can be as low as several eV. The drawback of such a system is that the detector array would only be able to measure the portion of the electron spectrum with sufficient energy to reach the detector after deceleration, rather than the entire spectrum. An instrument utilising this measurement scheme would occupy a middle region between a standalone TES array, sensitive to the entire spectrum, and a CHA that is only sensitive at any particular time to a narrow energy band with a maximum width of tens of eV. Potential implementation of a hybrid spectrometer utilising electron deceleration prior to TES measurement is investigated further in Section 8.3.

8.2.3 Electron Absorption Efficiency

The calculations in the previous subsection assume complete electron absorption efficiency; this assumption is not necessarily valid, as demonstrated by the measurements of Chapter 5 and Section 7.2 where the emission of secondary electrons was observed to be a primary mechanism of energy loss from the absorber. The use of electron optics, either integrated into the absorber itself or external to the absorber, can in theory prevent the emission of secondary electrons entirely. Electric field sensitivity measurements in Chapter 6 show the resilience of TESs to static electric fields, indicating that electrostatic lenses can be used in the vicinity of

TES arrays without issue. One method to reduce secondary electron emission would be to apply a positive bias to the absorber, as designed for in the devices in Section 7.3; applying a +20 V bias would prevent the emission of electrons with energies below 20 eV, thereby preventing the majority of secondary electron losses. Alternatively, a screening field could be placed just above the TES surface, decelerating incident electrons but also preventing secondary emission from the absorber surface. As discussed in Chapter 3.2, backscattered electron emission is of lesser importance than secondary emission as backscattered electrons typically carry a large proportion of the incident electron energy. Therefore, these losses act to distort the measured spectrum background rather than the important features of relative peak energies or heights. However, this effect would be detrimental for quantitative measurements and would need mitigation through the absorber design. Auger electron emission is an additional mechanism by which the incident electron energy can be lost. This process would result in losses at specific energies dependent on the absorber material used but the low probability of Auger emission makes this effect of negligible importance in a TES, especially when using low atomic mass elements for the absorber.

It may also be possible to characterise electron absorption inefficiencies *in-situ* and correct for this after performing the measurement. The measured losses can be determined by measuring electron beams at several fixed energies using the TES array. The observed energy losses from the input electron energy could then be deconvoluted from measured electron spectra, minimising the effect of absorption inefficiencies present in the TES array.

Electron optics can be used to prevent electrons escaping the absorber but electron emission is not the only mechanism of energy absorption inefficiency. Cathodoluminescence and X-ray fluorescence can both occur wherein electron absorption causes the emission of one or more photons. Based on the probability of such emission events occurring, neither of these loss mechanisms will have significant impact on the measured electron absorption spectrum at the electron energies present in standard XPS. The probability of cathodoluminescent photon emission from a metal film due to an electron with 10 keV energy is on the order of 10^{-5} [115]. An upper limit of X-ray emission probability can be obtained from [116] where the X-ray emission spectrum from bulk titanium using a 10 keV electron beam was simulated and experimentally measured. Both simulation and measurement place the probability of X-ray photon emission on the order of 10^{-3} , making the conservative assumption of isotropic photon emission. The electron impact energy used in these experiments is far greater than the energies present in standard XPS which lie below 2 keV. X-ray emission probability increases with impact energy and so the emission probability at XPS energies will be far lower than this upper limit of 10^{-3} . Additionally, when X-ray fluorescence occurs, a significant fraction of the incident electron energy escapes; the mean photon energy from a 10 keV electron

beam striking bulk titanium was 3 keV. Therefore, the same argument as for backscatter emission can be applied where large energy losses distort the background as opposed to the spectral peaks themselves. It should be noted however that X-ray emission will likely be an important consideration when applying TESs to higher energy techniques such as hard x-ray photoelectron spectroscopy (HAXPES).

The best choice of material to minimise both electron emission and X-ray emission losses is a material with low atomic mass. Such materials display smaller bremsstrahlung cross-sections, lower X-ray fluorescence and Auger yields and longer electron inelastic mean free paths and so simultaneously emit fewer photons and backscattered and secondary electrons. The lowest atomic mass, practically usable material for an electron absorber is carbon. The various allotropes of carbon provide flexibility in how to create a carbon absorber. Graphite is a natural choice though an amorphous carbon coating may also be suitable provided it is electrically conductive at cryogenic temperatures. Alternatively, carbon nanotubes forests may be an excellent choice as the surface structure of such a material would suppress electron emission from the absorber surface. These materials have found use as extremely effective photon absorbers for the same geometric reasons, with Vantablack being a notable example.

An important point to note when considering carbon absorbers is the high absorptivity of carbon to infrared radiation. As such, absorbers of this type will be more susceptible to thermal loading and photon noise. In addition, structuring the absorber surface to improve electron absorption efficiency, for example by roughening the surface or using carbon nanotube forests, will also have the effect of increasing absorbance of the infrared radiation.

The final absorption energy loss mechanism to consider is desorption of condensed gases from the absorber surface. As mentioned in Section 8.2.1, atmospheric gases condense on low-temperature surfaces in a cryostat, including the TES absorber. It is possible that a measurable portion of electron energy received by the absorber may be lost to the desorption of these gases. The significance of this loss mechanism to electron measurement is not currently known and requires characterisation, though it is possible that the act of absorbing electrons could degas the absorber surface over the course of a measurement.

Another possibility that will require monitoring is changing TES absorption efficiency over time due to surface contamination. Carbon deposition is often observed within vacuum systems with the carbon source being ambient hydrocarbons, notably from vacuum pump oil. Electron absorption properties are highly-surface sensitive, with a few nanometres of deposited carbon being sufficient to impart a measurable difference in absorption efficiency. This deposition is not a major problem, especially as carbon makes an ideal absorber material and the magnitude of deposited material will negligibly affect the device heat capacity, but will need characterising over time to understand the behaviour of the detector array.

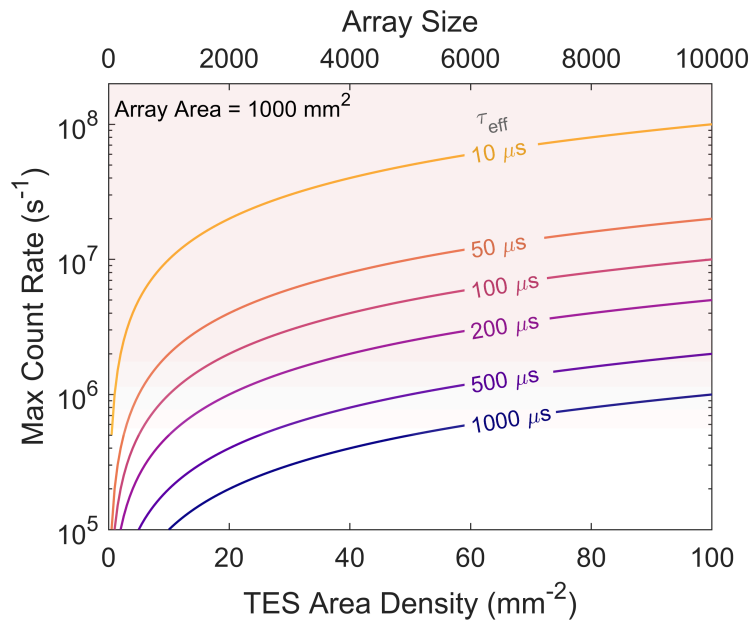


Fig. 8.2 Maximum count rate of a 1000 mm^2 area TES array at varying device areal densities. The shaded red region delineates the maximum measurement rate of concentric hemispherical analysers (CHAs) with the gradient onset representing the start of nonlinear detector response to high count rates.

The possibility of electron-induced damage on the TES array should also be considered. The relatively low electron energies present in XPS means that such beam damage is unlikely, especially considering TES X-ray calorimeters measuring comparable energies have not displayed measurable beam damage over time. However, the interaction between electrons and matter are very different from X-rays with matter and the possibility of electron-induced damage remains present, particularly when measuring high electron fluxes. The resilience of a TES to a sudden flash of a very high number of electrons is not known. While no TES degradation or damage to the readout was observed during the measurements in Section 5, there is the possibility of damaging the SQUID readout through electrostatic discharge when using an excessive electron beam current.

8.2.4 Count Rate

The effective measurement rate of an array of TES calorimeters is limited by the TES response time τ_{eff} , the array size and the particle flux incident on the array. The onset of pileup places an upper limit on count rate meaning optimal measurement rates are achieved

by distributing electron detection events evenly across the TES array at an average rate of one electron event per several τ_{eff} per detector; the simulations in Chapter 3 identified an average rate of 1 event per $10\tau_{\text{eff}}$ as a good balance between measurement rate and pileup.

The largest TES arrays numbers several thousand pixels though there is no theoretical limit to array size. Fig. 8.2 compares the maximum count rate of a TES array assuming each pixel receives on average one electron per $10\tau_{\text{eff}}$ at different array sizes and time constants. The shaded red region represents the maximum count rate of a CHA as limited by the dead-time of the delay-line detector (DLD). The region is shown with a gradient above 10^6 as at these count rates, the response of the DLD becomes non-linear with respect to electron number meaning there is no singly-definable upper limit. Fig. 8.2 also shows the count rates per detector number density at an array size of 1000 mm^2 . This array area was chosen as it lies within the range of microchannel plate areas used by CHAs. To achieve 100 detectors per square millimetre, the maximum square TES size would be $100 \mu\text{m} \times 100 \mu\text{m}$ with 100% fill-fraction. While the TES size is entirely reasonable, the complete detector fill-fraction is not; high fill-fraction TES X-ray calorimeter arrays have been demonstrated with 82% fill-fraction achieved by Lee *et al.* [71]. Using such a TES geometry, an array density of 100 mm^{-1} can be achieved using $80 \mu\text{m}$. The time constants shown in Fig. 8.2 are also entirely appropriate for these detectors with existing capabilities with effective time constants of tens of microseconds lying at the limit of practically demonstrated TES X-ray calorimeters [74].

In this regard, TES arrays are more than capable of matching and exceeding the maximum achievable count rates of CHAs using large arrays of calorimeter pixels. However, there is an important disparity between the maximum count rate of a CHA and its overall measurement rate that is highlighted when comparing TES calorimetry to CHAs. CHAs can only measure a narrow range of energies at a time and so over the course of a measurement, the observed count rate can vary by over an order of magnitude in an XPS measurement as the spectrum varies from prominent XPS peaks to low-level background. The CHA does not utilise its count rate capacity across the duration of its measurement. In contrast, the TES count rate can remain constant as the measured electron distribution does not vary over time. For this reason, TESs measurement capacity can be utilised more efficiently when measuring electron spectra, resulting in the conclusion from Section 3.5 that ten TESs with $120 \mu\text{s}$ would have comparable measurement rates to existing CHAs. Arrays of tens of TESs have the additional benefit that they would not require multiplexed readout and instead be read out using dedicated SQUIDs. Such an array would be simpler to design and operate and not display the resolution degradation observed in multiplexing. However, if higher measurement rates are desired, large array sizes with multiplexed readout is an excellent option. If an array

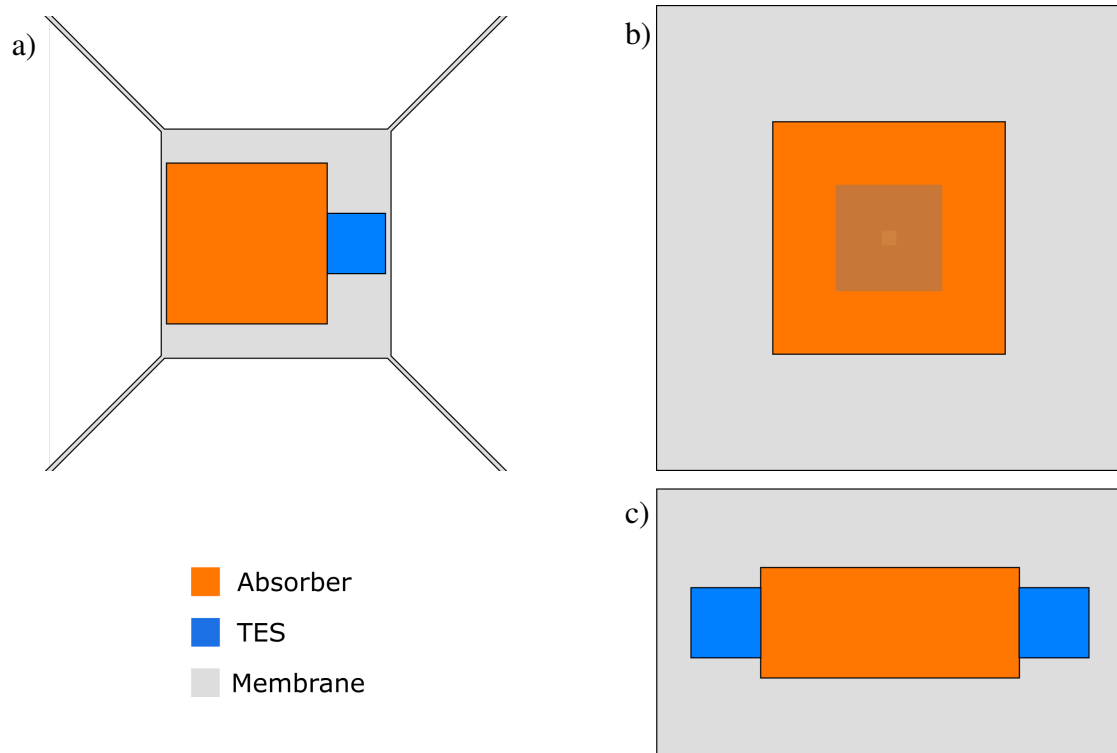


Fig. 8.3 a) Example sidecar TES geometry with absorber beside the superconducting TES film, on an island suspended by narrow legs. b) Membrane-suspended TES with the absorber above the TES. c) Position-sensitive TES with two TES films either side of the absorber.

of 1000 pixels were used, the measurement rate can be increased by two orders of magnitude without needing to increase the X-ray source intensity of lab-based XPS instruments. This is because the additional electrons being measured by the TES would be the ones collected by the CHA but discarded by the energy filtering step.

8.2.5 TES Geometry

There are a variety of possible TES geometries that can be used for electron spectroscopy but two features of particular relevance here are the thermal link geometry between the TES and the bath, and the absorber geometry. The thermal link geometry is relevant to the TES response time, energy resolution and fill-fraction. The absorber geometry is of course critically important to the device's absorption capabilities but is also relevant to its fill-fraction.

The two main forms of thermal link geometries are membrane-suspended TESs and leg-suspended TESs. A selection of example TES geometries are provided in Fig. 8.3. The

detectors shown in Fig. 6.1 and Fig. 7.11 are leg-suspended devices. These devices display lower values of n and therefore improved energy resolution following Eqn. 8.1 but at the cost of low fill-fractions. If fill-fraction is not important then leg-suspended devices offer the best performance but for applications where a wide electron collection area is necessary, this geometry may not be most appropriate. Suspended TESs utilising few-mode ballistic phonon transport between the TES and the bath may provide the best balance between low n and high fill-fraction. Such devices can be engineered with legs as short as $1\ \mu\text{m}$ with values of n approaching 2 [81].

In broad terms, there are three options for the TES absorber geometry. Firstly, a separate absorber may not be present at all with the superconducting film acting as both the absorber and energy sensor. This was the case in Fig. 6.1 and measurements in Section 5. Having no separate absorber is an excellent option for its simplicity and fast thermalisation but the design of the TES would be a compromise between absorption properties and superconducting transition properties. Additionally, integrating electron optics into such devices would prove challenging. Alternatively, a separate absorber may be placed beside or surrounding the TES as in Fig. 8.3a, in a sidecar arrangement. This design allows for control of the electron-absorber interaction through material choice and biasing the absorber, but there remains the possibility of stray electrons striking the superconductor directly. The third option is placing the absorber above the TES, as was used to achieve the high fill-fraction in [71]. In this example, the absorber was deposited above the superconductor but thermally connected to the superconducting film by a narrow stem in a mushroom-like arrangement (see Fig. 8.3b). Positioning the absorber above the superconducting film balances high fill-fraction with the benefits of a bespoke absorber but is a more challenging structure to fabricate.

A possible extension that could be of interest for high collection efficiency or angle-resolved measurements is the option of position-sensitive TESs where the location of the detection event can be localised, based upon the shape and time of the response. Examples of this are the reported in [83, 117], where two superconducting TES films were placed at opposite ends of the absorber (see Fig. 8.3c). By comparing the time difference of a given particle measurement between the two TES films and the different peak heights, the position of X-ray photon absorption could be localised within the detector itself. An alternative approach is shown in [118] where multiple absorbers are connected to the same superconducting film. The thermal conductance between each absorber pixel and TES film is chosen such that the observed pulse risetime identifies the pixel being measured. In such a design, the risetime is broadened by the measurable thermalisation time between absorber and superconducting film. With this arrangement, 20 separately identifiable pixels have been demonstrated within a single device. These position-sensitive TESs display a

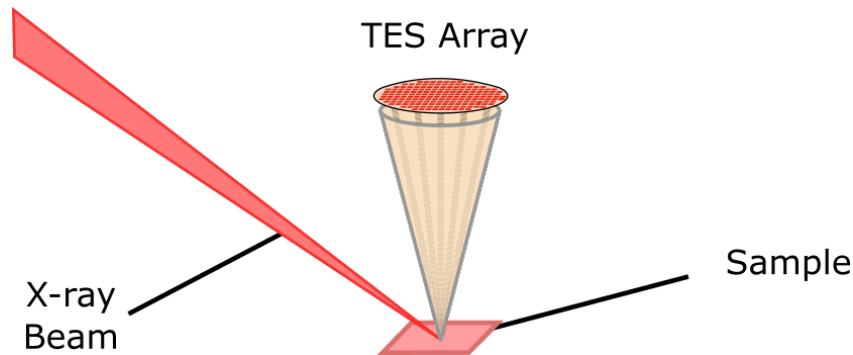


Fig. 8.4 Direct X-ray photoelectron measurement using an array of TESs without electron optics

trade-off between position sensitivity and energy resolution and so may not be appropriate for high-resolution measurements but could be of use for imaging, angle-resolved or coincidence measurements.

8.3 TES Electron Spectrometer Configurations

The types of TES spectrometer applicable to electron spectroscopy can broadly be characterised by the degree to which energy-resolved measurement relies upon the electron optics present in the instrument. On one extreme is a spectrometer with no optics and the observed electrons are emitted directly from the sample. The other extreme is a spectrometer where the entirety of the electron collection and energy discrimination is performed by the electron optical system. In this scenario, the role of the TES is resigned to electron counting; such an instrument is directly analogous to a CHA where the microchannel plate and delay-line detector is replaced by a TES array. There also exists spectrometer designs where energy resolution capabilities are balanced between the optics and TES calorimeters thereby providing capabilities not achievable using a TES array or CHA alone. This section will outline the benefits and trade-offs present in these three types of TES spectrometer.

8.3.1 Direct Spectrometer

The simplest TES spectrometer design is the direct spectrometer depicted in Fig. 8.4. This configuration benefits from its simplicity, and the possibility of angle-resolved electron measurement over a large solid angle. The collection efficiency is determined by the array size and absorber area; for applications where electron detection efficiency is favoured such as coincidence spectroscopy, large-area TES pixels would prove advantageous. As the

electron mean free path is of the order of nanometres, TES electron absorbers can be much thinner than the absorbers for TES X-ray calorimeters operating in a comparable energy range. As a result, TES electron absorbers can span larger areas than X-ray calorimeters whilst maintaining suitable heat capacities and therefore saturation energies. Suitable pixel areas for electron spectroscopy are dependent on the chosen saturation energy, operating temperature and absorber material and requires further calculation but for comparison, large format X-ray TES pixels can have areas above $800\ \mu\text{m} \times 800\ \mu\text{m}$ [119].

The efficiency of a direct detection TES array in terms of the overall proportion of emitted electrons detected can be increased by decreasing the distance between the TES and the sample but reducing this distance highlights a key disadvantage of the direct spectrometer arrangement; infrared loading on the TES array from non-cryogenically cooled surfaces. Black-body emission from a room-temperature sample is sufficient to heat a TES beyond its transition temperature unless the detector is positioned sufficiently far away from the sample with apertures or mesh blocking incident radiation. However, doing so greatly reduces the proportion of emitted electrons that can be detected by the TES array which is a primary advantage of this detector configuration, meaning that direct spectrometers are likely only practical for cryogenically cooled samples. An additional problem to consider is the rate at which the TES would observe X-ray photons scattered from the sample surface. These counts would require mitigation by using thin, low X-ray stopping power materials.

8.3.2 Hybrid Spectrometer

The second type of spectrometer presented is a hybrid between conventional electron spectrometers and TES calorimetry spectrometers. As discussed in Section 8.2.2, TES energy resolution scales with $\sqrt{E_{\text{sat}}}$ and so by reducing TES saturation energy, resolution can be improved. The hybrid spectrometer in Fig. 8.5 collects electrons emitted from the sample in a manner comparable to that used by CHAs. Instead of high-accuracy energy filtering using concentric hemispheres, a pair of electrostatic deflector plates are used to coarsely separate the incident electrons by energy into separate energy bins. Within each bin, the collected electrons are decelerated to within the saturation energy of the TES array positioned at the end. As an example, an XPS spectrum spanning 1500 eV could be divided into six bins, each of 250 eV energy width. Within each bin, the collected electrons are decelerated by a fixed amount such that the highest electron energy at the TES array is 250 eV. Therefore, the required TES saturation energy can be reduced by a factor of six from 1500 eV to 250 eV corresponding improved resolution limit of 0.3 eV FWHM at 200 mK. The resolution limit can be improved further by separating the spectrum into a larger number of bins, decelerated to lower energies.

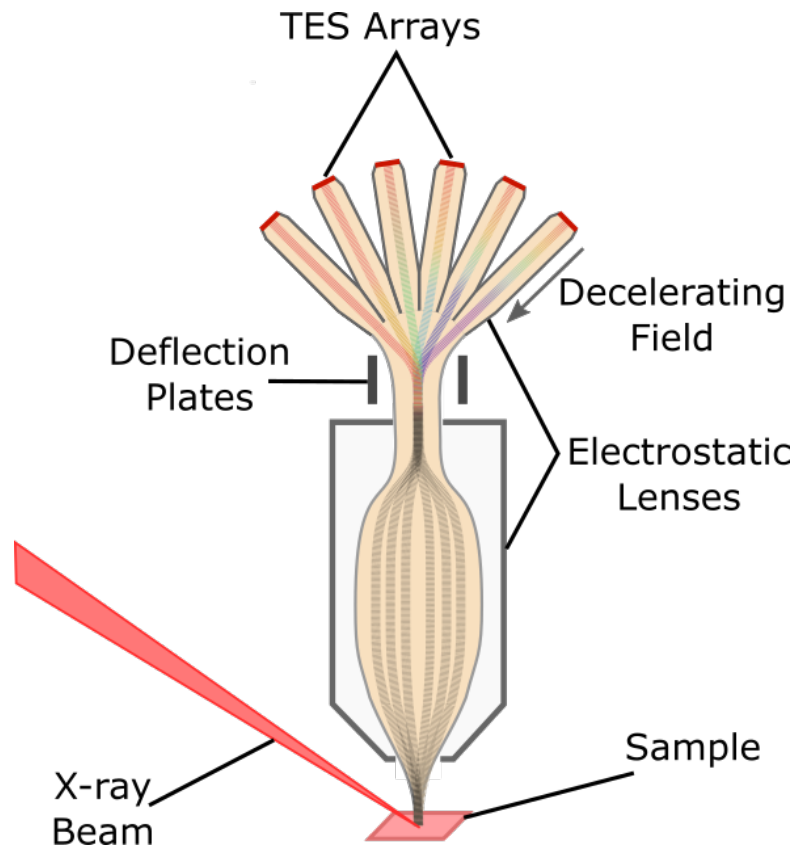


Fig. 8.5 Hybrid electron spectrometer design where photoelectrons are collected, coarsely dispersed by energy and decelerated prior to measurement by the TES.

This type of spectrometer provides a way to achieve improved resolution over existing CHAs whilst maintaining the ability of concurrent measurement of the entire electron spectrum emitted. This design also does not require line-of-sight to the sample and so could be used for non-cooled samples. The electron optics requirements for this type of spectrometer in terms of collection, dispersion and deceleration have already been achieved in conventional CHAs and so the challenge in creating a spectrometer of this design, beyond TES performance, lies in the engineering of integrating these components with the TES array and readout apparatus. It should be highlighted that only the components thermally connected to the TES array, surfaces in the detector line-of-sight and the readout system are required to be at cryogenic temperatures and so in principle, only a small number of components in the spectrometer need to be actively cooled.

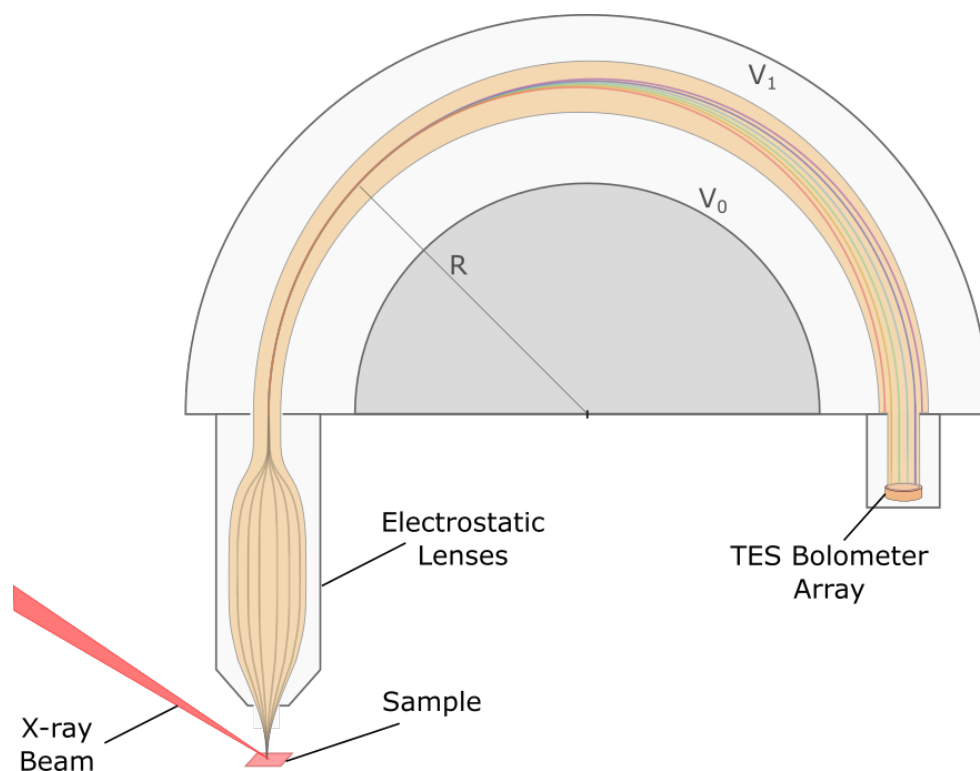


Fig. 8.6 TES bolometric array integrated with a concentric hemispherical analyser.

8.3.3 Bolometric Spectrometer

The final example spectrometer almost entirely resembles a CHA with the exception that an array of TESs are used for electron detection instead of an MCP. In a CHA, the role of the electron detector is solely in electron counting at a given position and time. The electron numbers present in these analysers are not sufficiently high for direct ultra-low current measurements and so particle counting techniques are employed instead. However, for most techniques, the specific electron detection time is irrelevant, only the number of electrons detected and their position on the delay-line detector (if present) is of importance. This same measurement could in principle be performed by an array of TES bolometers where the TESs are used to determine the relative number of particles absorbed based upon average power, but resolution of the observed electron energies is determined by the CHA pass energy and entrance optics.

In fixed analyser transmission (FAT) measurements, discussed in Section 1.2, the electron energy range passing between the hemispheres and reaching the MCPs remains consistent across the measurement. Replacing the MCP with a bolometer array would provide average measured power instead of number of electrons, but this measurement would perform the exact same function. The electrons reaching the TES array would have energies of the order

of 10 eV; electrons decelerated to 10 eV correspond to UV photon energies, beyond the range of any currently demonstrated TES bolometer, but in principle such an instrument is possible.

The advantage of bolometric measurement is that there is no detector dead-time allowing for greater measurement rates than provided by MCPs. In addition, the pixel sizes can be as small as several micrometres allowing for greater positional sensitivity of the array. Practical feasibility and utility of such a system remains to be investigated but the principle of a TES electron bolometer effectively demonstrates the range of possibility in TES electron spectroscopy, especially within the context of the previous described instruments.

8.4 Electron Coincidence Spectroscopy

In this chapter, we have primarily examined TESs within the context of XPS measurements as it is one of the most commonly used electron spectroscopy techniques with demanding resolution and measurement rate requirements. In this section, I will consider the application of TESs to electron coincidence spectroscopy. In general, coincidence spectroscopy investigates the properties of particles simultaneously emitted from a sample by the same energetic event; these emitted particles include electrons, ions and photons. By measuring the energy of the particles emitted by a single event (such as X-ray photon absorption), the energetic transfer mechanisms within the sample leading to the emission of these particles can be investigated. There are several forms of coincidence spectroscopy related to the measurement of different types of particles and emission mechanisms, but I will consider TES measurement within Auger-photoelectron coincidence spectroscopy (APECS) in particular here as it is complimentary to XPS but with very different detector requirements. It should be noted that the subject of TES calorimetry could be of great interest for the entire family of coincidence spectroscopy techniques as TES measurement can equally be performed for ion or photon calorimetry.

The basis of an APECS measurement is the simultaneous emission of a photoelectron and Auger electron due to the absorption of a single X-ray (or UV) photon. The incident photon causes emission of a core electron from the sample atom. The vacancy left by the photoelectron is then filled by a higher-energy outer electron with the excess energy released by Auger electron emission. APECS correlates observed photoelectron emission events to corresponding Auger events allowing for the study of relaxation and energy redistribution between specific atomic energy levels. Additionally, as APECS measurements select for correlated electron emission events, they suppress the uncorrelated events forming the observed electron background, improving signal-to-noise.

APECS measurements require two independent electron analysers capable of energy-resolved measurement of simultaneously emitted particles. One analyser would be set to observe Auger electrons emitted by a given transition with the second analyser used to monitor photoelectrons within an energy range of interest. Alternatively, the photoelectron energy can be fixed, with a range of Auger electron energies monitored. Simultaneous electron events observed by both detectors within the time uncertainty of the experiment (τ_Δ) are recorded. These events are a mixture of true co-emission events and uncorrelated but overlapping in time events. The energy distribution of uncorrelated but coincident events should remain equivalent even when imposing an arbitrary time delay on one of the measurement channels. Therefore, the uncorrelated spectrum can be measured by finding the coincidence spectrum between two detectors with a time delay imposed on one analyser larger than any physically relevant electron emission correlation time. Electronic lifetimes are typically on the order of femtoseconds [120], far shorter than the time resolution of existing electron spectrometers, and so the time delay necessary to determine the uncorrelated spectrum is simply a time larger than τ_Δ . The APECS spectrum is found by subtracting the true coincidence events from the uncorrelated events.

Quantitative estimation of the APECS count rates is provided in [121] but will be briefly covered here. In this analysis, two electron energy analysers are considered, both receiving electrons emitted from overlapping spatial volumes of the sample, V_i , where the subscript denotes the analyser; the volume of interest is the volume in common to the detectors, V_c . Isotropic electron emission is assumed from the sample surface. The rate of observing coincident events is dependent on the rate at which core holes are generated, the probability of subsequent Auger emission, and the probability of the detectors observing the both the Auger and photoelectron. This rate of true events (ν_T) can be estimated as

$$\nu_T = \phi_1 \phi_2 R V_c, \quad (8.2)$$

where R is the rate of core hole generation per unit volume and ϕ_i is the analyser collection efficiency, defined as the probability of emission and observation of an Auger electron given that the partner analyser has observed the corresponding photoelectron (or the inverse with photoelectron detection probability given an Auger electron has been observed).

The true count rate, ν_T , will be measured alongside the uncorrelated events whose rate is dependent on the measurement's time resolution, electron emission rate and signal to signal-plus-background ratio for each detector (γ_i). The signal in this ratio comes from electrons from the photoelectron or Auger emission peak of interest whereas the background are electrons emitted from alternate processes such as inelastically scattered electrons. From [121], the effective count rate, ν_{eff} , is defined as the inverse of the time required to observe a

signal-to-noise ratio of one after correcting for uncorrelated events. This rate is estimated as [121]

$$v_{\text{eff}} = \frac{\gamma_1 \gamma_2 \phi_1 \phi_2 R'}{\gamma_1 \gamma_2 + \Gamma R' \tau_{\Delta}}, \quad (8.3)$$

where $R' \equiv RV_c$ and Γ is a geometric constant defining the overlap of the measurement volumes of the two detectors with a minimum value of 4 when the two analyser volumes, V_1 and V_2 , match. The effective count rate saturates at high incident photon flux to

$$v_{\text{eff}}^0 = \frac{\gamma_1 \gamma_2 \phi_1 \phi_2}{\Gamma \tau_{\Delta}}, \quad (8.4)$$

demonstrating a key feature of coincidence spectroscopy that the measurement rate cannot solely be improved by increasing count rate. In actuality, for APECS, saturation is easily achieved with existing experimental designs and the key limitation is detector efficiency. In [121], at total electron count rates of several kHz, an effective count of 0.5 Hz was observed in the saturation limit. This low effective count rate is due in large part to the inherent inefficiency present in existing spectrometers. Consider a measurement where one CHA is monitoring a fixed photoelectron energy whilst the second CHA is observing a narrow 20 eV range corresponding to a chosen Auger peak. Only a fraction of the total number of emitted electrons are collected by either detector and of that fraction, only a narrow spectral range of electron energies pass through the CHA to be measured. For the CHA measuring the fixed photoelectron energy, this spectral range may encompass the entire photoelectron peak but for the Auger CHA measuring a 20 eV range, assuming a 1 eV range is measured at a time, 95% of received electrons are discarded.

Replacing CHAs with TESs changes the paradigm within which coincidence measurements can be made. As TESs are sensitive to the entire spectral range and naturally perform time-resolved measurements, if an XPS measurement was performed using a direct spectrometer such as in Fig. 8.4, coincidence measurements can naturally be extracted from the data. Correlations can be obtained between every TES pixel in the array rather than between entire instruments, as is the current state-of-the-art. Correlations can be found between any pair of energies within the entire spectrum allowing for 2-dimensional correlation spectrum matrices to be collected. Alternatively, if the correlations only between specific electron transitions are of interest, the hybrid spectrometer in Fig. 8.5 may be more appropriate where each bin could monitor its own spectral peak, optimising count rates towards energies of interest only.

The promise of TESs in coincidence spectroscopy is apparent but quantitative estimates of the potential benefits haven't yet been determined. I consider here two uses of TES in APECS in different scenarios to provide preliminary estimates of TES utility in this field; the

first follows the example in [121] where $\nu_{\text{eff}}^0 = 0.5$ Hz was observed but with TES arrays replacing the previous analysers. The second scenario considers a TES spectrometer measuring the entire emitted electron spectrum concurrently in a direct measurement configuration.

The example in [121] used two separate electron spectrometers to measure a specific photoelectron and Auger peak, respectively. The first spectrometer was fixed to measure Al $2p$ photoelectron emission from a 120 eV photon source. In this instrument, approximately 10% of the Al $2p$ photoelectron linewidth lay within the fixed analyser window (including plasmon losses). Estimating that 1% of emitted electrons entered the instrument, $\phi_1 = 1 \times 10^{-3}$. The second instrument was set to observe the *LVV* Auger emission; emission of a valence electron due to the recombination of the Al $2p$ hole with a different valence electron. The Auger spectrometer was used to measure a 20 eV range with 0.5 eV analyser window and so, assuming 1% of electrons are collected by the instrument also, $\phi_2 = 2.5 \times 10^{-4}$. The Al $2p$ hole decays almost exclusively by *LVV* emission and so the $\phi_{1,2}$ are primarily determined by the spectrometer and not the Auger emission probability. The signal to signal-plus-background ratios were estimated at $\gamma_1 = 1$ and $\gamma_2 = 0.5$ with significant background present beneath the Auger peak whilst the photoelectron peak displayed minimal background electrons. At an experimental timing resolution of 30 ns, $\nu_{\text{eff}}^0 = 1$ Hz was predicted with the observed rate being 0.5 Hz at total electron count rates of 6.5 kHz in the photoelectron analyser and 3 kHz in the Auger analyser. This calculation assumes the ideal case of $\Gamma = 4$.

Replacing the two analysers with TES spectrometers requires two important assumptions. Firstly, the performance of the electron collection optics remains the same such that approximately 1% of electrons are received by each spectrometer. Secondly, the spectral ranges received by each TES array is filtered in each spectrometer such that the first spectrometer only receives the photoelectron peak and the second only receives the 20 eV range about the *LVV* Auger peak. Under these conditions, $\phi_1 = \phi_2 = 1 \times 10^{-2}$, limited by the electron collection optics. We can retain the same values of γ and Γ but must consider τ_{Δ} separately.

TES arrival time resolution is set by temporal fluctuations in pulse timing, known as jitter, limited by the TES pulse risetime (defined by the electrical time constant τ_{el} and current noise) [122]. The limits of TES timing resolution at X-ray photon energies has historically been of little interest to the TES community but arrival time precision of optical photons is of great interest for quantum communication purposes. When performing calorimetric measurement of 1.5 eV photons, TES jitter times below 4 ns have been demonstrated with a 750 ns effective response time [122]. However, this example was not designed for high-resolution calorimetry but for optical photon counting, and so these time-resolutions cannot be assumed for our purposes. As an example of what is currently possible at kiloelectronvolt energies, in the measurements in Section 5, at the greatest tested sampling frequency of

200 kHz, electron arrival times could be localised within $5 \mu\text{s}$ uncertainty, limited by the sampling frequency. I will make a conservative estimate of $\tau_{\Delta} = 1 \mu\text{s}$ for electron calorimetry but it is very possible for this value to be improved upon.

Inserting these values of $\tau_{\Delta} = 1 \mu\text{s}$ and $\phi_1 = \phi_2 = 1 \times 10^{-2}$ in Eqn. 8.4 provides an effective count rate of 12.5 Hz, greater than the observed rate of 0.5 Hz in [121]. This TES example still assumes two independent analysers but the same analysis could equally be applied to the hybrid scheme in Fig. 8.5 where each measurement bin energy has been narrowed to a spectral peak of choice. As a result, each bin behaves as an independent analyser, with equivalent alignment to the sample detection volume. It may be possible for each bin to measure a specific transition allowing for correlations between multiple spectral peaks to be measured simultaneously.

It should be noted that there are a number of instrument types designed for electron coincidence spectroscopy with differing capabilities, including time-of-flight spectrometers capable of 2π or 4π collection angles [123–125]. The purpose of the comparison with [121] is not to compare TESs to the state-of-the-art which would require in-depth analysis beyond the scope of this thesis, but as a preliminary consideration as to whether TES electron coincidence spectroscopy is a reasonable prospect. The result of the comparison being that TES electron coincidence spectroscopy is feasible and complimentary to the use of TES spectrometers for conventional XPS measurements.

In the second scenario using a direct detection scheme as in Fig. 8.4, a TES array of 1000 mm^2 is positioned 80 mm from the sample with a fill-fraction of 0.5. Therefore, assuming isotropic electron emission from a flat sample, the electron collection efficiency, ϕ , is approximately 0.012. The signal to signal-plus-background ratio γ can be approximated using the proportion of the electron spectrum belonging to any observed XPS and Auger peaks in relation to the total spectral area. In this case, we will assume $\gamma = 0.1$ though this value is highly-dependent on the sample and photon energy used. As the measured sample volume is equivalent for every TES in the array, $\Gamma = 4$. Combining these values provides $v_{\text{eff}}^0 = 0.4 \text{ Hz}$ which is comparable to spectrometer in question. This value can be greatly improved by increasing the electron collection efficiency by using large area arrays, either by increasing the number of devices or using large-area TESs. In addition, the sample can be positioned closer to the TES array but stray X-ray photon measurement will need to be considered as a source of unwanted counts. The collection rate can also be improved by reducing τ_{Δ} , the limits of which are yet to be explored. One important feature of this measurement is that while the effective measurement rate is comparable to the previous example in [121], the spectral range being measured would be an order of magnitude greater as the entirety of the electron spectrum is being measured concurrently. If only particular

transitions are of interest, larger TES arrays, positioned closer to the sample with shorter time uncertainties would be needed to achieve comparable measurement rates.

8.5 Conclusion

This chapter combines the experience gained from simulated and experimental measurements in previous chapters to investigate the key considerations regarding the use of TES spectrometer arrays in electron spectroscopic measurements. The key factors that determine the design of such a spectrometer are the energy range, resolution and count rate but also infrared loading onto the TES array from black-body radiation from non-cryogenically cooled surfaces. The energy resolution and count rate is determined by the TES array design while the infrared loading can be minimised through the use of electron optics separating emitted electrons from the infrared line-of-sight. However, there are a range of possible instrument designs that can be used for TES electron measurement as shown by the three examples in Fig. 8.4, Fig. 8.5, Fig. 8.6.

The hybrid spectrometer design of Fig. 8.5 has several advantageous features that make it especially promising. Firstly, this style of instrument can be made where the TES array has no direct line-of-sight to the sample and so the sample can be measured at room temperature rather than at cryogenic temperatures. The instrument has coarse energy filtering allowing for only a specific portion of the electron spectrum to be measured at a time or the entire spectrum, depending on the experimental requirement. This is important when a specific electron energy peak is of interest so that the instrument can be configured to quickly measure only the energy range of interest. In addition, by separating the electron spectrum into energy bins and decelerating these electrons before measurement, TESs with reduced saturation energies and therefore improved energy resolutions can be used. In addition, as every electron detected has its energy and arrival time measured, instruments such as this can naturally provide coincidence spectroscopic measurements.

This chapter has also introduced the possibility of TESs for coincidence spectroscopy. Preliminary estimates suggest that TESs are capable detectors for electron coincidence measurements such as APECS but the most exciting benefit in this area is that such measurements could be performed by a single instrument in conjunction with standard XPS measurements, simply due to the nature of TES calorimetry, rather than requiring highly-specialised apparatus designed specifically for coincidence spectroscopy.

In general, electron spectroscopic measurement using TESs remains an exciting prospect with great potential to expand the horizons of electron spectroscopy, particularly with regards to measurements requiring high count rates such as for *in-situ* experiments. There are several

areas that require further investigation as discussed in this chapter, the most important of which are characterising electron-absorber interactions within the TES and optimising the resolution of TES electron calorimeters.

Chapter 9

Conclusions

9.1 Summary of Key Results

The purpose of this project was to investigate the use of TESs for electron spectroscopy. As TES electron measurement had not previously been demonstrated to my knowledge, assessing the potential of TESs in electron spectroscopy required three separate areas of investigation. The advantages of using TESs over existing electron spectrometers had to be quantitatively determined, TES electron calorimetry had to be demonstrated as a practical method of accurately measuring electron energies, and the manner in which TESs could be utilised in spectroscopic instruments had to be understood.

Existing electron spectrometers rely upon a combination of electron optics and particle-counting detectors to perform energy-resolved measurements; in contrast, each TES pixel is capable of acting as an independent spectrometer. Electron spectroscopy encompasses a wide range of techniques with differing analyser requirements and so I primarily focussed my investigation on the technique of X-ray photoelectron spectroscopy (XPS) due to its demanding energy resolution and count rate requirements. Chapter 3 used simulated TES electron measurement experiments to determine the capabilities of a TES electron spectrometer array. By comparing the simulated TES performance with the performance of concentric hemispherical analysers (CHAs), used for XPS measurements, I found that TESs are indeed a realistic and promising technology that could be of great benefit in XPS measurements. The energy resolution of a CHA is inherently balanced against its measurement rate. TESs do not have this inherent trade-off. Whilst a TES cannot achieve the best XPS resolutions attainable using CHAs (≈ 0.1 eV FWHM) without using temperatures below 50 mK and saturation energies below 500 eV, when energy resolution must be balanced against measurement rate, TES performance cannot be matched using CHAs. A small array of TES calorimeters can match the measurement rate of a CHA. Array sizes of tens of pixels can be directly read-out

using individually dedicated SQUIDs for optimal performance. Alternatively, TES arrays with multiplexed readout can number in the thousand or tens of thousands of pixels and so there is an enormous scope for increasing measurement rate.

Given that TES electron measurement had not been demonstrated previously and with very little discussion in the literature, a vital question to answer was whether TES electron calorimetry was even possible and so the experiment described in Chapter 4 was assembled as a proof-of-principle of TES electron calorimetry. The measurements obtained from this experimental apparatus (Chapter 5) clearly demonstrate TES electron calorimetry can be performed with electron energies spanning 0 to 2000 eV measured simultaneously by a single detector, with no foreseeable obstacle to higher energy measurement. Electron spectra scattered off a graphite target were also successfully measured in the first demonstration of using TES as electron spectrometers. These initial measurements achieved an energy resolution of 3 eV based upon the observed detector noise, an excellent result considering the TESs used were originally designed for infrared bolometry and adapted for the purposes of electron measurement. Devices optimised for electron calorimetry in the same energy range are expected to be capable of sub-eV energy resolutions.

Having demonstrated the viability of TES electron spectroscopy, Chapter 6 addresses an important aspect of operating TESs within any electron spectroscopy instrument; the sensitivity of TESs to static electric fields. Static electric fields can be used to accelerate, screen, focus and disperse charged particles and so are central to the operation of electron spectroscopic analysers. In the context of TES electron measurement, these DC fields can be used to enhance the electron absorption capabilities of the device by preventing the emission of secondary electrons, can screen unwanted low energy particles not of interest to the measurement, or controllably change the kinetic energy of the electrons incident on the TES to place the electron energy into the optimal energy sensitivity range of the device. However, utilising DC electric fields for any of these purpose requires knowing what effect these fields may have on TES operation.

The sensitivity of TESs to static electric fields had not been investigated previously and so I tested TES behaviour in the presence of fields up to 90 kV/m. No change in TES behaviour was observed up to the maximum tested field strength, demonstrating the resilience of these devices to applied electric fields. This result allows for closely integrating TESs with electron optical systems without degrading TES performance, including the possibility of utilising electron optics directly within the TES design to enhance electron absorption capabilities beyond that provided by the material properties of the electron absorber alone.

Chapter 7 presents the first set of TESs designed specifically for electron spectroscopy, and are capable of experimentally testing advantages of integrating electron optics into the

Table 9.1 Predicted TES performance capabilities for arrays designed for high-resolution and high count rate measurements. The energy resolutions (ΔE) have been calculated using Eqn. 2.39 and multiplied by a factor of 1.5 for the resolution-optimised array, and 1.75 for the rate-optimised array, to account for sub-optimal performance. The larger factor in the rate optimised array allows for resolution degradation due to the use of multiplexed readout. The count rates have been estimated assuming an average rate of one event every 10 effective time constants ($10\tau_{\text{eff}}$). The saturation energies (E_{sat}) have been chosen to encompass the range of electron energies generated by an Al $K\alpha$ X-ray source.

Type	ΔE (eV)	E_{sat} (eV)	τ_{eff} (μs)	Array Size	Count Rate (kHz)	Multiplexing	T_c (mK)
Resolution	0.7	1500	200	10	5	No	80
Rate	1.3	1500	100	100	100	Yes	200

TES itself. The TES geometry was chosen such that the absorber structure is electrically isolated from the superconducting bilayer. This isolation allows for a positive voltage bias to be applied to the absorber independent of the TES bias with the effect of this absorber bias being to enhancing electron energy absorption efficiency by suppressing secondary electron emission.

The experience gained from this body of work was collected in Chapter 8 to consider what role TESs could play in electron spectroscopy. Based upon the findings of this thesis, TESs are a promising prospect for XPS measurement due to their combination of energy resolution, measurement rate and detection efficiency. TESs designed for XPS applications will need to be optimised towards energy resolution as the resolution requirements in XPS lies near the thermodynamic limit of TES performance at cryogenic temperatures that are currently practically attainable. Table 9.1 shows the predicted TES performance for two arrays optimised for energy resolution and count rates. The energy resolution array does not use multiplexed readout but instead the pixels are directly read-out using dedicated SQUIDs. The energy resolutions shown are not the optimal resolutions but have instead been multiplied by a factor of 1.5 for the resolution-optimised array, and 1.75 for the rate-optimised array to account for inefficiencies from excess noise, such as from multiplexing and analysis errors.

A possible alternative approach to TES electron spectroscopy, as discussed in Chapter 8, is to utilise electron optics similar to that used in CHAs to perform coarse energy filtering with the high-precision measurement carried out by the TES. Such an instrument could be capable of greatly improving TES energy resolution beyond those shown in Table 9.1, by decelerating electrons prior to measurement. This hybrid approach could theoretically provide both the resolution performance of the CHA with the intrinsic energy sensitivity and count rate advantages of the TES.

9.2 Future Outlook

The findings of this thesis, whilst presented in the context of TES electron spectroscopy, are applicable to massive particle calorimetry more broadly. For example, many of the advantages and limitations of TESs discussed in Chapter 8 are equally applicable to the measurement of other charged particles, such as ions or muon beams. The field of massive particle calorimetry using TESs has had remarkably little attention and the possibilities of applying TESs to new areas such as scanning helium microscopy or coincidence spectroscopy remain to be understood.

The simulation work in Chapter 3 was of great value in determining the applicability of TESs in the entirely new context of XPS measurement. This simulation software utilised an idealised representation of TES behaviour, suitable when performing preliminary investigations in a new area of research. However, it can be refined to more accurately represent TES behaviour in a true electron spectroscopic measurement by more closely simulated TES-electron interactions, and by simulating TES behaviour in the non-linear measurement regime. Such a tool would be invaluable for prototyping TES device designs or deciding how best to integrate TES detector arrays within a large spectroscopic instrument.

An important area of study for any form of TES calorimetry is the interaction between the particle and the absorber. In the context of electron spectroscopy, a key measurement to characterise this interaction is that performed by a TES in response to a mono-energetic electron beam. Performing this measurement at high-resolution would allow for precise calibration of the TES response to electron energies but also to directly observe the prevalence of incomplete electron energy absorption both in terms of the amount of energy lost but also the statistics of when these events occur. A measurement of this kind is essential for determining the absorption efficiency of such detectors and improving upon it. Such a measurement also compliments well with investigating the effects of electron optics on both absorption efficiency and detector behaviour. Characterising the devices designed in Chapter 7 with the controllable absorber bias would allow for *in-situ* manipulation of electron-absorber interactions and control the subsequent absorption efficiency.

The observed resilience of TESs to static electric fields was a key result from this thesis as static electric fields can be used to control the interaction between charged particles and the detector. For example, unwanted charged particles below certain energy can be screened and prevented from striking the detector using DC electric fields. Such a system would be relevant would be in space-based applications where cosmic rays striking the satellite produce secondary electron showers that can impinge on the detector array. The use of a DC screening field in close proximity to the TES array could provide a simple, low-mass route to minimising unwanted particle detection events.

Looking beyond TESs for particle spectroscopy, it is also possible to use TES calorimeters as their own experimental platform. As mentioned previously, characterising TES electron absorption inefficiency is important for a spectroscopic detector but those same inefficiencies are dependent on electron-matter interactions within the absorber. Rather than aiming for high absorption efficiency, the TES absorber can be used as a platform to investigate the interaction between an electron or ion beam with the absorber material to investigate for example electron or photon emission energies and probabilities in absolute terms from the sample surface. Additionally, as electron beam interactions are very surface sensitive, probing only a few nanometres into the material, a thin coating could be applied to the absorber for a film to be tested under electron bombardment. Such measurements are distinct from typical electron spectroscopic methods as what is being measured is the energy deposited directly into the material and its deviation from the known source energy rather than trying to capture expelled particles or photons. Using a TES in this way would circumvent the challenges of the spectroscopy instrument being sensitive to only a particular range of emitted particles energies over a narrow solid angle.

References

- [1] W. S. M. Werner. Electron transport in solids for quantitative surface analysis. *Surface and Interface Analysis*, 31(3):141–176, 2001.
- [2] J. L. Hart, A. C. Lang, A. C. Leff, et al. Direct Detection Electron Energy-Loss Spectroscopy: A Method to Push the Limits of Resolution and Sensitivity. *Scientific Reports*, 7(1):8243, August 2017.
- [3] M. P. Seah and D. Briggs. *Practical Surface Analysis: Auger and X-ray Photoelectron Spectroscopy*. John Wiley & Sons, 1990.
- [4] M. P. Seah and G. C. Smith. Quantitative AES and XPS: Determination of the electron spectrometer transmission function and the detector sensitivity energy dependencies for the production of true electron emission spectra in AES and XPS. *Surface and Interface Analysis*, 15(12):751–766, 1990.
- [5] B. P. Reed, D. J. H. Cant, S. J. Spencer, et al. Versailles Project on Advanced Materials and Standards interlaboratory study on intensity calibration for x-ray photoelectron spectroscopy instruments using low-density polyethylene. *Journal of Vacuum Science & Technology A*, 38(6):063208, November 2020.
- [6] B. Wannberg. Electron optics development for photo-electron spectrometers. *Nuclear Instruments and Methods in Physics Research Section A: Accelerators, Spectrometers, Detectors and Associated Equipment*, 601(1):182–194, March 2009.
- [7] L. Gottardi and K. Nagayashi. A Review of X-ray Microcalorimeters Based on Superconducting Transition Edge Sensors for Astrophysics and Particle Physics. *Applied Sciences*, 11(9):3793, January 2021.
- [8] J. N. Ullom and D. A. Bennett. Review of superconducting transition-edge sensors for x-ray and gamma-ray spectroscopy*. *Superconductor Science and Technology*, 28(8):084003, July 2015.
- [9] W. B. Doriese, P. Abbamonte, B. K. Alpert, et al. A practical superconducting-microcalorimeter X-ray spectrometer for beamline and laboratory science. *Review of Scientific Instruments*, 88(5):053108, May 2017.
- [10] S. Collaboration, M. F. Albakry, I. Alkhatib, et al. A Strategy for Low-Mass Dark Matter Searches with Cryogenic Detectors in the SuperCDMS SNOLAB Facility, April 2023.

- [11] R. Strauss, G. Angloher, P. Bauer, et al. A prototype detector for the CRESST-III low-mass dark matter search. *Nuclear Instruments and Methods in Physics Research Section A: Accelerators, Spectrometers, Detectors and Associated Equipment*, 845:414–417, February 2017.
- [12] Y. Mitsuya, T. Konno, S. Takasu, et al. Photon Number Resolution with an Iridium Optical Transition Edge Sensor at a Telecommunication Wavelength. *Journal of Low Temperature Physics*, 210(3):498–505, February 2023.
- [13] D. Fukuda, G. Fujii, T. Numata, et al. Titanium-based transition-edge photon number resolving detector with 98% detection efficiency with index-matched small-gap fiber coupling. *Optics Express*, 19(2):870–875, January 2011.
- [14] D. H. Andrews, W. F. Brucksch, Jr., W. T. Ziegler, and E. R. Blanchard. Attenuated Superconductors I. For Measuring Infra-Red Radiation. *Review of Scientific Instruments*, 13(7):281–292, July 1942.
- [15] D. H. Andrews, R. D. Fowler, and M. C. Williams. The Effect of Alpha-particles on a Superconductor. *Physical Review*, 76(1):154–155, July 1949.
- [16] V. Narayanamurti, R. C. Dynes, P. Hu, et al. Quasiparticle and phonon propagation in bulk, superconducting lead. *Physical Review B*, 18(11):6041–6052, December 1978.
- [17] J. Clarke, G. I. Hoffer, P. L. Richards, and N. H. Yeh. Superconductive bolometers for submillimeter wavelengths. *Journal of Applied Physics*, 48(12):4865–4879, December 1977.
- [18] J. Hoyle, R. Humphris, and J. Boring. A superconducting thin-film low-energy particle detector. *IEEE Transactions on Magnetics*, 11(2):690–693, March 1975.
- [19] N. K. Sherman. Superconducting Nuclear Particle Detector. *Phys. Rev. Lett.*, 8(11):438–439, June 1962.
- [20] G. Gallinaro, G. Roba, and R. Tatarek. Molecular beam detection by fast superconducting bolometers. *Journal of Physics E: Scientific Instruments*, 11(7):628, July 1978.
- [21] M. J. Cardillo, G. E. Becker, G. D. Kubiak, et al. Granular aluminum superconducting bolometer as a molecular beam detector. *Journal of Vacuum Science and Technology*, 17(1):130–133, January 1980.
- [22] K. D. Irwin. SQUIDS and Transition-Edge Sensors. *Journal of Superconductivity and Novel Magnetism*, 34(6):1601–1606, June 2021.
- [23] K. Irwin, S. Nam, B. Cabrera, et al. A self-biasing cryogenic particle detector utilizing electrothermal feedback and a SQUID readout. *IEEE Transactions on Applied Superconductivity*, 5(2):2690–2693, June 1995.
- [24] W. Seidel, G. Forster, W. Christen, et al. Phase transition thermometers with high temperature resolution for calorimetric particle detectors employing dielectric absorbers. *Physics Letters B*, 236(4):483–487, March 1990.

- [25] R. Welty and J. Martinis. A series array of DC SQUIDS. *IEEE Transactions on Magnetics*, 27(2):2924–2926, March 1991.
- [26] H. Akamatsu, W. B. Doriese, J. A. B. Mates, and B. D. Jackson. Signal readout for Transition-Edge Sensor X-ray imaging spectrometers, September 2022.
- [27] K. D. Irwin. SQUID multiplexers for transition-edge sensors. *Physica C: Superconductivity*, 368(1):203–210, March 2002.
- [28] S. J. Smith, J. S. Adams, S. R. Bandler, et al. Performance of a Broad-Band, High-Resolution, Transition-Edge Sensor Spectrometer for X-ray Astrophysics. *IEEE Transactions on Applied Superconductivity*, 31(5):1–6, August 2021.
- [29] M. Durkin, J. S. Adams, S. R. Bandler, et al. Demonstration of Athena X-IFU Compatible 40-Row Time-Division-Multiplexed Readout. *IEEE Transactions on Applied Superconductivity*, 29(5):1–5, August 2019.
- [30] H. Akamatsu, D. Vaccaro, L. Gottardi, et al. Demonstration of MHz frequency domain multiplexing readout of 37 transition edge sensors for high-resolution x-ray imaging spectrometers. *Applied Physics Letters*, 119(18):182601, November 2021.
- [31] Y. Nakashima, F. Hirayama, S. Kohjiro, et al. Low-noise microwave SQUID multiplexed readout of 38 x-ray transition-edge sensor microcalorimeters. *Applied Physics Letters*, 117(12):122601, September 2020.
- [32] D. S. Akerib, P. D. Barnes, D. A. Bauer, et al. Preliminary limits on the WIMP-nucleon cross section from the cryogenic dark matter search (CDMS). *Nuclear Physics B - Proceedings Supplements*, 70(1):64–68, January 1999.
- [33] G. Angloher, M. Bruckmayer, C. Bucci, et al. Limits on WIMP dark matter using sapphire cryogenic detectors. *Astroparticle Physics*, 18(1):43–55, August 2002.
- [34] THE CDMS II COLLABORATION. Dark Matter Search Results from the CDMS II Experiment. *Science*, 327(5973):1619–1621, March 2010.
- [35] G. Angloher, A. Bento, C. Bucci, et al. Results on light dark matter particles with a low-threshold CRESST-II detector. *The European Physical Journal C*, 76(1):25, January 2016.
- [36] J. S. Adams, R. Baker, S. R. Bandler, et al. First operation of transition-edge sensors in space with the Micro-X sounding rocket. In *X-Ray, Optical, and Infrared Detectors for Astronomy IX*, volume 11454, pages 195–203. SPIE, January 2021.
- [37] S.-J. Lee, C. J. Titus, R. Alonso Mori, et al. Soft X-ray spectroscopy with transition-edge sensors at Stanford Synchrotron Radiation Lightsource beamline 10-1. *Review of Scientific Instruments*, 90(11):113101, November 2019.
- [38] M. Borghesi, B. Alpert, M. Balata, et al. An updated overview of the HOLMES status. *Nuclear Instruments and Methods in Physics Research Section A: Accelerators, Spectrometers, Detectors and Associated Equipment*, 1051:168205, June 2023.

- [39] M. Rajteri, M. Biasotti, M. Faverzani, et al. TES Microcalorimeters for PTOLEMY. *Journal of Low Temperature Physics*, 199(1):138–142, April 2020.
- [40] S. Yamada, T. Ohashi, Y. Ishisaki, et al. Super DIOS: Future X-ray Spectroscopic Mission to Search for Dark Baryons. *Journal of Low Temperature Physics*, 193(5):1016–1023, December 2018.
- [41] W. Cui. HUBS: A dedicated hot circumgalactic medium explorer. In *Space Telescopes and Instrumentation 2020: Ultraviolet to Gamma Ray*, page 311, December 2020.
- [42] E. Shirokoff, B. A. Benson, L. E. Bleem, et al. The South Pole Telescope SZ-Receiver Detectors. *IEEE Transactions on Applied Superconductivity*, 19(3):517–519, June 2009.
- [43] B. G. Keating, P. A. R. Ade, J. J. Bock, et al. BICEP: A large angular-scale CMB polarimeter. In *Polarimetry in Astronomy*, volume 4843, pages 284–295. SPIE, February 2003.
- [44] D. S. Swetz, P. A. R. Ade, M. Amiri, et al. OVERVIEW OF THE ATACAMA COSMOLOGY telescope: RECEIVER, INSTRUMENTATION, AND telescope SYSTEMS. *The Astrophysical Journal Supplement Series*, 194(2):41, June 2011.
- [45] S. R. Dicker, B. S. Mason, P. M. Korngut, et al. MUSTANG. First light and current status. In *2007 Joint 32nd International Conference on Infrared and Millimeter Waves and the 15th International Conference on Terahertz Electronics*, pages 331–332, September 2007.
- [46] D. J. Benford, J. G. Staguhn, T. J. Ames, et al. First astronomical images with a multiplexed superconducting bolometer array. In *Millimeter and Submillimeter Detectors and Instrumentation for Astronomy III*, volume 6275, pages 416–427. SPIE, July 2006.
- [47] C. L. Chang, P. Ade, K. Aird, et al. Detectors for the South Pole Telescope. *Physics Procedia*, 37:1381–1388, January 2012.
- [48] Z. D. Kermish, P. Ade, A. Anthony, et al. The POLARBEAR experiment. In *Millimeter, Submillimeter, and Far-Infrared Detectors and Instrumentation for Astronomy VI*, volume 8452, pages 366–380. SPIE, September 2012.
- [49] A. Orlando, R. W. Aikin, M. Amiri, et al. Antenna-coupled TES bolometer arrays for BICEP2/Keck and SPIDER. In *Millimeter, Submillimeter, and Far-Infrared Detectors and Instrumentation for Astronomy V*, volume 7741, pages 143–152. SPIE, July 2010.
- [50] R. J. Thornton, P. A. R. Ade, S. Aiola, et al. The Atacama Cosmology Telescope: The polarization-sensitive ACTPol instrument. *The Astrophysical Journal Supplement Series*, 227(2):21, December 2016.
- [51] M. D. Audley, W. S. Holland, W. D. Duncan, et al. SCUBA-2: A large-format TES array for submillimetre astronomy. *Nuclear Instruments and Methods in Physics Research Section A: Accelerators, Spectrometers, Detectors and Associated Equipment*, 520(1):479–482, March 2004.

- [52] J. A. Sobrin, A. J. Anderson, A. N. Bender, et al. The Design and Integrated Performance of SPT-3G. *The Astrophysical Journal Supplement Series*, 258(2):42, February 2022.
- [53] K. Harrington, T. Marriage, A. Ali, et al. The Cosmology Large Angular Scale Surveyor. In *Millimeter, Submillimeter, and Far-Infrared Detectors and Instrumentation for Astronomy VIII*, volume 9914, pages 380–400. SPIE, July 2016.
- [54] J. A. Grayson, P. A. R. Ade, Z. Ahmed, et al. BICEP3 performance overview and planned Keck Array upgrade. In *Proc.SPIE*, volume 9914, page 99140S, July 2016.
- [55] S. W. Henderson, R. Allison, J. Austermann, et al. Advanced ACTPol Cryogenic Detector Arrays and Readout. *Journal of Low Temperature Physics*, 184(3):772–779, August 2016.
- [56] S. R. Dicker, P. A. R. Ade, J. Aguirre, et al. MUSTANG 2: A Large Focal Plane Array for the 100 m Green Bank Telescope. *Journal of Low Temperature Physics*, 176(5):808–814, September 2014.
- [57] D. A. Harper, M. C. Runyan, C. D. Dowell, et al. HAWC+, the Far-Infrared Camera and Polarimeter for SOFIA. *Journal of Astronomical Instrumentation*, 07(04):1840008, December 2018.
- [58] B. Westbrook, P. A. R. Ade, M. Aguilar, et al. The POLARBEAR-2 and Simons Array Focal Plane Fabrication Status. *Journal of Low Temperature Physics*, 193(5):758–770, December 2018.
- [59] J. R. Stevens, N. F. Cothard, E. M. Vavagiakis, et al. Characterization of Transition Edge Sensors for the Simons Observatory. *Journal of Low Temperature Physics*, 199(3-4):672–680, May 2020.
- [60] L. Collaboration, E. Allys, K. Arnold, et al. Probing Cosmic Inflation with the LiteBIRD Cosmic Microwave Background Polarization Survey. *Progress of Theoretical and Experimental Physics*, 2023(4):042F01, April 2023.
- [61] P. C. Nagler, J. E. Sadleir, and E. J. Wollack. Transition-edge sensor detectors for the Origins Space Telescope. *Journal of Astronomical Telescopes, Instruments, and Systems*, 7(1):011005, January 2021.
- [62] T. Hashimoto, D. A. Bennett, W. B. Doriese, et al. Integration of a TES-based X-ray spectrometer in a kaonic atom experiment. *Journal of Low Temperature Physics*, 199(3):1018–1026, May 2020.
- [63] HEATES Collaboration, S. Okada, D. A. Bennett, et al. First application of superconducting transition-edge sensor microcalorimeters to hadronic atom X-ray spectroscopy. *Progress of Theoretical and Experimental Physics*, 2016(9):091D01, September 2016.
- [64] B. Calkins, P. L. Mennea, A. E. Lita, et al. High quantum-efficiency photon-number-resolving detector for photonic on-chip information processing. *Optics Express*, 21(19):22657–22670, September 2013.

- [65] M. P. Croce, M. K. Bacrania, E. M. Bond, et al. Superconducting Transition-Edge Sensor Microcalorimeters for Ultra-High Resolution Alpha-Particle Spectrometry. *IEEE Transactions on Applied Superconductivity*, 21(3):207–210, June 2011.
- [66] G. C. Hilton, J. M. Martinis, D. A. Wollman, et al. Impact energy measurement in time-of-flight mass spectrometry with cryogenic microcalorimeters. *Nature*, 391(6668):672–675, February 1998.
- [67] M. Frank. Mass spectrometry with cryogenic detectors. *Nuclear Instruments and Methods in Physics Research Section A: Accelerators, Spectrometers, Detectors and Associated Equipment*, 444(1):375–384, April 2000.
- [68] R. Smith, H. Takahashi, Y. Mitsuya, and T. Jodoi. Development of Transition Edge Sensors for the Detection of Secondary Electrons. *IEEE Transactions on Applied Superconductivity*, 33(5):1–3, August 2023.
- [69] R. Smith, M. Ohno, Y. Miura, et al. Microcalorimetry of Carbon Ion Beam for Medical Treatment by Transition Edge Sensor. *Journal of Low Temperature Physics*, 199(3):1012–1017, May 2020.
- [70] R. Smith, M. Ohno, Y. Mitsuya, and H. Takahashi. Optimized Detector Design of Transition-Edge Sensors for the Calorimetry of Carbon Ion Beams. *Journal of Low Temperature Physics*, 209(3):427–432, November 2022.
- [71] S. J. Lee, J. S. Adams, S. R. Bandler, et al. Fine pitch transition-edge sensor X-ray microcalorimeters with sub-eV energy resolution at 1.5 keV. *Applied Physics Letters*, 107(22):223503, December 2015.
- [72] J. N. Ullom, J. A. Beall, W. B. Doriese, et al. Optimized transition-edge x-ray microcalorimeter with 2.4eV energy resolution at 5.9keV. *Applied Physics Letters*, 87(19):194103, November 2005.
- [73] N. Iyomoto, S. R. Bandler, R. P. Brekosky, et al. Close-packed arrays of transition-edge x-ray microcalorimeters with high spectral resolution at 5.9keV. *Applied Physics Letters*, 92(1):013508, January 2008.
- [74] K. Mitsuda. TES X-ray microcalorimeters for X-ray astronomy and material analysis. *Physica C: Superconductivity and its Applications*, 530:93–97, November 2016.
- [75] R. Hijmering, P. Khosropanah, M. Ridder, et al. Effects of Magnetic Fields on Highly Sensitive TiAu TES Bolometers. *IEEE Transactions on Applied Superconductivity*, 23(3):2101505–2101505, June 2013.
- [76] S. J. Smith, J. S. Adams, C. N. Bailey, et al. Implications of weak-link behavior on the performance of Mo/Au bilayer transition-edge sensors. *Journal of Applied Physics*, 114(7):074513, August 2013.
- [77] R. Harwin. *Microscopic physics of transition edge sensors*. PhD thesis, University of Cambridge, 2020.

- [78] D. M. Glowacka, M. Crane, D. J. Goldie, and S. Withington. A Fabrication Route for Arrays of Ultra-low-Noise MoAu Transition Edge Sensors on Thin Silicon Nitride for Space Applications. *Journal of Low Temperature Physics*, 167(3):516–521, May 2012.
- [79] K. D. Irwin, G. C. Hilton, D. A. Wollman, and J. M. Martinis. Thermal-response time of superconducting transition-edge microcalorimeters. *Journal of Applied Physics*, 83(8):3978–3985, April 1998.
- [80] S. Withington, D. J. Goldie, and A. V. Velichko. Low-temperature thermal conductances of amorphous dielectric microbridges in the diffusive to ballistic transition. *Physical Review B*, 83(19):195418, May 2011.
- [81] D. Osman, S. Withington, D. J. Goldie, and D. M. Glowacka. Transition edge sensors with few-mode ballistic thermal isolation. *Journal of Applied Physics*, 116(6):064506, August 2014.
- [82] K. Irwin and G. Hilton. Transition-Edge Sensors. In C. Enss, editor, *Cryogenic Particle Detection*, Topics in Applied Physics, pages 63–150. Springer, Berlin, Heidelberg, 2005.
- [83] E. Figueroa-Feliciano. *Theory and Development of Position-Sensitive Quantum Calorimeters*. PhD thesis, Stanford University, 2001.
- [84] J. C. Mather. Bolometer noise: Nonequilibrium theory. *Applied Optics*, 21(6):1125–1129, March 1982.
- [85] S. H. Moseley, J. C. Mather, and D. McCammon. Thermal detectors as x-ray spectrometers. *Journal of Applied Physics*, 56(5):1257–1262, September 1984.
- [86] A. Szymkowiak, R. Kelley, S. Moseley, and C. Stahle. Signal processing for microcalorimeters. *Journal of Low Temperature Physics*, 93(3-4):281–285, 1993.
- [87] J. S. Adams, S. R. Bandler, L. E. Brown, et al. Real-Time Data Processing for X-Ray Spectroscopy. *AIP Conference Proceedings*, 1185(1):274–277, December 2009.
- [88] S. H. Moseley, J. C. Mather, and D. McCammon. Thermal detectors as x-ray spectrometers. *Journal of Applied Physics*, 56(5):1257–1262, September 1984.
- [89] P. Ripoché and J. Heyl. Progress toward optimizing energy and arrival-time resolution with a transition-edge sensor from simulations of x-ray-photon events. *Journal of Astronomical Telescopes, Instruments, and Systems*, 7(1):018002, February 2021.
- [90] D. J. Fixsen, S. H. Moseley, B. Cabrera, and E. Figueroa-Feliciano. Pulse estimation in nonlinear detectors with nonstationary noise. *Nuclear Instruments and Methods in Physics Research Section A: Accelerators, Spectrometers, Detectors and Associated Equipment*, 520(1):555–558, March 2004.
- [91] J. W. Fowler, B. K. Alpert, D. A. Bennett, et al. A reassessment of absolute energies of the x-ray L lines of lanthanide metals. *Metrologia*, 54(4):494–511, August 2017.

- [92] D. Yan, J. C. Weber, K. M. Morgan, et al. Transition-Edge Sensor Optimization for Hard X-ray Applications. *IEEE Transactions on Applied Superconductivity*, 31(5):1–5, August 2021.
- [93] S. R. Bandler, E. Figueroa-Feliciano, N. Iyomoto, et al. Non-linear effects in transition edge sensors for X-ray detection. *Nuclear Instruments and Methods in Physics Research Section A: Accelerators, Spectrometers, Detectors and Associated Equipment*, 559(2):817–819, April 2006.
- [94] P. Peille, M. T. Ceballos, B. Cobo, et al. Performance assessment of different pulse reconstruction algorithms for the ATHENA X-ray Integral Field Unit. In *Space Telescopes and Instrumentation 2016: Ultraviolet to Gamma Ray*, volume 9905, pages 1709–1722. SPIE, July 2016.
- [95] B. Cobo, N. Cardiel, M. T. Ceballos, and P. Peille. Pulse processing in TES detectors: Comparative of different short filter methods based on optimal filtering: Case study for Athena X-IFU. In *Space Telescopes and Instrumentation 2020: Ultraviolet to Gamma Ray*, volume 11444, pages 1333–1344. SPIE, December 2020.
- [96] M. S. Chung and T. E. Everhart. Simple calculation of energy distribution of low-energy secondary electrons emitted from metals under electron bombardment. *Journal of Applied Physics*, 45(2):707–709, February 1974.
- [97] C. Walker, M. El-Gomati, A. Assa'd, and M. Zadražil. The secondary electron emission yield for 24 solid elements excited by primary electrons in the range 250-5000 eV: A theory/experiment comparison. *Scanning*, 30(5):365–380, September 2008.
- [98] M. M. EL Gomati, C. G. H. Walker, A. M. D. Assa'd, and M. Zadražil. Theory Experiment Comparison of the Electron Backscattering Factor from Solids at Low Electron Energy (250-5,000 eV): Electron backscattering factor from solids. *Scanning*, 30(1):2–15, January 2008.
- [99] Z. J. Ding, H. M. Li, K. Goto, et al. Energy spectra of backscattered electrons in Auger electron spectroscopy: Comparison of Monte Carlo simulations with experiment. *Journal of Applied Physics*, 96(8):4598–4606, October 2004.
- [100] W. Smekal, W. S. M. Werner, and C. J. Powell. Simulation of electron spectra for surface analysis (SESSA): A novel software tool for quantitative Auger-electron spectroscopy and X-ray photoelectron spectroscopy. *Surface and Interface Analysis*, 37(11):1059–1067, 2005.
- [101] K. M. Patel, S. Withington, C. N. Thomas, et al. Simulation method for investigating the use of transition-edge sensors as spectroscopic electron detectors. *Superconductor Science and Technology*, 34(12):125007, October 2021.
- [102] R. A. Fisher. Theory of Statistical Estimation. *Mathematical Proceedings of the Cambridge Philosophical Society*, 22(5):700–725, July 1925.

- [103] C. R. Rao. Information and the Accuracy Attainable in the Estimation of Statistical Parameters. In S. Kotz and N. L. Johnson, editors, *Breakthroughs in Statistics: Foundations and Basic Theory*, Springer Series in Statistics, pages 235–247. Springer, New York, NY, 1992.
- [104] R. Welty and J. Martinis. Two-stage integrated SQUID amplifier with series array output. *IEEE Transactions on Applied Superconductivity*, 3(1):2605–2608, March 1993.
- [105] C. G. Pappas, J. W. Fowler, D. A. Bennett, et al. A Highly Linear Calibration Metric for TES X-ray Microcalorimeters. *Journal of Low Temperature Physics*, 193(3):249–257, November 2018.
- [106] K. Goto and Y. Takeichi. Carbon reference Auger electron spectra measured with a high-performance cylindrical mirror analyzer. *Journal of Vacuum Science & Technology A*, 14(3):1408–1414, May 1996.
- [107] Planck HFI Core Team, P. A. R. Ade, N. Aghanim, et al. *Planck* early results. IV. First assessment of the High Frequency Instrument in-flight performance. *Astronomy & Astrophysics*, 536:A4, December 2011.
- [108] R. C. Zeller and R. O. Pohl. Thermal Conductivity and Specific Heat of Noncrystalline Solids. *Physical Review B*, 4(6):2029–2041, September 1971.
- [109] P. w. Anderson, B. I. Halperin, and c. M. Varma. Anomalous low-temperature thermal properties of glasses and spin glasses. *The Philosophical Magazine: A Journal of Theoretical Experimental and Applied Physics*, 25(1):1–9, January 1972.
- [110] W. A. Phillips. Tunneling states in amorphous solids. *Journal of Low Temperature Physics*, 7(3):351–360, May 1972.
- [111] Albert C. Thompson, Janos Kirz, David T. Atwood, et al. *X-Ray Data Booklet*. Lawrence Berkeley National Laboratory, University of California, third edition edition, September 2009.
- [112] N. A. Wakeham, J. S. Adams, S. R. Bandler, et al. Refinement of Transition-Edge Sensor Dimensions for the X-Ray Integral Field Unit on ATHENA. *IEEE Transactions on Applied Superconductivity*, 33(5):1–6, August 2023.
- [113] A. M. Kadin. Spatial Structure of the Cooper Pair. *J Supercond Nov Magn*, 20(4):285–292, May 2007.
- [114] J. M. Martinis, G. C. Hilton, K. D. Irwin, and D. A. Wollman. Calculation of TC in a normal-superconductor bilayer using the microscopic-based Usadel theory. *Nuclear Instruments and Methods in Physics Research Section A: Accelerators, Spectrometers, Detectors and Associated Equipment*, 444(1):23–27, April 2000.
- [115] F. J. García de Abajo. Optical excitations in electron microscopy. *Reviews of Modern Physics*, 82(1):209–275, February 2010.

- [116] L. Tian, J. Zhu, M. Liu, and Z. An. Bremsstrahlung spectra produced by kilovolt electron impact on thick targets. *Nuclear Instruments and Methods in Physics Research Section B: Beam Interactions with Materials and Atoms*, 267(21):3495–3499, November 2009.
- [117] S. J. Smith, C. H. Whitford, G. W. Fraser, and D. J. Goldie. Characterisation and modelling of transition edge sensor distributed read-out imaging devices. *Nuclear Instruments and Methods in Physics Research Section A: Accelerators, Spectrometers, Detectors and Associated Equipment*, 559(2):500–502, April 2006.
- [118] S. J. Smith, J. S. Adams, S. R. Bandler, et al. Toward 100,000-Pixel Microcalorimeter Arrays Using Multi-absorber Transition-Edge Sensors. *Journal of Low Temperature Physics*, 199(1):330–338, April 2020.
- [119] K. M. Morgan, S. E. Busch, M. E. Eckart, et al. Large Area Transition Edge Sensor X-ray Microcalorimeters for Diffuse X-ray Background Studies. *Journal of Low Temperature Physics*, 176(3):331–336, August 2014.
- [120] J. C. Fuggle and S. F. Alvarado. Core-level lifetimes as determined by x-ray photoelectron spectroscopy measurements. *Physical Review A*, 22(4):1615–1624, October 1980.
- [121] E. Jensen, R. A. Bartynski, S. L. Hulbert, and E. D. Johnson. Auger photoelectron coincidence spectroscopy using synchrotron radiation. *Review of Scientific Instruments*, 63(5):3013–3026, May 1992.
- [122] A. Lamas-Linares, B. Calkins, N. A. Tomlin, et al. Nanosecond-scale timing jitter for single photon detection in transition edge sensors. *Applied Physics Letters*, 102(23):231117, June 2013.
- [123] J. H. D. Eland, O. Vieuxmaire, T. Kinugawa, et al. Complete Two-Electron Spectra in Double Photoionization: The Rare Gases Ar, Kr, and Xe. *Physical Review Letters*, 90(5):053003, February 2003.
- [124] M. Hattass, T. Jalowy, A. Czasch, et al. A 2π spectrometer for electron–electron coincidence studies on surfaces. *Review of Scientific Instruments*, 75(7):2373–2378, June 2004.
- [125] T. Arion and U. Hergenhan. Coincidence spectroscopy: Past, present and perspectives. *Journal of Electron Spectroscopy and Related Phenomena*, 200:222–231, April 2015.